Analysis and Control of Nonlinear Vibration in Inertial Actuators

Laurence Ian Wilmshurst

A thesis submitted for the degree of

Doctor of Philosophy

University of Southampton

Faculty of Engineering and the Environment

Institute of Sound and Vibration Research

August 2015

Abstract

Proof-mass actuators are typically used to supply a secondary control force to a supporting structure for the purpose of improving its performance through active vibration control. These devices comprise a magnetic proof-mass that accelerates in response to an input current, and the resulting inertia provides a reaction force on the actuator casing and the structure itself. Due to design constraints and the need to prevent actuator damage, the displacement of the proof-mass is usually bounded by its stroke length, which is determined by the distance between the actuator end stops. If the proof-mass reaches the end of the stroke, it will collide with the end stops, thereby imparting large shocks to the supporting structure that may destabilise the closed-loop system. This phenomenon, known as stroke saturation, is strongly nonlinear and invalidates the linear Nyquist stability criterion, which significantly complicates the assessment of closed-loop stability. As an example, stroke saturation may occur when using proof-mass actuators in active car suspensions, due to large impulsive forces from the road.

The aim of this thesis is to examine the dynamical behaviour of several proof-mass actuators using experimental measurements, including the effects of stroke saturation and other nonlinearities. The experimental data is used to establish a Simulink model of an inertial actuator by applying nonlinear identification techniques. It is found that the actuator dynamics can be represented using a nonlinear single-degree-of-freedom system, where the actuator nonlinearities are modelled using various polynomial and piecewise terms. This is confirmed by comparing the model results with the experimental data.

Using the Simulink model, it is shown that the actuator nonlinearities significantly reduce the closed-loop gain margin by exploiting regions of potential instability that are present in the underlying linear closed-loop system. Therefore, the relationship between the actuator nonlinearities and the closed-loop stability depends on the choice of underlying linear controller, as the actuator nonlinearities tend to accentuate underlying stability issues rather than induce instability by themselves.

To prevent stroke saturation from destabilising the closed-loop system, an on-off control law may be applied by implementing a knock detector and deactivating the control signal for a short time period once stroke saturation is detected. Provided that a suitable deactivation period is specified, the on-off control law is able to prevent stroke saturation from destabilising the closed-loop system, thereby increasing the closed-loop gain margin.

Table of Contents

List of Figures

List of Tables

Declaration of Authorship

I, Laurence Wilmshurst, declare that this thesis entitled,

"Analysis and Control of Nonlinear Vibration in Inertial Actuators"

and the work presented in it are my own and has been generated by me as the result of my own original research.

I confirm that:

1. This work was done wholly or mainly while in candidature for a research degree at this University;
2. Where any part of this thesis has previously been submitted for a degree or any other qualification at this University or any other institution, this has been clearly stated;
3. Where I have consulted the published work of others, this is always clearly attributed;
4. Where I have quoted from the work of others, the source is always given. With the exception of such quotations, this thesis is entirely my own work;
5. I have acknowledged all main sources of help;
6. Where the thesis is based on work done by myself jointly with others, I have made clear exactly what was done by others and what I have contributed myself;
7. Parts of this work have been published as listed at the end of chapter 1.

Signed: L. I. Wilmshurst

Date: 01/08/2015

List of Abbreviations

FFT: Fast Fourier transform

FRF: Frequency response function

IIR: Infinite impulse response

LCO: Limit-cycle oscillation

LSE: Least-square-error

MDOF: Multi-degree-of-freedom

MIMO: Multi-input multi-output

MISO: Multi-input single-output

SDOF: Single-degree-of-freedom

SISO: Single-input single-output

VFC: Velocity feedback control

Acknowledgements

First of all, I would like to thank my primary supervisor Dr Maryam Ghandchi-Tehrani for having the courage to take me on as her first Ph.D student. Her enthusiasm, diligence, and friendly attitude have been indispensible for helping me through the twists and turns of completing a Ph.D, and I feel very fortunate to receive such good academic support. I'm certain that she will continue to be an excellent supervisor for future Ph.D students. I would also like to thank my secondary supervisor Professor Stephen Elliott for his excellent advice and comments, and his ability to see the bigger picture at the most crucial times of the project.

Next, I would like to thank my reviewers Dr Neil Ferguson and Professor Steve Daley for their hard work and helpful constructive feedback, which enabled me to improve the thesis and prepare for the viva.

My colleagues and friends also deserve credit for their helpful comments and companionship during the day-to-day aspects of the Ph.D. Many thanks to Nikhil Banda, Zhenbin Zhang, Eduardo Latorre Iglesias, Alicia Costalago Meruelo, Qiyun Jin, Xianying Zhang, Marcos Simon Galvez, Guido Zarini, Andrew Causon, Luigi Simeone, Manuela Bung, and Caroline Davie.

I would like to thank my parents for their encouragement and understanding during my time as a Ph.D student. It was through their support in my pursuits that I was able to study at the ISVR in the first place, and I feel very fortunate to have been given this opportunity.

Last, but certainly not least, I am deeply indebted to my darling wife Ye Wilmshurst for her considerable patience, faithfulness, kindness, and love. She has helped me through a lot of challenging times and preserved my sanity during the long periods of thesis writing during the final stages. Thank you, I am very proud of you.

Laurence Ian Wilmshurst
Institute of Sound and Vibration Research
August 2015

Chapter 1

Introduction

1.1 Motivation

In control engineering, the design and implementation of effective control systems is crucial for the successful operation of modern technology. The basis of control engineering is to improve the performance of an otherwise uncontrolled system, whether it gives greater precision, better adaptation to changes in its environment, or prevents instability from occurring. Key examples of man-made control systems include cruise control, active car suspensions, thermostats, and robotics [1]; however, many control systems also occur naturally, such as the active feedback mechanism in the human cochlear [2], the regulation of the internal temperature of the body [3], and the feedback loops that control the climate of the planet [4]. Two examples are illustrated in Figure 1.1.

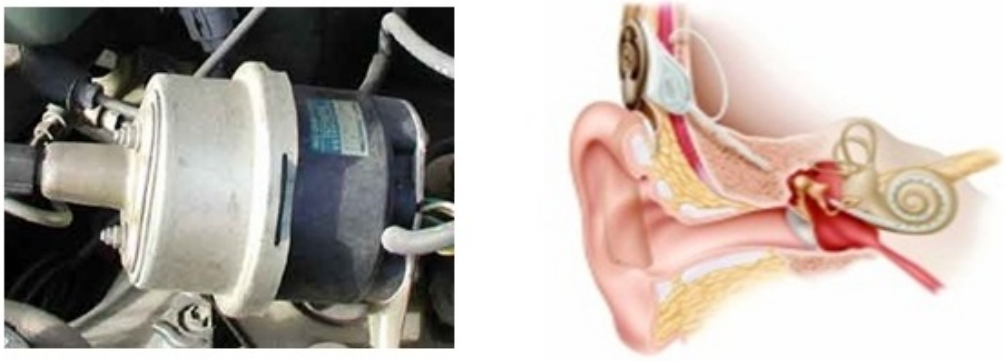

Figure 1.1: Illustrations of a cruise control system [5] and the human auditory system [2].

This thesis is primarily concerned with applying vibration control to structures [6], which is often required to improve the performance of the structure and minimise unwanted vibrations. Examples include: active tendon control of cable-stayed bridges [7], vibration control of an AgustaWestland W30 helicopter airframe [8], and active engine mounts in road vehicles [9].

Under ideal circumstances, the structure undergoing control is assumed to behave as a linear system, where the principle of superposition applies and the structural response can be written as a linear combination of the loading forces. Here, the structural dynamics may be modelled by the following linear equation,

$$\mathbf{M}\ddot{\mathbf{y}}(t) + \mathbf{C}\dot{\mathbf{y}}(t) + \mathbf{K}\mathbf{y}(t) = \mathbf{f}(t) \tag{1.1}$$

where **M, C, K** are the mass, damping, stiffness matrices respectively;

$\mathbf{y}(t), \dot{\mathbf{y}}(t), \ddot{\mathbf{y}}(t)$ are the structural displacement, velocity, and acceleration vectors;

$\mathbf{f}(t)$ represents the loading forces.

However, there are many types of structures that do not conform to this ideal behaviour, due to the presence of structural nonlinearities. Simple examples of structural nonlinearities include friction and backlash in joints [10], buckling and deformation in plate structures [11], and nonlinear stiffening suspensions [12]. In particular, there is an increasing demand for smart, lightweight, flexible structures that have multi-functional capabilities, such as damage detection, shape morphing, and adaptability to varying environmental conditions [13]. These structures are especially susceptible to nonlinear, large-amplitude vibrations. Since structural nonlinearities occur in a wide class of engineering problems, it is often necessary to account for the nonlinear dynamics of the structure.

The equation of motion for a general nonlinear structure may be written as,

$$\mathbf{M}\ddot{\mathbf{y}}(t) + \mathbf{C}\dot{\mathbf{y}}(t) + \mathbf{K}\mathbf{y}(t) + \mathbf{f}_{\mathbf{NL}}(\mathbf{y}(t), \dot{\mathbf{y}}(t)) = \mathbf{f}(t) \tag{1.2}$$

where $\mathbf{f}_{\mathbf{NL}}(\mathbf{y}(t), \dot{\mathbf{y}}(t))$ is a vector function of velocity and displacement that is capable of representing a wide range of nonlinear dynamic behaviour. This nonlinear function has the effect of greatly increasing the mathematical complexity of the structural dynamics, which cannot be described using linear superposition. These nonlinear dynamics are often detrimental to the performance to the structure, and minimising their effects is one such control objective.

Traditionally, vibration control was carried out using passive structural modifications, which involves changing the mass, stiffness and damping matrices of the structure by mechanical means. Whilst this approach ensures that the modified structure is guaranteed to remain stable, due to the positive-definite symmetric property of the matrices, it is often ineffective at low frequencies, where the resonant modes of the structure are most prominent. Additionally, these modifications tend to add mass to the structure, which is contradictory to the modern requirements for lightweight structures.

In order to control the low-frequency resonant modes of a structure, active vibration control may be utilised to modify the mass, damping, or stiffness matrices of a structure by electro-mechanical means, using acceleration, velocity, or displacement feedback [14]. This approach has received considerable attention over the past few decades as a solution to low-frequency vibration problems in the civil [15], marine [16], and aerospace [8] industries. Particular examples include the use of displacement feedback control to move the first few structural modes away from problematic forcing frequencies [17], and the use of decentralised velocity feedback control to implement skyhook damping [18]. Velocity feedback is particularly advantageous for flexible, lightweight structures with little inherent damping, and is a popular method for reducing the magnitude of the first few structural resonances through active damping [19].

In a practical scenario, the feedback loop is created by placing numerous accelerometers on the structure for the purpose of measuring the structural acceleration. Using a controller matrix, a series of control voltages $\mathbf{u}(t)$ that are proportional to the structural states are obtained from the measured accelerometer signals. These control voltages are then used to drive a series of actuators, in order to generate the secondary forces $\mathbf{f_s}(t)$ required to control the structure. By assuming a pure-gain linear controller, the secondary control forces may be written as,

$$\mathbf{f_s}(t) = -\mathbf{BGDy}(t) - \mathbf{BHD}\dot{\mathbf{y}}(t) - \mathbf{BLD}\ddot{\mathbf{y}}(t) \tag{1.3}$$

where $\mathbf{G}, \mathbf{H}, \mathbf{L}$ are the displacement, velocity, and acceleration control gain matrices;

$\mathbf{B}$ is the actuator distribution matrix;

$\mathbf{D}$ is the sensor distribution matrix.

If the secondary control force is applied to a linear structure that is fully controllable and observable, the closed-loop equations of motion become,

$$(\mathbf{M}+\mathbf{BLD})\ddot{\mathbf{y}}(t)+(\mathbf{C}+\mathbf{BHD})\dot{\mathbf{y}}(t)+(\mathbf{K}+\mathbf{BGD})\mathbf{y}(t)=\mathbf{f}(t) \tag{1.4}$$

such that the mass, damping, and stiffness matrices may be chosen arbitrarily by careful consideration of the displacement, velocity, and acceleration feedback control matrices.

Since these modified matrices may become non-symmetric, active vibration control offers a greater degree of flexibility than passive structural modification. However, this also leads to the possibility that the closed-loop system will become unstable. In the occurrence of instability, the structural states exponentially increase over time, resulting in control failure and, in extreme cases, the destruction of the structure and potential loss of life. Therefore, it is imperative to assess the absolute stability of the closed-loop system to ensure that the modified structure will remain stable under all reasonable operating conditions. This control objective must be met in conjunction with the performance requirements for the controller to be effective.

1.2 Methods for analysing closed-loop stability

It is well-known that all poles of a system should lie on the left-hand side of the complex plane to guarantee stability, since this corresponds to exponential decay. Therefore, the relative stability of a closed-loop system may be assessed by defining its transfer function in terms of the open-loop system and controller, and then finding the location of the closed-loop poles.

In the context of active vibration control, the control loop is defined by the open-loop plant matrix $\mathbf{H}(s)$, which is the transfer function between the actuator inputs $\mathbf{u}(t)$ and the accelerometer outputs $\ddot{\mathbf{y}}(t)$ when no feedback control is applied, and the controller matrix $\mathbf{G}(s)$. The control loop is closed when the output control voltages of $\mathbf{G}(s)$ are used as the actuator inputs to $\mathbf{H}(s)$, as illustrated in Figure 1.2. The closed-loop transfer function $\bar{\mathbf{H}}(s)$ is given by,

$$\bar{\mathbf{H}}(s)=\big(\mathbf{I}+\mathbf{G}(s)\mathbf{H}(s)\big)^{-1}\mathbf{H}(s) \tag{1.5}$$

and therefore, the closed-loop poles are found by solving the characteristic equation,

$$\det\big(\mathbf{I}+\mathbf{G}(s)\mathbf{H}(s)\big)=0 \tag{1.6}$$

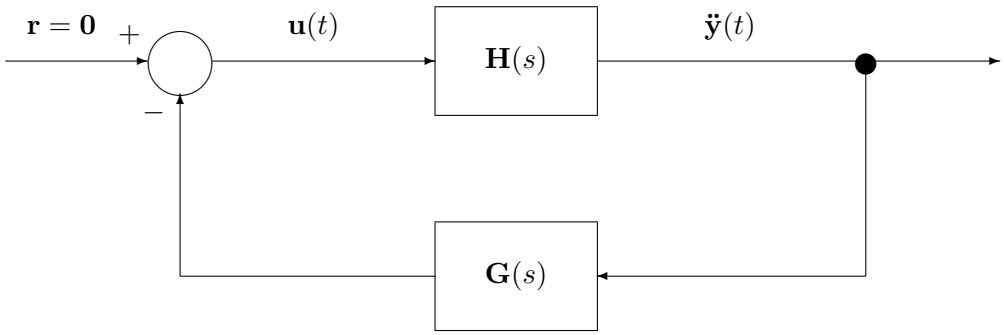

Figure 1.2: Example of the open-loop plant matrix $\mathbf{H}(s)$, which contains the dynamics of the actuators, structure, and sensors, with feedback controller $\mathbf{G}(s)$.

If the open-loop plant and controller matrix are *single-input single-output* (SISO), then Eq. 1.6 reduces to,

$$1 + G(s)H(s) = 0 \tag{1.7}$$

Eq. 1.7 shows that the poles of the closed-loop system are related to the zeros of the open-loop plant and controller. This indicates that the relative stability of the closed-loop system may be assessed from the Nyquist contour (locus) of $G(s)H(s)$. This is the basis of the Nyquist stability criterion [20].

A common method for ensuring closed-loop stability, in principle, is to use collocated sensor-actuator pairs to control the structure [19], where the control force is applied in the same location as the structural acceleration is measured. In this manner, the mass, damping, and stiffness matrices remain positive-definite symmetric, and the closed-loop system is unconditionally stable. This may be demonstrated using the interlacing pole-zero property [19], where each pole has a corresponding zero (shown in Figure 1.3) that prevents the root loci from entering the right-hand of the complex plane.

In practical applications, however, it is difficult or impossible to achieve exact collocation, for two reasons. Firstly, the sensors and actuators are rarely placed at exactly the same location in a distributed mass structure. Secondly, the sensors and actuators also exhibit their own dynamic behaviour, thereby introducing additional poles and zeros that invalidate the interlacing pole-zero property [21]. As a result, most feedback control systems are conditionally stable, and so it is important to assess the relative closed-loop stability.

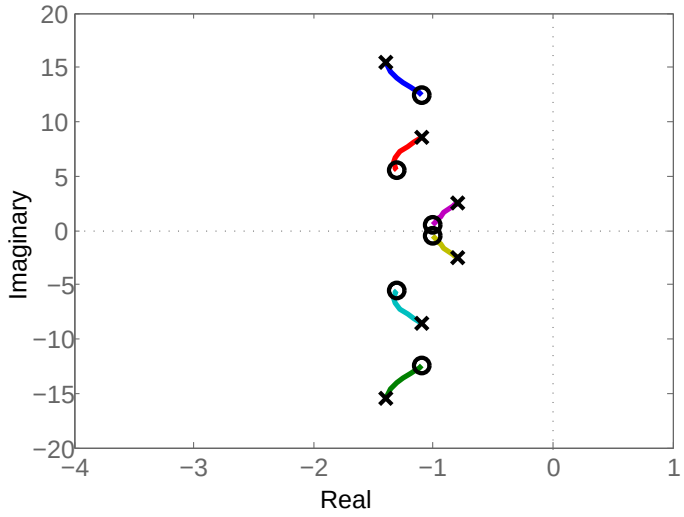

Figure 1.3: Illustration of the interlacing pole-zero property for collocated control systems on a root locus map.

1.3 Inertial actuators

Proof-mass actuators, otherwise known as inertial actuators, are widely used in active control applications to control lightweight, high-performance, flexible structures with low inherent damping. These actuators comprise a proof-mass, which is attached to the actuator casing via a spider suspension, a current-carrying coil, and a magnet that is either fixed or moves with the proof-mass. The control force is generated by the inertia of the proof-mass, which accelerates in response to the current in the coil and provides a reaction force on the actuator casing. By attaching these actuators to a supporting structure, the current induces an electromotive force that acts between the proof-mass and the structure. A cross-section of a proof-mass actuator is shown in Figure 1.4.

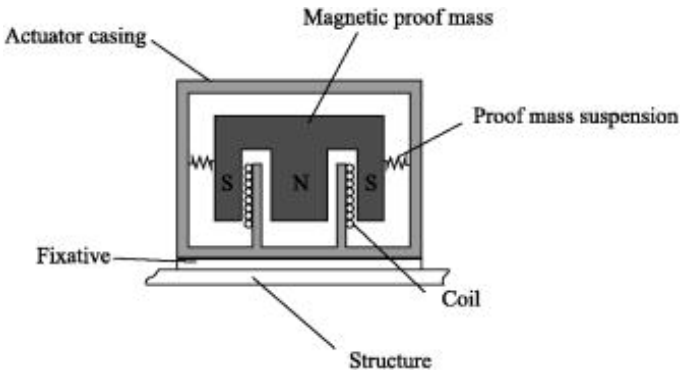

Figure 1.4: Cross section of inertial actuator. Reproduced with permission from [22].

There are two key advantages with using proof-mass actuators to provide active feedback control. Firstly, the actuators are capable of applying large forces to a structure, relative to their weight [23]. Secondly, there is no need for a "ground" reference to provide ineria, since the actuators are attached to the structure [24]. For these reasons, proof-mass actuators are often encountered in pioneering applications such as space exploration [25], where gravitational effects are negligible. These space structures operate in extreme environments that feature large variations in pressure, temperature, radiation *etc.* [26], which pose numerous engineering challenges. Ensuring the closed-loop stability of these structures is a paramount issue, as the consequences of instability would be disastrous.

Since proof-mass actuators essentially behave as a mass-spring-damper oscillator, their force-voltage dynamics are typically modelled using a linear second-order single-degree-of-freedom system, with a complex pole pair and two repeated zeros at the origin of the complex plane. Here, the actuator exhibits a single low-frequency resonance at the peak force frequency, denoted by ω_f, and tends to a constant gain g_a above this frequency. Provided that the lowest frequency of the control bandwidth is above a critical frequency, denoted by ω_a, the actuator behaves as an *ideal force generator*, with a constant gain g_a and zero phase (displayed in Figure 1.5). This leads to the condition that the first structural resonance should be well above the natural frequency of the actuator for optimal control [27].

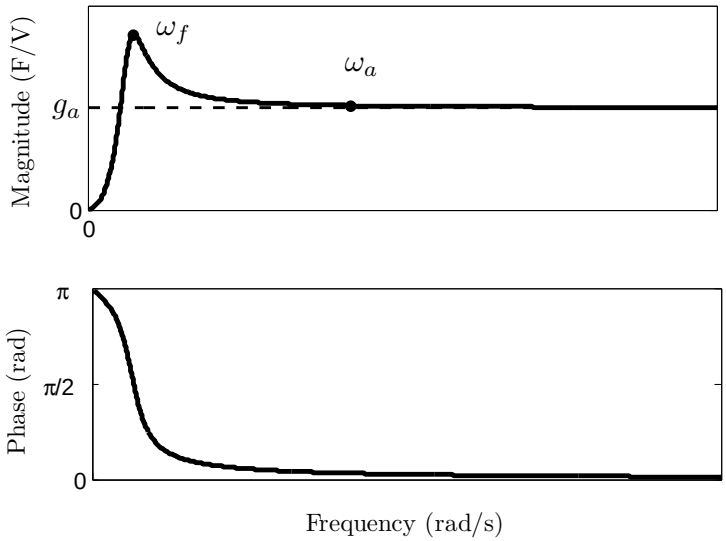

Figure 1.5: Bode plots of an inertial actuator model, with peak force frequency ω_f and critical frequency ω_a, where the ideal force generator assumption becomes valid.

There are also two inherent drawbacks with using inertial actuators. The first drawback is that the resulting control system is non-collocated [21,28]. This is because the proof-mass dynamics are coupled with the structural dynamics, and the electromotive force of the actuator is applied between the proof-mass and the structure. Consequently, the closed-loop system may be prone to instability, particularly when velocity feedback control is utilised. In this case, the poles of the actuator move towards the right-hand side of the complex plane as the control gain increases, since the actuator mode is amplified by the feedback controller [21].

This problem may, in principle, be overcome using a phase-loop compensator to account for the phase shift introduced at the natural frequency of the actuator [29]. However, the effectiveness of these compensators may be reduced by variations and uncertainties in the open-loop plant, particularly with regards to weak nonlinearities in the actuator or structure. Furthermore, the compensator may detrimentally affect the closed-loop stability if pole-zero flipping occurs [19], and so care must be taken when designing and implementing such compensators.

The second drawback with using inertial actuators is the finite stroke length, which imposes limits on the maximum proof-mass displacement and, therefore, the effective control force. If the input to the actuator is sufficiently large (either mechanical or electrical), the displacement of the proof-mass will reach the end of its stroke and collide with the end stops of the actuator casing, thereby resulting in impulsive shocks that can damage the structure and destabilise the closed-loop system. This phenomenon, known as *stroke saturation*, is illustrated in the force-time signal in Figure 1.6.

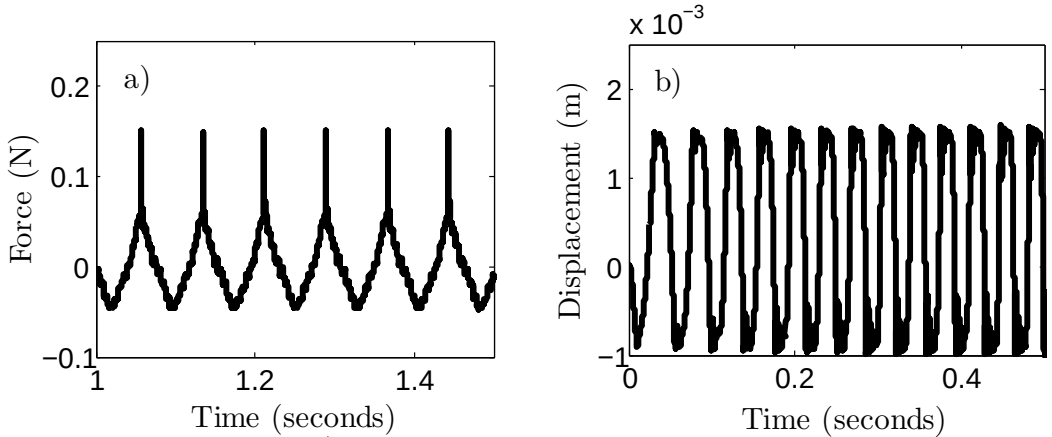

Figure 1.6: Illustrations of a) force-time signal with stroke saturation and b) limit-cycle oscillation behaviour as a result of stroke saturation.

Ideally, an inertial actuator will operate within its intended regime and the possibility of stroke saturation may be neglected, particularly if the feedback controller is relatively conservative. However, in many control applications, the actuators may sometimes be driven beyond their intended operating region, and the resulting dynamics are strongly nonlinear. For example, actuator nonlinearity may occur when using proof-mass actuators in active car suspensions, where large, impulsive excitation forces from the road cause the actuators to saturate. The actuator nonlinearities are typically detrimental to the stability of the structure, since they may destabilise the closed-loop system for conditions that are shown to be stable using linear analysis. An example of a limit-cycle oscillation induced by the destabilising effects of stroke saturation is shown in Figure 1.6b). Furthermore, the effects of stroke saturation are particularly severe for MIMO systems with multiple actuators, since the destabilisation of one control loop will result in the destabilisation of all the control loops [30].

The problem of stroke saturation was highlighted by Chase *et al.* [24], where a velocity feedback controller is applied to a buckling beam and the effects of destabilisation are observed. This problem was overcome using a secondary controller that helps prevent stroke saturation from occurring, and so the destabilising effects are reduced. However, the focus of the study is using active vibration control to stabilise an inherently unstable open-loop system rather than preventing destabilisation in the closed-loop system. Moreover, the additional controller does not completely prevent stroke saturation from occurring, and so closed-loop stability is not guaranteed.

In previous studies [23, 31], a variety of linear and nonlinear feedback controllers are considered for the prevention of stroke saturation, yet the primary motivation is to prevent damage rather than to ensure closed-loop stability, which is not mentioned. More recently, Baumann and Elliott [22] modelled the effects of stroke saturation as a nonlinear polynomial stiffness that becomes very large when the displacement of the proof-mass is saturated. These velocity-feedback simulations confirmed that stroke saturation may lead to closed-loop destabilisation, and it was speculated that the impulsive forces associated with stroke saturation overcome the inherent damping of the open-loop system. However, the findings of the study were not verified with experimental data, and no solution for preventing closed-loop destabilisation was presented.

A typical method for counteracting the destabilising effects of stroke saturation is to introduce nonlinearity into the controller dynamics. For example, hard-clipping saturation

may be deliberately introduced into the controller for the purpose of limiting the control voltage, thereby preventing actuator saturation occurring as a result of large control inputs [32]. Assuming a simple pure-gain velocity feedback controller with saturation, the controller dynamics are described as follows,

$$u(t) = \begin{cases} d \cdot \text{sign}(\dot{y}(t)) & \text{if } |\dot{y}(t)| \geq d \\ h\dot{y}(t) & \text{if } |\dot{y}(t)| < d \end{cases} \tag{1.8}$$

Whilst this approach is useful for preventing damage to the actuator or structure, it is not entirely capable of preventing the occurrence of stroke saturation or closed-loop destabilisation. This is because the proof-mass will still hit the end stops by mechanical means if a sufficiently large force is applied to the actuator or structure (*e.g.* on an active car suspension). Furthermore, it is well-known that applying saturation in the feedback controller has the effect of introducing limit-cycle oscillation behaviour if the closed-loop system is conditionally stable. Alternatively, feedback linearisation methods may be used to counteract weaker nonlinearities in the actuator suspension, yet this approach is not suitable for linearising the effects of stroke saturation, due to the complex dynamics.

Since stroke saturation cannot always be prevented from occurring, it is imperative to ensure that the stability of the closed-loop system is guaranteed within the specified gain margin, otherwise the system may become unstable and fail, with potentially disastrous repercussions.

1.4 Thesis overview

The primary aim of the thesis is to further develop the literature in this area by analysing the dynamics of several inertial actuators using experimental data and model simulations. Additionally, a nonlinear control law is devised for the purpose of preventing closed-loop destabilisation, based on temporarily deactivating the control signal when stroke saturation is detected. In principle, this ensures that the control force can no longer overcome the inherent damping of the structure.

First, a review of common types of structural nonlinearities (cubic stiffness, clearance, backlash *etc.*) with several analytical and numerical techniques (describing function, Volterra series, Runge-Kutta, Nyquist, Lyapunov *etc.*) is given in chapter 2. In chapter 3, an investigation into the effects of linear state feedback control on structural nonlin-

earities is conducted, using pole placement techniques on simple nonlinear systems such as Duffing oscillators. This led to the extension of the linear Sherman-Morrison receptance method [33, 34] to these nonlinear systems through the use of harmonic balance or Volterra series methods. In addition, bifurcation minimisation strategies are considered using pole placement and the nonlinear optimisation of the displacement and velocity feedback gains.

An experimental study of several inertial actuators, including a Micromega IA-01, a DataPhysics IV40, and a Labworks FG-142 actuator, is undertaken in chapter 4. For these experiments, the actuator in question is attached to a rigid block via a force sensor, which is used to measure the blocked force in response to sinusoidal input voltages. Using time-domain and frequency-domain analysis on the measured signals, the dynamics of these actuators were assessed to identify nonlinear behaviour, including suspension stiffness and stroke saturation. In addition, the first-order force-voltage and displacement-voltage transfer functions were obtained over a variety of excitation amplitudes.

In chapter 5, the experimental data taken from the Micromega IA-01 actuator is analysed in more detail for the purpose of identifying the underlying linear and nonlinear dynamics. The aim of this analysis is to construct a Simulink model of the actuator that can accurately emulate the dynamics observed experimentally. First, the underlying linear dynamics are considered, where the linear parameters are identified using linear least-squares methods. Next, the suspension nonlinearities are identified using two possible methods: the first method minimises the error between the simulated and measured peak resonance frequencies using nonlinear least-squares, and the second method utilises the measured restoring force surfaces of the actuator. These methods give consistent results. Finally, the stroke saturation dynamics are identified using contact parameters, such as the impact duration, coefficient of restitution, impulse magnitude *etc.*, and the stroke length is obtained from the restoring force curves.

In chapter 6, the Micromega actuator is applied to a flexible plate structure, and a simple SISO velocity feedback loop is devised. The dynamics of the open-loop plant were measured experimentally, and a nonlinear lumped parameter model of the actuator-plate configuration was devised in Simulink by curve-fitting to these measurements, based on the previously identified actuator model. By applying nonlinear analytical methods, such as the circle criterion and Lyapunov exponents, the stability characteristics of the lumped-parameter model were assessed as a means of predicting the closed-loop stability of the

physical system. It was found that the actuator nonlinearities greatly reduce the closed-loop stability margin, where limit-cycle oscillations are observed for velocity feedback gains that are far smaller than the linear Nyquist threshold. Using the total mechanical energy of the system as a Lyapunov function, it is shown that the actuator nonlinearities cause destabilisation by exploiting regions of potential instability in the underlying linear system, which greatly increases the kinetic energy of the proof-mass. To counteract the destabilising effects, a means of detecting the occurrence of stroke saturation was devised, using an accelerometer as a knock detector. This detection scheme is used as the basis of two types of nonlinear control laws, where the feedback gain is modified when stroke saturation is detected.

In chapter 7, the linear velocity feedback control loop was implemented on the physical actuator-plate configuration using a dSpace controller, and the closed-loop stability was assessed. It was found that the stability characteristics of the physical system were in agreement with the model predictions, where the occurrence of stroke saturation resulted in closed-loop destabilisation for relatively small feedback gains. An on-off nonlinear control law was then implemented and its performance was assessed; the results show that the control law, which temporarily deactivates the control signal when stroke saturation is detected, is able to stabilise the closed-loop system in most circumstances, thereby increasing the effective closed-loop gain margin. The findings and conclusions of this research are stated in chapter 8.

1.5 Original contributions

The main contributions of this thesis are as follows,

1. Development of the iterative Sherman-Morrison receptance method. The linear Sherman-Morrison receptance method has been extended to a simple class of nonlinear structures by using an iterative scheme to account for the structural nonlinearity when the eigenvalues are assigned. To achieve this, the nonlinearity is represented using a describing function or Volterra series model, which is updated iteratively as the feedback gains converge to the required solution.

2. Application of experimental analysis and identification techniques for nonlinear inertial actuators. The dynamics of several types of inertial actuator were measured experimentally, and it was found that each actuator exhibits a weak stiffening nonlinearity in the suspension. The effects of stroke saturation were observed in two of the inertial actuators through the appearance of impulses in the force-time signals. Using nonlinear identification techniques, a Simulink model of the Micromega IA-01 actuator was constructed, which can emulate its dynamic behaviour with a high degree of accuracy.

3. Application of Lyapunov methods to establish physical causes of destabilisation. Using Lyapunov stability analysis, it was confirmed that stroke saturation may result in closed-loop destabilisation (as observed experimentally). In addition, it was found that the suspension nonlinearities reduce the gain margin in a less pronounced manner, and should also be taken into account when assessing closed-loop stability. The actuator nonlinearities are capable of destabilising the closed-loop system by exploiting regions of potential instability in the underlying linear closed-loop system.

4. Development of a simple nonlinear controller that prevents closed-loop destabilisation. A nonlinear on-off control law was designed and employed for the purpose of preventing closed-loop destabilisation. It was found that the closed-loop system may be stabilised under certain conditions by using the control law, where the control signal is deactivated for a short period of time when stroke saturation is detected, using an accelerometer as a knock detector.

Some of this work was presented to the wider academic community through journal papers and conference papers,

1. L. Wilmshurst, M. Ghandchi-Tehrani, S. J. Elliott. Active Vibration Control of a Duffing Oscillator using the Receptance Method. *International Conference on Noise and Vibration Engineering* (17^{th} - 19^{th} September 2012)

2. M. Ghandchi-Tehrani, L. I. Wilmshurst, S. J. Elliott. Receptance method for active vibration control of a nonlinear system. *Journal of Sound and Vibration* vol. 332, no. 19, pp. 4440 - 4449. 2013

3. L. I. Wilmshurst, M. Ghandchi-Tehrani, S. J. Elliott. Nonlinear vibrations of a stroke-saturated inertial actuator. *11th International Conference on Recent Advances in Structural Dynamics* (1$^{\text{st}}$ - 4$^{\text{th}}$ July 2013).

4. M. Ghandchi-Tehrani, L. I. Wilmshurst, S. J. Elliott. Bifurcation control of a Duffing oscillator using pole placement. Accepted for publication in January 2014. *Journal of Vibration and Control*

5. L. I. Wilmshurst, M. Ghandchi-Tehrani, S. J. Elliott. Active control and stability analysis of flexible structures using nonlinear proof-mas actuators. *Proceedings on the 9th International Conference on Structural Dynamics* (30$^{\text{th}}$ June - 2$^{\text{nd}}$ July 2014)

6. L. I. Wilmshurst, M. Ghandchi-Tehrani, S. J. Elliott. Preventing stroke saturation in proof-mass actuators using a detection scheme. *The 21st International Congress on Sound and Vibration* (13$^{\text{th}}$ - 17$^{\text{nd}}$ July 2014)

7. ISMA 2014 L. I. Wilmshurst, M. Ghandchi-Tehrani, S. J. Elliott. Nonlinear identification of proof-mass actuators accounting for stroke saturation. *International Conference on Noise and Vibration Engineering* (19$^{\text{th}}$ - 21$^{\text{st}}$ September 2014)

Two additional journal papers are currently in preparation for publication, based on the topics covered in chapters 6 and 7.

Chapter 2

Nonlinear Structural Dynamics

2.1 Introduction to nonlinear systems

The dynamics of a nonlinear structure are typically defined by a set of nonlinear differential equations that do not conform to the linear superposition principle [35]. This makes control problems challenging, since these dynamics are dependent on the excitation amplitude [36], and therefore, linear concepts such as normal mode transformation, frequency response functions, and Nyquist stability analysis cannot be directly applied to nonlinear problems.

In mathematical terms, all linear time-invariant systems conform to the following state-space representation,

$$\begin{aligned} \dot{\mathbf{x}} &= \mathbf{A}\mathbf{x} + \mathbf{B}\mathbf{u} \\ \mathbf{y} &= \mathbf{C}\mathbf{x} + \mathbf{D}\mathbf{u} \end{aligned} \tag{2.1}$$

where $\mathbf{A}, \mathbf{B}, \mathbf{C}, \mathbf{D}$ (the state, input, output, and feedforward matrices respectively) are amplitude-invariant and fully describe the system dynamics. In contrast, nonlinear systems are characterised using the following state-space representation,

$$\begin{aligned} \dot{\mathbf{x}} &= \mathbf{f}(\mathbf{x}, \mathbf{u}, t) \\ \mathbf{y} &= \mathbf{g}(\mathbf{x}, \mathbf{u}, t) \end{aligned} \tag{2.2}$$

which is far more generalised than Eq. 2.1. Devising general methods for assessing nonlinear systems is therefore particularly difficult, as an enormous range of dynamic possibilities needs to be covered. This can be summarised using the following analogy,

> *"Happy families are all alike; every unhappy family is unhappy in its own way."*— Leo Tolstoy, *Anna Karenina*

In this case, happy families are synonymous with linear systems and unhappy families are synonymous with nonlinear systems. The increased mathematical complexity of nonlinear systems means that finding analytical solutions to Eq. 2.2 is rarely possible. Instead, it is often necessary to obtain a solution numerically using simulations, which are less intuitive than analytical solutions and only reveal the behaviour of the nonlinear system for the specified situation. As a result, crucial dynamic behaviour of the nonlinear system, such as regions of instability, may be missed if these particular situations are not considered.

Motivation for nonlinear systems

Given that nonlinear systems often present considerable difficulties when undertaking performance and stability analysis, most structures are modelled using the assumption that the structural dynamics are linear [37]. This greatly simplifies the analysis of the structure, and enables the control engineer to make various assumptions about its dynamics, such as exponential evolution, amplitude-invariancy, and a single set of isolated equalibria [12]. However, it is also important to consider the inadequacies and limitations of the use of linear models when assessing the dynamics of a structure.

The first issue to consider is that linear systems rely on the superposition principle, which is very difficult to prove for all possible scenarios (amplitudes, frequencies, initial conditions *etc.*) and will eventually break down. As a consequence, all physical systems are nonlinear to some extent. Nonlinear systems have been encountered in almost all engineering sectors, where examples of nonlinear behaviour include: geometric nonlinearities in pendulums, clamped-clamped beams [38], turbine blades [39], and cable-stayed bridges [7], flexible wings with aerodynamic loading [40], helicopter blades [41], hydraulic actuators with friction and backlash nonlinearities [42], and drilling tools with stick-slip motion [43].

In some of these applications, nonlinear behaviour is destructive and needs to be controlled, particularly when system destabilisation occurs. Key examples include the nonlinear flutter phenomenon in commercial aircraft, which may destabilise the aircraft structure above a given flight speed threshold, and the cable-deck mode coupling of cable-stayed bridges, which results in large vibration amplitudes that can destroy the bridge.

In both cases, it is clear that both nonlinearities may cause life-threatening conditions that must be prevented; it is therefore vital that these nonlinearities are accounted for in the design and simulation phase.

The second issue to consider is that linear systems are not capable of exhibiting the rich dynamic phenomena [12] that occur in nonlinear systems, even when the nonlinearity is relatively simple. Nonlinear systems typically exhibit interesting and complex behaviour that does not occur in linear systems, including limit-cycle oscillations, bifurcations, and chaos. Key examples of these dynamic phenomena are as follows,

1. Super (sub)-harmonic oscillations. Whereas the steady-state output of a linear system to a monoharmonic input is also monoharmonic at the fundamental frequency, nonlinear systems tend to exhibit super(sub)-harmonic responses at integer multiples (factors) of the fundamental frequency, due to energy transfer between these frequencies.

2. FRF distortion. The FRF of a linear system is amplitude-invariant and expressed in terms of poles and zeros. In contrast, the first-order FRFs of a nonlinear system (if they exist) are also dependent on the excitation amplitude, resulting in variations in the peak resonance frequency as the excitation amplitude increases.

3. Bifurcations and deterministic chaos. The output response of a linear structure is always uniquely defined for a given input; conversely, nonlinear systems may exhibit multiple output response possibilities, depending on the initial conditions. This phenomenon is known as bifurcation. In extreme cases, the nonlinearity may result in a quasi-stochastic output response to a monoharmonic input, which varies strongly with the initial conditions; a form of deterministic chaos. Various procedures, such as the $0-1$ test for chaos [44], are used to determine whether the output signal is chaotic or purely stochastic.

4. Limit-cycle oscillations. A limit-cycle oscillation is a self-sustaining isolated periodic orbic that has a closed trajectory in phase space. For linear structures, limit-cycle oscillations may only occur in unperturbed marginally stable systems, which are unlikely to occur in practice. For nonlinear systems, the amplitude and frequency of limit-cycle oscillations are determined by the type of nonlinearity. A particular example of a nonlinear system that features limit-cycle oscillations is the Van-de-Pol oscillator [45].

5. Finite escape time. Whereas the states of an unstable linear system will tend to infinity as time tends to infinity, it is possible for the states of several types of nonlinear systems to reach infinity in a finite period of time.

6. Multiple isolated equilibria. A linear system has a single isolated equilibrium set at $\dot{\mathbf{x}}, \mathbf{x} = \mathbf{0}$. In contrast, nonlinear systems may exhibit multiple isolated equilibria that satisfy $\mathbf{f}(\mathbf{x}) = \mathbf{0}$. Several examples of nonlinear systems with multiple equilibria include the simple pendulum (equilibia at $y = [0, \pi]$) and buckling plates and beams [38].

7. Sum and difference frequencies. The combined response of a linear system to a series of dynamic loads, applied simultaneously, is always the sum of the individual responses to the loads applied independently [37]. This is not the case for nonlinear systems, since the superposition principle does not hold. As a result, the combined response of a nonlinear system to dual harmonic inputs (of frequencies ω_1 and ω_2) will contain frequency components at the sum $(\omega_1 + \omega_2)$ and difference $(\omega_1 - \omega_2)$ of the excitation frequencies.

An additional consideration is that nonlinear behaviour may be advantageous for the effective operation of a particular system. One interesting example of a beneficial nonlinearity is the active feedback mechanism in the cochlear [2], which allows us to hear low-level sounds with greater fidelity, thereby increasing the dynamic range of our hearing. Other examples of advantageous nonlinearities can be found in musical instruments; the sound-generating mechanism in violins exploits the stick-slip phenomenon [46], and musical gongs rely intrinsically on nonlinearities for their unique sounds [47]. Gongs typically exhibit geometric nonlinearities, such that when they are struck, the input energy initially excites the lower modes of vibration, and the energy is then transferred to higher frequencies over time, giving the characteristic rising note of the instrument. Several examples of systems with nonlinear dynamics are shown in Figure 2.1.

Furthermore, nonlinear behaviour may be exploited in certain applications, such as harvesting energy from limit-cycle oscillations [48]. Current design and control methods are generally based on the assumptions of linearity and so nonlinearities are either avoided, if possible, or compensated for, thereby making the design overly conservative.

Figure 2.1: Illustrations of systems that exhibit nonlinear behaviour. In most of these cases, the nonlinearity is beneficial.

Despite the considerable challenges associated with developing analytical tools that can be applied to general nonlinear systems, there are various techniques that can be used to analyse and model the dynamics of nonlinear structures. These methods are typically based on linear concepts and extended to the nonlinear domain, including higher-order frequency response functions using the Volterra series [49, 50], describing functions [51], Lyapunov methods [52, 53] and the nonlinear Nyquist and circle criteria [54]. These analytical tools are reviewed in this chapter. Additional methods include averaging [55], perturbation and multiple scales [56, 57], normal form transformation [58, 59], and nonlinear normal modes [60, 61].

When applying active vibration control to a structure, it is typically assumed that structural nonlinearities are the primary cause of nonlinear dynamics in the control path. In this thesis, we primarily consider the use of a linear feedback controller applied to a nonlinear structure, including actuator nonlinearities. However, a control engineer may also intentionally introduce nonlinear behaviour in the controller for the purpose of improving the control performance in terms of the reaction time, accuracy, and control effort. Examples include the nonlinear receding horizon control of an F-16 aircraft fighter [62], which requires a fast, high-performance controller to handle extreme manoeuvres, and the nonlinear control of electric machinery [63]. The design and implementation of a nonlinear controller is considered in the final two chapters of this thesis.

In this chapter, we initially consider structural nonlinearities that are likely to occur in inertial actuators and have a profound effect on the plant dynamics. We then review the analytical methods discussed above in conjunction with the numerical Runge-Kutta solvers, and consider techniques for analysing the stability of a nonlinear system.

2.2 Common structural nonlinearities

Dynamic structures may exhibit a large number of possible nonlinearities, including Coloumb friction between joints [64], stiffening nonlinearities in aircraft wings [65], backlash in hydraulic actuators [42], *etc.* This section focuses on some of the most common nonlinearities that are observed in practice and are particularly relevant to this thesis. A more comprehensive literature review on structural nonlinearities may be found in reference [66].

2.2.1 Cubic stiffness: the Duffing oscillator

The Duffing oscillator is a relatively simple second-order nonlinear system that features cubic stiffness [38], and is a popular choice for illustrating the effects of nonlinearities on the structural dynamics and demonstrating our understanding of nonlinear systems. This is because the Duffing oscillator, despite its simplicity, is capable of exhibiting almost all the rich dynamic phenomena associated with nonlinear systems, including bifurcations, harmonic distortion, and the jump phenomenon [67].

Examples of structures that exhibit cubic stiffness include loudspeakers with weakly nonlinear suspension stiffness [68], harmonically excited pendulums [38], and cantilever beams suspended between two magnets [6, 69]. In each case, the cubic nonlinearity is obtained by truncating a Taylor series expansion of the nonlinearity at the third-order term; therefore, these systems only approximate the behaviour of a Duffing oscillator within a specific displacement range. Since the suspension of a proof-mass actuator is similar in principle to a loudspeaker suspension, we can expect this type of nonlinearity to be observable in the actuators.

One of the most interesting and well-known characteristics of a Duffing oscillator is the tendency towards chaotic behaviour when driven by a large, periodic force, which has been covered in great detail [70,71]. This undesirable phenomenon is attributed to several types of bifurcations that can occur in Duffing oscillators, such as period-doubling [72], Hopf bifurcation [73], and saddle node bifurcation [74].

The equation of motion for a Duffing oscillator, known as the Duffing equation, may be written as follows,

$$m\ddot{y}(t) + c\dot{y}(t) + k_1 y(t) + k_3 y^3(t) = f(t) \tag{2.3}$$

where m, c, k_1 are the linear mass, damping and stiffness terms;

k_3 is the nonlinear cubic stiffness term;

$y(t), \dot{y}(t), \ddot{y}(t)$ represent the displacement, velocity, and acceleration of the structure respectively;

$f(t)$ is the loading applied to the structure.

Assuming sinusoidal loading of the form $f(t) = F\sin(\omega t + \phi)$, an approximate solution to Eq. 2.3 can be written as an infinite Fourier series that includes the fundamental forcing frequency and its odd-order harmonics,

$$y(t) = \sum_{n=0}^{\infty} Y_{2n+1} \sin([2n+1]\omega t + \phi_{2n+1}) \tag{2.4}$$

With the inclusion of the cubic stiffness term, the restoring force becomes a nonlinear function of displacement. Depending on whether k_3 is positive (negative), the Duffing oscillator exhibits hardening (softening) characteristics, where the effective stiffness increases (decreases) with structural displacement (as shown in Figure 2.2). For the softening case ($k_3 < 0$), the structure will become unstable if the displacement amplitude is large enough; however, in most practical applications, instability is prevented by the inclusion of higher-order nonlinearities that become dominant at larger displacement amplitudes. For example, a pendulum behaves as a softening Duffing oscillator at small displacement amplitudes, yet instability is prevented by an additional positive fifth-order nonlinearity that dominates at larger displacement amplitudes. Moreover, the presence of negative linear stiffness ($k_1 < 0$) results in the appearance of two isolated equilibria away from $\mathbf{x} = \mathbf{0}$.

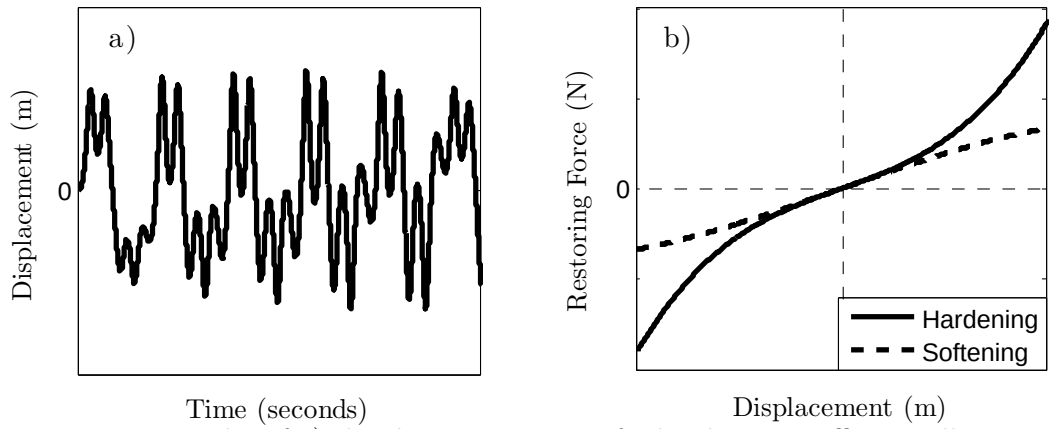

Figure 2.2: Examples of a) the chaotic response of a hardening Duffing oscillator, and b) the nonlinear restoring force curve.

2.2.2 Saturation: clearance and backlash

Saturation phenomena are particularly ubiquitous in active vibration control applications, primarily due to mechanical clearance and backlash nonlinearities in the structure and the actuators. One of the most straightforward ways of emulating the dynamics of these saturation nonlinearities is to utilise a hard clipping model, where the maximum structural or actuator displacement ($y_{out}(t)$) is limited at the saturation threshold d,

$$y_{out}(t) = \begin{cases} d \cdot \text{sign}(y(t)) & \text{if } |y(t)| \geq d \\ y(t) & \text{if } |y(t)| < d \end{cases} \tag{2.5}$$

This type of saturating nonlinearity occurs naturally in various applications as a result of physical limitations, including magnetic saturation (ferromagnetic material is fully magnetised), amplifier saturation (voltage output reaches the maximum voltage of the power supply), and digital saturation (maximum number of bits of an operating system is reached). An illustration of the effects of hard clipping saturation on the output displacement and the restoring force are shown in Figures 2.3a) and 2.3b) respectively.

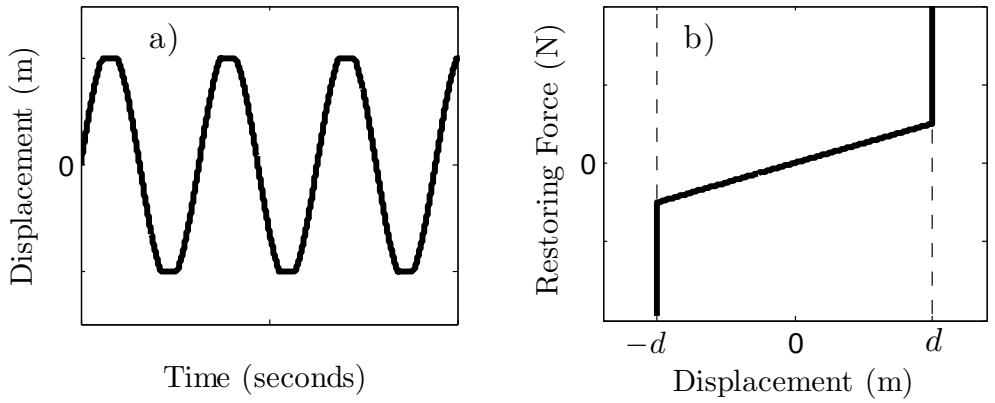

Figure 2.3: Examples of a) the time response, and b) the restoring force curve of the hard clipping nonlinearity.

There are two primary drawbacks of using the hard clipping model for clearance nonlinearities. Firstly, there is the inherent assumption that the end stop is infinitely rigid and does not account for any deformation effects, which is unlikely to occur in practice. Secondly, the model assumes that the external loading forces the structure against its end stop for a relatively large period of time, whereas a sinusoidal forcing function is out-of-phase with the displacement response, and so the contact period is actually much

shorter than suggested in Figure 2.3a). By accounting for these contact dynamics, a better description of clearance and backlash nonlinearities may be achieved by considering a piecewise model, which is given as follows,

$$f_{rf}(t) = \begin{cases} k_1 y(t) + f[y(t) - d)] & \text{if } y(t) \geq d \\ k_1 y(t) & \text{if } |y(t)| < d \\ k_1 y(t) + f[y(t) + d)] & \text{if } y(t) \leq -d \end{cases} \tag{2.6}$$

Here, f_{rf} denotes the restoring force of the linear stiffness and clearance nonlinearity[1], and $f[y(t) - d)]$ is a function that describes the dynamic behaviour of the clearance nonlinearity, including the effects of deformation. In most cases, this function is assumed to be linear, resulting in the *piecewise linear* stiffness model. The piecewise linear model (illustrated in Figure 2.4) is beneficial for identifying and analysing nonlinear structures with clearance or backlash [37], since the piecewise terms are relatively simple to work with. In addition, Nagurka and Huang [75] demonstrated that the impact parameters associated with the clearance nonlinearity, such as the contact time and coefficient of restitution, can be directly related to the stiffness and damping terms of a piecewise linear model, thereby providing a convenient means of modelling impact dynamics.

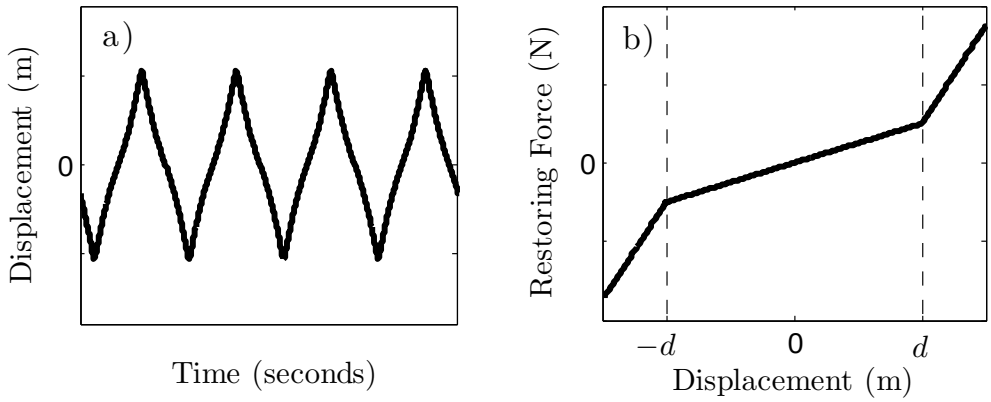

Figure 2.4: Examples of a) the time response, and b) the restoring force curve of the piecewise nonlinearity.

[1]In Eq. 2.6, the term $k_1 y(t)$ is expressed instead of the more usual term $k_1 d$ during clearance, in order to differentiate between the suspension stiffness and the effective stiffness associated with the clearance nonlinearity.

The primary limitation of using the piecewise linear model for clearance nonlinearities is that the stiffness and damping terms correspond to single values for the contact time and coefficient of restitution. This is fine if the impact dynamics are relatively simple, and the impact parameters are relatively constant; however, a linear piecewise model is not able to account for variations in the contact time and coefficient of restitution for more complex clearance nonlinearities, such as stroke saturation [76,77]. These cases necessitate the use of the general piecewise model shown in Eq. 2.6, where $\big[y(t)-d)\big]$ is a nonlinear function. Whilst the general piecewise model is more versatile than the piecewise linear model, it is also more complex, and the function $f\big[y(t)-d)\big]$ therefore needs to chosen carefully to accurately model the impact dynamics.

2.3 Describing functions using the harmonic balance method

The harmonic balance method [12] is one of the most well-established techniques for analysing nonlinear systems, and is widely used in mechanical and electrical applications. Using this approach, the nonlinear system is formulated as a Lur'e problem [78] (displayed in Figure 2.5), where the forward path features the underlying linear, time-invariant system $H(s)$, and the nonlinearities $f[y(t),\dot{y}(t)]$ are contained in the feedback path. Using this Lur'e representation of a nonlinear system requires the following assumptions,

1. The linear and nonlinear components of the nonlinear system are separable.
2. The underlying linear system is time-invariant.
3. The nonlinearity is memoryless.

The next step is to analyse the response of the composite system to sinusoidal excitation. Whilst the nonlinearity may introduce harmonic distortion into the response, these harmonics may be neglected if $H(s)$ exhibits low-pass characteristics, due to attenuation through filtering. Therefore, the steady-state response of the composite system may be approximated by a sinusoid at the fundamental forcing frequency, so that,

$$f(t) = F\sin(\omega t+\phi) \rightarrow y(t) \approx Y\sin(\omega t) \tag{2.7}$$

Since $f(t)$ and $y(t)$ are both sinusoids of frequency ω, the nonlinear structural dynamics can then be described in linear terms, and the system is said to quasi-linearised.

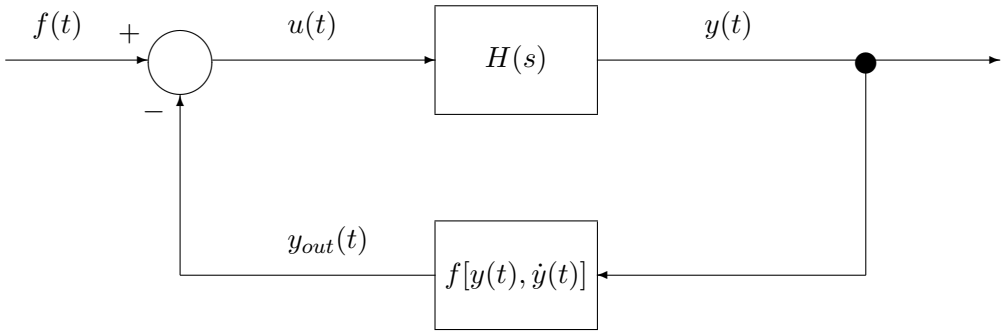

Figure 2.5: A general nonlinear system modelled using a Lur'e representation, with a linear feedforward path and nonlinear feedback path.

2.3.1 A Duffing oscillator example

As an example, we consider the dynamics of a Duffing oscillator, which may be expressed using the following Lur'e representation,

$$\frac{Y(s)}{F(s)} = H(s) = (ms^2 + cs + k_1)^{-1}, \qquad f[y(t), \dot{y}(t)] = k_3 y^3(t) \tag{2.8}$$

By assuming that the displacement response of the Duffing oscillator is sinusoidal and includes the fundamental frequency ω, the relationship between $y_{out}(t)$ and $y(t)$ in Figure 2.5 is expressed as,

$$y_{out}(t) = Y^3 \sin^3(\omega t) = \frac{Y^3}{4}\Big(3\sin(\omega t) - \sin(3\,\omega t)\Big) \tag{2.9}$$

The higher-order harmonic $\sin(3\,\omega t)$ may be neglected, due to the low-pass filtering effects of $H(s)$. Therefore, the nonlinearity acts as a quasi-linear, amplitude-dependent gain in the equation of motion, which can now be written as follows,

$$m\ddot{y}(t) + c\dot{y}(t) + k_1 y(t) + \Big(\frac{3}{4}k_3 Y^2\Big)y(t) = f(t) \tag{2.10}$$

Taking the Fourier transform of Eq. 2.10 and rearranging the terms yields the first-order composite pseudo-FRF, denoted by $\Lambda_1(j\omega, Y)$, which describes the response of the nonlinear system to monoharmonic excitation at the fundamental forcing frequency,

$$\Lambda_1(j\omega, Y) = \frac{Y(j\omega)}{F(j\omega)} = \Big[k_1 - m\omega^2 + j\omega c + \Big(\frac{3}{4}k_3 Y^2\Big)\Big]^{-1} \tag{2.11}$$

Here, it is apparent that the first-order pseudo-FRF of a Duffing oscillator behaves as an amplitude-varying quasi-linear FRF, where the amplitude dependency is introduced by the nonlinearity. The amplitude-varying term is known as the *describing function*, which describes the nonlinearity as a quasi-linear modification to the dynamic stiffness, and is used as an approximate representation of the nonlinearity in the frequency-domain [51]. Using this method, the first-order pseudo-FRFs can be used to obtain the steady-state response amplitude of a nonlinear system, in a similar manner to linear systems, but are only applicable for a specific excitation level [12], since the FRFs are amplitude-variant.

In order to ascertain the first-order pseudo-FRF, it is necessary to know the response amplitude $Y(j\omega)$. This is obtained by substituting the sinusoidal terms specified in Eq. 2.7 into Eq. 2.10, applying the identity $F\sin(\omega t+\phi) = F\Big[\sin(\omega t)\cos(\phi)+\cos(\omega t)\sin(\phi)\Big]$ to the excitation force, and equating the coefficients of $\sin(\omega t)$ and $\cos(\omega t)$,

$$\Big[k_1 - m\omega^2 + \Big(\frac{3}{4}k_3 Y^2\Big)\Big]Y(j\omega) = F\cos(\phi) \tag{2.12}$$

$$c\omega Y(j\omega) = F\sin(\phi) \tag{2.13}$$

Squaring and summing Eq. 2.12 and Eq. 2.13 results in the following cubic equation in $Y^2(j\omega)$,

$$\frac{9}{16}k_3^2 Y^6 + 1.5k_3(k_1 - m\omega^2)Y^4 + \Big[(k_1 - m\omega^2)^2 + (c\omega)^2\Big]Y^2 - F^2 = 0. \tag{2.14}$$

There are six potential solutions to this equation, and since $\{Y \in \Re \,|\, Y > 0\}$, negative or complex solutions may be disregarded as unphysical. Depending on the discriminant Δ, Eq. 2.14 will have either one or three positive real solutions for $Y(j\omega)$.

If there is a single positive real solution, then the steady-state system response is uniquely defined for the system parameters and the sinusoidal excitation signal. However, if there are three positive real solutions, then the steady-state system response will tend to one of three possible amplitudes, depending on the initial conditions. This leads to bifurcation in the first-order pseudo-FRF, which occurs when the nonlinear dynamics are dominant (*i.e.* k_3 and F are large). An example of the bifurcation phenomenon is shown in the first-order pseudo-FRF illustrated in Figure 2.6, where it is apparent that the peak resonance is distorted within the bifurcation region $\Delta\omega$. The frequency range of the bifurcation region is defined by the transition frequencies ω_{min} and ω_{max}, which are determined as the frequencies where $\Delta = 0$. This is explored in more detail in chapter 3.

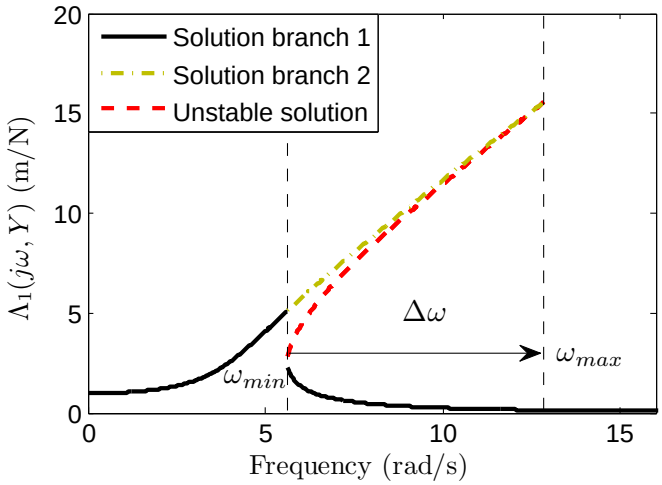

Figure 2.6: Illustration of an exemplary first-order pseudo-FRF of a Duffing oscillator.

2.3.2 Sinusoidal-input describing functions

For a general nonlinearity $f[y(t), \dot{y}(t)]$, the describing function, denoted by $N(j\omega, Y)$, is determined by the first-order coefficient of the complex Fourier series,

$$N(j\omega, Y) = \frac{2j}{t_0 Y} \int_0^{t_0} f\big[Y\sin(\omega t), \omega Y \cos(\omega t)\big] e^{-j\omega t}\, dt \tag{2.15}$$

This is known as the *sinusoidal-input describing function* (SIDF), since the describing function is only valid for sinusoidal inputs. Other types of describing functions, such as the two-sinusoidal-input describing function (TSIDF), random-input describing function (RIDF), and the higher-order sinusoidal-input describing function (HOSIDF) may also be derived [79], but are not considered in this thesis.

Since in this case the describing function acts as a modification to the dynamic stiffness of the underlying linear system, the first-order pseudo-FRFs of a general nonlinear system may be written as,

$$\Lambda_1(j\omega, Y) = \Big[k_1 - m\omega^2 + j\omega c + N(j\omega, Y)\Big]^{-1} \tag{2.16}$$

provided that the describing function is an accurate representation of the nonlinearity and the excitation amplitude is held constant. Since the describing function is dependent on the excitation source, Eq. 2.16 shows that the first-order pseudo-FRFs vary with the type of excitation applied to the nonlinear system, in addition to the excitation amplitude. For consistency, the use of sinusoidal excitation is considered exclusively in this thesis.

Several examples of the describing functions obtained for common structural nonlinearities, which are presented by Ozer *et. al.* [80], are illustrated in Table 2.1. Here, we can observe that the displacement-dependent describing functions are purely real, whereas the velocity-dependent describing functions are purely imaginary. This is because the displacement- and velocity-dependent describing functions act as amplitude-varying stiffness and damping terms. If the nonlinearity exhibits both types of dependencies, such as friction-controlled backlash, then the describing function is complex, resulting in a frequency-dependent phase shift.

The main advantage of the sinusoidal-input describing function is its ability to generalise the linear FRF techniques to a variety of nonlinear systems in the frequency-domain using quasi-linear first-order pseudo-FRFs. Furthermore, the method may be extended to multi-degree-of-freedom systems using a describing function matrix [81].

Having said this, there are two inherent limitations of the sinusoidal-input describing function. Firstly, it relies on the assumption that the response of the nonlinear system is approximately monoharmonic, which may not be the case if the nonlinearity is strong. Although the harmonic responses may be accounted for using higher-order sinusoidal-input describing functions [79], these methods are only accurate if the nonlinearity is relatively simple. Secondly, the sinusoidal-input describing function can only be applied to symmetric nonlinearities, as described in the next section. Since even-order, asymmetric nonlinearities are also a common occurrence, it is important to account for these nonlinearities using alternative means.

2.3.3 Dual-input describing functions

The presence of an even-order, asymmetric nonlinearity in a dynamic structure has the effect of introducing a DC offset into the displacement response. Therefore, the sinusoidal-input describing function is not an accurate representation of such nonlinearities, as the DC offset is not considered. Instead, the *dual-input describing function* [79], which features a combined sinusoidal and bias DC input, is used to represent asymmetric nonlinearities. Assuming the excitation force to a structure with asymmetric nonlinearities is monoharmonic, the displacement response of the structure can be approximated as a sinusoid with a DC bias,

$$f(t) = F\sin(\omega t + \phi) \rightarrow y(t) \approx Y_1 \sin(\omega t) + Y_0 \tag{2.17}$$

Type of nonlinearity	Illustration	Describing function representation
Cubic stiffness	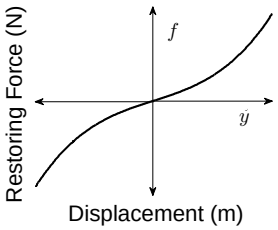	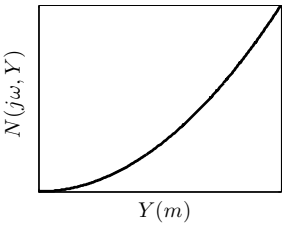 $N(j\omega, Y) = \frac{3}{4}k_3 Y^2$
Piecewise stiffness	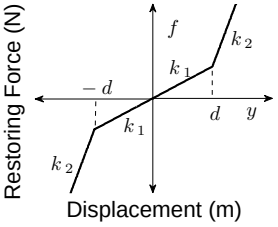	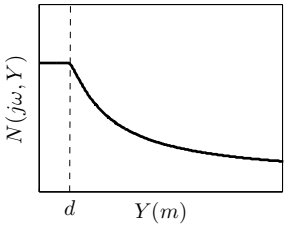 $N(j\omega, Y) = \Big[\arcsin\Big(\frac{d}{Y}\Big) + \frac{d}{Y}\sqrt{1-\Big(\frac{d}{Y}\Big)^2}\Big] \cdot \frac{2}{\pi}(k_2 - k_1) + k_2$
Cubic damping	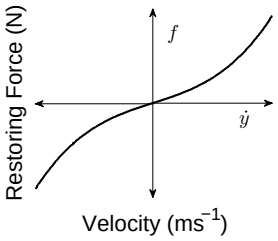	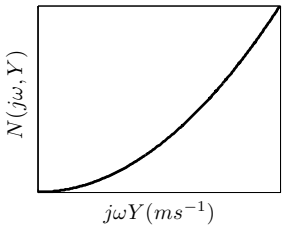 $N(j\omega, Y) = j\omega\Big(\frac{3}{4}c_3\omega^2 Y^2\Big)$
Coulomb friction	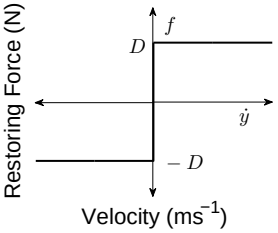	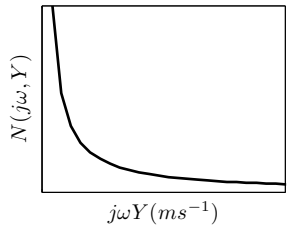 $N(j\omega, Y) = j\omega\Big(\frac{4D}{\pi Y}\Big)$

Table 2.1: Table of describing functions for common structural nonlinearities [80].

The dual-input describing function, denoted by $N(j\omega, Y_0, Y_1)$, is then obtained as follows,

$$N(j\omega, Y_0, Y_1) = \frac{2j}{t_0 Y} \int_0^{t_0} f\big[Y_1 \sin(\omega t) + Y_0, \omega Y_1 \cos(\omega t)\big] e^{-j\omega t}\, dt \tag{2.18}$$

As an example, we consider the asymmetric Duffing oscillator, which has the following equation of motion,

$$m\ddot{y}(t) + c\dot{y}(t) + k_1 y(t) + k_2 y^2(t) + k_3 y^3(t) = f(t) \tag{2.19}$$

where the nonlinearity $k_2 y^2(t)$ is even-order and asymmetric. Using Eq. 2.18, the dual-input describing function of the composite nonlinearities is,

$$N(j\omega, Y_0, Y_1) = 2k_2 Y_0 + 3k_3 Y_0^2 + 0.75 k_3 Y_1^2 \tag{2.20}$$

and the first-order pseudo-FRF becomes,

$$\Lambda_1(j\omega, Y_0, Y_1) = \Big[k_1 - m\omega^2 + j\omega c + N(j\omega, Y_0, Y_1)\Big]^{-1} \tag{2.21}$$

Therefore, the first-order pseudo-FRF is now dependent on the DC displacement amplitude Y_0 in addition to the fundamental displacement amplitude Y_1. This indicates that although the first-order pseudo-FRF is defined at the fundamental frequency, the output displacement amplitude Y_1 is dependent on Y_0 due to harmonic interaction. For the asymmetric Duffing oscillator, the relationship between Y_0 and Y_1 is estimated by substituting Eq. 2.17 into Eq. 2.19 and collecting the DC components in the resulting equation,

$$k_3 Y_0^3 + k_2 Y_0^2 + (k_1 + 1.5 k_3 Y_1^2) Y_0 + 0.5 k_2 Y_1^2 = 0 \tag{2.22}$$

By specifying Y_0 as the variable to be found, it is apparent that Eq. 2.22 is cubic in Y_0. Assuming a hardening nonlinearity ($k_3 > 0$), it can be shown that Eq. 2.22 satisfies $\Delta < 0$, where Δ is the discriminant of Eq. 2.22, and therefore has only one real solution. A proof that demonstrates this property is given in Appendix A. Provided that k_1, k_2, k_3, Y_1 are known, an approximate solution to Eq. 2.22 can be obtained numerically using MATLAB's fmincon solver, and is defined as,

$$Y_0 \approx f\big[k_1, k_2, k_3, Y_1\big] \tag{2.23}$$

This enables the describing function to be expressed in terms of the frequency, the fundamental displacement amplitude, and the structural parameters, thereby removing the

explicit dependency on the DC amplitude Y_0.

Whilst the dual-input describing function is an effective means of representing asymmetric nonlinearities, it is also subject to the same limitations as the sinusoidal-input describing function. Furthermore, if a sufficiently accurate estimate of Y_0 cannot be obtained, then this parameter may need to be obtained through direct experimental measurements, which presents a number of challenges and requires the use of sophisticated equipment.

2.4 Volterra series representation

The Volterra series, devised by Vito Volterra to describe population growth [50], is a non-parametric model used to represent the input-output relationship of single-valued weakly nonlinear systems, and is a popular method in control engineering applications for signal processing and system identification purposes. One of the key advantages of the Volterra series is that it acts as a natural extension of linear convolution theory to nonlinear systems, since the output signal is approximated using the input signal and an infinite series of Volterra kernels. This approach also forms the basis of the non-linear output frequency response function (NOFRF) utilised by Billings, Lang & co-workers [82, 83]. First, the output response of the nonlinear system, defined as $y(t)$, to an input signal, $f(t)$, is described as a combined sum of generalised responses,

$$y(t) = \sum_{n=1}^{\infty} y_n(t) \tag{2.24}$$

where the first generalised response $y_1(t)$ is the underlying linear response ascertained from the linear convolution integral,

$$y_1(t) = \int_{-\infty}^{\infty} h_1(\tau_1) f(t-\tau_1) \mathrm{d}\tau_1 \tag{2.25}$$

$h_1(\tau_1)$ being the underlying linear impulse response. The higher-order responses are ascertained as,

$$y_2(t) = \int_{-\infty}^{\infty} \int_{-\infty}^{\infty} h_2(\tau_1, \tau_2) f(t-\tau_1) f(t-\tau_2) \mathrm{d}\tau_1 \mathrm{d}\tau_2 \tag{2.26}$$

$$y_3(t) = \int_{-\infty}^{\infty} \int_{-\infty}^{\infty} \int_{-\infty}^{\infty} h_3(\tau_1, \tau_2, \tau_3) f(t-\tau_1) f(t-\tau_2) f(t-\tau_3) \mathrm{d}\tau_1 \mathrm{d}\tau_2 \mathrm{d}\tau_3 \tag{2.27}$$

Here, $h_2(\tau_1, \tau_2), h_3(\tau_1, \tau_2, \tau_3)$ are generalised versions of the linear impulse response $h_1(\tau_1)$, and represent the Volterra kernels. If the system is approximately linear, these higher-order impulse responses are negligible, and the output response can be adequately described using Eq. 2.25. Thus, the Volterra series are a natural extension of the linear convolution integral in the time-domain.

A similar approach can be taken in the frequency-domain by defining the response $Y(j\omega)$ as follows,

$$Y(j\omega) = Y_1(j\omega) + Y_2(j\omega, j\omega) + Y_3(j\omega, j\omega, j\omega) + \cdots \tag{2.28}$$

where $Y_1(j\omega)$ is the response of the underlying linear system,

$$Y_1(j\omega) = H_1(j\omega)F(j\omega) \tag{2.29}$$

with $H_1(j\omega)$ and $F(j\omega)$ being the Fourier transforms of $h_1(\tau_1)$ and $x(t)$ respectively. The higher-order responses are determined using generalised frequency response functions,

$$Y_2(j\omega, j\omega) = H_2(j\omega_1, j\omega_2)F(j\omega_1)F(j\omega_2) \tag{2.30}$$

$$Y_3(j\omega, j\omega, j\omega) = H_3(j\omega_1, j\omega_2, j\omega_3)F(j\omega_1)F(j\omega_2)F(j\omega_3) \tag{2.31}$$

These higher-order frequency response functions $H_2(j\omega_1, j\omega_2)$, $H_3(j\omega_1, j\omega_2, j\omega_3)$, are obtained from the multi-dimensional Fourier transforms of the Volterra kernels. Since the Volterra series contains an infinite number of terms, it is not possible to directly implement the theory into practice; instead, a suitable number of Volterra kernels, denoted by N, is chosen, and the Volterra series is truncated at this number. Therefore, the response can be approximated as,

$$Y(j\omega) \approx \sum_{n=1}^{N} H_n(j\omega_1, \cdots, j\omega_n) \prod_{m=1}^{N} F_m(j\omega_m) \tag{2.32}$$

This equation can be extended into the complex domain as follows [84],

$$Y(s) \approx \sum_{n=1}^{N} H_n(s_1, \cdots, s_n) \prod_{m=1}^{N} F_m(s_m) \tag{2.33}$$

If the excitation source is a single harmonic (*i.e.* $F(j\omega) = F\mathrm{e}^{j\omega t}$), then it is trivial to show from Eq. 2.32 that the output may be written as,

$$\begin{aligned} y(t) \approx & H_1(j\omega)F\mathrm{e}^{j\omega t} + H_2(j\omega, j\omega)F^2\mathrm{e}^{2j\omega t} + H_3(j\omega, j\omega, j\omega)F^3\mathrm{e}^{3j\omega} + \cdots + \\ & H_N(j\omega, \cdots, j\omega)F^N\mathrm{e}^{Nj\omega} \end{aligned} \tag{2.34}$$

However, in practice, the closest source to harmonic excitation is a sinusoidal signal, which is composed of two harmonics (*i.e.* $F(s) = F(\mathrm{e}^{st} + \mathrm{e}^{-st})/2$). Since the system is nonlinear, it is not possible to consider each harmonic separately and apply the superposition principle, as for linear systems; the combined response must be directly ascertained. Therefore, the frequency response function for sinusoidal excitation will differ from the frequency response function established for harmonic excitation.

It was established by Gifford [85], followed by Storer and Tomlinson [86], through the use of harmonic probing that the harmonics in the sinusoidal signal will interact with each other, and energy is transferred to the sum and difference frequencies of the harmonics. A sinusoidal signal of the form $F(j\omega) = F(\mathrm{e}^{j\omega t} + \mathrm{e}^{-j\omega t})/2$ is applied to Eq. 2.32 to obtain,

$$y(t) \approx G_1(j\omega, t) + G_2(j\omega, j\omega, t) + G_3(j\omega, j\omega, j\omega, t) + \cdots + G_N(j\omega, \cdots, j\omega, t) \tag{2.35}$$

where,

$$G_1(j\omega, t) = H_1(j\omega)\Big(\frac{F}{2}\Big)\mathrm{e}^{j\omega t} + H_1(-j\omega)\Big(\frac{F}{2}\Big)\mathrm{e}^{-j\omega t} \tag{2.36}$$

$$\begin{aligned} G_2(j\omega, j\omega, t) =& H_2(j\omega, j\omega)\Big(\frac{F}{2}\Big)^2\mathrm{e}^{j2\omega t} + H_2(-j\omega, -j\omega)\Big(\frac{F}{2}\Big)^2\mathrm{e}^{-j2\omega t} + \\ & 2H_2(j\omega, -j\omega)\Big(\frac{F}{2}\Big)^2 \end{aligned} \tag{2.37}$$

$$\begin{aligned} G_3(j\omega, j\omega, j\omega, t) =& H_3(j\omega, j\omega, j\omega)\Big(\frac{F}{2}\Big)^3\mathrm{e}^{j3\omega t} + H_3(-j\omega, -j\omega, -j\omega)\Big(\frac{F}{2}\Big)^3\mathrm{e}^{-j3\omega t} + \\ & 3H_3(j\omega, j\omega, -j\omega)\Big(\frac{F}{2}\Big)^3\mathrm{e}^{j\omega t} + 3H_3(j\omega, -j\omega, -j\omega)\Big(\frac{F}{2}\Big)^3\mathrm{e}^{-j\omega t} \end{aligned} \tag{2.38}$$

The n'th-order pseudo-FRF is then ascertained by collecting the terms associated with $\mathrm{e}^{\pm jn\omega t}$, such that,

$$\begin{aligned} \Lambda_1(j\omega) =& \frac{Y(j\omega)}{F(j\omega)} \approx H_1(j\omega) + 3H_3(j\omega, j\omega, -j\omega)\Big(\frac{F}{2}\Big)^2 + \cdots + \\ & nH_n(j\omega, \cdots, -j\omega)\Big(\frac{F}{2}\Big)^{n-1}, \qquad n = 5, 7, 9, \cdots \end{aligned} \tag{2.39}$$

$$\Lambda_2(2j\omega) = \frac{Y(2j\omega)}{F^2(j\omega)} \approx \frac{1}{2}H_2(j\omega, j\omega) + \cdots + \frac{n}{4(n-2)!}H_n(j\omega, \cdots, -j\omega)\Big(\frac{F}{2}\Big)^{n-2}, \quad n = 4, 6, 8, \cdots \tag{2.40}$$

$$\Lambda_n(nj\omega) = \frac{Y(nj\omega)}{F^n(j\omega)} \approx \frac{1}{2^{n-1}}H_n(j\omega, \cdots, j\omega) + \frac{(n+1)!}{n!2^n}H_{n+2}(j\omega, \cdots, -j\omega)\Big(\frac{F}{2}\Big)^2 + \cdots, \quad n = 1, 2, 3, \cdots \tag{2.41}$$

This approach provides a versatile means of estimating the pseudo-FRFs of an arbitrary nonlinear structure using higher-order FRFs, which are functions of the underlying linear FRFs and the nonlinear parameters. In this manner, the nonlinearities act as modifications to the underlying linear receptance of the structure; this directly contrasts with describing functions, which modify the dynamic stiffness of the structure. Furthermore, the Volterra series approximation can also be directly applied to nonlinear systems with multiple-degrees-of-freedom.

Having said this, there are two inherent drawbacks with using the Volterra series to approximate a response of a nonlinear structure,

1. Representation. Due to the use of higher-order polynomial terms in the approximation, a Volterra series representation is primarily applicable to structures with continuous polynomial nonlinearities. If the structural nonlinearity is relatively complicated (*e.g.* contains discontinuities), then it may not be possible to utilise a Volterra series representation.

2. Convergence. It is well-known that the Volterra series only converge on the correct solution when the structural nonlinearities are relatively weak [87, 88]. If the nonlinearities are strong, then the Volterra series will diverge, resulting in an inaccurate approximation. Several criteria [89, 90] have been established for ascertaining the threshold between a convergent and divergent Volterra series representation for the Duffing oscillator. It was found that the threshold decreased near the peak resonance, and that the upper limits of the Volterra series representation were indicated by the presence of the shock jump phenomenon.

To summarise, the Volterra series represent nonlinearities in terms of the input excitation amplitude and the higher-order FRFs, and does not require knowledge of the displacement amplitude or dynamic stiffness. This approach is advantageous for estimating the first-order pseudo-FRF of a nonlinear system using experimental measurements, since there is no need for the linear mass, stiffness, and damping terms to be known. However, the limitations of a Volterra series representation should be taken into account, particularly with regards to the complexity and strength of the structural nonlinearities.

2.5 Time-domain simulations of nonlinear systems

Since nonlinear systems rarely yield exact closed-form analytical solutions to their equations of motion, the displacement-time response of a nonlinear structure is typically ascertained using simulation environments such as Simulink. Using a set of initial conditions and a state-space representation of the nonlinear dynamics, a numerical solver is used to approximate the time response of the nonlinear system. The primary advantage of numerical solvers is that the time response of the actual nonlinear system is simulated, with no quasi-linearisation or infinite series approximations. However, it is difficult to make generalisations, as the simulations only reveal the behaviour of the nonlinear system for very specific situations.

Here, the analysis is divided into two sections. The first section briefly covers the numerical solvers that are used to conduct simulations in Simulink. The second section demonstrates the use of these solvers using an exemplary Duffing oscillator. The third section introduces the stepped-sine method, which is a popular technique for obtaining the first-order pseudo-FRF of a nonlinear structure using time-domain simulations and experimental measurements.

2.5.1 Numerical solvers in Simulink: Runge-Kutta methods

The Simulink environment features an extensive library of numerical solvers, and it is beyond the scope of this thesis to conduct a full review of each solver. Instead, we focus on the types of solvers and their application within the thesis.

Each numerical solver is based on the general Runge-Kutta formula, which begins with the initial value problem,

$$\dot{\mathbf{x}} = \mathbf{f}(t, \mathbf{x}), \qquad \mathbf{x}(t_0) = \mathbf{x_0} \tag{2.42}$$

Here, $f(t, y)$ represents the nonlinear state vector, and $t_0, \mathbf{x_0}$ denote the initial time and state vector. Using a step size $\Delta h = t[n+1] - t[n]$ and the initial data, the general Runge-Kutta formula can be stated as follows,

$$\mathbf{x}[n+1] = \mathbf{x}[n] + \sum_{i=1}^{N} \Delta h b_i r_i \tag{2.43}$$

where $t = n\Delta h$ is the time vector, N is the order of the Runge-Kutta solver, b represents a vector of coefficients, and r is a vector of increments based on the slope at different points of the interval. This repeats until the total simulation time T is reached. For further details, see reference [91].

There are two types of solvers in the Simulink environment: variable-step, where the step size is allowed to vary with each calculation step (*e.g.* ode45, ode23), and fixed-step, where the step size is held constant (*e.g.* ode3, ode1). Since we may wish to perform frequency-domain analysis on the simulated time histories through the discrete Fourier transform, it is necessary to utilise a fixed-time solver to obtain these time histories. This has the effect of increasing the computation time of the simulation, as the step-time should be relatively small to account for abrupt changes.

The default fixed-step solver in Simulink is the ode3 solver, which utilises the Bogacki-Shampine method, based on a third-order Runge-Kutta formula [92]. This solver exhibits a reasonable trade-off between accuracy and computation time, and is the primary solver used to generate the simulations in this thesis.

2.5.2 Simulations of a Duffing oscillator

As a numerical example, we simulate the displacement-time responses of a Duffing oscillator to monoharmonic excitation using the ode3 solver. First, we consider the initial value problem in Eq. 2.42 and write the equations of motion in state-space form,

$$\mathbf{x} = \begin{bmatrix} x_1(t) \\ x_2(t) \end{bmatrix} = \begin{bmatrix} y(t) \\ \dot{y}(t) \end{bmatrix} \tag{2.44}$$

$$\mathbf{f}(t, \mathbf{x}) = \begin{bmatrix} x_2 \\ \frac{1}{m}\Big(F\sin(\omega t + \phi) - cx_2(t) - k_1 x_1(t) - k_3 x_1^3(t)\Big) \end{bmatrix} \tag{2.45}$$

such that the states correspond to the displacement and velocity responses of the Duffing oscillator. The following parameters are defined for the simulation,

$$m = 1 \text{ kg}, \, c = 0.1 \text{ Ns/m}, \, k_1 = 50 \text{ N/m},$$
$$k_3 = 50,000 \text{ N/m}^3, \, \omega = 2\pi \text{ rad/s}$$

For the next step, the model was constructed in Simulink (see Figure 2.7), and the simulated displacement-time response of the Duffing oscillator was obtained using a simulation time $T = 800$ seconds, a step time $\Delta h = 0.001$ seconds, and initial conditions $\mathbf{x_0} = \mathbf{0}$. Two excitation amplitudes were considered; the first specified value ($F = 2$ N) is relatively small, whereas the second specified value ($F = 25$ N) is much larger and results in strong nonlinear dynamics. Since the initial response of the system exhibits transient behaviour, the first one hundred seconds of the simulated signals was discarded to ensure that only the steady-state response remains.

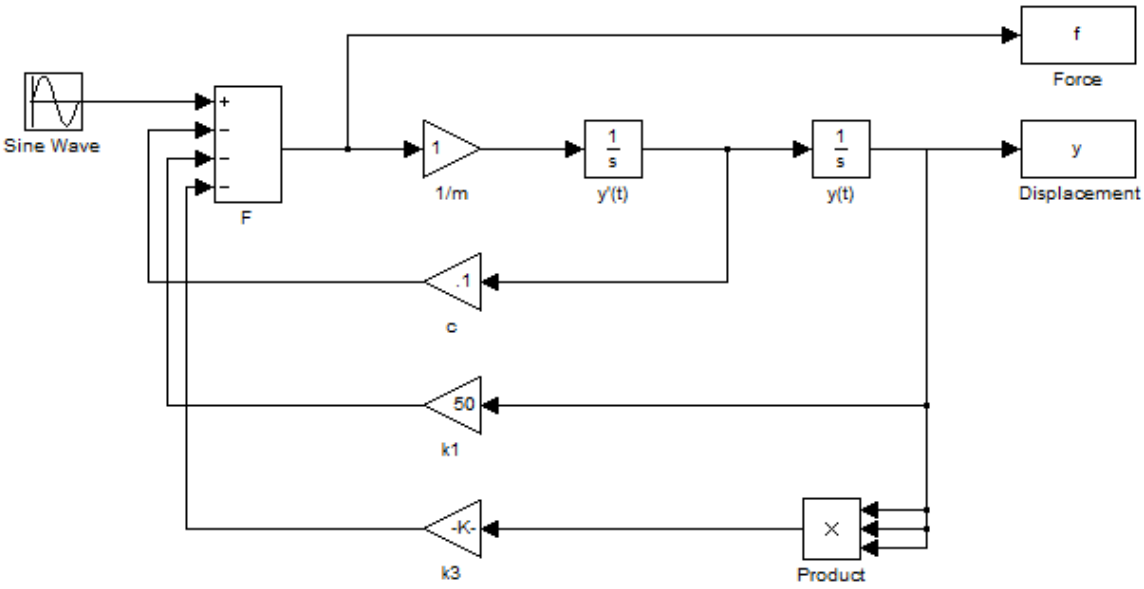

Figure 2.7: Simulink model of the Duffing oscillator.

The steady-state displacement-time histories are shown in Figures 2.8a) and 2.9a) alongside their respective Fourier transforms in Figures 2.8b) and 2.9b). Here, it is apparent that when the lower excitation amplitude is used, the displacement response is approximately sinusoidal, as expected. The spectral content indicates that several odd-order harmonics are also present in the displacement response, which are negligible in comparison to the fundamental amplitude. Conversely, when the higher excitation amplitude is

used, the displacement response exhibits chaotic behaviour, and the spectrum reveals the generation of additional subharmonics and combined resonances, which are commonly associated with bifurcation and chaos [93].

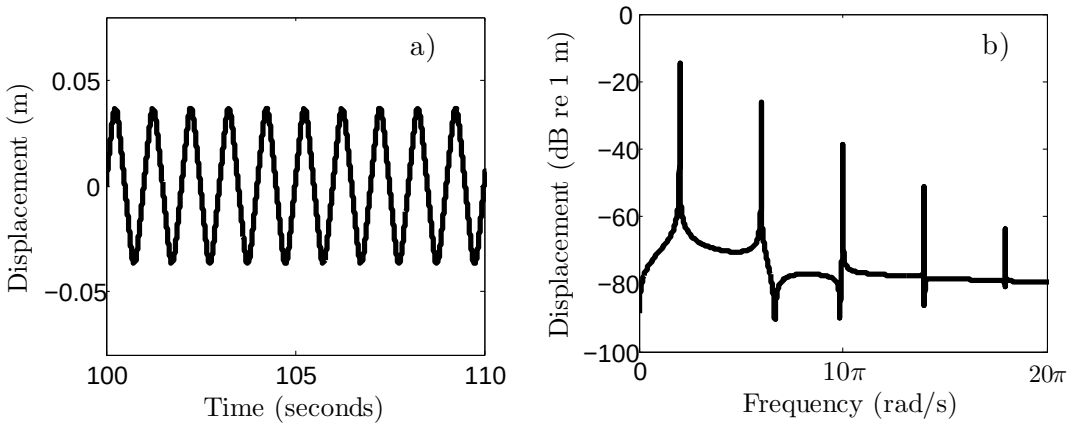

Figure 2.8: Displacement response of the Duffing oscillator to sinusoidal excitation of amplitude $F = 2$ N, $\omega = 2\pi$ in the a) time-domain, and b) frequency-domain.

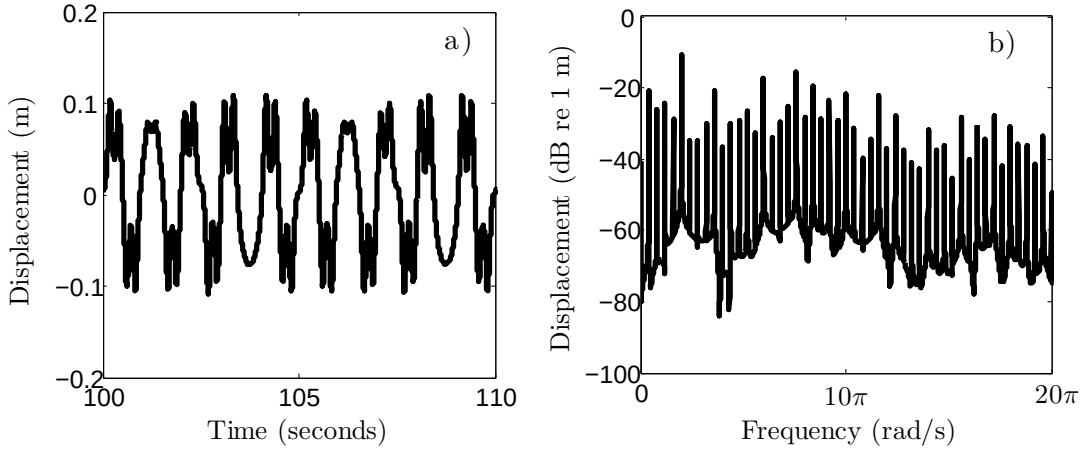

Figure 2.9: Displacement response of the Duffing oscillator to sinusoidal excitation of amplitude $F = 25$ N, $\omega = 2\pi$ in the a) time-domain, and b) frequency-domain.

The amplitude threshold for subharmonic generation can be determined using the three-dimensional response spectrum map established by Li and Billings [94]. Here, the response specta at a single excitation frequency is obtained over a range of excitation amplitudes, in order to detect the presence of subharmonics and combined resonances. An example of a response spectrum map is shown in Figure 2.10, which illustrates the generation of sub-

harmonics, combined resonances, and bifurcation as the excitation amplitude increases. This demonstrates that the numerical simulations yield much more detailed information about the nonlinear behaviour of the structure than using the describing function or Volterra series representations.

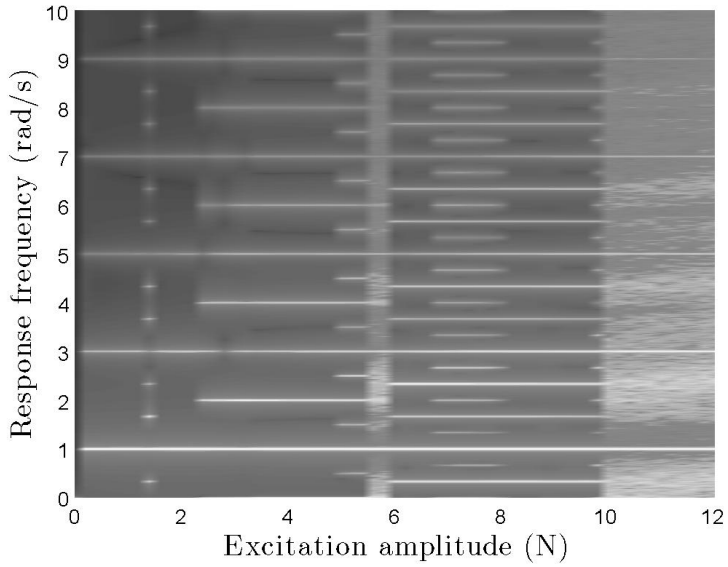

Figure 2.10: Response spectrum map showing the magnitude of the displacement response against the response frequency and excitation amplitude with $\omega = 1$ rad/s. Reproduced from [93].

2.5.3 The stepped-sine method

One of the most popular approaches for obtaining the first-order pseudo-FRF using numerical simulations or experimental measurements is the stepped-sine method [95]. First, a sinusoidal excitation force of amplitude F_1 and frequency ω_1 is applied to the nonlinear system, and the resulting displacement response $y(t, \omega_1)$ is recorded alongside the excitation force $f(t, \omega_1)$ over the time period T. Next, the test is repeated at a new excitation frequency ω_2, and another set of recorded data is obtained. By repeating this procedure across a range of excitation frequencies (from ω_1 to ω_N), holding the excitation amplitude constant, the result is a three-dimensional matrix that contains the time series data of the displacement and force signals for each excitation frequency. If one wishes to consider a range of excitation amplitudes (from F_1 to F_N), the data matrix may be extended to four dimensions to account for this dependency.

$$\mathbf{F} = \begin{bmatrix} F_1 & F_2 & \cdots F_N \end{bmatrix} \rightarrow \boldsymbol{\omega} = \begin{bmatrix} \omega_1 & \omega_2 & \cdots \omega_N \end{bmatrix} \tag{2.46}$$

Using this data matrix, the first-order pseudo-FRF may be obtained by taking the Fourier transforms of the force-time and displacement-time signals at the fundamental excitation frequency, provided that the time series data is sufficiently truncated to discard the transient response. For the excitation frequency ω_n (where $\{n \in \mathbb{N} \,|\, 1 \leq n \leq N\}$),

$$Y(j\omega_n) = \int_{-\infty}^{\infty} y(t, \omega_n) \mathrm{e}^{j\omega_n t}\, dt, \quad F(j\omega_n) = \int_{-\infty}^{\infty} f(t, \omega_n) \mathrm{e}^{j\omega_n t}\, dt \tag{2.47}$$

$$\Lambda_1(j\omega_n, Y) = \frac{Y(j\omega_n)}{F(j\omega_n)} \tag{2.48}$$

In this manner, the first-order pseudo-FRF may be obtained numerically or experimentally over the specified amplitude and frequency range.

There are numerous advantages to be considered when using the stepped sine method. Firstly, the excitation signal has a narrow frequency bandwidth, which enables structural nonlinearities to be excited and detected with relative ease [95]. Secondly, the signal-to-noise ratio of the measurements is usually very high. Thirdly, monoharmonic excitation signals are relatively simple to work with, in comparison with random, swept-sine, or impulsive excitation methods. For these reasons, the pseudo-FRFs obtained using the stepped-sine method tend to be accurate and consistent.

The primary difficulty with the stepped-sine method is the large number of excitation amplitudes and frequencies required to accurately characterise the nonlinear dynamics of a structure. This is time-consuming in comparison with broadband excitation methods, which do not excite the nonlinearity as easily. The difficulty can be partially overcome by optimising the resolution of the excitation frequencies around peak resonances, or using recursive methods [95]. Furthermore, it is relatively simple to automate the measurement procedure, and so the additional measurement time required is not normally a problem.

As a demonstration, the stepped-sine method is used to obtain the first-order pseudo-FRFs of the Duffing oscillator using the numerical time simulations. The new parameters are,

$$m = 1 \text{ kg}, \, c = 0.4 \text{ Ns/m}, \, k_1 = 50 \text{ N/m},$$
$$k_3 = 50,000 \text{ N/m}^3, \, F = 0.2 \text{ N}$$

Here, the excitation amplitude is large enough to cause bifurcation in the first-order pseudo-FRF. Therefore, within the bifurcation region, the solution for the simulated

displacement-time response is dependent on the initial conditions. To account for this dependency, two sets of variable initial conditions are utilised for the numerical solvers, which are determined by the steady-state displacement and velocity amplitudes obtained at the previous frequency. This may be expressed as follows,

$$\mathbf{x_{0,n}} = \begin{bmatrix} Y(j\omega_{n-1}) \\ \omega_{n-1}Y(j\omega_{n-1}) \end{bmatrix}, \mathbf{x_{0,1}} = \begin{bmatrix} 0 \\ 0 \end{bmatrix}$$

The first set starts with a relatively high frequency and tends towards lower frequencies (decreasing frequency), whereas the second set starts with a low frequency and tends towards higher frequencies (increasing frequency). Using these sets, the force-time and displacement-time histories of the Duffing oscillator were simulated over 42 excitation frequencies, ranging from $\omega_1 = 1$ rad/s to $\omega_N = 20$ rad/s, whilst retaining the original simulation time and step size. Using Eq. 2.47, the first-order pseudo-FRFs were obtained, and are shown in relation to the pseudo-FRFs obtained using the describing function method in Figure 2.11.

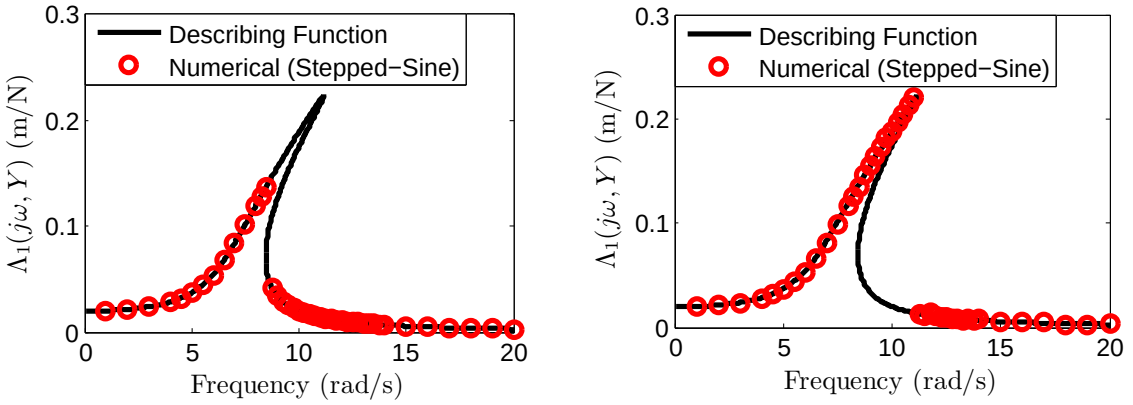

Figure 2.11: Comparison of the first-order pseudo-FRFs obtained using the describing function representation and the numerical simulations, for a) decreasing frequency and b) increasing frequency.

Here, it is apparent that the first-order pseudo-FRFs obtained with the stepped-sine method exhibit the jump phenomenon around the peak resonance frequency. The frequency where the jump phenomenon occurs varies with the initial conditions; Figure 2.11a) shows that the jump occurs around the lower transition frequency ω_{min} when the

first set of initial conditions are used, whereas in Figure 2.11b) the jump occurs around the upper transition frequency ω_{max} for the second set of initial conditions. This demonstrates that the measured pseudo-FRF varies according to the direction of the frequency vector used for the stepped-sine approach.

2.6 Stability analysis of nonlinear systems

Whereas the stability of linear systems is typically assessed using Nyquist theory, as discussed in the introductory chapter, nonlinear stability analysis is primarily conducted using Lyapunov methods, which can be applied to a large number of nonlinear systems and give detailed information about the stability characteristics of the system. Additional tools used for analysing the stability of nonlinear systems include the phase plane trajectory method [96], the nonlinear Nyquist criteria [54], the circle and Popov criteria [54], and Lyapunov exponents [97].

Several of these methods are examined with regards to their ability to predict the overall stability, as well as considering the existence and characteristics of limit-cycle oscillations.

2.6.1 Lyapunov stability

The Lyapunov theory of dynamic systems offers a useful representation for the stability of general nonlinear systems. In addition to specifying whether the nonlinear system is stable or not, Lyapunov theory is capable of revealing additional stability characteristics, such as the stability region (local and global stability) and the type of stability (stable, asympotically stable, or exponentially asymptotically stable). The theory is divided into two methods; the first method is Lyapunov's First (indirect) Method, with Lyapunov exponents, and the second method is Lyaponuv's Second (direct) Method. The indirect method is used to assess the local stability of the equilibrium points, whereas the direct method is used to ascertain the overall stability characterisitics of the nonlinear system.

a) Lyapunov's indirect method

First, the dynamics of the nonlinear system is expressed in autonomous form with no input,

$$\dot{\mathbf{x}} = \mathbf{f}(\mathbf{x}) \tag{2.49}$$

where $\mathbf{f}(\mathbf{0}) = \mathbf{0}$ is a known equilibrium point. An approximation of the linear state matrix $\mathbf{A}$ is given by taking the Jacobian matrix $\mathbf{J}(\mathbf{x})$ of $\mathbf{f}(\mathbf{x})$ and linearising around the equilibrium point,

$$\mathbf{J}(\mathbf{x}) = \left.\frac{\partial \mathbf{f}(\mathbf{x})}{\partial \mathbf{x}}\right|_{\mathbf{x}=\mathbf{0}} \tag{2.50}$$

The local stability of the nonlinear system is then assessed from the eigenvalues λ_j of the linearised Jacobian matrix evaluated at the origin,

- System is **locally stable** if $\mathrm{Re}(\lambda_j) < 0$ for **all** λ_j
- System is **either locally stable or unstable** if $\mathrm{Re}(\lambda_j) = 0$ for **any** λ_j
- System is **locally unstable** if $\mathrm{Re}(\lambda_j) > 0$ for **any** λ_j

This method may also be applied to additional equilibrium points that may exist, in order to assess their stability. The main drawback of the indirect method is the emphasis on local stability around the equilibrium points, with no observations about the overall global stability.

b) Lyapunov exponents

The Lyapunov exponents of the nonlinear system represent the behaviour of the system about the initial condition $\mathbf{x_0}$, which then vary with time as the trajectory of the system evolves. In this case, we ignore the variation with time and focus on the eigenvalues of the Jacobian matrix at the initial condition $\mathbf{x_0}$,

$$\mathbf{J}(\mathbf{x}) = \left.\frac{\partial \mathbf{f}(\mathbf{x})}{\partial \mathbf{x}}\right|_{\mathbf{x}=\mathbf{x_0}} \tag{2.51}$$

Eigenvalues with negative real parts indicates stability in the local region; conversely, eigenvalues with positive real parts indicate that the system trajectory will initially tend away from the equilibrium position, which suggests that the region is locally unstable. These regions of stability and instability around the origin may be identified by plotting the real Lyapunov exponents against the relevant state variables. As an example, the Jacobian matrix of a single-degree-of-freedom Duffing oscillator may be written as,

$$\mathbf{J}(\mathbf{x}) = \begin{bmatrix} 0 & 1 \\ \frac{-1}{m}\left(k_1 + 3k_3 y^2\right) & -\frac{c}{m} \end{bmatrix} \tag{2.52}$$

The real exponents of an exemplary bi-stable Duffing oscillator ($k_1 < 0, k_3 > 0$) are shown against $x_0 = y$ in Figure 2.12. Here, it is apparent that the real exponents are positive when y is small (which indicates an unstable equilibrium region) and negative for larger values of y (which indicates that the system stabilises further away from the equilibrium).

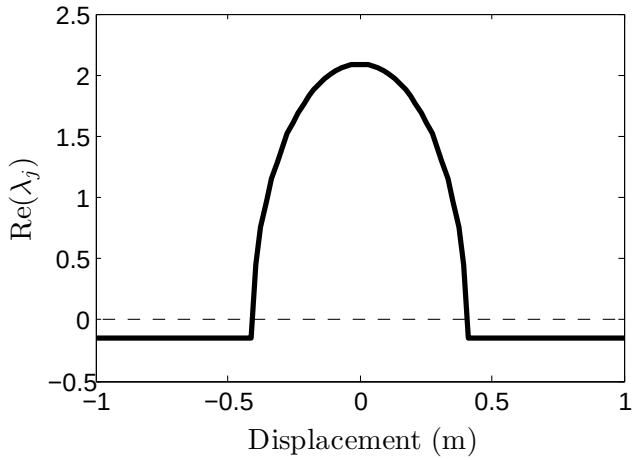

Figure 2.12: Illustration of the Lyapunov exponents of a bi-stable Duffing oscillator against y.

c) Lyapunov's direct method

Lyapunov's Second Method (direct method) is a highly convenient way of establishing the stability of the equilibrium point(s) of a dynamic system. Unlike Lyapunov's First Method, which is used to determine the local stability of the equilibrium points, Lyapunov's Second Method can also establish the nature of the stability (stable or asymptotically stable) in a local and global sense.

The general stability of a nonlinear system may be assessed using an arbitrary Lyapunov function, denoted as $V(\mathbf{x})$, which acts as an energy-like variable. If the trajectory of the Lyapunov function is decreasing across all the states of the system, then the system is said to be asymptotically stable. Therefore, the Lyapunov function and its Lie derivative $\dot{V}(\mathbf{x})$ are used in conjunction to determine the overall stability. To ensure that the nonlinear system is asymptotically stable, $V(\mathbf{x})$ and $\dot{V}(\mathbf{x})$ should satisfy the following conditions,

1. $V(\mathbf{x})$ and $\dot{V}(\mathbf{x})$ must both be functions of **all** elements of $\mathbf{x}$.
2. $V(\mathbf{x}) = 0$ if and only if $\mathbf{x} = 0$.
3. $V(\mathbf{x}) > 0$ for $\mathbf{x} \in S \quad \{S \subseteq \mathbb{R}^n \,|\, S \neq 0\}$.
4. $\dot{V}(\mathbf{x}) = 0$ if and only if $\mathbf{x} = 0$.
5. $\dot{V}(\mathbf{x}) < 0$ for $\mathbf{x} \in S \quad \{S \subseteq \mathbb{R}^n \,|\, S \neq 0\}$.

If the set S has the property $\{S : \mathbb{R}^n \to \mathbb{R} \,|\, S \neq 0\}$ and the state vector is radially unbounded $\big(\|\mathbf{x}\| \to \infty \Rightarrow \mathbf{f}(\mathbf{x}) \to \infty\big)$, then, provided all other conditions are satisfied, the system is said to be globally asymptotically stable.

For a linear time-invariant system, the Lyapunov function and its Lie derivative may be expressed in the quadratic form $V(\mathbf{x}) = \mathbf{x^T P x}$ and $\dot{V}(\mathbf{x}) = -\mathbf{x^T Q x}$, where $\mathbf{P} = \mathbf{P^T}$ and $\mathbf{Q} = \mathbf{Q^T}$ are symmetric matrices that are related by the Lyapunov equation,

$$\mathbf{A^T P} + \mathbf{PA} = -\mathbf{Q} \tag{2.53}$$

In this case, the conditions for global asymptotic stability are satisfied if $\mathbf{P}$ and $\mathbf{Q}$ are positive-definite for *any* arbitrary choice of Lyapunov function. It should be noted that if one particular choice of candidate does not yield positive-definite $\mathbf{P}$ and $\mathbf{Q}$ matrices, global asymptotic stability may still be proven using an alternative candidate choice.

Whilst the direct method is a powerful tool for examining the general stability of nonlinear systems, there are often considerable difficulties with finding a suitable Lyapunov candidate that satisfies all the conditions for asymptotic stability; conversely, it is very difficult to prove instability, since the existence of a suitable Lyapunov candidate must be ruled out. Common types of Lyapunov candidates include quadratic polynomials, multiple functions [98] and piecewise terms [99]. Additional methods for obtaining suitable Lyapunov candidates is the subject of ongoing research.

2.6.2 Nonlinear Nyquist criterion using describing functions

Whilst the linear Nyquist techniques discussed in the introductory chapter are not directly applicable to nonlinear structures, they can be applied indirectly by using a Lur'e representation for the structure. In this manner, it is possible to take advantage of powerful, well-established analytical tools for linear systems with feedback, for the purpose of detecting and analysing limit-cycle oscillation behaviour. This is known as the *nonlinear Nyquist criterion.*

First, the nonlinear system is illustrated using the diagram shown in Figure 2.5, where the nonlinear function is replaced with a describing function representation (displayed in Figure 2.13). Using Nyquist theory with Lur'e analysis, the first-order pseudo-transfer function may be expressed in feedback form,

$$\Lambda_1(j\omega, Y) = \frac{H(j\omega)}{1 + N(j\omega, Y)H(j\omega)} \tag{2.54}$$

The condition for limit-cycle oscillations in the nonlinear system may be given as follows,

$$1 + N(j\omega, Y)H(j\omega) = 0 \tag{2.55}$$

which may be rearranged to yield,

$$H(j\omega) = -\frac{1}{N(j\omega, Y)} \tag{2.56}$$

Eq. 2.56 states that the existence of a limit-cycle oscillation is dependent on the intersection of the linear Nyquist plot with the negative inverse of the describing function in the Nyquist domain. If the nonlinearities are exclusively associated with stiffness or damping, then the right-hand term in Eq. 2.56 will lie on the negative real axis or positive imaginary axis respectively; therefore, the Nyquist diagram of $H(j\omega)$ should cross the relevant axis for limit-cycle oscillations to occur.

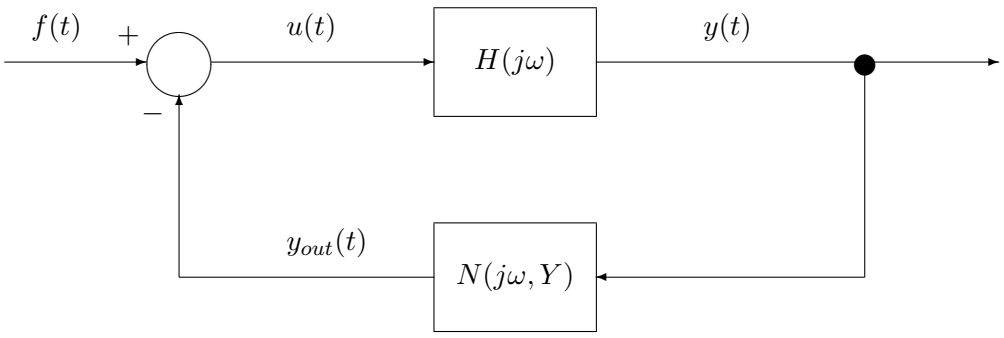

Figure 2.13: Representation of a nonlinear system in the frequency domain, with a linear feedforward path, and a describing function in the feedback path.

Furthermore, if the describing function is bounded to a particular sector (*e.g.* $0 < N(j\omega, Y) < 1$), then $H(j\omega)$ must also cross the axis within this sector when mapped to its inverse. This is demonstrated in Figure 2.14.

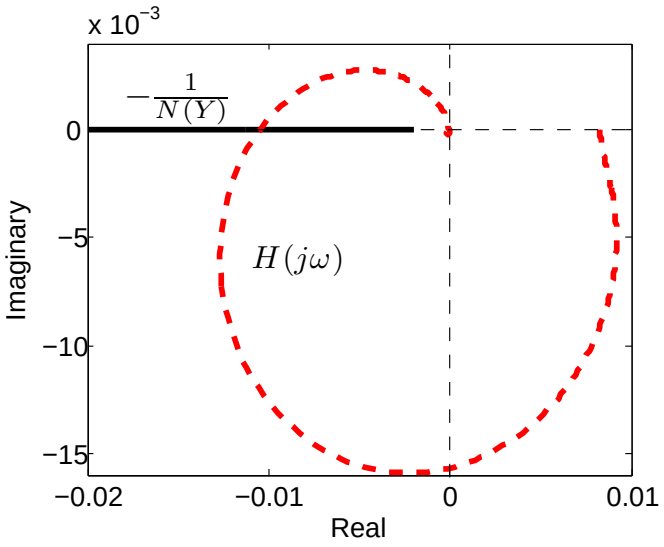

Figure 2.14: Nyquist plot of $H(j\omega)$ against the negative inverse describing function. A limit-cycle oscillation is predicted at the point of intersection.

If a limit-cycle oscillation is predicted, then its stability characteristics may be assessed by examining the negative inverse describing function as Y increases; if it moves from infinity to the origin, then the limit-cycle oscillation remains stable. Conversely, the negative inverse describing function moving from the origin to infinity indicates an unstable limit-cycle oscillation. In addition, the amplitude and frequency of the limit-cycle oscillation may be approximated as the amplitude Y associated with the inverse describing function and the frequency at the intersection point. This approach can yield accurate results if $H(j\omega)$ has sufficient low-pass characteristics, and the limit-cycle oscillation is approximately sinusoidal. The method may also be extended to nonlinear multi-degree-of-freedom structures using the describing function matrix.

Having said this, the describing function approach may also fail badly in certain scenarios;

1. Limit-cycle oscillations may be falsely predicted by the describing function approximation where none exist [100].
2. Limit-cycle oscillations may not be predicted by the describing function approximation where one exists [100].
3. The amplitude and frequency predictions may be greatly inaccurate if the limit-cycle oscillation is not sinusoidal.

Therefore, the describing function approximation should be verified using simulations to establish the accuracy of the predictions.

2.6.3 Circle criterion

The circle criterion acts as an extension to the Nyquist criterion by using the nonlinear function[2] $f\big(y\big)$ instead of the describing function approximation in the feedback loop. First, we assume that the nonlinearity is an odd-order function, such that,

$$f\big(y\big)y \geq 0 \tag{2.57}$$

and the nonlinearity is therefore bounded by the sector $[0, \infty)$. Using Lyapunov's direct method, the nonlinear system is globally asymptotically stable if positive-definite matrices $\mathbf{P}, \mathbf{Q}$ exist for the following Lyapunov candidate,

$$V(\mathbf{x}) = \mathbf{x^T P x} \tag{2.58}$$

$$\dot{V}(\mathbf{x}) = -\mathbf{x^T Q x} - 2f\big(y\big)y \tag{2.59}$$

The Kalman-Yakubovich-Popov lemma [101] states that $\mathbf{P}, \mathbf{Q}$ may both be positive-definite if $H(s)$ is strictly positive real, thereby satisfying the conditions for global asymptotic stability. Provided that $H(s)$ is a SISO transfer function, $H(s)$ is strictly positive real if,

- All poles of $H(s)$ lie in the left-hand complex plane (*i.e.* $H(s)$ is stable).
- $\mathrm{Re}\big(H(j\omega)\big) \geq 0 \ \forall \omega \in \Re$ (*i.e.* the Nyquist plot of $H(j\omega)$ lies in the right-hand complex plane).

Since the Nyquist plot of $H(j\omega)$ will wander into the left-hand complex plane for orders greater than unity (*e.g.* a linear single-degree-of-freedom system is second-order), the strictly positive real condition for $H(s)$ is restrictive and often difficult to satisfy. This requirement may be relaxed if the nonlinearity is bound by a sector condition, with a minimum $k_1 y(t)$ and maximum $k_2 y(t)$,

$$k_1 \leq \frac{f\big(y\big)}{y} \leq k_2 \tag{2.60}$$

[2]Here, the system output $y(t)$ is generalised to any state that is nonlinear, instead of being restricted to displacement

In this manner, the stability of the nonlinear system is determined by $H(s)$ and the sector $[k_1, k_2]$. Using loop transformations [54], the linear transfer function $H(s)$ and nonlinearity $f\big(y\big)$ becomes $\hat{H}(s)$ and $\hat{f}\big(y\big)$ respectively, where,

$$\hat{H}(s) = \frac{k_2 H(s) + 1}{k_1 H(s) + 1} \tag{2.61}$$

$$\hat{f}\big(y\big) = \frac{f\big(y\big) - k_1 y}{k_2 y - f\big(y\big)} \tag{2.62}$$

The transformed nonlinearity in Eq. 2.62 has the sector $[0, \infty)$. Therefore, the nonlinear system is globally asymptotically stable if $\hat{H}(s)$ is strictly positive real, which imposes the following conditions,

- The roots of $k_1 H(s) + 1 = 0$ lie in the left-hand side of the complex plane.
- $\mathrm{Re}\big(\hat{H}(j\omega)\big) \geq 0 \;\; \forall \omega \in \Re$.

From these conditions, we can concur that $\hat{H}(j\omega)$ should be stable and its locus should be confined to the right-hand side of the complex plane. These requirements may be defined in terms of the original linear transfer function $H(s)$ by considering the relationship between $\hat{H}(s)$ and $H(s)$,

$$H(s) = \frac{\hat{H}(s) - 1}{k_2 - k_1 \hat{H}(s)} \tag{2.63}$$

This yields the transformation Z from the $\hat{H}(s)$ domain to the $H(s)$ domain,

$$Z = \frac{\hat{Z} - 1}{k_2 - k_1 \hat{Z}} \tag{2.64}$$

In the $\hat{H}(s)$ domain, the boundary between a stable and unstable system is the entire imaginary axis. Applying transformation Z maps the imaginary axis to a circle with diameter $[\frac{-1}{k_1}, \frac{-1}{k_2}]$ in the $H(s)$ domain. The entire left-hand plane in the $\hat{H}(s)$ domain lies inside this circle in the $H(s)$ domain, whereas the right-hand plane lies outside this circle. Therefore, $\hat{H}(s)$ is strictly positive real if the locus of $H(j\omega)$ stays outside this circle, and the nonlinear system is globally asymptotically stable. This is shown in Figure 2.15.

It should be noted that if $k_1 = 0$, then the circle becomes a line as the diameter tends to $-\infty$, and so the locus of $H(j\omega)$ should stay to the right of $-\frac{1}{k_2}$ for this case.

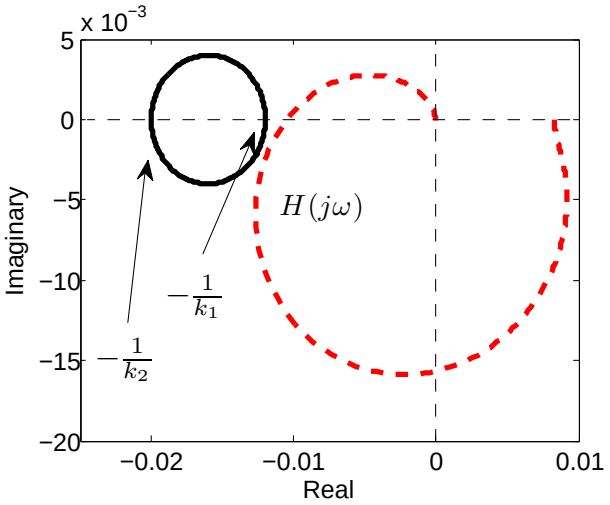

Figure 2.15: Nyquist plot of $H(j\omega)$ in conjunction with the circle bound by $-\frac{1}{k_2}$ and $-\frac{1}{k_1}$. The locus should not penetrate the circle to ensure asymptotic stability.

To summarise, the circle criterion is a convenient method for ascertaining the stability of a nonlinear system by utilising Nyquist, Lur'e, and Lyapunov analysis. The method can be extended to nonlinear multiple-degrees-of-freedom using the *multivariable circle criterion* [54]. The results are usually consistent with the nonlinear Nyquist criterion, as the describing function representation is also contained within the circle. Furthermore, the nonlinearity is allowed to vary with time. The primary limitations of the circle criterion are the restrictions on the form of nonlinearity (static, memoryless, odd-order, symmetric) and the lack of further information about the stability of the system if the circle is penetrated by the locus.

2.7 Concluding remarks

In this chapter, we have examined the nonlinear behaviour of structures and their potential causes. Although there are many types of structural nonlinearities, the primary nonlinearities of interest are stiffness nonlinearities and saturation, both of which may occur in inertial actuators. Several popular methods for modelling structural nonlinearities, including describing functions, Volterra series, and numerical simulations, are investigated and their strengths and weaknesses are discussed. Finally, the stability of a nonlinear structure may be assessed using popular techniques such as Lyapunov theory, the nonlinear Nyquist criterion, and the circle criterion.

Chapter 3

State Feedback Control for Nonlinear Systems

3.1 Introduction

One popular technique for controlling the vibration levels of a structure is to reassign its eigenvalues to a new set of values using active vibration control. Eigenvalue assignment attracted considerable interest from the active control community following Wonham's theorem [102] that the eigenvalues of a linear time-invariant system that is controllable and observable may be assigned arbitrarily with state feedback. The development of the independent modal-space control method by Meriovitch [103] ensured that, in principle, a single structural mode could be controlled independently of other modes.

Recently, Ram and Mottershead [33] established the linear Sherman-Morrison receptance method, which assigns the eigenvalues using measured receptances instead of modelling the mass, damping, and stiffness matrices. This approach has two advantages over most conventional state-space methods. Firstly, it is not necessary to measure or estimate all the states of the system using an observer; only the available states are required to assign the eigenvalues. Secondly, there is no need for model reduction, and so the uncertainties, assumptions, and errors associated with finite element models are avoided.

The aim of this chapter is to extend the pole placement techniques developed using linear state feedback to a class of single-degree-of-freedom structures with relatively simple nonlinearities, using the Duffing oscillator as an exemplary system. Similar pole placement strategies for nonlinear systems have been considered by Liu [104] using neural networks,

and it is apparent that re-assigning the poles of a nonlinear system presents a number of challenges.

Firstly, the poles of a nonlinear structure are generally less well-defined in comparison to linear structures, since nonlinear systems typically exhibit an infinite number of poles as a result of harmonic responses. Secondly, the effects of bifurcation, chaos, jump phenomena, and limit-cycle oscillations that are associated with nonlinear systems may be detrimental to the performance and stability of the structure [105]; therefore, the control aims are typically more complex than for linear structures. Thirdly, accounting for structural nonlinearities greatly increases the mathematical complexity of these techniques, and may require the use of numerical methods for accurate eigenvalue assignment.

In the first section, the linear Sherman-Morrison receptance method is extended to simple nonlinear systems through the use of describing functions and the Volterra series [34]. In order to ensure accurate assignment, the method is updated iteratively to account for changes in the nonlinear structural dynamics as a result of the feedback control. The iterative procedure is first demonstrated trivially by using an extended harmonic balance method, where the structural parameters are assumed to be known. Next, it is shown that the iterative procedure may also be applied using measured open-loop receptances and Volterra series approximations, and does not require *a priori* knowledge of the system parameters or the form of the nonlinearity. In the second section, several alternative techniques are explored for the purposes of assigning eigenvalues that exhibit desirable closed-loop properties [106], such as the minimisation of the bifurcation region and the maximisation of the excitation force required for closed-loop bifurcation to occur.

3.2 Iterative Sherman-Morrison receptance method

As stated in the introduction, the Sherman-Morrison receptance method is an empirical technique that is used to reassign the eigenvalues of a linear structure using measured receptances, such that the dynamic behaviour is more desirable. In order to extend this method to nonlinear structures, it is necessary to include the structural nonlinearities in the feedback gain matrix. Here, the equation of motion for a general second-order nonlinear system with control can be written as,

$$m\ddot{y}(t) + c\dot{y}(t) + k_1 y(t) + f_{NL}\big[y(t), \dot{y}(t)\big] = f(t) + u(t), \tag{3.1}$$

where m, c, k_1 are the linear structural parameters;

$f(t)$ is the primary excitation force;

$y(t), \dot{y}(t)$ represent the structural displacement and velocity respectively;

$f_{NL}\big[y(t), \dot{y}(t)\big]$ is the nonlinear restoring force as a function of $y(t)$ and $\dot{y}(t)$;

$u(t)$ is the secondary control force.

In this case, the control force $u(t)$ can be described as a linear combination of the structural states,

$$u(t) = -\mathbf{G}\mathbf{x}(\mathbf{t}), \tag{3.2}$$

where $\mathbf{x}(\mathbf{t}) = \begin{bmatrix} y(t) & \dot{y}(t) \end{bmatrix}^T$ represents the structural states and $\mathbf{G} = \begin{bmatrix} g & h \end{bmatrix}$ are the displacement and velocity feedback gains to be determined.

The control force is used to move the fundamental open-loop poles $\lambda_{1,2}$ of the nonlinear system to the desired closed-loop poles $\mu_{1,2}$. Since nonlinear systems have an infinite number of poles, the pole assignment considered here is for the peak resonance of the fundamental pole pair.

The effect of feedback control on the structural dynamics can be modelled as a Lur'e problem, which is illustrated in Figure 3.1. Therefore, the equation of motion for the closed-loop system may be written as,

$$m\ddot{y}(t) + (c+h)\dot{y}(t) + (k_1+g)y(t) + f_{NL}\big[y(t), \dot{y}(t)\big] = f(t), \tag{3.3}$$

Using the linear receptance method, the standard procedure is to invert the open-loop dynamical equation, as given by Eq. 3.1 with $u(t) = 0$, in order to express the control problem in terms of the receptance, which can be directly measured. However, the structure undergoing control is nonlinear, and so the structural response contains superharmonics at integer multiples of the fundamental forcing frequency ω.

By assuming that the structure has low-pass characteristics [107], most of the structural energy is concentrated at the fundamental forcing frequency ω. This means that the first-order open-loop pseudo-receptance $\Lambda_1(j\omega, Y_o)$ can be substituted for $H(j\omega)$ in the receptance method to approximate the structural dynamics (Y_o being the open-loop displacement amplitude response). Unlike linear receptances, the first-order pseudo-receptance is dependent on the displacement amplitude as well as the location of the poles and zeros. This dependency is modelled using the describing function $N(s, Y)$ of

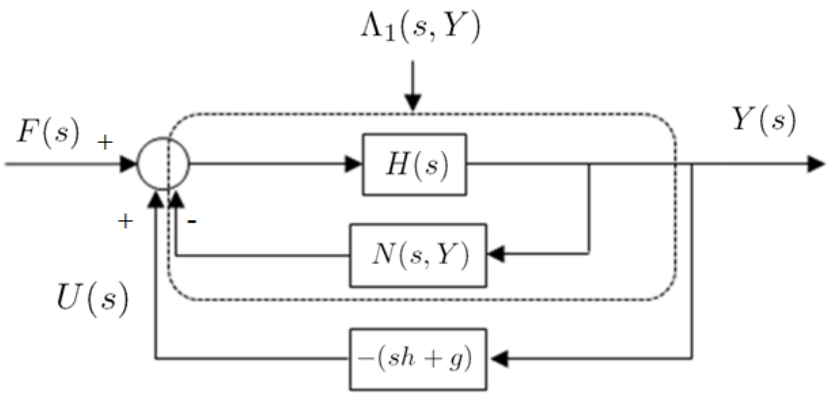

Figure 3.1: Nonlinear system with state feedback control modelled as a Lur'e representation.

the nonlinear structure, which can be viewed as the first-order Laplace transform of the nonlinear restoring force $f_{NL}\big[y(t), \dot{y}(t)\big]$. Thus, by setting $u(t) = 0$ in Eq. 3.1 and assuming that the displacement response to sinusoidal excitation is of the form $y(t) \approx Y\sin(\omega t)$, taking the Laplace transform of Eq. 3.1 yields,

$$[ms^2 + cs + k_1 + N(s, Y_o)]Y(s) = F(s), \tag{3.4}$$

and the first-order open-loop pseudo-receptance is found from $Y(s) = \Lambda_1(s, Y_o)F(s)$,

$$\Lambda_1(s, Y_o) = [ms^2 + cs + k_1 + N(s, Y_o)]^{-1}. \tag{3.5}$$

Similarly, taking the Laplace transform of Eq. 3.3 yields,

$$[ms^2 + (c + h)s + (k_1 + g) + N(s, Y_c)]Y(s) = F(s), \tag{3.6}$$

Y_c being the closed-loop displacement amplitude. The first-order closed-loop pseudo-receptance $\bar{\Lambda}_1(s, Y_c)$ is,

$$\bar{\Lambda}_1(s, Y_c) = [ms^2 + (c + h)s + (k_1 + g) + N(s, Y_c)]^{-1}. \tag{3.7}$$

Eq. 3.6 indicates that the state feedback and describing function act as scalar updates to the dynamic stiffness of the underlying linear open-loop system. Therefore, the closed-loop receptance can be expressed in terms of the open-loop receptance and the feedback gains using the Sherman-Morrison formula [108],

$$\bar{\Lambda}_1(s, Y_c) = \Lambda_1(s, Y_c) - \frac{\Lambda_1(s, Y_c)(sh + g)\Lambda_1(s, Y_c)}{1 + (sh + g)\Lambda_1(s, Y_c)}, \tag{3.8}$$

which yields the characteristic equation for the desired closed-loop poles,

$$1 + (\mu_j h + g)\Lambda_1(\mu_j, Y_c) = 0, \quad j = 1, 2, \tag{3.9}$$

Rearranging in a matrix form, the feedback control gains are obtained using,

$$\mathbf{G} = -\begin{bmatrix} \mu_1\Lambda_1(\mu_1, Y_c) & \Lambda_1(\mu_1, Y_c) \\ \mu_2\Lambda_1(\mu_2, Y_c) & \Lambda_1(\mu_2, Y_c) \end{bmatrix} \begin{bmatrix} 1 \\ 1 \end{bmatrix}, \tag{3.10}$$

which is equivalent to the linear Sherman-Morrison equation [108]. However, if we examine Eq. 3.10 carefully, we notice that the original open-loop receptance $\Lambda_1(\mu_j, Y_o)$ has been replaced with the modified open-loop receptance $\Lambda_1(\mu_j, Y_c)$, due to the change in displacement amplitude. In other words, the nonlinearity of the closed-loop system must be taken into account when assigning the closed-loop poles. The inter-dependent relationship between the structural nonlinearities and the control parameters complicates the process of finding the true feedback gains required for accurate pole assignment, since the determination of $\Lambda_1(\mu_j, Y_c)$ requires knowledge of h and g. Having said this, the problem, in principle, may be overcome by iteratively modifying $\mathbf{G}$, Y_c, and $\Lambda_1(\mu_j, Y_c)$, until they converge on the correct solution.

In order to establish the concepts behind the iterative procedure, several representations of the open-loop and closed-loop systems are shown in Figure 3.2 using input-output diagrams. The first input-output diagram represents the open-loop system, which features the open-loop displacement response amplitude $Y_o(s)$. This representation is used non-iteratively to obtain initial estimates of the feedback gains by replacing $\Lambda_1(\mu_j, Y_c)$ with $\Lambda_1(\mu_j, Y_o)$ in Eq. 3.10.

The second diagram illustrates the closed-loop system using the form given in Eq. 3.7. Here, the control force is included in the structural dynamics for the purpose of altering $\Lambda_1(s, Y_o)$ to $\bar{\Lambda}_1(s, Y_c)$, which is the typical formulation used for a control problem. This representation is used to obtain the closed-loop displacement amplitude $Y_c(s)$ from the feedback control gains.

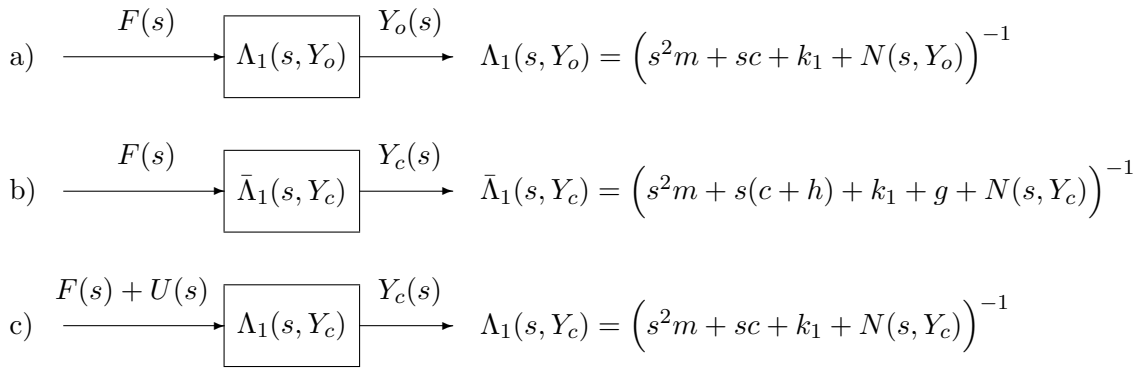

Figure 3.2: Input-output diagrams of a) the open-loop system, b) the closed-loop system represented as a modified transfer function and c) the closed-loop system represented with a modified input.

The third diagram gives an alternative representation of the closed-loop system, where the control force is used to modify the input excitation level applied to the open-loop system. This representation specifies what actually occurs in practice, with the modified input excitation resulting in the closed-loop structural displacement amplitude $Y_c(s)$. The modified open-loop pseudo-receptance is used in Eq. 3.10 to determine the feedback control gains from $Y_c(s)$, which is ascertained using the representation in the second diagram.

It is evident that in order to find the correct feedback gains, an initial set of feedback gains, obtained by replacing $\Lambda_1(\mu_j, Y_c)$ with $\Lambda_1(\mu_j, Y_o)$ in Eq. 3.10, is used to estimate the closed-loop displacement amplitude Y_c with the second representation and the modified open-loop pseudo-receptance $\Lambda_1(\mu_j, Y_c)$ with the third representation. Using $\Lambda_1(\mu_j, Y_c)$, Eq. 3.10 is then applied to obtain a better estimate of the feedback control gains, and the process is repeated iteratively. If the true feedback gains are correctly determined, then $\mathbf{G}$, Y_c, and $\Lambda_1(\mu_j, Y_c)$ will have converged to stable values. Conversely, incorrect feedback gains will result in variations as a result of inconsistencies between the associated parameters. Thus, the iterative procedure can be described as follows,

1. Find or approximate $\Lambda_1(\mu_j, Y_o)$ using either theoretical knowledge or empirical measurements of the system. For the latter approach, the first-order open-loop pseudo-receptance $\Lambda_1(j\omega, Y_o)$ is measured using sinusoidal excitation at an appropriate amplitude level for the system in question. Additional pseudo-receptance measurements at a variety of excitation amplitude levels may be useful for identifying the form and relative strength of the nonlinearity. Using this knowledge, a curve-fit model may be used to estimate $\Lambda_1(\mu_j, Y_o)$, in a similar manner to the linear receptance method.

2. Obtain an initial estimate of the feedback control gains, denoted as $\mathbf{G_k}$, by substituting $\Lambda_1(j\omega, Y_o)$ into Eq. 3.10.

3. Estimate the closed-loop displacement amplitude, denoted as $Y_{c,k}$, using $\mathbf{G_k}$ and the second formulation in Figure 3.2. This can be achieved using the extended harmonic balance method or a Volterra series representation [34]. In either case, $Y_{c,k}$ is a function of $\mathbf{G_k}$ and the underlying linear closed-loop receptance $\bar{H}_1(j\omega_\mu)$, where $\omega_\mu = \Im m(\mu_j)$. The latter parameter is obtained from the underlying linear open-loop receptance, $H_1(j\omega_\mu)$, using the linear Sherman-Morrison formula.

4. Update the open-loop pseudo-receptance, denoted as $\Lambda_1(\mu_j, Y_{c,k})$, using the estimate of the closed-loop displacement amplitude, as shown by the third formulation given in Figure 3.2. Again, this can be accomplished using either the harmonic balance or Volterra series method. In either case, $\Lambda_1(\mu_j, Y_{c,k})$ is a function of $\mathbf{G_k}$ and $Y_{c,k}$.

5. Apply the updated open-loop pseudo-receptance $\Lambda_1(\mu_j, Y_{c,k})$ to Eq. 3.10, in order to obtain a new estimate for the feedback gains $\mathbf{G_{k+1}}$.

6. Repeat the procedure from point 3 until $\mathbf{G_{k+1}}$ converges on the correct solution.

The accuracy of this iterative procedure is dependent on several factors, including the form and relative strength of the structural nonlinearity, and the location of the closed-loop poles in relation to the open-loop poles. For example, the method has been shown to work particularly well for structures with polynomial stiffness nonlinearities, such as the Duffing oscillator, since the nonlinearity is very simple and the first-order pseudo-receptances are well-defined. Moreover, it can be shown that applying state feedback

control has the effect of controlling the harmonic responses of the structure in addition to fundamental response [34]. However, the method does not work well for structures with ill-defined transfer functions, such as the Van der Pol oscillator [45], and structures with complicated discontinuous nonlinearities.

Using a Duffing oscillator as an exemplary structure, the implementation of this iterative procedure is demonstrated using the extended harmonic balance method and the Volterra series representation. The trickiest part of the procedure is estimating the closed-loop displacement amplitude and updating the open-loop pseudo-receptance, as defined in the third and fourth steps, particularly when a Volterra series representation is utilised. On one hand, the extended harmonic balance method is very reliable and delivers accurate results, but requires knowledge of the structural parameters and the form of the nonlinearity. On the other hand, the Volterra series approach utilises measured pseudo-receptances, and so is a better extension of the linear receptance method, but the results are unreliable for strongly nonlinear systems that feature sub-harmonics [93], due to the divergent property of the Volterra series from the correct solution. Therefore, the results are only reliable if the nonlinearity is relatively weak or the closed-loop poles are placed far from the open-loop poles.

3.2.1 Extended harmonic balance method

First, the input force $f(t)$ is defined as an exponentially evolving sinusoid of the form,

$$f(t) = Fe^{\sigma t}\sin(\omega t + \phi), \tag{3.11}$$

and therefore, the following trial solution can be substituted into the Duffing equation in Eq. 2.3,

$$y(t) = Ye^{\sigma t}\sin(\omega t), \tag{3.12}$$

$$\dot{y}(t) = \sigma Ye^{\sigma t}\sin(\omega t) + \omega Ye^{\sigma t}\cos(\omega t), \tag{3.13}$$

$$\ddot{y}(t) = \sigma^2 Ye^{\sigma t}\sin(\omega t) + 2\sigma\omega Ye^{\sigma t}\cos(\omega t) - \omega^2 Ye^{\sigma t}\sin(\omega t). \tag{3.14}$$

Then, the substitution $f(t) = Fe^{\sigma t}\big[\sin(\omega t)\cos(\phi) + \cos(\omega t)\sin(\phi)\big]$ is applied to Eq. 3.11, and the coefficients in Eqs. 3.12, 3.13, and 3.14 are equated,

$$\Big[m(\sigma^2 - \omega^2) + c\sigma + k_1\Big]Ye^{\sigma t} + 0.75k_3Y^3e^{3\sigma t} = Fe^{\sigma t}\sin(\phi), \tag{3.15}$$

$$\Big[2m\sigma + c\Big]\omega Y = F\cos(\phi). \tag{3.16}$$

This is an extension of the terms given in Eqs. 2.12 and 2.13, resulting in the so-called extended harmonic balance method. By assuming that $e^{3\sigma t}$ can be subdivided into a $e^{\sigma t}$ term, with higher-order terms that are ignored in a similar manner to the classical harmonic balance method, Eq. 3.15 becomes,

$$\Big[m(\sigma^2 - \omega^2) + c\sigma + k_1 + 0.75k_3Y^2\Big]Y = F\sin(\phi), \tag{3.17}$$

and then by squaring and summing Eqs. 3.16 and 3.17, the extended cubic equation is,

$$\Big[m(\sigma^2 - \omega^2) + c\sigma + k_1 + 0.75k_3Y^2\Big]^2 Y^2 + (2m\sigma + c)^2(\omega Y)^2 = F^2. \tag{3.18}$$

The result is a cubic equation in Y^2,

$$\begin{aligned} &\frac{9}{16}k_3^2Y^6 + 1.5k_3(k_1 + m(\sigma^2 - \omega^2) + c\sigma)Y^4 + \\ &\Big[(k_1 + m(\sigma^2 - \omega^2) + c\sigma)^2 + ((c + 2m\sigma)\omega)^2\Big]Y^2 - F^2 = 0. \end{aligned} \tag{3.19}$$

If $\sigma = 0$, then Eq. 3.19 reverts to the standard cubic equation stated by Eq. 2.14. By accounting for the state feedback control, Eq. 3.19 becomes,

$$\begin{aligned} &\frac{9}{16}k_3^2Y^6 + 1.5k_3(k_1 + g + m(\sigma^2 - \omega^2) + (c + h)\sigma)Y^4 + \\ &\Big[(k_1 + g + m(\sigma^2 - \omega^2) + (c + h)\sigma)^2 + ((c + h + 2m\sigma)\omega)^2\Big]Y^2 - F^2 = 0, \end{aligned} \tag{3.20}$$

such that the closed-loop displacement Y_c can be obtained from the structural parameters, the feedback gains, and the closed-loop poles $\mu_{1,2}$ by solving Eq. 3.20. This displacement amplitude is then substituted into the describing function $N(s, Y_c)$ and applied to the representation in Figure 3.2c), in order to yield the updated modified open-loop pseudo-receptance $\Lambda_1(\mu_j, Y_c)$.

Numerical example

This procedure may be demonstrated using a Duffing oscillator with the following structural parameters,

$$m = 1 \text{ kg},\ c = 0.1 \text{ Ns/m},\ k_1 = 40 \text{ N/m},\ k_3 = 1 \text{ N/m}^3,\ F = 20 \text{ N} \tag{3.21}$$

These parameters yield the following open-loop poles at the peak resonance frequency,

$$\lambda_{1,2} = \frac{-c}{2m} \pm \sqrt{\frac{k_1(1 - c^2/4k_1m) + 0.75k_3Y^2(j\omega)}{m}} = -0.05 \pm j13.94. \tag{3.22}$$

In this case, we wish to assign a set of closed-loop poles $\mu_{1,2}$ to the structure, for the purpose of increasing the structural damping and altering the peak resonance frequency. The choice of location for the closed-loop poles, in relation to the open-loop poles, determines the influence of the structural nonlinearities in acquiring the feedback gains for accurate assignment. To exemplify this, an illustration of the structural displacement amplitude is shown in the complex domain in Figure 3.3; this is obtained by substituting the structural parameters into Eq. 3.20 and solving the cubic equation. Here, it can be seen that in the complex region around the open-loop poles, the peak resonance becomes distorted, eventually resulting in frequency-domain bifurcation. Therefore, the open-loop structure exhibits strongly nonlinear dynamics around the open-loop poles, which will have a pronounced effect when the desired closed-loop poles are located close to $\lambda_{1,2}$. Conversely, the nonlinear effects are relatively weak when the closed-loop poles are placed far away from open-loop poles, and so the non-iterative receptance method may yield acceptable feedback gains for these cases.

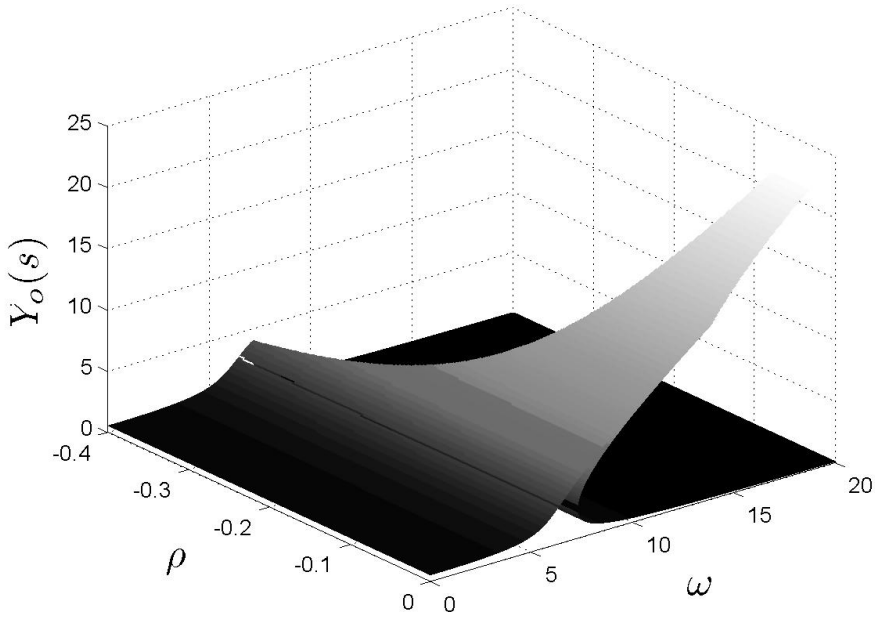

Figure 3.3: Open-loop displacement amplitude of the Duffing oscillator in the complex domain.

For the purposes of this demonstration, the desired closed-loop poles are chosen as follows,

$$\mu_{1,2} = \frac{-(c+h)}{2m} \pm \sqrt{\frac{(k_1+g)(1-(c+h)^2/4(k_1+g)m) + 0.75k_3Y^2(j\omega)}{m}} = -0.1 \pm j11, \tag{3.23}$$

These closed-loop poles are located close to the open-loop poles, such that the importance of the iterative approach can be demonstrated. First, the structural parameters and the closed-loop poles are applied to Eq. 3.19 to obtain the open-loop displacement amplitude $Y_o(\mu_j) = \begin{bmatrix}10.49 & 10.29 & 0.25\end{bmatrix}$ m at the closed-loop pole locations. The closed-loop poles are located close to the open-loop poles, and so the open-loop structural dynamics are strongly nonlinear in this region, hence the multiple possible solutions for $Y_o(\mu_j)$. Experience showed that the smallest solution should be chosen for $Y_o(\mu_j)$.

The next step is to substitute $Y_o(\mu_j)$ into the describing function $N(\mu_j, Y_o) = 0.046$, which is applied to the open-loop receptance to obtain $\Lambda_{1,2}(\mu_j, Y_o) = -0.0124 \pm j0.0002$. By using Eq. 3.10, an initial estimate of the feedback gains $\mathbf{G_k} = \begin{bmatrix}80.96 & 0.1\end{bmatrix}$ is found. Using these feedback gains, the closed-loop poles are located at,

$$\mu_{1,2} = -0.1 \pm j12.89. \tag{3.24}$$

Although the real part of the assigned closed-loop pole pair is correct, the imaginary part is well above the pre-determined value in Eq. 3.23, thereby indicating that the displacement feedback gain is overestimated as a result of ignoring the effects of the closed-loop structural nonlinearities on the closed-loop system. The accuracy of the feedback gains may now be improved by implementing the iterative scheme.

First, the closed-loop displacement amplitude $Y_c(j\omega_\mu) = 2.95$ m is obtained by substituting the feedback gains $\mathbf{G_k}$ into Eq. 3.20 at the imaginary part of the closed-loop pole location. This displacement amplitude is then used to obtain the closed-loop describing function $N(j\omega_\mu, Y_c) = 6.93$, which is substituted into Eq. 3.5 in the place of $N(\mu_j, Y_o)$ to estimate the modified open-loop pseudo-receptance $\Lambda_1(\mu_j, Y_c) = -0.0135 \pm j0.0002$. Applying this updated parameter to Eq. 3.10 results in a new set of feedback gains, and the procedure is repeated iteratively until convergence occurs. The convergence of the displacement feedback gain and the closed-loop displacement amplitude (shown in Figure 3.4) is relatively slow due to the strong nonlinearities, but is otherwise smooth.

Using this iterative approach, the final converged feedback gains are found to be $\mathbf{G} = \begin{bmatrix}19.03 & 0.1\end{bmatrix}$, thereby assigning the closed-loop poles at their pre-determined values,

$$\mu_{1,2} = -0.1 \pm j10.9995. \tag{3.25}$$

A comparison of the open-loop and closed-loop pseudo-receptances, which is shown in Figure 3.5, indicates that the effect of the iteration is to reduce the peak resonance frequency of the closed-loop structure by accounting for the nonlinear stiffness of the Duffing oscillator. Here, the iterative approach is used to assign the closed-loop poles with a high degree of accuracy, with small errors occurring from the strongly nonlinear dynamics and the approximations involved in the extended harmonic balance method.

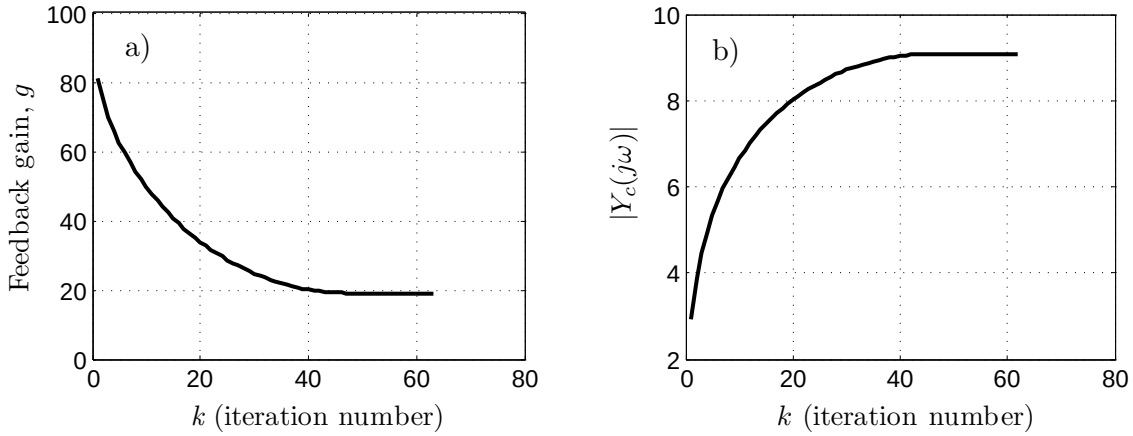

Figure 3.4: Convergence of a) the displacement feedback gain and b) the closed-loop displacement amplitude using the extended harmonic balance method.

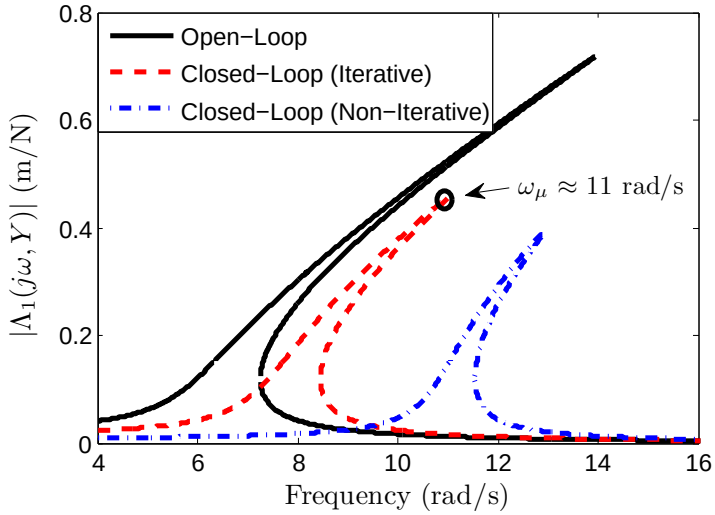

Figure 3.5: Illustration of the open-loop and closed-loop pseudo-receptances, obtained using the non-iterative (linear) and iterative Sherman-Morrison receptance method. The latter approach is able to account for the closed-loop nonlinearity to correctly assign the peak resonance at 11 rad/s.

3.2.2 Volterra series method

Whilst the extended harmonic balance method is capable of assigning poles with a high degree of accuracy, even if the structural dynamics are strongly nonlinear, there are three primary disadvantages that should be taken into account. Firstly, an exact model of the nonlinear system is required, including the structural parameters and the form of the nonlinearity. Since this model is used extensively to assign the closed-loop poles, small errors in the model may result in inaccurate assignment. Secondly, the harmonic balance equation needs to be re-derived for different types of nonlinearities; this is impractical for systems with multiple-degrees-of-freedom, or with complicated nonlinearities. Thirdly, the procedure is not a natural extension of the Sherman-Morrison receptance method, since it is based on modifying the dynamic stiffness using the describing function. These problems can be alleviated using a Volterra series representation, which was introduced in the previous chapter. Since the nonlinear system is described in terms of the input excitation amplitude, the underlying linear FRFs, and the nonlinear parameters, the effects of the controller can be expressed by modifications to the underlying linear receptance, and therefore lends itself more readily to the Sherman-Morrison receptance method.

To obtain expressions for the higher-order frequency response functions, the approximation of $y(t)$ given by Eq. 2.35 is substituted into the equation of motion and the coefficients of the exponential terms are equated. For a Duffing oscillator, this yields the following equations for the first three orders,

$$\left[\frac{F}{2}e^{j\omega t}\right] \qquad \begin{aligned}(-\omega^2 m + j\omega c + k_1)H_1(j\omega) &= 1,\\ H_1(j\omega) &= (-\omega^2 m + j\omega c + k)^{-1}\end{aligned} \tag{3.26}$$

$$\left[\frac{F}{2}e^{-j\omega t}\right] \qquad \begin{aligned}(-\omega^2 m - j\omega c + k_1)H_1(-j\omega) &= 1,\\ H_1(-j\omega) &= H_1^*(j\omega)\end{aligned} \tag{3.27}$$

$$\left[\left(\frac{F}{2}\right)^2 e^{2j\omega t}\right] \qquad \begin{aligned}(-4\omega^2 m + 2j\omega c + k_1)H_2(j\omega, j\omega) &= 0,\\ H_2(j\omega, j\omega) &= 0\end{aligned} \tag{3.28}$$

$$\left[\left(\frac{F}{2}\right)^2\right] \qquad 2H_2(j\omega, -j\omega) = 0 \tag{3.29}$$

$$\left[\left(\frac{F}{2}\right)^2 e^{-2j\omega t}\right] \qquad \begin{gathered}(-4\omega^2 m - 2j\omega c + k_1)H_2(-j\omega, -j\omega) = 0,\\ H_2(-j\omega, -j\omega) = 0\end{gathered} \tag{3.30}$$

$$\left[\left(\frac{F}{2}\right)^3 e^{3j\omega t}\right] \qquad \begin{gathered}(-9\omega^2 m + 3j\omega c + k_1)H_3(j\omega, j\omega, j\omega) + k_3 H_1^3(j\omega) = 0,\\ H_3(j\omega, j\omega, j\omega) = -k_3 H_1^3(j\omega)H_1(3j\omega)\end{gathered} \tag{3.31}$$

$$\left[\left(\frac{F}{2}\right)^3 e^{j\omega t}\right] \qquad \begin{gathered}H_3(j\omega, j\omega, -j\omega) + k_3 H_1^2(j\omega)H_1^*(j\omega) = 0,\\ H_3(j\omega, j\omega, -j\omega) = -k_3 H_1^2(j\omega)H_1^*(j\omega)\end{gathered} \tag{3.32}$$

$$\left[\left(\frac{F}{2}\right)^3 e^{-j\omega t}\right] \qquad \begin{gathered}H_3(j\omega, -j\omega, -j\omega) + k_3 H_1(j\omega)H_1^{*2}(j\omega) = 0,\\ H_3(j\omega, -j\omega, -j\omega) = H_3^*(j\omega, j\omega, -j\omega)\end{gathered} \tag{3.33}$$

$$\left[\left(\frac{F}{2}\right)^3 e^{-3j\omega t}\right] \quad \begin{gathered}(-9\omega^2 m - 3j\omega c + k_1)H_3(-j\omega, -j\omega, -j\omega) + k_3 H_1^3(-j\omega) = 0,\\ H_3(-j\omega, -j\omega, -j\omega) = H_3^*(j\omega, j\omega, j\omega)\end{gathered} \tag{3.34}$$

The expression for a generalised frequency response function of a Duffing oscillator, with arbitrary order, is given as follows,

$$H_{n,i} = -k_3 H_1((n-2i)j\omega)\sum H_{n_1,i_1}H_{n_2,i_2}H_{n_3,i_3} \tag{3.35}$$

where,

$$H_{n,i} = H_n(\overbrace{j\omega, \cdots, j\omega}^{\text{n terms}}, \underbrace{-j\omega, \cdots, -j\omega}_{\text{i terms}}) \tag{3.36}$$

$$n_1 + n_2 + n_3 = n, \quad \{n_{1,2,3} \in 2k+1, \forall k \in \mathbb{N}, n_{1,2,3} \leq n-2\} \tag{3.37}$$

$$i_1 + i_2 + i_3 = i, \quad \{i_{1,2,3} \in \mathbb{N}, i_{1,2,3} \leq i\} \tag{3.38}$$

Eq. 3.36 indicates that the complexity of the expression increases with the order of the generalised FRFs, since knowledge of all the additional lower-order FRFs is required. Fortunately, the Volterra kernels also diminish in importance as the order is increased,

such that it is normally sufficient to utilise a few generalised frequency response functions as an approximation. Furthermore, it is apparent from Eq. 3.36 that knowledge of the underlying linear receptance $H_1(j\omega)$, the excitation amplitude, and the nonlinear parameter(s) is sufficient to obtain the higher-order FRFs of a nonlinear system. In practice, $H_1(j\omega)$ may be measured experimentally by carefully choosing an input excitation amplitude such that the system response is dominated by the underlying linear dynamics (*e.g.* a small excitation amplitude for a Duffing oscillator). Identifying the form and relative strength of the nonlinear parameters is more difficult, and may be achieved by applying curve-fitting methods to the measured data, provided that the nonlinearity is simple and relatively weak. Using Eq. 2.39, the open-loop displacement amplitude $Y_o(j\omega)$ can be approximated as follows,

$$\begin{aligned} Y_o(j\omega) \approx H_1(j\omega)F(j\omega) + \frac{3}{4}H_3(j\omega, j\omega, -j\omega)F^3(j\omega) + \cdots + \\ \frac{n}{2^{n-1}}H_n(j\omega, \cdots, -j\omega)F^n(j\omega), \quad n = 5, 7, 9, \cdots \end{aligned} \tag{3.39}$$

Since $Y_o(j\omega)$ may be obtained experimentally, the primary unknowns in Eq. 3.39 are the higher-order FRFs, which may be ascertained directly by curve fitting a suitable nonlinear model to the measured data. This nonlinear model may be estimated using additional identification methods (e.g. see reference [109]).

Numerical example

This procedure is demonstrated using a Duffing oscillator, with the structural parameters given in Eq. 3.21. In this case, we wish to assign the following closed-loop poles at $F(j\omega) = 20$ N,

$$\mu_{1,2} = -0.35 \pm j13 \tag{3.40}$$

Using the iterative Sherman-Morrison procedure, the initial aim is to obtain the open-loop pseudo-receptance at the closed-loop pole location, $\Lambda_1(\mu_j, Y_o)$. It is assumed that the system parameters are unknown, where only the excitation amplitude $F(j\omega)$ and the equivalent open-loop pseudo-receptance $\Lambda_1(j\omega, Y_o)$ are available. An illustration of the open-loop pseudo-receptance at $F(j\omega) = 20$ N in Figure 3.6b) indicates that the nonlinearity is relatively strong, since bifurcation is present. Therefore, in order to obtain a good approximation of the underlying linear open-loop receptance $H_1(j\omega)$, the open-loop

pseudo-receptance is obtained at a relatively low amplitude $F(j\omega) = 1$ N. Furthermore, the open-loop pseudo-receptance is also obtained at $F(j\omega) = 2$ N and $F(j\omega) = 3$ N for the purpose of finding a suitable Volterra series representation. By applying curve-fitting to these measured FRFs [85, 86], a seventh-order Volterra model of a Duffing oscillator is found to be sufficient for the purpose of representing the open-loop pseudo-receptance,

$$\begin{aligned}\Lambda_1(j\omega, Y_o) = f(j\omega, H_1(j\omega), k_3) \approx H_1(j\omega) + 0.75H_3(j\omega, j\omega, -j\omega)F^2(j\omega) + \\ 0.625H_5(j\omega, j\omega, j\omega, -j\omega, -j\omega)F^4(j\omega) + \\ 0.5469H_7(j\omega, j\omega, j\omega, j\omega, -j\omega, -j\omega, j\omega)F^6(j\omega)\end{aligned} \tag{3.41}$$

where $k_3 = 1$ is found. A rational fraction polynomial model is then curve-fitted [110] to $H_1(j\omega)$ for the purpose of obtaining a general Laplace-domain model $\hat{H}_1(s)$, as required by the method. The model is of the form,

$$\hat{H}_1(s) = \frac{0.025}{0.025s^2 + 0.0025s + 1} \tag{3.42}$$

which is used to estimate the underling linear open-loop receptance at the closed-loop pole location, $H_1(\mu_j) \approx 8.37 \times 10^{-3} + j5.49 \times 10^{-4}$. By applying $H_1(\mu_j)$ to Eq. 3.35 and Eq. 3.41, the estimation $\Lambda_1(\mu_j, Y_o) \approx 8.37 \times 10^{-3} + j5.49 \times 10^{-4}$ is obtained. Since $\Lambda_1(\mu_j, Y_o)$ and $H_1(\mu_j)$ are almost exactly equivalent, we can infer that the closed-loop poles are sufficiently far from the open-loop poles to render the higher-order FRFs negligible in the open-loop pseudo-receptance.

Estimations of the open-loop pseudo-receptances are made using the Volterra model, which are shown alongside the open-loop pseudo-receptances for $F(j\omega) = 1$ N, $F(j\omega) = 3$ N and $F(j\omega) = 20$ N in Figures 3.6a) and 3.6b). These results indicate that the Volterra model is convergent at low excitation amplitudes, yet becomes divergent when higher excitation amplitudes are considered. Since the closed-loop poles are far from the open-loop poles, the divergent behaviour near the peak resonance will not affect the accuracy of the assignment. However, if the closed-loop poles were assigned near the open-loop poles, the divergent behaviour would detrimentally affect the accuracy of the estimation of $\Lambda_1(\mu_j, Y_o)$, and, ultimately, the estimation of the feedback gains. Therefore, the closed-loop poles should be assigned far away from the open-loop poles to prevent the divergence of the Volterra model becoming an issue.

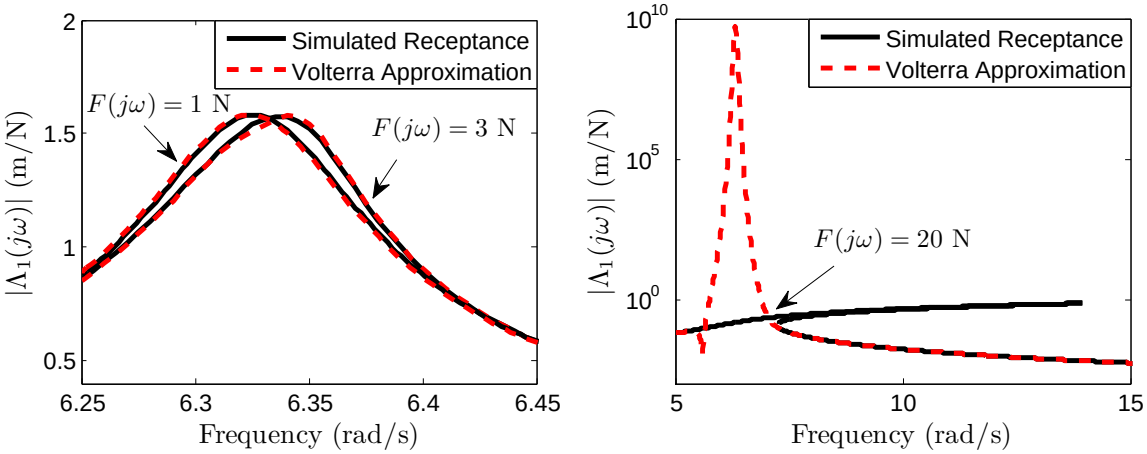

Figure 3.6: Illustration of the simulated open-loop pseudo-receptances and the approximations obtained with the Volterra model for a) 3 N and b) 20 N.

The second step of the iterative procedure is to obtain the initial estimated feedback control gains $\mathbf{G_k} = \begin{bmatrix} 206.08 & 0.5 \end{bmatrix}$ using Eq. 3.10. These feedback gains are then used in the third step in order to estimate the closed-loop displacement amplitude $Y_c(j\omega_\mu)$. In order to achieve this, it is necessary to ascertain the underlying linear closed-loop receptance $\bar{H}_1(j\omega_\mu)$ from $H_1(j\omega_\mu)$ using the Sheman-Morrison formula in Eq. 3.8. Here, $\bar{H}_1(j\omega_\mu) = 1.02 \times 10^3 - j0.11$ is obtained. By using the established Volterra model in Eq. 3.41, the closed-loop displacement amplitude can then be estimated by substituting $\bar{H}_1(j\omega_\mu)$ in the model. This results in the complex value $Y_c(j\omega_\mu) = 0.6 - j1.85$.

In the fourth step, the open-loop pseudo-receptance is updated using $Y_c(j\omega_\mu)$. Here, the open-loop pseudo-receptance is expressed in terms of the displacement amplitude as follows. Consider that $\Lambda_1^{-1}(j\omega, Y_c) = \bar{\Lambda}_1^{-1}(j\omega, Y_c) - \mathbf{G}\begin{bmatrix} Y_c(j\omega) & j\omega Y_c(j\omega) \end{bmatrix}^T$. Applying the Sherman-Morrison formula to this expression and correcting for the differences in $j\omega_\mu$ and μ_j results in the following formula,

$$\Lambda_1(\mu_j, Y_c) \approx \frac{Y_c(j\omega_\mu)}{F(j\omega_\mu)(j\omega_\mu h_k + g_k)(Y_c(j\omega_\mu))} - H_1(j\omega_\mu) + H_1(\mu_j) \tag{3.43}$$

Using this equation results in $\Lambda_1(\mu_j, Y_c) = -8.60 \times 10^{-3} + j4.93 \times 10^{-4}$. The updated open-loop pseudo-receptance is then applied to Eq. 3.10 to obtain a new set of feedback gains, and the procedure is repeated until convergence occurs. The convergence of the displacement feedback gain and the closed-loop displacement amplitude is relatively quick, as shown in Figure 3.7, in comparison to the convergence shown in Figure 3.4.

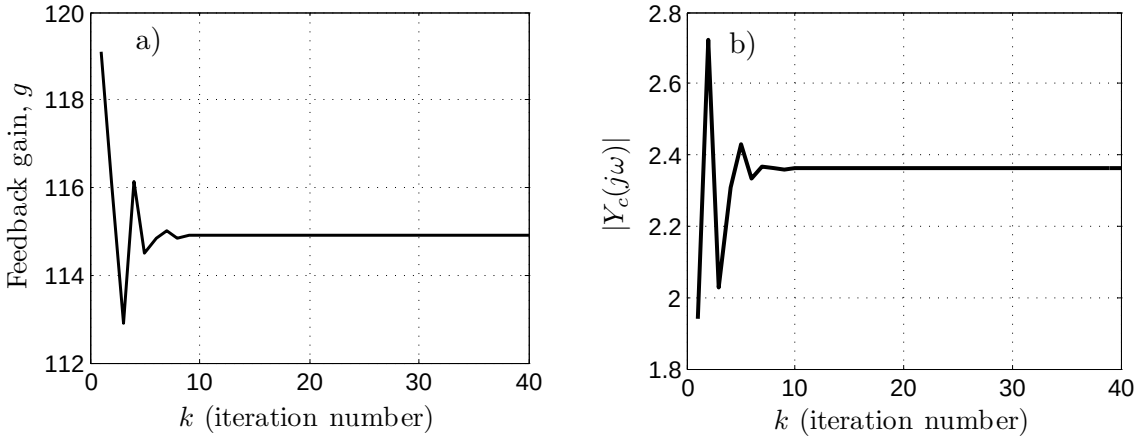

Figure 3.7: Convergence of a) the displacement feedback gain and b) the closed-loop displacement amplitude using the Volterra series representation.

Here, the final converged feedback gains are $\mathbf{G} = \begin{bmatrix} 114.90 & 0.58 \end{bmatrix}$, which results in the following pole assignment,

$$\mu_{1,2} = -0.3412 \pm j12.8716 \tag{3.44}$$

Comparing the assigned closed-loop poles to the pre-determined values shown in Eq. 3.40 indicates an error of approximately 2.5 % and 1 % for the real and imaginary parts respectively, which appears to be reasonable. A comparison of the open-loop pseudo-receptance $\Lambda_1(j\omega, Y_o)$, the closed-loop pseudo-receptance $\bar{\Lambda}_1(j\omega, Y_c)$ (obtained at the excitation level $F(j\omega) = 20$ N), and the underlying linear closed-loop receptance $\bar{H}_1(j\omega)$ is shown in Figure 3.8. This shows that the amplitude of the peak resonance is greatly reduced by the feedback control, whereas the peak resonance frequency is greatly increased, as specified. Furthermore, it is apparent that nonlinear distortion is present in $\bar{\Lambda}_1(j\omega, Y_c)$ relative to $\bar{H}_1(j\omega)$, thereby demonstrating that a Volterra series representation is capable of accounting for weak nonlinearities in the closed-loop pseudo-receptance.

3.2.3 Comparison and discussion

Although the extended harmonic balance method yields a more accurate assignment, this occurs as a result of an idealised case, whereas the discrepancies in the Volterra method are caused by approximations and errors that are more commonly found in practical situations. Some examples of factors that reduce the accuracy of the assignment include,

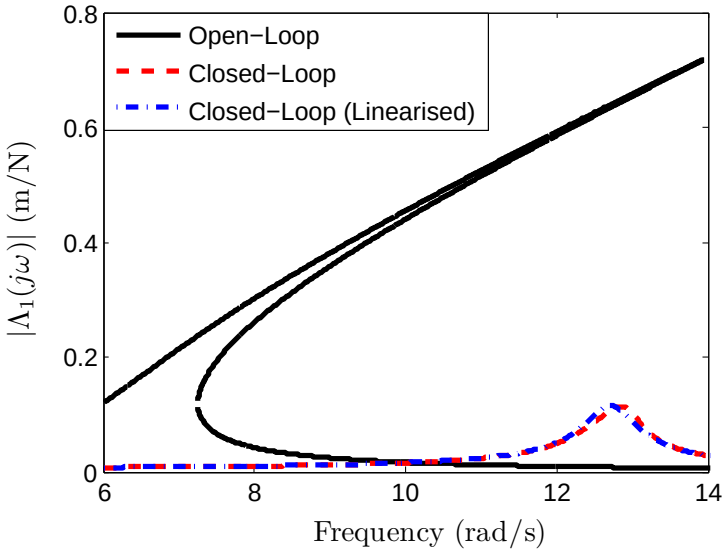

Figure 3.8: Illustration of the open-loop pseudo-receptance, the closed-loop pseudo-receptance (dashed line), and the underlying linear closed-loop receptance $\bar{H}_1(j\omega)$ (dash-dot line).

1. The finite resolution of the frequency vector used to measure the open-loop pseudo-receptances.
2. Weak, but non-negligible nonlinearities present in the measured pseudo-receptance $H_1(j\omega)$.
3. Approximations in the rational fraction polynomial model used to represent the underlying linear receptance.
4. Errors in identifying the form and relative strength of the nonlinearity.
5. Approximations in using a Volterra series representation to model the nonlinearity and to estimate the closed-loop displacement amplitude.

The majority of these approximations and errors appear to occur when either the closed-loop poles are assigned close to the open-loop poles, where the open-loop pseudo-receptance is strongly nonlinear in the Laplace domain, or when the closed-loop pseudo-receptance exhibits strong nonlinearities. In this case, the primary cause of the discrepancies between the assigned closed-loop poles and the pre-defined values is the use of a Volterra series representation to model the nonlinearity. Since the Volterra model is reasonably accurate, as illustrated in Figure 3.6, the discrepancies are almost negligible, which demonstrates

that the Volterra method is robust to small errors in the model. However, the presence of larger errors in the approximation, in conjunction with the other factors, may either result in an inaccurate assignment or convergence failure. The convergence properties of the iterative method have not yet been examined in great detail, and is a potential topic for future work.

If the pole assignment is not sufficiently accurate, it may be desirable to increase the damping and natural frequency of the closed-loop pseudo-receptance, such that the closed-loop poles are moved further away from the open-loop poles. This reduces the relative strength of the nonlinearity, and therefore linear eigenvalue assignment techniques are sufficient if the closed-loop poles are particularly far from the open-loop poles. However, the feedback gains required to assign the closed-loop poles increases with the distance from the open-loop poles, such that a suitable compromise between control effort and accurate pole assignment is sought. Therefore, the iterative Sherman-Morrison receptance method offers advantages over the non-iterative Sherman-Morrison receptance method by accounting for structural nonlinearities and reducing the control effort required for accurate assignment.

3.3 Bifurcation control of a Duffing oscillator

In the previous chapter, the Duffing oscillator is shown to exhibit frequency-domain bifurcation, where three possible displacement amplitude solutions exist in the cubic equation given by the harmonic balance method [111]. This results in dynamic behaviour that is generally undesirable, including the jump phenomenon, sub-harmonics and chaos [93,112]. Whilst chaotic behaviour may be advantageous in certain applications [113], the unpredictable behaviour is detrimental to many mechanical systems [105] and may result in instabilities.

Active feedback control offers a means of circumventing these effects by modifying the dynamic behaviour such that bifurcation region is minimised in the closed-loop pseudo-receptance [106]. This may be achieved using the nonlinear pole assignment techniques discussed in the previous section by allocating the closed-loop poles at specific locations that exhibit bifurcation minimisation properties. For example, moving the poles further to the left-hand side of the complex plane to increase damping has the effect of reducing the magnitude of the peak resonance, and thereby reducing the bifurcation region in

the closed-loop pseudo-receptance. Additional constraints may be applied to the pole placement procedure in order to minimise the control effort, such as assigning closed-loop poles within an elliptical region in the complex domain. Moreover, a maximum forcing amplitude may be specified to ensure that bifurcation does not occur in the frequency-domain beneath this threshold. Numerical examples of these pole assignment techniques are demonstrated using an exemplary Duffing oscillator.

3.3.1 Bifurcation region

The cubic equation associated with the Duffing oscillator is of the form,

$$AY^6(j\omega) + BY^4(j\omega) + CY^2(j\omega) + D = 0 \tag{3.45}$$

where A, B, C, D represent the coefficients of Eq. 2.14. Treating negative or complex solutions of Y as unphysical, the number of real solutions to Eq. 3.45 is dependent on the discriminant Δ, which is given by,

$$\Delta = 18ABCD - 4B^3D + B^2C^2 - 4AC^3 - 27A^2D^2 \tag{3.46}$$

If $\Delta < 0$, then Eq. 3.45 has one real and two complex solutions, and therefore, the Duffing oscillator will have a unique response amplitude for the specified excitation amplitude and frequency. However, if $\Delta > 0$, then Eq. 3.45 has three real solutions, which results in the bifurcation phenomenon. The transition between these two states occurs at $\Delta = 0$, where Eq. 3.45 exhibits a double real root. The excitation frequencies that satisfy this condition are denoted by the transition frequencies ω_{min} and ω_{max}, which indicate where bifurcation starts to occur. These transition frequencies determine the bifurcation region $\Delta\omega$, which is defined as the frequency range of the bifurcation phenomenon.

By setting Eq. 3.46 to zero, the following characteristic equation appears from the coefficients of Eq. 3.45,

$$\alpha\omega^{10} + \beta\omega^8 + \gamma\omega^6 + \delta\omega^4 + \epsilon\omega^2 + \kappa = 0 \tag{3.47}$$

where the coefficients are given by Eq. 3.48. Eq. 3.47 is a quintic equation in ω^2, and therefore, ω_{min} and ω_{max} must be determined numerically by applying the system parameters to the equation. Once Eq. 3.47 is solved, the bifurcation length $\Delta\omega$ is obtained from $\omega_{max} - \omega_{min}$.

$$\alpha = -\left(\frac{3k_3m^2c}{4}\right), \beta = \frac{(3k_3mc)^2\left(2k_1m - c^2\right)}{2},$$

$$\gamma = \frac{-9k_3^2}{16}\left(4c\left(c^5 + 6k_1m\right) - 3k_3F^2m^3 - 16k_1m\right),$$

$$\delta = \frac{-9k_3^2}{16}\left(9k_3F^2m\left(k_1m - 3c^2\right) + 8c^4k_1^2 - 16c^2k_1^3m\right), \tag{3.48}$$

$$\epsilon = \frac{9k_1k_3^2}{16}\left(9k_3F^2\left(k_1m - 3c^2\right) - 4c^2k_1^3\right),$$

$$\kappa = \frac{-9k_3^2}{256}\left(3k_3F^2\left(81k_3F^2m + 16k_1^3\right) - 4c^2k_1^3\right).$$

In the case of no damping, Eq. 3.47 reduces to,

$$\omega^6 - 3\omega_n^2\omega^4 + 3\omega_n^4\omega^2 - \omega_n^6 - \frac{k_3}{m^3}\left(\frac{9F^2}{4}\right)^2 = 0 \tag{3.49}$$

Eq. 3.49 is a cubic equation with one real solution and two complex solutions, which indicates that the transition frequency ω_{max} has disappeared due to the peak resonance extending to infinity in the frequency domain. Thus, ω_{min} is the solution to Eq. 3.49 and can be written as,

$$\omega_{min}^2 = \omega_n^2 + \left(\sqrt[3]{k_3\left(\frac{9F}{4}\right)^2}\right) \Big/ m \tag{3.50}$$

such that ω_{min} is approximately equivalent to the natural frequency ω_n and increases (decreases) with the excitation amplitude F for positive (negative) values of k_3.

Now, we investigate the effect of a linear state feedback controller on the bifurcation region of the Duffing oscillator. The system parameters are given as,

$$m = 1 \text{ kg}, c = 0.1 \text{ Ns/m}, k_1 = 20 \text{ N/m}, k_3 = 0.8 \text{ N/m}^3, F = 20 \text{ N}. \tag{3.51}$$

The velocity and displacement feedback gains are defined by h and g respectively, such that the stiffness and damping terms are modified to $k_1^* = k_1 + g$ and $c^* = c + h$. By applying these modified terms and the additional system parameters to the characteristic equation Eq. 3.47, the transition frequencies and bifurcation region of the closed-loop pseudo-receptance are found from the two real numerical solutions of this equation. An illustration of the effect of velocity feedback control on the bifurcation region is shown in

Figures 3.9a) and 3.9b), where Figure 3.9a) shows the discriminant Δ against ω and h and Figure 3.9b) shows the closed-loop pseudo-receptance for various velocity feedback control gains. Similar illustrations for displacement feedback control are shown in Figures 3.10a) and 3.10b).

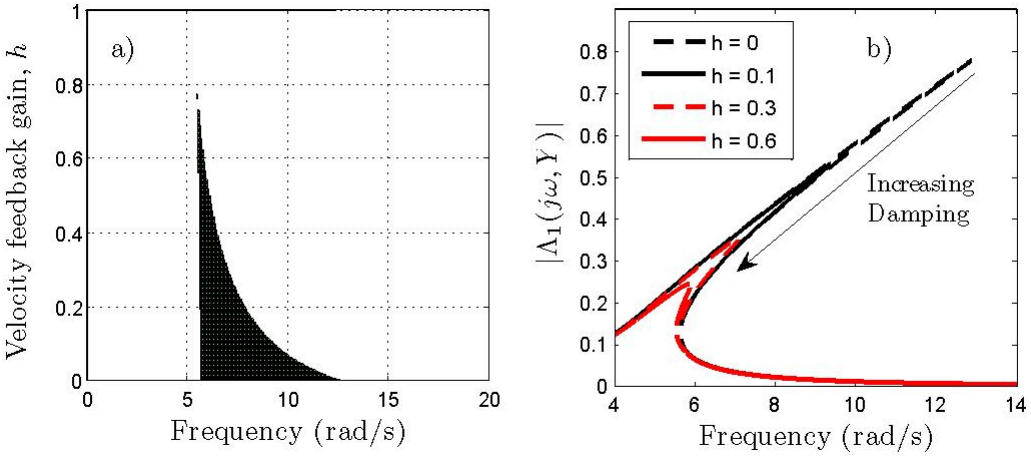

Figure 3.9: Effect of velocity feedback control on a) the discriminant, where dark regions indicate where $\Delta > 0$ and bifurcation occurs, and b) the closed-loop pseudo-receptance.

In Figure 3.9a), it can be seen that the upper transition frequency ω_{max} falls rapidly as the velocity feedback gain increases due to the greater damping, whereas the lower transition frequency ω_{min} is relatively independent of h, such that Eq. 3.50 provides a reasonable approximation of this value. Therefore, the bifurcation length reduces with an increasing velocity feedback gain until $h > 0.7$, where the bifurcation region is effectively reduced to zero and the displacement response is unique at all frequencies. Similarly, Figure 3.10a) shows that increasing the displacement feedback gain has the effect of increasing ω_{min} and ω_{max} due to the increase in the peak resonance frequency, and the bifurcation region gradually tends towards zero. However, a greater control effort is required to implement this in relation to velocity feedback control.

Having seen that positive values of h and g have the effect of reducing the bifurcation region, it is apparent that closed-loop poles may be assigned with sufficient control effort to minimise or eliminate bifurcation in the closed-loop pseudo-receptance. In order to achieve this, however, it is necessary to consider the conditions for bifurcation to occur in the pseudo-receptance, such that the pole assignment can be constrained for the purpose of preventing these conditions from being met.

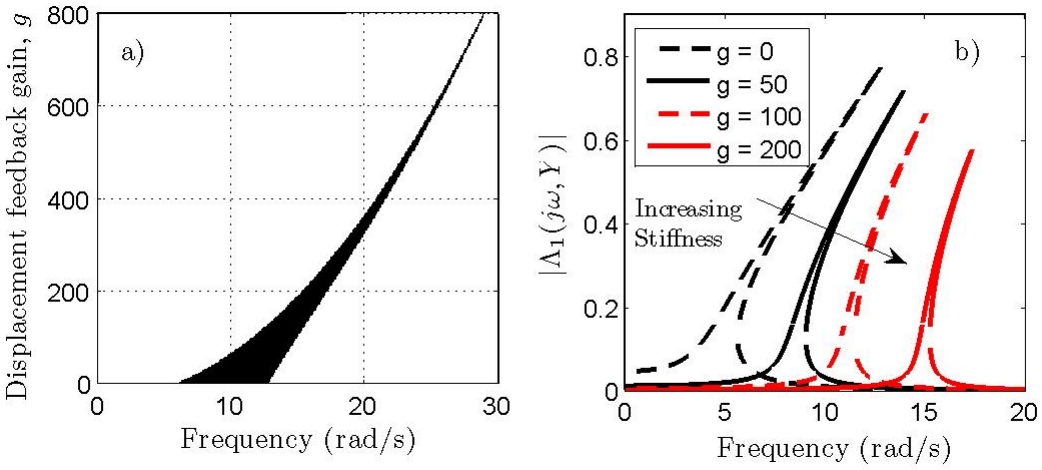

Figure 3.10: Effect of displacement feedback control on a) the discriminant, where dark regions indicate where $\Delta > 0$ and bifurcation occurs, and b) the closed-loop pseudo-receptance.

3.3.2 Threshold amplitude

One of the conditions for the presence of bifurcation in the pseudo-receptance is that the displacement amplitude $Y(j\omega)$ of the Duffing oscillator must exceed a specific threshold amplitude, denoted as Y_B. If $Y(j\omega) < Y_B \ \forall\omega$, then bifurcation will not occur in the pseudo-receptance. Y_B is obtained from the maximum displacement amplitude $Y_{max}(j\omega_j)$ of the closed-loop system when bifurcation is eliminated with the least possible control effort. This criterion can be met by minimising a cost function $J_1(h, g) = \|\Delta\omega + \boldsymbol{\beta}\mathbf{G}\|$, where $\boldsymbol{\beta} = \begin{bmatrix}\beta_1 & \beta_2\end{bmatrix}$ is a vector of weighting terms that influences the prominence of the control effort in relation to the bifurcation region. Generally, the weighting terms are set to zero when $\Delta\omega > 0$, such that the control effort and the bifurcation region can be minimised independently of each other.

The maximum displacement amplitude $Y_{max}(j\omega_j)$ is found from the peak resonance frequency ω_j, which is expressed by,

$$\omega_j = \sqrt{\frac{2k_1^* m - (c^*)^2}{2m^2} + \frac{0.75k_3 Y^2(\omega_j)}{m}} \tag{3.52}$$

Substituting ω_j into the cubic equation for the Duffing oscillator results in the following expression,

$$Y_{max}^4(j\omega_j) + \frac{4k_1^* m - (c^*)^2}{3k_3 m} Y_{max}^2(j\omega_j) - \frac{4mF^2}{3(c^*)^2 k_3} = 0 \tag{3.53}$$

for which the positive real solution is,

$$Y_{max}(j\omega_j) = \left(\frac{\left(c^*\right)^2 - 4k_1^* m + \sqrt{\left(\left(c^*\right)^2 - 4k_1^* m\right)^2 + 48k_3 F^2 m^3 / \left(c^*\right)^2}}{6k_3 m} \right)^{\frac{1}{2}} \tag{3.54}$$

provided that $k_3 > 0$. If $k_3 < 0$, $Y_{max}(j\omega_j)$ is found numerically from the largest solution of the cubic equation. The feedback gains obtained by minimising $J_1(h, g)$ results in a closed-loop pseudo-receptance that satisfies $Y_{max}(j\omega_j) \approx Y_B$.

Using MATLAB's fmincon command to minimise $J_1(h, g)$, the threshold amplitude Y_B is illustrated against the modified stiffness k_1^* and damping c^* terms in Figures 3.11a) and 3.11b) respectively. These figures highlight one of the more interesting features of Y_B; it is relatively independent of the linear parameters, and is therefore unaffected by the state feedback controller. Confirmation of this phenomenon is shown in Figure 3.12, which shows the relationship between $Y_{max}(j\omega_j)$ and $\Delta\omega$ as the linear system parameters vary, and Figure 3.13, which illustrates a series of closed-loop pseudo-receptances assigned at $Y_{max}(j\omega_j) = Y_B$. Thus, once Y_B is established for the Duffing oscillator in question, a set of closed-loop poles can be assigned with the constraint $Y_{max}(j\omega_j) < Y_B$ to ensure that bifurcation is eliminated in the closed-loop pseudo-receptance.

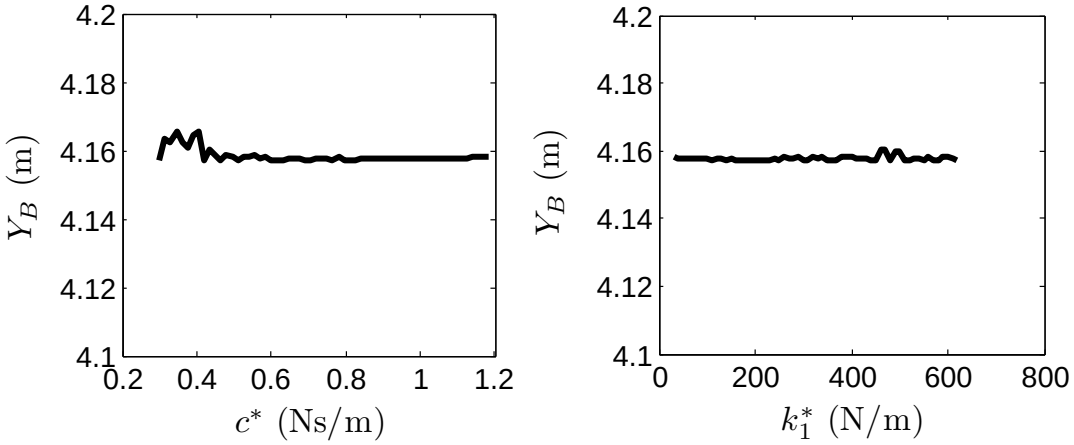

Figure 3.11: Variation of the bifurcation threshold with a) the modified damping and b) the modified linear stiffness terms.

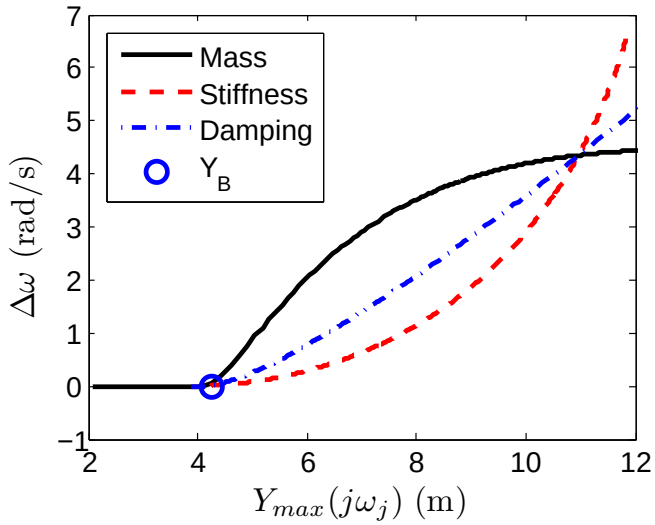

Figure 3.12: Variation of $\Delta\omega$ and $Y_{max}(j\omega_j)$ as the linear system parameters vary, converging on a single value as $\Delta\omega \to 0$.

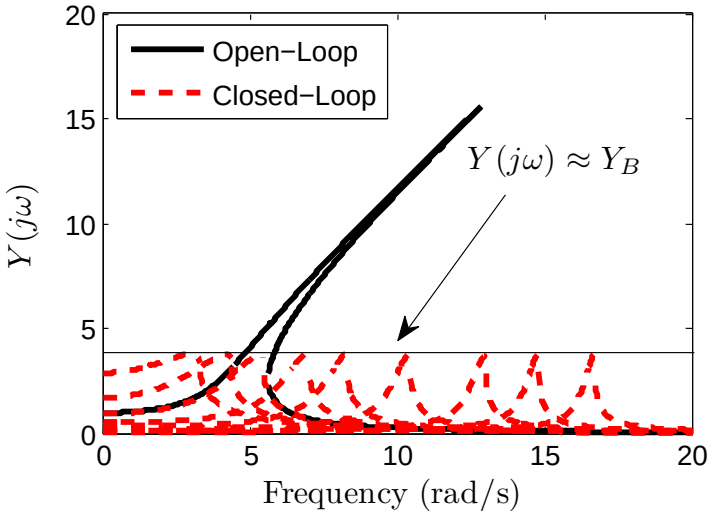

Figure 3.13: Illustration of the bifurcation threshold amplitude of various closed-loop pseudo-receptances, which is independent of the peak resonance frequency.

3.3.3 Amplitude assignment

In order to assign closed-loop poles with a particular maximum displacement amplitude, it is necessary to leave either the real or imaginary part of the pole undefined, as a closed-loop pole pair has a unique maximum displacement amplitude associated with it [1]. Several numerical examples are presented for the purpose of demonstrating this procedure.

[1] If the problem is extended to a multi-degree-of-freedom system, this over-constraintment is not an issue, as closed-loop poles may be assigned regardless of the closed-loop displacement amplitudes.

Hardening stiffness

First, a hardening Duffing oscillator with the parameters specified in Eq. 3.51 is considered. Since the excitation level is high, this system is strongly nonlinear and exhibits bifurcation, which can be observed in Figure 3.13. The open-loop poles of the Duffing oscillator are,

$$\lambda_{1,2} = -0.05 \pm j12.85 \tag{3.55}$$

The threshold amplitude Y_B is obtained using MATLAB's fmincon solver, with the constraints $h, g > 0$, to minimise the cost function $J_1(h, g)$, where the weighting terms are specified as $\boldsymbol{\beta} = \begin{bmatrix} 0.1 & 0.1 \end{bmatrix}$. This results in the feedback gains $\mathbf{G} = \begin{bmatrix} 0.67 & 0.88 \end{bmatrix}$, and the corresponding closed-loop displacement amplitude $Y(j\omega)$ is shown in Figure 3.14. Here, it is apparent that the closed-loop system is at the bifurcation threshold, such that $Y_{max}(j\omega_j) \approx Y_B$. Using Eq. 3.54, $Y_B \approx 3.78$ m is obtained.

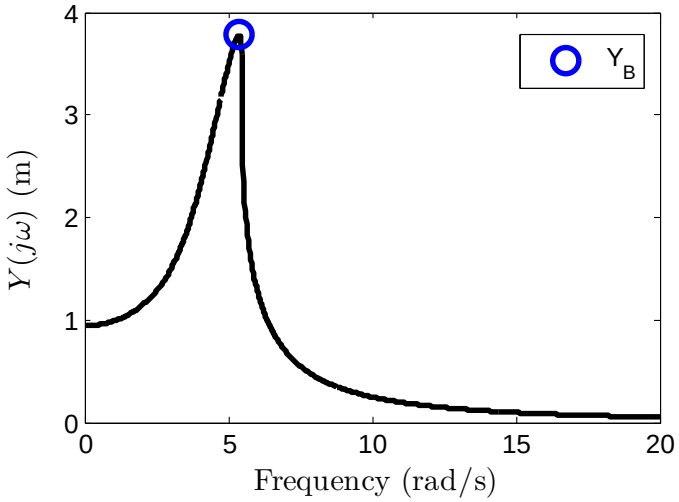

Figure 3.14: Illustration of closed-loop pseudo-receptance with the maximum displacement amplitude assigned at the bifurcation threshold amplitude.

It is illustrated in Figure 3.13 that the displacement response of the open-loop system at the peak resonance frequency is about 15 m, which is well above this bifurcation threshold amplitude. Therefore, we wish to assign the maximum closed-loop displacement amplitude as $Y(\omega_j) = 3$ m to ensure that Y_B is not exceeded, whilst assigning the closed-loop poles to,

$$\mu_{1,2} = \sigma \pm j9 \tag{3.56}$$

No assignment is considered for the real part of the poles, so that the problem is not over-constrained.

In this case, the imaginary part of the pole is assigned by minimising the cost function $J_2(h, g) = \|\omega_j - \Im m(\mu_{1,2})\|$, subject to the constraint of assigning $Y_{max} = 3$ m. Using the fmincon solver, the feedback control gains are obtained as $\mathbf{G} = \begin{bmatrix} 55.74 & 0.64 \end{bmatrix}$, and the closed-loop poles converge to $\mu_{1,2} = -0.37 \pm j9$, which confirms that the imaginary part of the closed-loop pole pair is correctly assigned. Moreover, applying Eq. 3.54 to the closed-loop system confirms that $Y_{max} = 3$ m, as defined. The closed-loop displacement amplitude is shown in Figure 3.15 alongside the open-loop displacement amplitude, and illustrates that the bifurcation region is removed in the closed-loop system as a result of state feedback control.

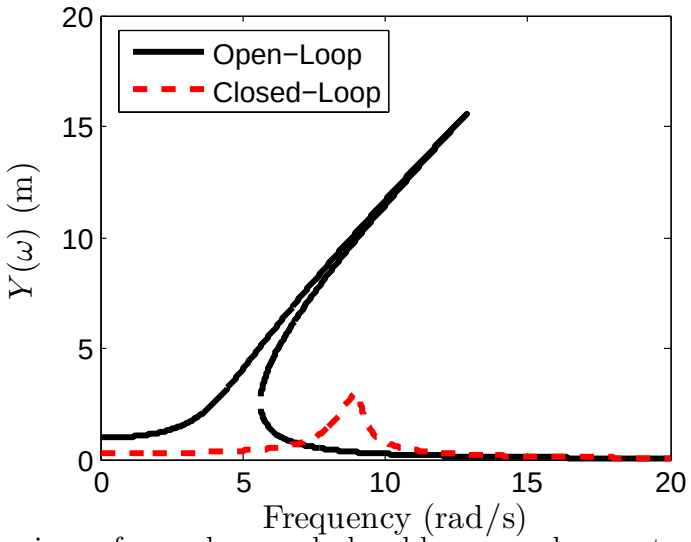

Figure 3.15: Comparison of open-loop and closed-loop pseudo-receptances, where the maximum displacement amplitude of the closed-loop receptance is below the bifurcation threshold amplitude.

Softening stiffness

Next, we consider a more interesting case, where $k_3 = -0.8$ N/m^3 is defined, such that the cubic stiffness term is negative and the Duffing oscillator exhibits softening behaviour [114]. If we apply the characteristic equation given by Eq. 3.47, it is apparent that the equation no longer yields two real solutions, and so $\Delta\omega$ cannot be obtained directly.

Fortunately, we can take advantage of the symmetric properties of the Duffing oscillator to obtain $\Delta\omega$ and Y_B by using the equivalent hardening Duffing oscillator ($k_1 = |k_1|, k_3 = |k_3|$). Then, similar techniques can be utilised to reassign the poles of the system whilst constraining $Y_{max}(j\omega_j)$.

One additional consideration in this case is that the system is inherently unstable due to the total spring force $k_1 y(t) + k_3 y^3(t)$ decreasing in magnitude as $|y(t)|$ increases, until the sign is reversed. The point of instability can be approximately defined as the unstable equilibria $y_e = \pm\sqrt{-k_1^*/k_3}$ of the Duffing oscillator [38], and therefore, by increasing k_1^* using displacement feedback, the closed-loop stability margin becomes greater than the open-loop stability margin.

In this case, the open-loop poles are found to be real and non-symmetric,

$$\lambda_{1,2} = -1.84, 1.74, \tag{3.57}$$

where the positive real eigenvalue indicates that the system becomes unstable when the higher steady-state solution branch is reached within the bifurcation region. Using the equivalent hardening Duffing oscillator illustrated in the previous case, we know that $Y_B \approx 3.78$ m, and so bifurcation can be avoided by assigning $Y_{max}(j\omega_j) < 3.78$ m. As with the previous case, we wish to assign the closed-loop poles $\mu_{1,2} = \sigma \pm j9$ and the maximum closed-loop displacement amplitude $Y_{max}(j\omega_j) = 3.78$ m. Minimising $J_3(h, g)$ results in the feedback control gains $\mathbf{G} = \begin{bmatrix} 66.54 & 0.64 \end{bmatrix}$, with the corresponding closed-loop poles $\mu_{1,2} = -0.37 \pm j9$. Here, we can see that the velocity feedback gain h is unchanged from the previous example, whereas the displacement feedback gain g is increased. This is due to the displacement amplitude reducing the peak resonance frequency, which requires a larger value for g to compensate for this. A comparison of the open-loop and closed-loop displacement responses shown in Figure 3.16 indicates that $Y_{max}(j\omega_j)$ is correctly assigned at 3 m.

It should be noted that the feedback control does not guarantee closed-loop stability; if the initial conditions are relatively large, the system response will tend to the higher-order solution branches observed in Figure 3.16, resulting in instability. These solutions cannot be completely removed using linear state feedback control, since this requires a higher-order stiffness term to overcome the negative cubic stiffness. However, unlike the open-loop system, the closed-loop system has negative real pole components, which indicates that the system is no longer inherently unstable. Furthermore, the unstable

equilibria y_e increase in value as a result of the displacement feedback control, which results in a greater stability margin.

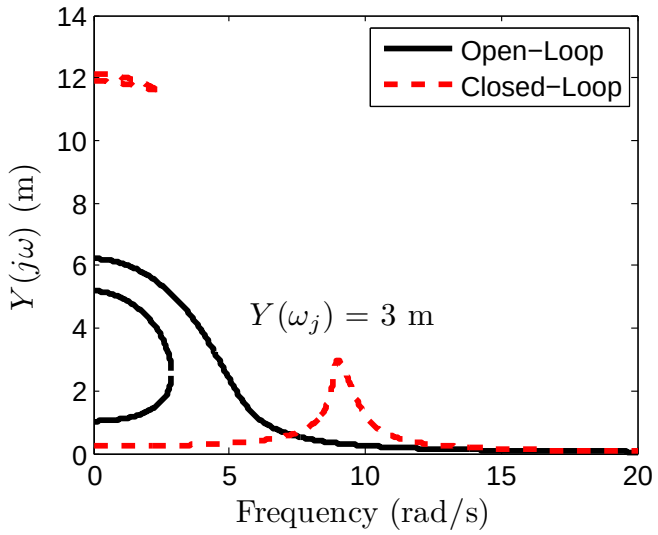

Figure 3.16: Comparison of the open-loop and closed-loop pseudo-receptances for a softening Duffing oscillator. The open-loop system is intrinsically unstable, whereas the closed-loop system requires large initial conditions to become unstable.

Bi-stable stiffness

The final amplitude assignment case under consideration in this section features a Duffing oscillator with positive cubic stiffness and negative linear stiffness, known as the bi-stable or double-well Duffing oscillator [115]. The new stiffness parameters are defined as $k_1 = -20$ N/m and $k_3 = 0.8$ N/m^3. This change in parameters has the effect of reversing the stable and unstable equilibrium points, such that $y_e = 0$ is now an unstable equilibrium position and $y_e = \pm\sqrt{-k_1^*/k_3}$ are stable equilbria that are determined by the initial conditions. The bi-stable Duffing oscillator can be used to model the dynamics of stable systems with snap-through oscillations, such as curved beams, or a cantilever beam interacting with two magnets [38].

In order to prevent snap-through oscillations from occurring, the poles of the system are reassigned such that the linear stiffness is positive and the equilibrium point $y_e = 0$ is stable. The open-loop poles are found to be,

$$\lambda_{1,2} = -0.05 \pm j12.05 \tag{3.58}$$

which indicates that the system is stable, due to the positive cubic stiffness. Using $Y_B = 3.78$ m from the equivalent hardening Duffing oscillator, the closed-loop poles are again assigned as $\mu_{1,2} = \sigma \pm j9$ whilst constraining $Y_{max}(j\omega_j) = 3$ m. Minimising $J_2(h, g)$ results in the feedback control gains $\mathbf{G} = \begin{bmatrix} 95.74 & 0.64 \end{bmatrix}$, where g is increased by a factor of $2|k_1|$ relative to the first case, since the negative linear stiffness must be overcome. The assigned closed-loop poles are $\mu_{1,2} = -0.37 \pm j9$, and Eq. 3.54 yields the correct assigned value of $Y_{max}(j\omega_j) = 3$ m. This is verified in Figure 3.17, which shows a comparison of the open-loop and closed-loop displacement responses.

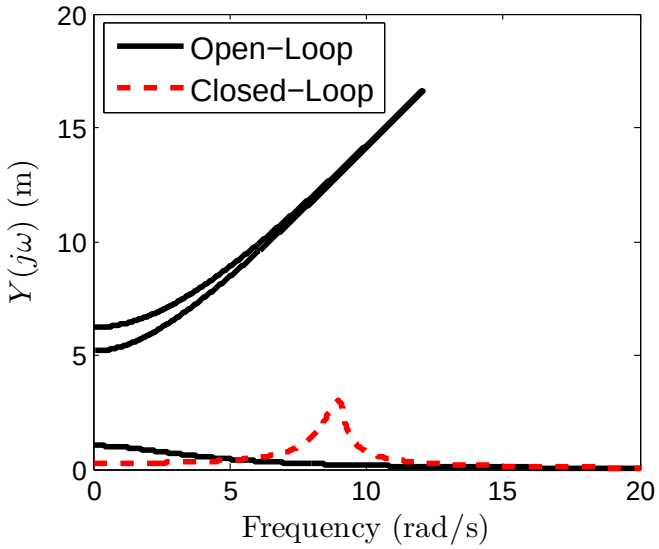

Figure 3.17: Comparison of open-loop and closed-loop pseudo-receptances for a bi-stable Duffing oscillator. The open-loop peak resonance is significantly curved due to the negative linear stiffness and the positive cubic stiffness, whereas the closed-loop system behaves as a hardening Duffing oscillator.

To confirm that the unforced closed-loop system tends to the equilibrium point $y_e = 0$, a Simulink model of the bi-stable Duffing oscillator is constructed, and a time-domain simulation of the system response from the initial condition $y_0 = -10$ m is conducted using the ode45 solver. First, the uncontrolled system response is simulated over a period of fifty seconds. Next, the controller is switched on after a period of twenty seconds has elapsed, and the resulting system response is simulated and compared to the uncontrolled response in Figure 3.18. Here, it is apparent that the uncontrolled response tends to the equilibrium point $y_e = -\sqrt{-k_1/k_3} = -5$ m whilst exhibiting snap-through oscillations, whereas y_e

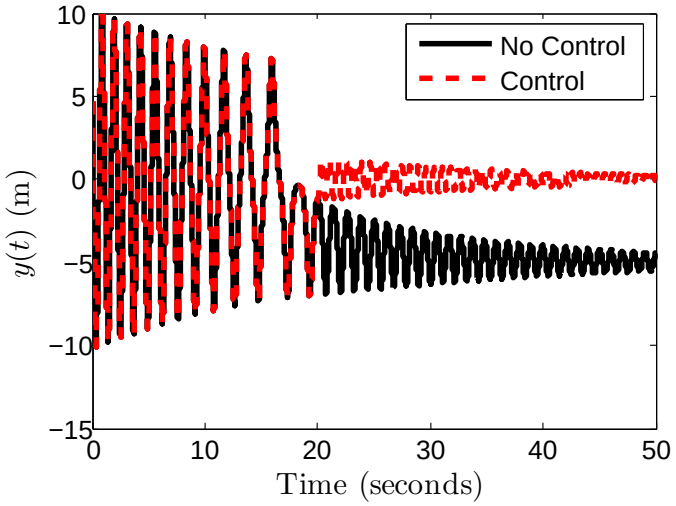

Figure 3.18: Illustration of the time-responses of the bi-stable Duffing oscillator, with control (switched on at $t = 20$ seconds) and without control.

shifts rapidly towards zero once the controller is switched on. Since the modified linear stiffness is now positive, the closed-loop system behaves as a hardening Duffing oscillator, and therefore, the snap-through oscillations are prevented from occurring.

3.3.4 Elliptical eigenvalue assignment

As an alternative means of minimising or removing the bifurcation region in the closed-loop pseudo-receptance, we consider assigning an initial set of pre-determined closed-loop poles that is further optimised with respect to the bifurcation region and the control effort. Here, an elliptical region is defined around the closed-loop poles in the complex plane, and is explored for additional desirable pole locations. This is because the initial choice for the pole location may be non-optimal, such as a non-minimum value for $\Delta\omega$, or a particularly large control effort that is required for accurate assignment. The optimisation is achieved by placing a new set of closed-loop poles at a location within the elliptical region where $\Delta\omega$ is minimised in the closed-loop pseudo-receptance. For this purpose, the elliptical region is defined with the initial closed-loop poles as the central point, with semi-axes denoted as a and b that correspond to the real and imaginary tolerances of the closed-loop pole respectively. Thus, the optimised closed-loop poles are constrained using an

elliptical equation of the form,

$$\frac{(x_\mu - \Re e(\mu_{1,2}))^2}{a^2} + \frac{(y_\mu - \Im m(\mu_{1,2}))^2}{b^2} \leq 1 \tag{3.59}$$

where x_μ and y_μ correspond to the real and imaginary parts of the optimised closed-loop poles. Once the closed-loop pole pair is optimised for minimising the bifurcation region and the control effort, the feedback gains required to implement the poles are obtained.

Numerical example 1

As an initial example, the Duffing oscillator with the system parameters given in Eq. 3.51 is used, and the initial set of closed-loop poles to be assigned is,

$$\mu_{1,2} = -0.3 \pm j7.5 \tag{3.60}$$

Using the iterative Sherman-Morrison receptance method [34], the feedback gains required to assign the closed-loop poles are obtained as $\mathbf{G} = \begin{bmatrix} 24.5 & 0.5 \end{bmatrix}$. Applying the characteristic equation specified by Eq. 3.47 reveals that $\Delta\omega = 0.13$ rad/s in the closed-loop pseudo-receptance, and so the closed-loop poles represent a non-minimum solution for reducing the bifurcation region. Therefore, the closed-loop poles need to be reassigned in order to obtain an optimal solution that is close to the original closed-loop pole location set. An elliptical region around the closed-loop poles $(\Re e(\mu_{1,2})), (\Im m(\mu_{1,2})) = (-0.3, \pm 7.5)$ is defined with relatively small tolerance values $a = 0.02$ and $b = 0.5$, such that the optimised closed-loop poles are close to the initial closed-loop pole location set. The closed-loop poles are then optimised by minimising $J_1(h, g)$ whilst applying the elliptical constraint specified by Eq. 3.59. This yields the feedback gains $\mathbf{G} = \begin{bmatrix} 32.63 & 0.53 \end{bmatrix}$, which results in the following closed-loop poles,

$$\mu_{1,2} = -0.32 \pm j7.89 \tag{3.61}$$

The location of the closed-loop poles are shown in the complex plane alongside the open-loop poles in Figure 3.19a), and the corresponding open-loop and closed-loop pseudo-receptances are shown in Figure 3.19b). These figures illustrate that the optimised closed-loop poles are assigned at the edge of the ellipse, where the corresponding damping and natural frequency is slightly higher than at the centre. However, the bifurcation minimisation is constrained by the tolerances associated with the elliptical region, such

that the bifurcation region $\Delta\omega = 0.11$ rad/s is a minimal, yet non-zero solution to the constrained problem. Therefore, bifurcation remains present in the closed-loop pseudo-receptance, despite the optimisation.

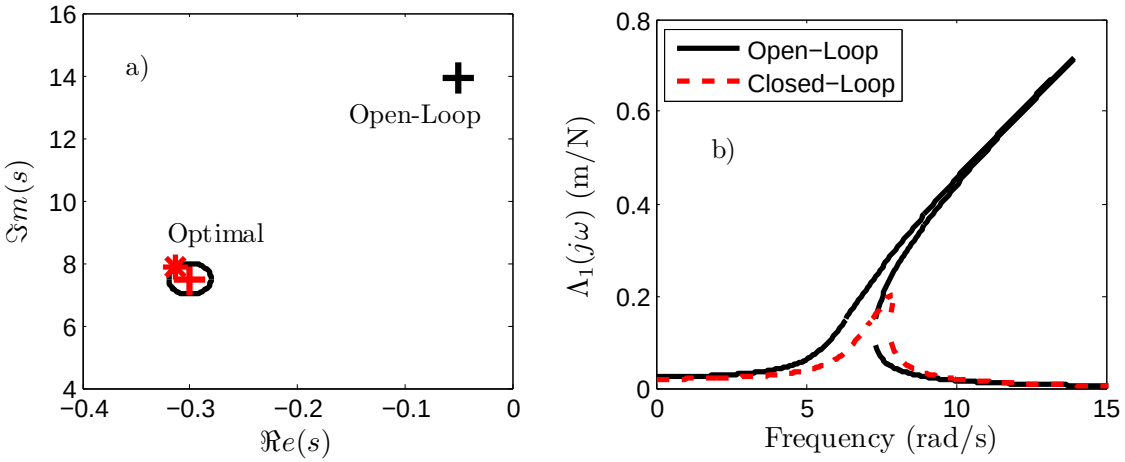

Figure 3.19: Pole assignment in an elliptical region: a) pole location in the complex plane for $a = 0.02$, $b = 0.5$ and b) open-loop and closed-loop receptances.

Numerical example 2

In order to completely remove the bifurcation region from the closed-loop pseudo-receptance, the elliptical region around the poles should be enlarged by increasing the tolerances a and b. In this example, a new set of tolerance values are assigned as $a = 0.2$ and $b = 1$. Implementing the bifurcation minimisation algorithm using the fmincon solver yields the feedback gains $\mathbf{G} = \begin{bmatrix} 18.90 & 0.68 \end{bmatrix}$, which results the following closed-loop poles,

$$\mu_{1,2} = -0.39 \pm j6.87 \tag{3.62}$$

Figure 3.20a) shows the location of the assigned closed-loop poles in the complex plane with regards to the open-loop poles and the elliptical region. Here, it is illustrated that the optimised closed-loop pole location is no longer of the edge of the elliptical region, which indicates that the problem is not overly constrained and bifurcation region can be removed from the closed-loop receptance. This is confirmed in Figure 3.20b), which shows that the maximum displacement amplitude is at the bifurcation threshold amplitude; therefore, minimal control effort is used to assign the optimal closed-loop poles.

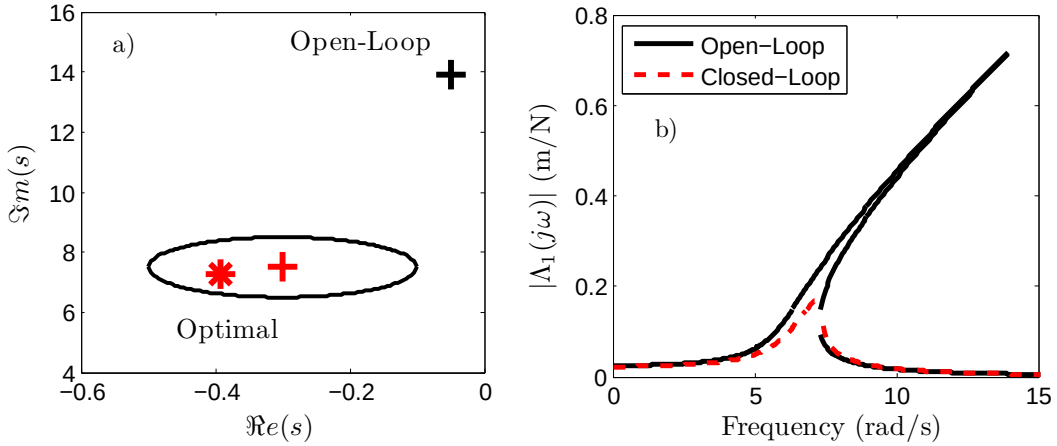

Figure 3.20: Pole assignment in an elliptical region: a) pole location in the complex plane for $a = 0.2$, $b = 1$ and b) open-loop and closed-loop receptances.

3.3.5 Force assignment

So far, we have assumed that the excitation amplitude F remains constant for the problem in question, whereas in practice, we often have little or no control over this parameter. Therefore, it is necessary to account for changes in the dynamic behaviour of the system as F varies. In this case, we assume that the exemplary hardening Duffing oscillator is subjected to a harmonic disturbance of the form $f(t) = F\sin(\omega t)$, where F and ω are unknown. Particular emphasis is placed upon F, which is allowed to vary with time, according to the excitation source. This complicates attempts to control the bifurcation region using pole placement, since the imaginary part of the closed-loop pole pair is affected by variations in F.

First, the discriminant of the cubic equation, as specified in Eq. 3.46, is plotted against the excitation amplitude and frequency in Figure 3.21. Here, it is apparent from the transition frequencies that increasing F also increases $\Delta\omega$ and ω_j, such that a higher excitation amplitude will result in a larger bifurcation region in the receptances. Therefore, it is useful to state a maximum amplitude F_{max} that the Duffing oscillator can be subjected to before bifurcation occurs in the closed-loop pseudo-receptance. This can be achieved by minimising the cost function $J_3(F) = \|\Delta\omega + \alpha_1 F^{-1}\|$, where α_1 is a weighting term. F^{-1} is used to prevent under-estimations in F_{max}, such that a small excitation amplitude will result in a large error. It is therefore necessary to ensure that $F > 0$ for convergence to occur in the cost function.

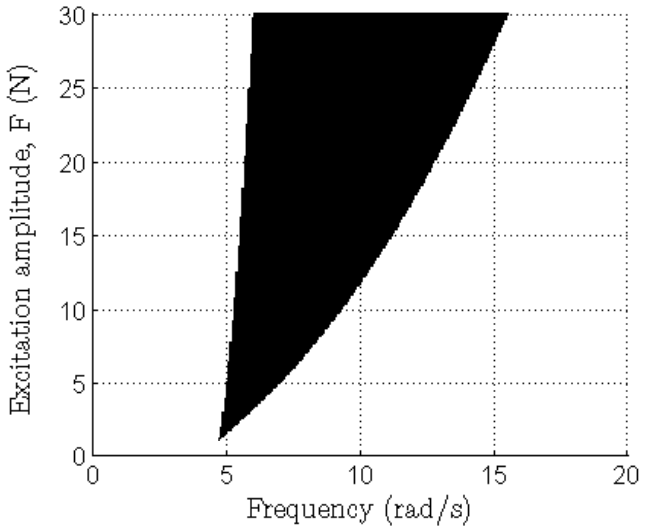

Figure 3.21: Open-loop discriminant Δ against excitation amplitude and frequency, where the bifurcation region increases with the excitation amplitude.

In a previous example, a set of closed-loop poles were assigned for the purpose of eliminating bifurcation from the system response, assuming a constant excitation amplitude $F = 20$ N. Keeping the control gains constant at $\mathbf{G} = \begin{bmatrix} 55.74 & 0.64 \end{bmatrix}$, the cost function $J_3(F)$ is minimised to obtain $F_{max} \approx 29.43$ N. At this excitation level, the closed-loop poles are $\mu_{1,2} = -0.37 \pm j9.3$, and the bifurcation threshold amplitude becomes $Y_B \approx 4.27$ m. This closed-loop pseudo-receptance is shown in Figure 3.22, where it can be seen that $Y_{max}(j\omega_j)$ is at the bifurcation threshold amplitude.

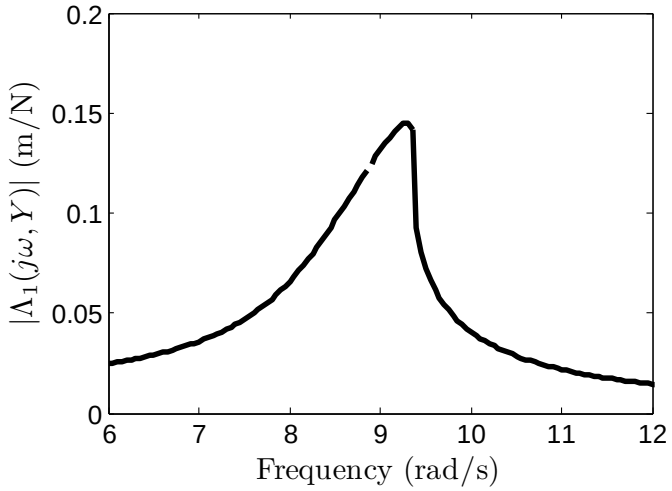

Figure 3.22: Closed-loop pseudo-receptance obtained using $F_{max} = 29.43$ N.

In order to achieve a greater degree of control, a pre-determined value $F_{max} = 100$ N is chosen, and a set of closed-loop poles that satisfy this condition is assigned. For this case, the bifurcation threshold amplitude $Y_B \approx 6.55$ m is established by minimising $J_1(h, g)$ using F_{max}. Next, a constraint that the maximum displacement amplitude $Y_{max}(\omega_j) = 6.5$ m is applied to the minimisation problem, such that bifurcation will not occur until the excitation amplitude $F = F_{max}$ is reached, provided that the effective system parameters remain constant. Since we wish to minimise the control effort when assigning the necessary closed-loop poles, the cost function $J_1(h, g)$ is utilised with $\Delta\omega$ set to zero and the weighting parameters $\boldsymbol{\beta} = \begin{bmatrix} 1 & 50 \end{bmatrix}$ to emphasise the minimisation of h. Minimising $J_1(h, g)$, subject to the amplitude constraint $Y_{max}(\omega_j) = 6.5$m, results in the new feedback gains $\mathbf{G} = \begin{bmatrix} 9.38 & 2.02 \end{bmatrix}$. The resulting closed-loop poles are,

$$\mu_{1,2} = -1.05 \pm j7.32 \tag{3.63}$$

and using Eq. 3.54 confirms that the maximum displacement amplitude $Y(\omega_j) \approx 6.5$ m is correct. To ensure that bifurcation does not occur until $F > 100$ N, the bifurcation region is obtained as a function of F using Eq. 3.47, and is shown in Figure 3.23a). Here, it is apparent that $\Delta\omega = 0$ when $F \leq F_{max}$, and so bifurcation is prevented from occurring until the excitation amplitude exceeds F_{max}.

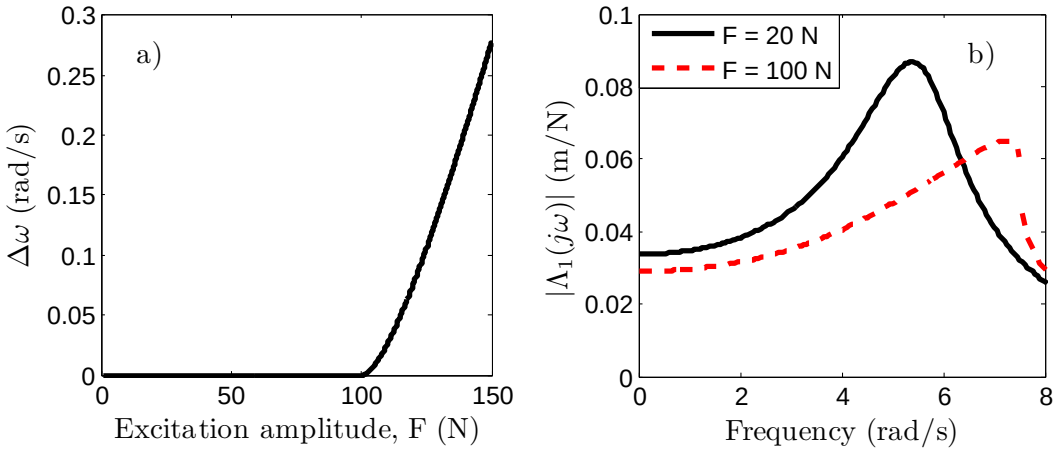

Figure 3.23: Assignment of maximum excitation amplitude: (a) the bifurcation length against excitation amplitude and (b) closed-loop pseudo-receptances for $F = 20$ N and $F = 100$ N.

Using the original excitation level $F = 20$ N, the closed-loop poles are found to be,

$$\mu_{1,2} = -1.05 \pm j5.48 \tag{3.64}$$

where the imaginary part of the pole set is decreased as a result of the lower excitation amplitude. A comparison of the closed-loop receptances for $F = 20$ N and $F = 100$ N is illustrated in Figure 3.23b).

3.4 Concluding remarks

This chapter demonstrates the use of pole placement techniques for a simple class of nonlinear systems using linear state feedback control. The linear Sherman-Morrison receptance method is extended to these nonlinear systems by utilising an interative procedure that accounts for the closed-loop nonlinear dynamics by updating the displacement amplitude response, the modified open-loop pseudo-receptance, and the feedback gains until convergence occurs. Two possible representations are considered for implementing the iterative scheme; the first representation utilises an extension of the classical harmonic balance approach for characterising the open-loop and closed-loop nonlinearities with describing functions, whereas the second representation relies on a Volterra series approximation.

A comparison of the two methods was conducted by applying the iterative procedure to reassign the poles of a single-degree-of-freedom Duffing oscillator for both cases. It was found that the extended harmonic balance approach is able to assign closed-loop poles with a high degree of accuracy, regardless of the strength of the nonlinearity, and indicates the validity of the concepts behind the iterative procedure. However, its weaknesses include a lack of generality and the requirement to know the structural parameters, including the form and relative strength of the nonlinearity and the linear mass, damping and stiffness terms. This restricts its use in practical situations. In contrast, the Volterra series approach makes use of nonlinear curve-fit approximations to measured pseudo-receptances, which does not require knowledge of the system parameters, and is therefore a natural extension of the Sherman-Morrison receptance method.

The primary weakness of the Volterra series method is that the representation fails to converge in regions where the nonlinearity is relatively strong, and so accurate assignment is only achieved when the system is weakly nonlinear. In addition, the Volterra series

method is slightly less accurate than the extended harmonic balance method, given the use of approximate representations in the iterative procedure instead of idealised parameters.

In the second section, a numerical study is presented for the purpose of demonstrating that the bifurcation region of a single-degree-of-freedom Duffing oscillator may be controlled using appropriate pole placement strategies. It was found that the system features a bifurcation threshold amplitude that is independent of the linear system parameters and the state feedback controller, and so is robust to modelling errors in practice. Thus, bifurcation control is achieved by assigning closed-loop poles that prevent this threshold from being exceeded using an amplitude constraint. Various other factors are considered, including the minimisation of the control effort and the maximisation of the forcing amplitude required for bifurcation to occur. These factors can be successfully implemented in the pole placement strategy by applying constraints to the assignment using cost functions.

One particular issue with these methods is the lack of generality to other nonlinear systems, since the equation that describes the bifurcation region must be re-derived for each case. However, the primary focus of these numerical studies is to place the pole assignment techniques discussed in the first section in a wider context by considering the amalgamation of pole placement strategies with the control of frequency-domain bifurcation. This enables the closed-loop poles to be assigned automatically by choosing specific desirable properties, such as a minimal control effort or bifurcation region.

There is plenty of scope for improving and refining these pole placement strategies in future work. One particular area of improvement is extending these methods to nonlinear systems with multiple-degrees-of-freedom. The Volterra series method may be extended in this manner by considering multi-input Volterra theory [116] or nonlinear output frequency response functions [117] as a means of modelling the measured pseudo-receptances. However, this may prove to be more difficult for the numerical approaches, and may require the assumption that the equations of motion can be fully decoupled. Further topics of interest include replacing the Volterra series representation with a NARMAX model [118] that retains the benefits of the Volterra series without convergence issues, and ensuring that the convergence of the feedback gains is sufficiently robust to modelling errors.

Chapter 4

Dynamic Analysis of Nonlinear Inertial Actuators

4.1 Introduction

The introductory chapter covers the role of inertial actuators in active vibration control as force-voltage transducers that generate the counteracting control forces from the control signals through the inertia of a moving proof-mass. The dynamics of these actuators is typically characterised using force-voltage transfer functions, which determine the magnitude and phase of the control force relative to an input voltage.

Previous studies [19] have shown that the force-voltage transfer function of an inertial actuator can be approximately described using a linear single-degree-of-freedom model for small control inputs. The natural frequency ω_p and damping ratio ζ_p of the actuator is determined by the mass, damping, and stiffness properties of the proof-mass and the suspension mounting. Above this natural frequency, the actuator approximates an *ideal force generator*, where the control force is proportional and in phase with the control signal. In this case, the coupling between the actuator and the structure can be neglected. As a result, it is often stated that the damping (stiffness) of the structural modes can be increased using velocity (displacement) feedback control if the first structural resonance is well above the natural frequency of the actuator.

However, it is also important to consider that the effective control force is limited by actuator saturation when the control input is large, resulting in strongly nonlinear dynamics. This phenomenon is determined by the stroke of the proof-mass, which is

limited either mechanically (stroke saturation) or electronically (hard clipping) to prevent damage occurring from over-excursions. Numerical and experimental studies conducted by Baumann and Elliott [22] demonstrate that actuator saturation is detrimental to the closed-loop stability margin, due to the destabilising control inputs to the actuator. In general, applying active vibration control to large-scale structures requires the generation of large control forces; as a consequence, the operating region of the actuators may lie close to the saturation limit, and so it is necessary to account for the nonlinear actuator dynamics, particularly with regards to closed-loop stability.

The purpose of this chapter is to investigate the dynamics of three types of inertial actuators, which all feature a moving proof-mass, but vary in terms of weight, functionality, intended operation design, and saturation characteristics,

1. Micromega IA-01 inertial actuator. This type of actuator is small and lightweight, featuring an internal proof-mass (32 g) and a maximum force output of 1.6 N. Advantages include: low suspension stiffness (180 N/m), low natural frequency (12 Hz), easily attached to a supporting structure. Drawbacks include: susceptibility to gravitational loading due to low suspension stiffness, designed for use in a horizontal configuration only, small force output.
2. DataPhysics IV40 inertial actuator. This type of actuator is relatively large and heavy (1.21 kg), and is attached to a supporting structure via its central spigot, using the body itself as the moving proof-mass. Since there are no end stops, saturation is provided by the hard clipping of the matched amplifier. Advantages include: large maximum force output (30 N), relatively low natural frequency (35 Hz), can be attached to supporting structure at any angle, no end stops. Drawbacks include: heavy casing, cannot mount to small, lightweight structures, susceptibiliy to stiction nonlinearity if mounted incorrectly.
3. Labworks FG-142 inertial actuator. This actuator is medium-sized and relatively lightweight, featuring an internal proof-mass (120 g) and a maximum force output of 17 N. Advantages include: easy to mount, relatively low natural frequency (45 Hz), can be used in a horizontal or vertical configuration. Drawbacks include: susceptibility to rattling nonlinearities if mounted incorrectly.

First, the force transmitted from the actuator to the structure is theoretically derived, and it is shown that the blocked force can be utilised if the supporting structure is sufficiently rigid. Next, the blocked force of each actuator is measured experimentally using sinusoidal excitation over a large range of excitation amplitudes and frequencies, and the resulting force-time signals are analysed in the time- and frequency-domains. Additionally, the blocked force-voltage transfer functions are ascertained for each excitation amplitude, in order to examine the linear and nonlinear dynamics of the actuators. Finally, a comparison of the dynamics of each actuator is given in section 4.5.

4.2 Theoretical background

4.2.1 Force-voltage dynamics of an inertial actuator

The force-voltage transfer function of an inertial actuator is derived in part from reference [19], which is extended to account for the actuator nonlinearities. First, the equation of motion for the mechanical part is given by,

$$m_p\ddot{y}_p(t) + c_{p,m}\dot{y}_p(t) + k_p y_p(t) + f_{NL}(y_p(t), \dot{y}_p(t)) = f_e(t) \tag{4.1}$$

where $m_p, c_{p,m}, k_p$ represent the proof-mass and suspension properties respectively;

$y_p(t), \dot{y}_p(t), \ddot{y}_p(t)$ represent the proof-mass displacement, velocity, and acceleration;

$f_{NL}(y_p(t), \dot{y}_p(t))$ is an unknown term that represents the actuator nonlinearities;

$f_e(t)$ is the internal electromotive force generated by the input voltage.

The electromotive force is proportional to the current in the actuator coil, denoted by $i(t)$. Using Lorentz's law,

$$f_e(t) = T_e i(t) \tag{4.2}$$

where T_e is a transduction coefficient that is determined by the product of the magnetic flux density and the coil length. The relationship between the current in the coil and the input voltage, denoted by $v_e(t)$, is governed by,

$$Li'(t) + Ri(t) = v_e(t) - T_e\dot{y}_p(t) \tag{4.3}$$

where L, R is the inductance and resistance of the coil respectively, $i'(t)$ is the current flow rate with respect to time, and $T_e\dot{y}_p(t)$ is the counter-electromotive force induced by the motion of the proof-mass. Taking the Laplace transform of Eq. 4.3 and rearranging

yields,

$$I(s) = G_e(s)V_e(s) - sT_eY_p(s) \tag{4.4}$$

where $G_e(s)$ is the electrical compliance of the coil,

$$G_e(s) = \frac{1}{sL + R} \tag{4.5}$$

Substituting Eq. 4.5 into Eqs. 4.2 and 4.1 after taking the Laplace transform of both equations and rearranging yields the relationship between the proof-mass displacement and the input voltage,

$$\Big(m_p s^2 + \big(c_{p,m} + T_e G_e(s) T_e\big)s + k_p + N\big(s, Y_p\big)\Big)Y_p(s) = T_e G_e(s) V_e(s) \tag{4.6}$$

where $N\big(s, Y_p\big)$ is the describing function of the actuator nonlinearities. Moreover, Eq. 4.6 indicates that the counter-electromotive force acts as additional damping, and so the effective damping term, denoted as c_p, is determined from both these terms,

$$c_p = c_{p,m} + T_e G_e(s) T_e \tag{4.7}$$

The reaction force of the actuator is equal to the inertia of the proof-mass, such that,

$$f(t) = -m_p \ddot{y}_p(t), \qquad F(s) = -m_p s^2 Y_p(s) \tag{4.8}$$

Therefore, by assuming that the inductance L is small enough to be neglected at low frequencies, $G_e(s)$ becomes a constant, and substituting Eq. 4.8 into Eq. 4.6 results in the force-voltage transfer function,

$$H_e(s, V) = \frac{F(s)}{V_e(s)} = \frac{-m_p T_e G_e s^2}{m_p s^2 + c_p s + k_p + N\big(s, Y_p\big)} \tag{4.9}$$

In practice, the input voltage cannot be measured directly, due to the effects of the counter-electromotive force. Instead, it is necessary to define the transfer function according to the voltage of the control signal, denoted by $v(t)$, which is the input voltage taken before the amplification stage. This approach is more practical, since it accounts for the amplifier dynamics and describes the actual relationship between the control signal and the control force. By assuming that the amplifier dynamics can be described as a pure gain in the frequency region of interest and substituting $s = j\omega$, the force-voltage transfer function becomes,

$$H(j\omega, V) = \frac{F(j\omega)}{V(j\omega)} = g_a \frac{-m_p\omega^2}{k_p - m_p\omega^2 + jc_p\omega + N\big(s, Y_p\big)} \tag{4.10}$$

where g_a is the so-called actuator gain that is determined by the product of the transduction coefficient, the coil impedance, and the amplifier gain. This term is positive, due to the transduction coefficient being negative.

If the actuator nonlinearities are sufficiently small, then $N\big(s, Y_p\big)$ can be neglected, and Eq. 4.10 tends to the linear force-voltage transfer function stated by Preumont,

$$H(j\omega) = g_a \frac{-\omega^2}{\omega_p - \omega^2 + j2\zeta_p\omega_p\omega} \tag{4.11}$$

where ω_p, ζ_p represent the natural frequency and damping ratio respectively. The Bode plots of the actuator, as shown in Figure 1.5, indicate that the force-voltage transfer function tends to the actuator gain g_a when $\omega \gg \omega_p$; this demonstrates that the actuator behaves as an ideal force generator above the natural frequency, with constant amplitude and zero phase.

4.2.2 Force transmission to supporting structure

When the inertial actuator is attached to a flexible supporting structure, the dynamics of the actuator become strongly coupled with the structure. To account for these effects, the proof-mass is coupled to a single-degree-of-freedom flexible structure via its suspension, and the corresponding structural mass is connected to an inertial reference via additional stiffness and damping parameters [22, 119]. Here, the single-degree-of-freedom model is used to represent the first resonance of the supporting structure. This results in a lumped-parameter two-degree-of-freedom model, as shown in Figure 4.1, which can be expressed in matrix form,

$$\mathbf{M}\ddot{\mathbf{y}}(t) + \mathbf{C}\dot{\mathbf{y}}(t) + \mathbf{K}\mathbf{y}(t) + \mathbf{f_{NL}}(\mathbf{y}(t), \dot{\mathbf{y}}(t)) = \mathbf{f_e}(t) \tag{4.12}$$

where **M, C, K** are the mass, damping, stiffness matrices respectively;

$\mathbf{f_{NL}}(\mathbf{y}(t), \dot{\mathbf{y}}(t))$ is a vector function that describes the actuator nonlinearities;

$\mathbf{y}(t), \dot{\mathbf{y}}(t)$ are the displacement and velocity vectors respectively, where $\mathbf{y}(t) = \begin{bmatrix} y_s(t) & y_p(t) \end{bmatrix}^T$;

$\mathbf{f_e}(t)$ is the electromotive forcing vector.

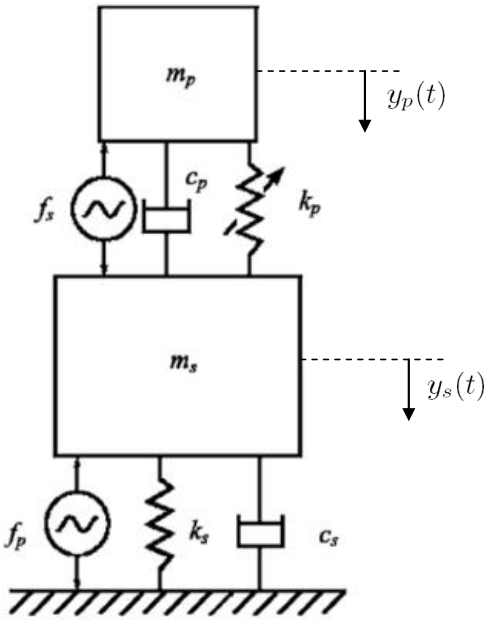

Figure 4.1: Two-degree-of-freedom lumped parameter system used to model the actuator-structure dynamics. Reproduced from [22].

The matrices and vectors in Eq. 4.12 are given as follows,

$$\mathbf{M} = \begin{bmatrix} m_s & 0 \\ 0 & m_p \end{bmatrix}, \mathbf{C} = \begin{bmatrix} c_s + c_p & -c_p \\ -c_p & c_p \end{bmatrix}, \mathbf{K} = \begin{bmatrix} k_s + k_p & -k_p \\ -k_p & k_p \end{bmatrix}$$
$$\mathbf{f_{NL}}(\mathbf{y}(t), \dot{\mathbf{y}}(t)) = \begin{bmatrix} -f_{NL}(\mathbf{y}(t), \dot{\mathbf{y}}(t)) \\ f_{NL}(\mathbf{y}(t), \dot{\mathbf{y}}(t)) \end{bmatrix}, \mathbf{f_e}(t) = \begin{bmatrix} g_a v(t) \\ -g_a v(t) \end{bmatrix} \tag{4.13}$$

where m_s, c_s, k_s are the mass, damping, and stiffness terms corresponding to the first resonance of the supporting structure. The sign of the electromotive forcing vector is dictated by the negative transduction coefficient T_e. In this case, the equation of motion for the proof-mass actuator is obtained from the lower matrix terms,

$$m_p \ddot{y}_p(t) + c_p\Big(\dot{y}_p(t) - \dot{y}_s(t)\Big) + k_p\Big(y_p(t) - y_s(t)\Big) + f_{NL}(\mathbf{y}(t), \dot{\mathbf{y}}(t)) = -g_a v(t) \tag{4.14}$$

where $y_s(t), \dot{y}_s(t)$ represent the displacement and velocity of the structural mass respectively. Using Eqs. 4.8 and 4.14, the force transmitted from the actuator to the supporting structure is given by,

$$f(t) = c_p\Big(\dot{y}_p(t) - \dot{y}_s(t)\Big) + k_p\Big(y_p(t) - y_s(t)\Big) + f_{NL}(\mathbf{y}(t), \dot{\mathbf{y}}(t)) + g_a v(t) \tag{4.15}$$

From Eq. 4.15, two special cases can be considered [29]. In the first case, the open-loop transmitted force is obtained by setting $v(t) = 0$, such that the proof-mass moves in response to base excitation from the structural mass. In the second case, the motion of the structure is neglected by setting $y_p(t), \dot{y}_p(t) = 0$, and the transmitted force is primarily determined by the actuator dynamics. Therefore, the transmitted force can be expressed as follows,

$$f(t) = H_{m0}(j\omega, V)v(t) - Z_{e0}(j\omega)\dot{y}_s(t) \tag{4.16}$$

where $H_{m0}(j\omega, V)$ is the blocked force-voltage transfer function of the actuator (i.e. the FRF of $f(t)$ and $v(t)$ when the structural mass is motionless), and $Z_{e0}(j\omega)$ is the open-circuit mechanical impedance of the actuator (i.e. the FRF of $f(t)$ and $\dot{y}_s(t)$ with no electromotive force). These terms may be obtained by applying the Fourier transform to Eq. 4.15 and rearranging the terms; here, $H_{m0}(j\omega, V)$ is found to be equivalent to the force-voltage FRF given by Eq. 4.11 (no attachment), whereas the mechanical impedance of the actuator, $Z_{e0}(j\omega)$, is,

$$Z_{e0}(j\omega) = j\omega m_p \frac{j\omega c_p + k_p + N\big(j\omega, Y_p\big)}{k_p - m_p\omega^2 + jc_p\omega + N\big(j\omega, Y_p\big)} \tag{4.17}$$

The relationship between the force transmitted to the structure and the structural velocity can be described using the mechanical impedance of the structure, denoted as $Z_s(j\omega)$. Substituting this term into Eq. 4.16 yields,

$$f(t) = H_{m0}(j\omega, V)v(t) - \frac{Z_{e0}(j\omega)}{Z_s(j\omega)}f(t) \tag{4.18}$$

where $Z_s(j\omega)$ is simply,

$$Z_s(j\omega) = j\omega m_s + c_s + k_s/j\omega \tag{4.19}$$

By rearranging Eq. 4.18, the relationship between the force transmitted to the structure and the input voltage, denoted as the free-velocity force-voltage transfer function $H_t(j\omega, V)$, can be expressed as follows,

$$H_t(j\omega, V) = \frac{H_{m0}(j\omega, V)}{1 + \left(\dfrac{Z_{e0}(j\omega)}{Z_s(j\omega)}\right)} \tag{4.20}$$

It is apparent in Eq. 4.20 that the force-voltage tranfer function is determined by the blocked force-voltage transfer function and the ratio of the impedance terms. When the

mechanical impedance of the structure is much larger than that of the actuator (i.e. $Z_s(j\omega) \gg Z_{e0}(j\omega)$), the impedance terms in Eq. 4.20 can be neglected, and $H_t(j\omega, V)$ tends to the blocked force-voltage transfer function given by $H_{m0}(j\omega, V)$. Therefore, if the supporting structure is sufficiently rigid ($\omega_s \gg \omega_p$, where ω_s is the first resonance of the supporting structure), the structural dynamics can be ignored, and the transmitted force is equivalent to the blocked force. This condition is used to obtain the force-voltage transfer functions of the actuator using experimental measurements, regardless of the dynamics of the supporting structure.

4.3 Experimental procedure

4.3.1 Experimental setup

The force-voltage dynamics of each actuator is measured experimentally as follows. First, the actuator is attached to a rigid supporting structure via a force transducer that is used to measure the output force $f(t)$ of the actuator. Next, a discrete-time input voltage signal, denoted by $v[n]$, is defined in MATLAB, which is converted to a continuous-time input voltage $v(t)$ using an ADA converter and amplified to $v_e(t)$, accounting for the counter-electromotive force in Eq. 4.3. The force transducer measures the force response of the actuator as a voltage $\hat{v}_f(t)$ that is proportional to $f(t)$. Finally, the transducer signal is conditioned ($v_f(t)$) and converted to the discrete-time signal $v_f[n]$ that is recorded in MATLAB. Additionally, the input voltage $v(t)$ is measured ($v_v[n]$) to account for the latency of the ADA converter. This configuration is illustrated in Figure 4.2.

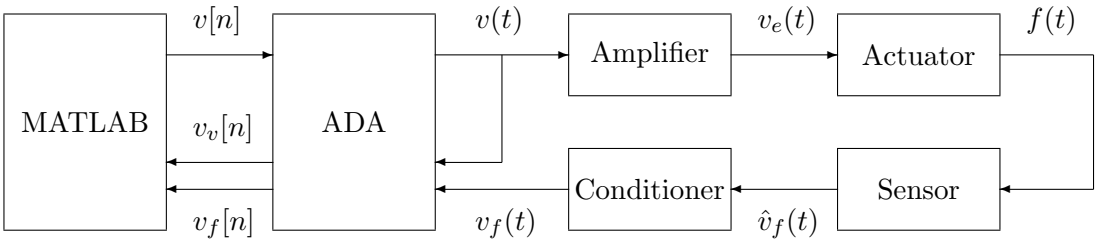

Figure 4.2: A block diagram of the experimental setup, including the MATLAB-defined input signal $v[n]$, the continuous-time input signal $v(t)$, the measured input signal $v_v[n]$, the amplified input voltage $v_e(t)$, the actuator force $f(t)$, the transducer signal $\hat{v}_f(t)$, the conditioned transducer signal $v_f(t)$, and the measured transducer signal $v_f[n]$.

Actuator and supporting structure

As stated in the introduction, there are three types of inertial actuators under consideration: a Micromega IA-01, a DataPhysics IV40, and a Labworks FG-142 actuator. The supporting structure comprises two steel blocks that are clamped together to increase the mechanical impedance, thereby ensuring that we can neglect the structural dynamics. As a means of attaching the actuator to the supporting structure, the force sensor is screwed into a stud that is then glued to the centre of the steel blocks. The mechanism for mounting the actuator to the force sensor varies for each of the three cases, where the mounting configurations are shown in Figure 4.3.

In the first case, the Micromega IA-01 actuator is screwed directly into the bore hole of the force sensor (see Figure 4.3a) and mounted horizontally, as required by its design. Conversely, in the second case, the DataPhysics IV40 actuator is mounted vertically to the force sensor using an adaptive screw thread (see Figure 4.3b), due to its greater mass.

In the third case, the Labworks FG-142 actuator is also mounted vertically to the force sensor. Since the through mounting hole of the actuator has no thread, a more complicated mounting configuration was required to attach the actuator to the force sensor. Here, a screw was placed into the through mounting hole and attached via a nut, which was then glued to another nut that was screwed onto the force transducer. This is shown in Figure 4.3c).

Figure 4.3: Configurations of a) Micromega IA-01, b) DataPhysics IV40, and c) Labworks FG-142 actuators when mounted to the rigid supporting structure.

Source generation and data acquisition (MATLAB)

All source generation and data acquisition tasks were performed in MATLAB via the ADA converter. Using monoharmonic source signals, the force-voltage transfer functions are obtained using the stepped-sine approach. The duration of the source signals is ten seconds and the sampling rate is $f_s = 51.2$ kHz. The excitation frequency range is 5 Hz to 10 kHz to capture the first actuator mode and the higher-order resonances with sufficient accuracy. The time histories of the resulting discrete-time response signals $v_v[n]$ and $v_f[n]$ are then measured over the duration of the source signals. Since these measured signals are both subjected to the latency of the ADA converter, a better comparison of the voltage-time signals $v_v[n]$ and force-time signals $v_f[n]$ can be made than if the source signals $v[n]$ are utilised directly.

As discussed in chapter 2, the stepped-sine approach is advantageous for revealing nonlinear behaviour through narrowband excitation. In this case, the approach is useful for highlighting nonlinearities in the actuators. To ensure that the measurements are time-efficient, a variable frequency resolution is utilised to accurately characterise the actuator responses around the peak resonance frequencies whilst minimising the amount of measured data away from these frequencies, where variations are less pronounced.

Information concerning the actuator parameters, such as the moving mass, natural frequency, and transduction coefficient, is shown in Tables 4.1, 4.2, and 4.3 for the Micromega IA-01, DataPhysics IV40, and Labworks FG-142 actuators respectively. These parameters are primarily taken directly from manufacturer data; the notable exceptions are the peak force frequency and the higher-order resonance frequency, which are obtained from preliminary measurements of the actuator dynamics. This influences the frequency and amplitude vectors used to implement the stepped sine method. For example, the Micromega IA-01 actuator initially features an exponential frequency vector, such that a high resolution (0.1 Hz) is achieved at low frequencies close to the actuator peak resonance and a lower resolution (1 Hz) is used at higher frequencies away from the peak resonance. This is used for index numbers up to 117. The voltage amplitude vector V was initially defined as 0.1 Volts for the purpose of driving the actuator within its (approximately) linear operating region. This voltage amplitude was then increased in increments of 0.05 Volts up to a maximum of 0.6 Volts, which was just below the saturation threshold of the amplifier.

Table 4.1: Physical parameters of the Micromega IA-01 actuator.

Parameter	**Micromega IA-01 Actuator**
Moving mass	0.032 kg
Natural frequency	8.7 Hz
Higher-order resonance frequency	3.8 kHz
Peak force frequency	12 Hz
Damping ratio	0.4
Transduction coefficient	1.6 N/A
Maximum force	3.2 N
Frequency vector	$\omega(i) = 2\pi\cdot \begin{bmatrix} 5\times 1.02^{i-1} \\ 60:10:100 \\ 200:100:2\text{k} \\ 2.05\text{k}:50:4\text{k} \\ 4.2\text{k}:200:5\text{k} \\ 5.5\text{k}:500:10\text{k} \end{bmatrix}$
Frequency index	$i = \boxed{0:1:117}$
Amplitude vector	$V = \boxed{0.1:0.05:0.6}$

Table 4.2: Physical parameters of the DataPhysics IV40 actuator.

Parameter	**DataPhysics IV40 Actuator**
Moving mass	1.21 kg
Natural frequency	32.2 Hz
Higher-order resonance frequency	3.2 kHz
Peak force frequency	32.5 Hz
Damping ratio	0.03
Transduction coefficient	5.6 N/A
Maximum force	30 N
Frequency vector	$\omega(i) = 2\pi\cdot \begin{bmatrix} 5:2:15 \\ 16:1:32 \\ 32.1:.1:34 \\ 36:2:110 \\ 120:20:200 \\ 300:100:3\text{k} \\ 3.02\text{k}:20:4\text{k} \\ 4.5\text{k}:500:10\text{k} \end{bmatrix}$
Amplitude vector	$V = \boxed{0.1:0.1:0.3}$

Table 4.3: Physical parameters of the Labworks FG-142 actuator.

Parameter	**Labworks FG-142 Actuator**
Moving mass	0.12 kg
Natural frequency	22.3 Hz
Higher-order resonance frequency	1.7 kHz
Peak force frequency	45 Hz
Damping ratio	0.5
Transduction coefficient	6 N/A
Maximum force	17 N
Frequency vector	$\omega(i) = 2\pi \cdot \begin{bmatrix} 5:1:16 \\ 18:2:40 \\ 41:1:50 \\ 55:5:100 \\ 200:100:1\text{k} \\ 1.05\text{k}:50:1.6\text{k} \\ 1.7\text{k}:100:2\text{k} \\ 2.5\text{k}:500:10\text{k} \end{bmatrix}$
Amplitude vector	$V = \boxed{0.1:0.2:0.5}$

Similarly, the DataPhysics IV40 and Labworks FG-142 actuator measurements feature a variable frequency resolution, which is chosen according to the resonance frequencies of interest. For each actuator, the input voltage amplitude was initially defined as $V = 0.1$ Volts, where the actuator dynamics are approximately linear. The voltage amplitude was then increased incrementally up to a maximum of 0.3 Volts and 0.5 Volts respectively, where the actuator nonlinearities are more pronounced.

Data acquisition (ADA)

The ADA converter used in this experiment was a National Instruments NI-cDAQ-9174 interface, where the NI 9264 and NI 9239 modules are applied for output D-A conversion and input A-D conversion respectively. This interface features a maximum sampling rate of 51.2 kHz, which was required to capture the rapid dynamical behaviour associated with actuator saturation.

The latency of the ADA converter can be ascertained from the transfer function between the source signals $v[n]$ and the recorded voltage signals $v_v[n]$. Since the ADA converter behaves as a pure delay with unity magnitude and linear phase, the latency is ascertained as 800 microseconds. For further details, see Appendix B.

Amplification

To account for the different characteristics of each actuator, two amplifiers were utilised in this experiment. The first of these is a fixed-gain Micromega Dynamics Rack-04-45N amplifier (shown in Figure 4.4), which is used solely to excite the Micromega IA-01 actuator. The DataPhysics IV40 and Labworks FG-142 actuators are excited using a variable-gain DataPhysics SignalForce 30 W Model PA 30E power amplifier (shown in Figure 4.4) where the gain was kept constant for all measurements.

The transfer function of the Micromega Dynamics Rack-04-45N amplifier was obtaining using the stepped-sine method by measuring the input signals ($v(t)$) and output signals ($v_e(t)$). Since the counter-electromotive force of the actuator has the effect of distorting the output signals, the actuator was replaced by a 3 Ohm resistor as the equivalent output resistance load. The transfer function, which is given in Appendix B, indicates that the amplifier behaves as a pure gain over the frequency region of interest, with little variation in the magnitude or phase. The gain of the amplifier is 11 dB.

Force sensor

The force transducer used in this experiment is a PCB 208C01 quartz sensor, which is attached between the actuator and supporting structure (see Figure 4.3). The natural frequency of the transducer is very high (36 kHz), which indicates that the transducer casing is sufficiently rigid to negate its dynamic effects on the measurements. The relationship between the actuator force ($f(t)$) and the voltage output of the transducer ($v_f(t)$) is determined by the transducer sensitivity, denoted by T_s (i.e. $v_f(t) = T_s f(t)$). The stated sensitivity of the transducer is $T_s = 112.4$ mV/N.

Conditioner

The output voltage of the PCB force transducer ($\hat{v}_f(t)$) was conditioned ($v_f(t)$) using a PCB ICP Sensor Signal Conditioner Model 480B10 (shown in Figure 4.4). The transfer function of the signal conditioner is measured using stepped-sine excitation, and is illustrated in Appendix B. Here, it is apparent that the conditioner behaves as a pure gain of unity magnitude with negligible phase change in the frequency range of interest.

Figure 4.4: Illustration of equipment used in the experimental setup.

4.3.2 Post-processing

Using the measured signals $v_v[n]$ and $v_f[n]$, the velocity-time and force-time histories respectively are obtained as follows,

$$\begin{aligned} v(t) =& v_v[n], \qquad t = n\Delta \\ f(t) =& v_f[n]/T_s, \qquad t = n\Delta \end{aligned} \tag{4.21}$$

where $\Delta = 1/f_s$. To ensure that the transient response has decayed sufficiently, the first second of each of the measured signals is discarded, thereby retaining the steady-state responses.

The next step is to filter the force-time signals to remove the DC component that caused by static loading to the force transducer. This enables the time histories to be numerically integrated for the purpose of obtaining the velocity-time and displacement-time signals, which reveal further information on the actuator characteristics. A well-known problem with the presence of DC components in a pre-integrated signal is the drift phenomenon, where the low-frequency and DC components are amplified over time due

to the low-pass filtering property of the integration process. This is shown as follows,

$$\ddot{\tilde{y}}_p(t) = \ddot{y}_p(t) + c_0 \tag{4.22}$$

where $\ddot{\tilde{y}}_p(t)$ is the measured acceleration-time signal, which is proportional to the force-time signal, $\ddot{y}_p(t)$ is the true acceleration-time signal, and c_0 is the DC component introduced by the force transducer. Integrating this signal yields,

$$\dot{\tilde{y}}_p(t) = \int (\ddot{y}_p(t) + c_0)\, dt = \dot{y}_p(t) + c_0 t + c_1 \tag{4.23}$$

where $\dot{y}_p(t)$ is the desired velocity signal and c_1 is a new DC component. It can be seen that the original DC component c_0 in the acceleration-time signal now varies linearly with time in the velocity signal, thereby resulting in the drift phenomenon. In order to prevent the drift phenomenon from occurring, it is necessary to sufficiently attenuate the low-frequency and DC components; this requires the use of high-pass filters in digital controllers when applying active control in practice [120]. In this case, the sampling rate (51.2 kHz) far exceeds the lowest frequency of interest (5 Hz), and it is therefore difficult to design a digital filter that will sufficiently attenuate these low-frequency and DC components in real-time without the use of downsampling. Since we can utilise offline processing to filter the signals, an alternative approach is taken in the frequency-domain using Ribeiro's method [121]. For details on this filtering procedure, see Appendix C.

Using this filtering approach, the velocity-time and displacement-time signals are obtained from the force-time signals as follows,

$$\dot{y}_p(t) = \frac{1}{m_p} \int f(t)\, dt \tag{4.24}$$

$$y_p(t) = \int \dot{y}_p(t)\, dt \tag{4.25}$$

where the proof-mass m_p is taken from the manufacturer data and the integration process in Eq. 4.24 is performed numerically using MATLAB's cumptrapz function.

By utilising the voltage-time and filtered force-time signals, the force-voltage FRFs are then obtained using the stepped-sine approach,

$$H(j\omega_i) = \frac{F_i(j\omega_i)}{V_i(j\omega_i)} \tag{4.26}$$

where $F_i(j\omega_i)$ and $V_i(j\omega_i)$ are the Fourier transforms of $f(t)$ and $v(t)$ measured at the fundamental frequency ω_i. Since these FRFs represent the first-order force response (at the fundamental excitation frequency), the equivalent first-order displacement-voltage transfer function, denoted as $H_p(j\omega)$, is ascertained from the relation,

$$H_p(j\omega) = -m_p\omega^2 H(j\omega) \tag{4.27}$$

These displacement-voltage transfer functions are used to estimate the peak resonance frequency of the actuator, since the actuator is most susceptible to saturation in this frequency region.

4.4 Results

The results obtained from the experimental measurements are given in the time- and frequency-domains. In the time domain, the force-time signals are examined for harmonic distortion, which is an indication of the presence of actuator nonlinearities [12]. Typically, these nonlinearities are most pronounced around the natural frequency of the actuator, since their effects are stronger at higher amplitudes. Therefore, the force-time responses that lie close to this natural frequency are of particular interest. The corresponding velocity-time and displacement-time signals, which are ascertained from the force-time histories, are also shown for the purpose of examining the contact mechanics of the stroke-saturated actuators.

In the frequency-domain, the force responses are illustrated for the purpose of examining the harmonics introduced by the nonlinear processes, which are not easily examined in the time-domain. The relative strength of the harmonics can indicate the type of nonlinearity; for example, weak nonlinearities are revealed by harmonics that rapidly decrease in magnitude with increasing frequency, whereas impact-related nonlinearities exhibit a continuous train of harmonics across the frequency spectrum. Additionally, the force-voltage and displacement-voltage transfer functions are shown, and the effects of the nonlinearities on the natural frequency of the actuator are examined.

4.4.1 Time-domain

Micromega IA-01 actuator

It was noted that the Micromega IA-01 inertial actuator exhibits stroke saturation around the peak resonance frequency for excitation amplitudes $V \geq 0.35$ Volts, which represents the threshold between the intended operating region and the stroke-saturated region of the actuator. Therefore, the actuator responses to excitation signals that are beneath this threshold are used to reveal additional nonlinear processes, besides stroke saturation, that are exhibited by the actuator.

Figures 4.5 and 4.6 shows the force-time responses of the actuator at small excitation amplitudes ($V < 0.35$ Volts) for the excitation frequencies $\omega = 16\pi$ rad/s and $\omega = 26\pi$ rad/s respectively. The first of these excitation frequencies is close to the peak resonance frequency ω_p, whereas the second excitation frequency is well above the peak resonance frequency (where the actuator behaves as an ideal force generator). In Figure 4.5, it is apparent that the response signals exhibit harmonic distortion, even at the lowest excitation amplitude $V = 0.1$ Volts. Conversely, the force-time signals in Figure 4.6 are approximately monoharmonic. This confirms that the actuator is weakly nonlinear beneath the saturation threshold; since the nonlinear effects are most pronounced near the peak resonance, the nonlinearity may be attributed to the actuator suspension.

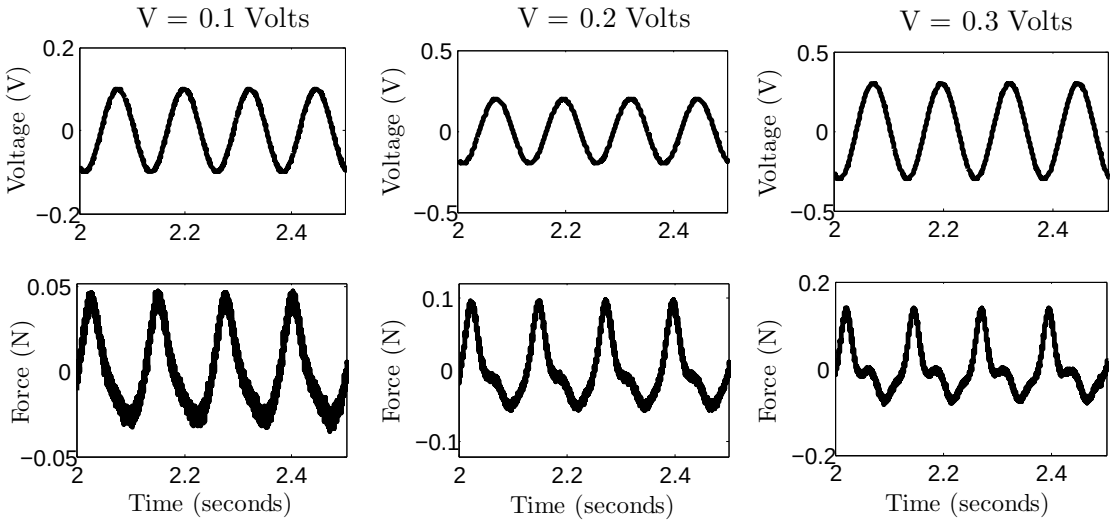

Figure 4.5: Measured voltage-time and force-time signals of the Micromega actuator at $\omega = 16\pi$ rad/s.

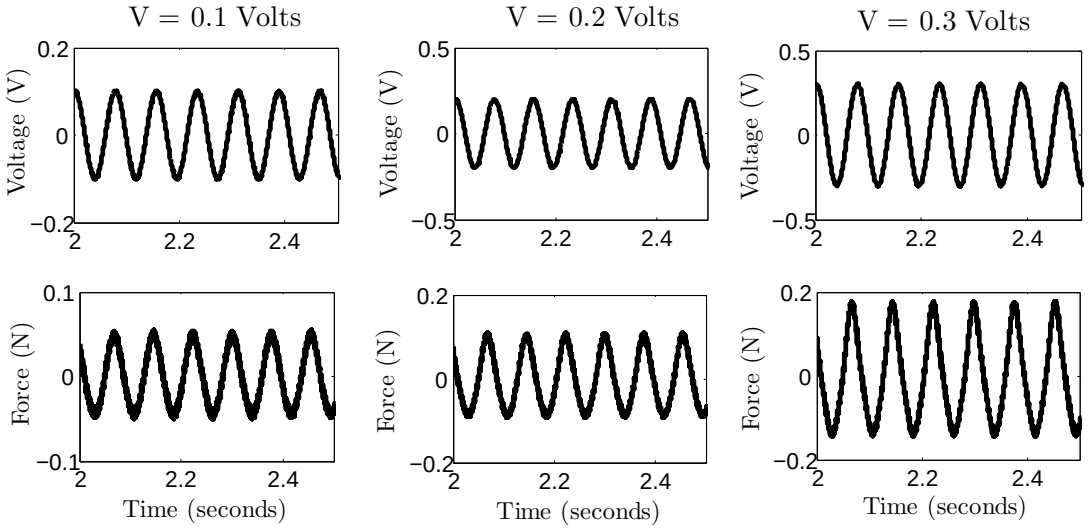

Figure 4.6: Measured voltage-time and force-time signals of the Micromega actuator at $\omega = 26\pi$ rad/s.

The force-time actuator responses obtained at large excitation amplitudes ($V > 0.35$ Volts) are illustrated in Figures 4.7 and 4.8. Here, the presence of stroke saturation is confirmed by the appearance of large impulses in the force responses. These impulses are asymmetric and only occur in the positive direction, thereby indicating that the stroke length is biased towards a particular end stop. Furthermore, it is apparent that as the excitation amplitude increases, the magnitude of the impulses also increase, and double- or triple-impacts may occur [122]. The latter feature is interesting and infers that a single collision does not overcome the proof-mass inertia, resulting in further collisions.

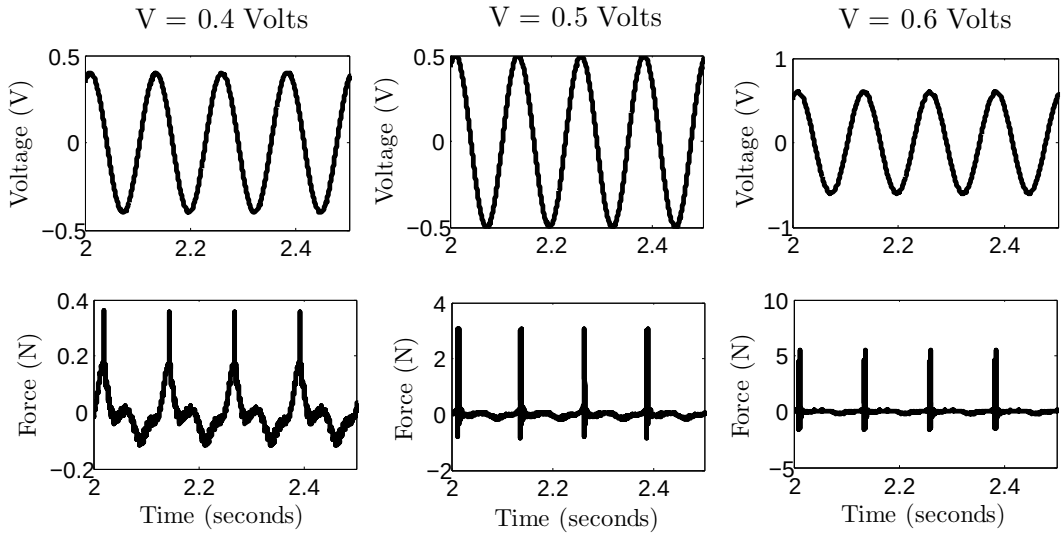

Figure 4.7: Measured voltage-time and force-time signals of the Micromega actuator at $\omega = 16\pi$ rad/s.

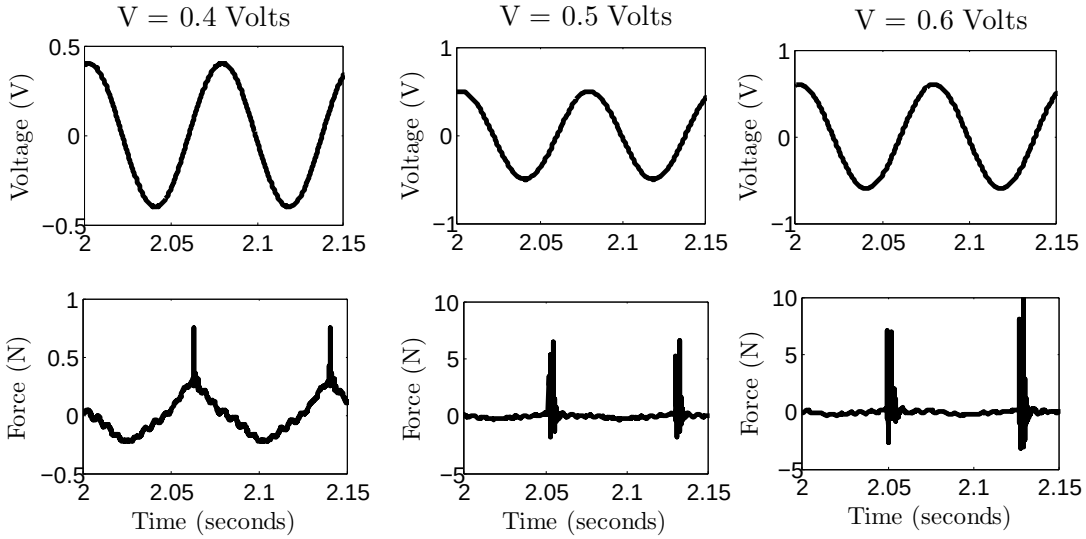

Figure 4.8: Measured voltage-time and force-time signals of the Micromega actuator at $\omega = 26\pi$ rad/s.

Using the filtering and integration procedure, the velocity-time and displacement-time actuator responses are obtained from the corresponding force-time signals. By analysing the velocity-time signals (displayed in Figure 4.9), it is apparent that stroke saturation causes abrupt changes in velocity (as marked) close to the zero crossing point. The presence of several abrupt velocity changes in quick succession indicates multiple impacts, which occur when the zero crossing point is not passed during the first impact. This indicates that the proof-mass has not changed direction during the initial collision, thereby necessitating additional collisions. These findings have important implications for the coefficient of restitution, which is discussed in chapter 5.

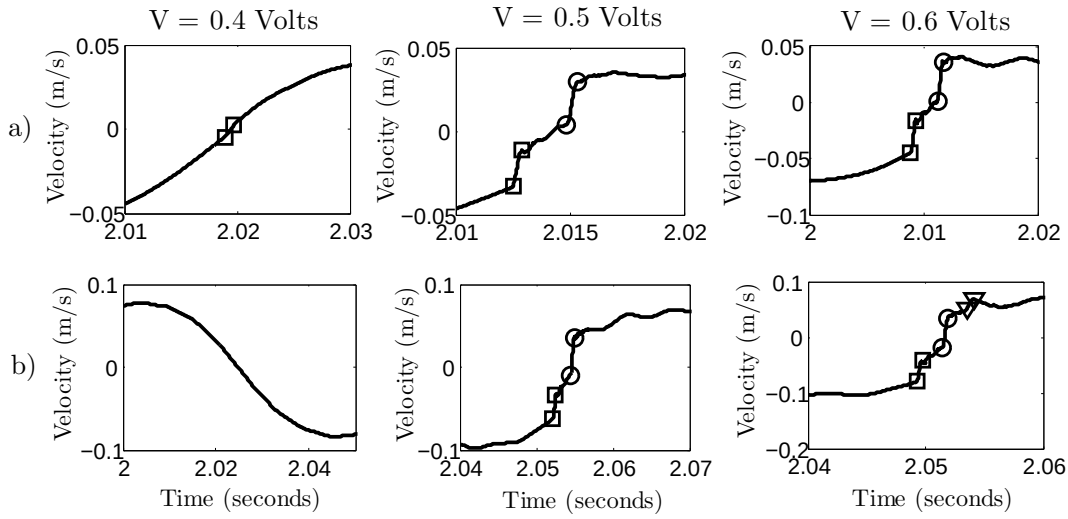

Figure 4.9: Measured velocity-time signals of the Micromega actuator, obtained at a) $\omega = 16\pi$ rad/s, and b) $\omega = 26\pi$ rad/s. The start and end of each collision is marked.

The displacement-time signals (shown in Figure 4.10) are approximately monoharmonic due to the low-pass filtering effect of integration, yet the proof-mass displacement is limited in the negative direction as a result of stroke saturation. This results in harmonic distortion at large excitation amplitudes, where the negative proof-mass displacement appears to reach the saturation threshold at approximately 1 mm. However, careful observation reveals that the saturation threshold is inconsistent and appears to increase with excitation amplitude; this is because the proof-mass displacement has a small, but non-negligible DC component introduced by asymmetric actuator nonlinearities. Without further information, it is not possible to ascertain the DC component of the proof-mass displacement from the measured force-time signals. Instead, it is necessary to estimate the DC component using a nonlinear model, which is explored in chapter 5.

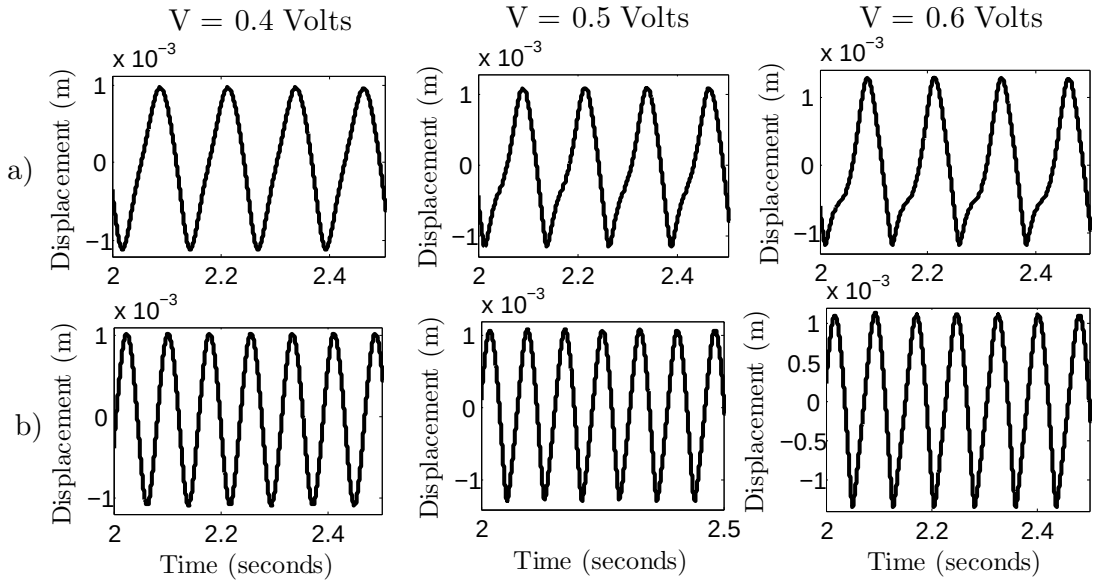

Figure 4.10: Measured displacement-time signals of the Micromega actuator, obtained at a) $\omega = 16\pi$ rad/s, and b) $\omega = 26\pi$ rad/s.

DataPhysics IV40 actuator

The DataPhysics IV40 inertial actuator does not exhibit the stroke saturation phenomenon, as the inertial mass is provided through the external body. When matched with the linear DataPhysics SignalForce 30 W Model PA 30E power amplifier, the amplifier output becomes saturated well before any mechanical saturation within the actuator itself can be observed (as a means of protecting the actuator). It is therefore difficult to

determine the physical limits of this actuator without risking damage to the voice coil or suspension. However, the experimental measurements indicate that the actuator exhibits weakly nonlinear behaviour in the central spigot suspension, which is revealed by exciting the actuator at sufficiently low frequencies.

Figure 4.11 illustrates the force-time responses of the inertial actuator alongside the corresponding excitation signals. The excitation frequency $\omega = 26\pi$ rad/s is well below the peak resonance frequency of the actuator and the resulting force responses contain a small degree of harmonic distortion, thereby indicating that the actuator suspension is weakly nonlinear when low-frequency excitation is used.

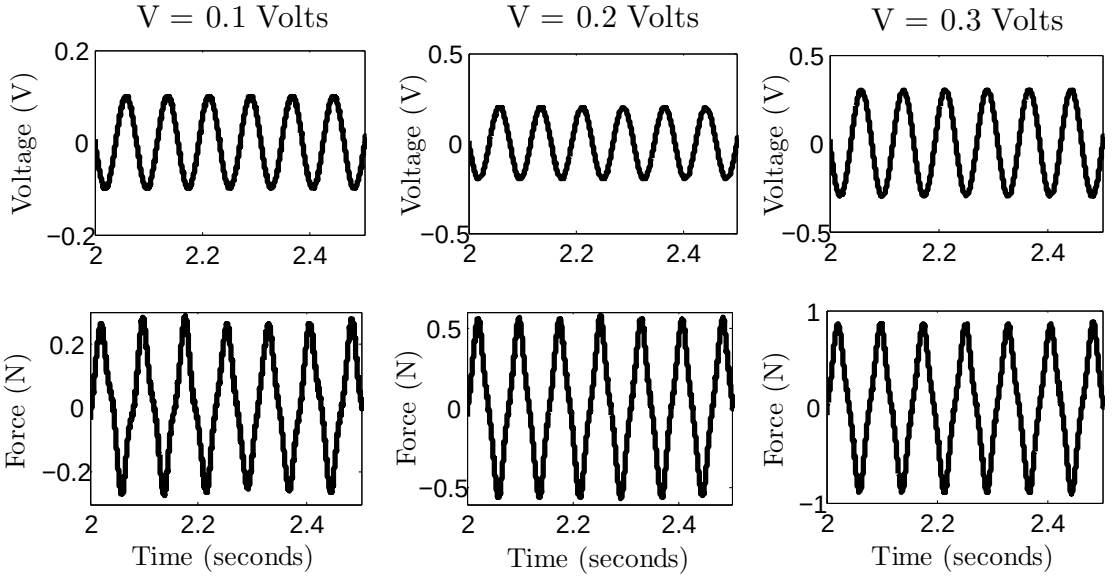

Figure 4.11: Measured voltage-time and force-time signals of the DataPhysics actuator at $\omega = 26\pi$ rad/s.

To confirm that the actuator force response does not exhibit harmonic distortion within the intended operating region, the force responses obtained using the excitation frequency $\omega = 70\pi$ rad/s, which is close to the natural frequency of the actuator, are shown in Figure 4.12. Here, it is apparent that the force signals are approximately sinusoidal, with negligible harmonic distortion. This indicates that the actuator exhibits a relatively linear response when the excitation frequency is close to the natural frequency. Furthermore, the force output of the actuator is fairly large around the natural frequency, reaching a peak of several tens of Newtons, due to the greater inertial mass.

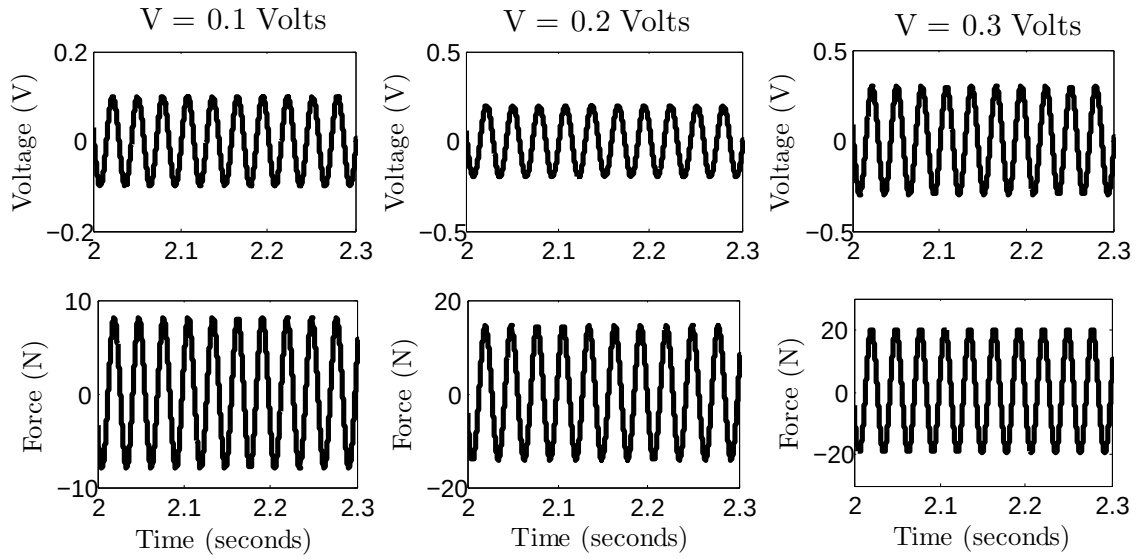

Figure 4.12: Measured voltage-time and force-time signals of the DataPhysics actuator at $\omega = 70\pi$ rad/s.

The velocity-time signals of the actuator are ascertained from the force-time signals and illustrated in Figure 4.13. Theis figure indicate that the signals are approximately mono-harmonic as a result of the low-pass filtering effect of integration, which confirms that the suspension nonlinearities are relatively weak. The peak value of the velocity-time signals tends towards 0.1 ms^{-1}, which appears to be reasonable for this type of actuator. This indicates that the actuator has a very large output force-to-velocity ratio, which occurs as a result of a relatively high natural frequency and a large inertial mass.

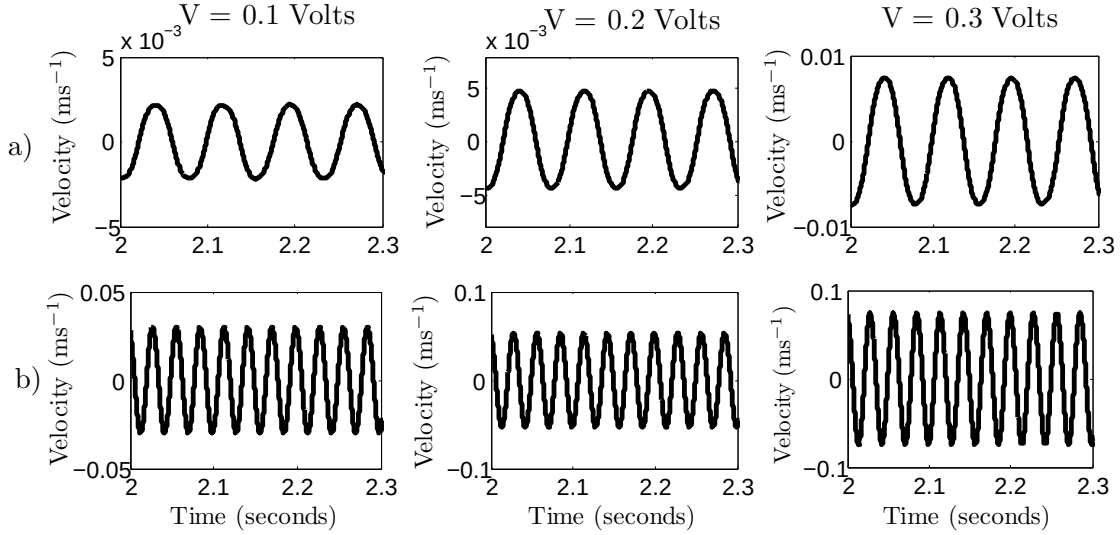

Figure 4.13: Measured velocity-time signals of the DataPhysics actuator, obtained at a) $\omega = 26\pi$ rad/s, and b) $\omega = 70\pi$ rad/s.

Labworks FG-142 actuator

The Labworks FG-142 inertial actuator exhibits stroke saturation around the natural frequency when $V = 0.5$ Volts, which acts as the threshold of the intended operating region. Additional actuator nonlinearities can be observed within the intended operating region, in a similar manner to the Micromega IA-01 inertial actuator. It should be noted that this actuator exhibits the largest damping ratio of all the actuators under consideration. As a result, there is a large degree of variability between the peak force resonance frequency and the natural frequency of the actuator.

Figures 4.14 and 4.15 illustrates the force-time responses of the actuator for all excitation amplitudes and the excitation frequencies $\omega = 30\pi$ rad/s and $\omega = 92\pi$ rad/s respectively. The first of these excitation frequencies is close to the natural frequency of the actuator, whereas the second excitation frequency is well above the natural frequency, where the actuator behaves as an ideal force generator.

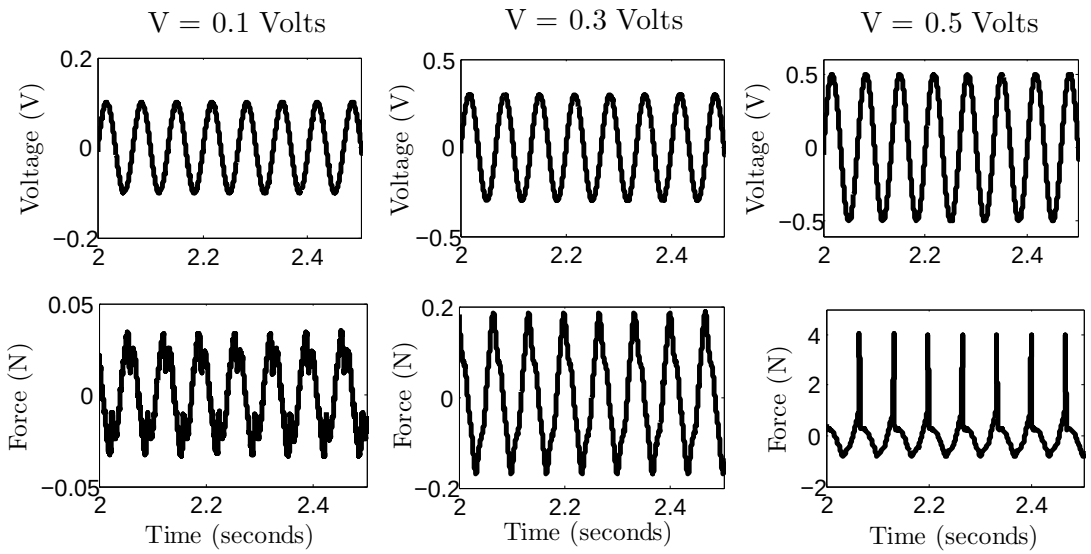

Figure 4.14: Measured voltage-time and force-time signals of the Labworks actuator at $\omega = 30\pi$ rad/s.

In Figure 4.14, it is apparent that the force-time signals contain a large degree of harmonic distortion, even at lower excitation amplitudes. This suggests that the actuator exhibits a relatively strong suspension nonlinearity within its intended operating region. At the highest excitation amplitude, the characteristic impulses of stroke saturation can be seen in the force-time response. These effects of stroke saturation differ from the Micromega IA-01 actuator, as the impulses occur earlier in the cycle and the contact time is longer. This infers that the end stops of the Labworks FG-142 actuator are relatively soft.

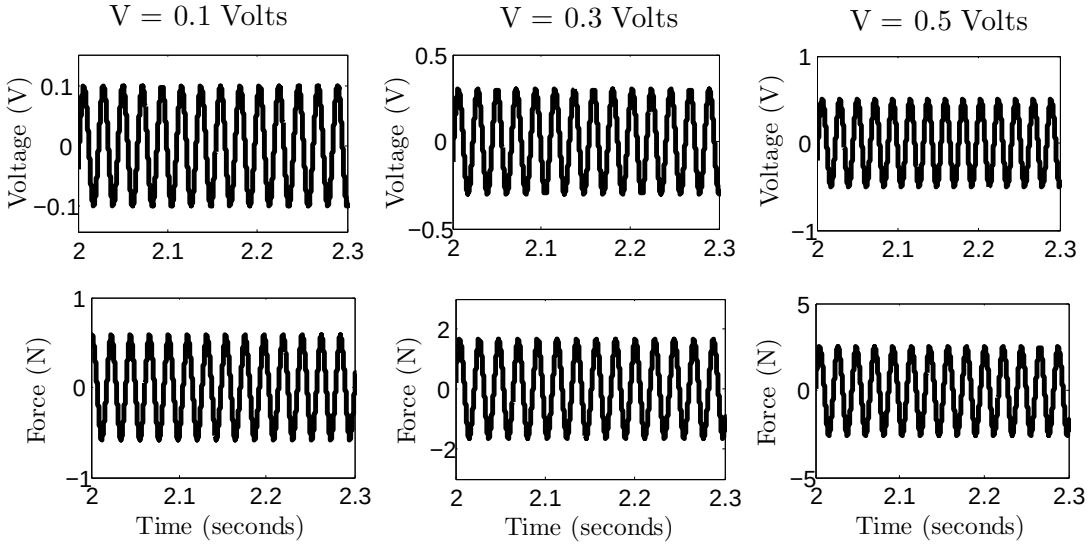

Figure 4.15: Measured voltage-time and force-time signals of the Labworks actuator at $\omega = 92\pi$ rad/s.

In Figure 4.15, the force-time signals are approximately monoharmonic, which shows that the actuator nonlinearities are negligible within this frequency region. In addition, the force-to-voltage ratio is much higher than in Figure 4.14, since the excitation frequency is close to the peak force resonance frequency.

The velocity-time and displacement-time signals, which are obtained from the force-time signals, are displayed in Figures 4.16 and 4.17 respectively. For $\omega = 30\pi$ rad/s, the velocity-time signals contain harmonic distortion, thereby illustrating that the suspension nonlinearity is relatively strong. At the highest excitation amplitude, the duration of the impulses is marked (with circles). Since the separation and approach velocities have different signs, it is apparent that a single collision is sufficient to overcome the inertia of the proof-mass, and so double-impacts are not observed. For $\omega = 92\pi$ rad/s, the velocity-time signals are approximately monoharmonic.

Figure 4.17 shows that the displacement of the proof-mass, in general, is much lower than that of the Micromega IA-01 inertial actuator, since the inertial mass is greater and the natural frequency is higher. For $V = 0.5$ Volts, $\omega = 30\pi$ rad/s, the displacement of the proof-mass becomes limited at around 8×10^{-4} m in the negative direction, due to the stroke saturation phenomenon. This is the approximate stroke length of the actuator.

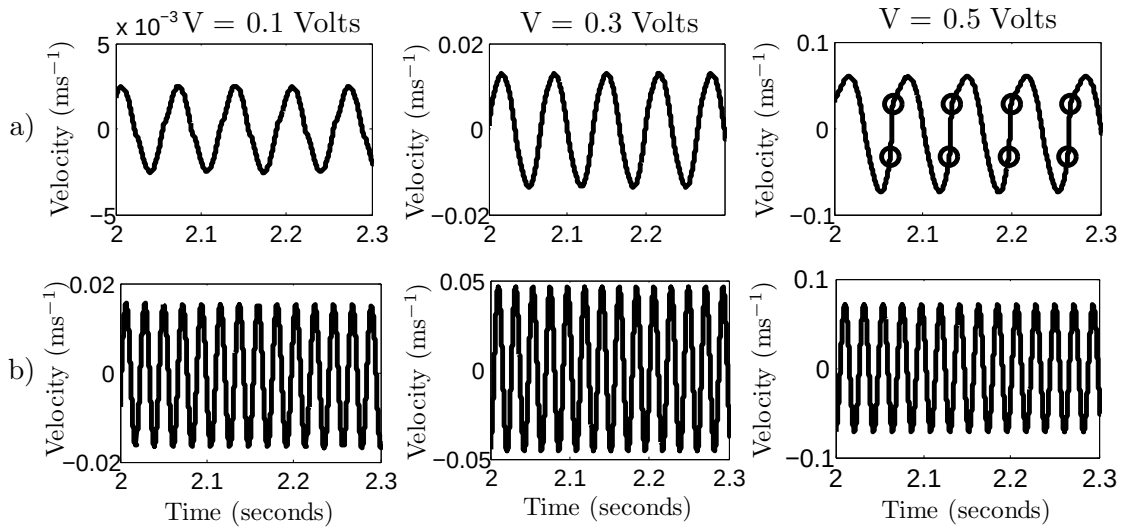

Figure 4.16: Measured velocity-time signals of the Labworks actuator, obtained at a) $\omega = 30\pi$ rad/s, and b) $\omega = 92\pi$ rad/s. The start and end of each collision is marked.

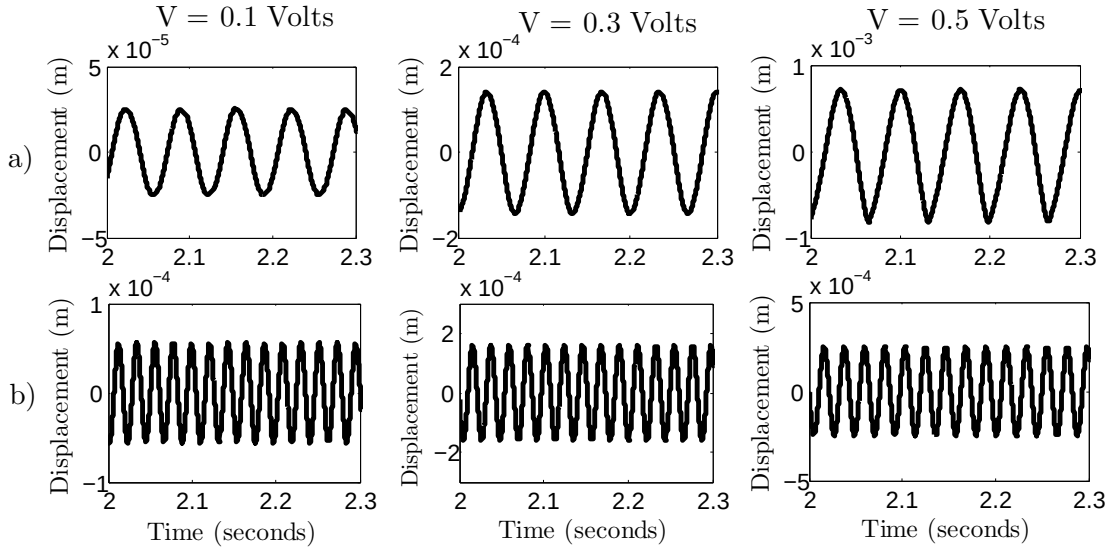

Figure 4.17: Measured displacement-time signals of the Labworks actuator, obtained at a) $\omega = 30\pi$ rad/s, and b) $\omega = 92\pi$ rad/s.

4.4.2 Frequency-domain spectra

Micromega IA-01 actuator

In order to independently investigate the suspension nonlinearities and the saturation nonlinearities of the Micromega IA-01 actuator, the spectra of two force responses shown in Figures 4.5 and 4.8 are displayed in Figure 4.18. The first of these spectra, shown in Figure 4.18a), corresponds to the force response obtained at $\omega = 16\pi$ rad/s, $V = 0.3$

Volts, where the nonlinear suspension dynamics are relatively pronounced. In contrast, Figure 4.18b) displays the force response obtained at $\omega = 26\pi$ rad/s, $V = 0.5$ Volts, where the actuator is primarily subject to stroke saturation.

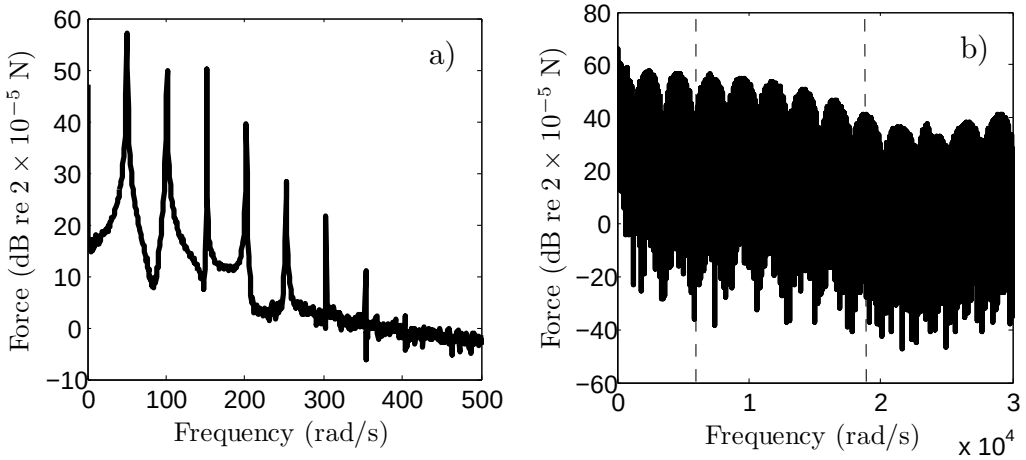

Figure 4.18: Spectral content of two force response signals, including a) $\omega = 16$ rad/s, $V = 0.3$ Volts (see Figure 4.5), and b) $\omega = 26$ rad/s, $V = 0.5$ Volts (see Figure 4.8).

Figure 4.18a) reveals that the suspension nonlinearity manifests itself as several even-order superharmonics that decrease rapidly in magnitude until the noise floor is reached, thereby confirming that the nonlinearity is relatively weak. In addition, the even-order harmonics indicate that the actuator exhibits an even-order suspension nonlinearity, which introduces asymmetry. Since one key feature of an asymmetrical system, such as the quadratic oscillator [123], is the presence of a DC component, this is further confirmation that a DC component is present in the displacement-time signals in Figure 4.10.

Figure 4.18b) illustrates that the impulses associated with stroke saturation introduce a continuous train of harmonics into the force spectra, which indicates that stroke saturation is a strongly nonlinear process. The envelope of these harmonics is determined by the duration, number, and shape of the impulses through the duality principle [124]. It is assumed that the impulses can be modelled by a rectangular function of amplitude A and duration ΔT, denoted by $W(t)$,

$$W(t) = \begin{cases} A & t_0 \leq t \leq t_0 + \Delta T \\ 0 & t < t_0, t > t_0 + \Delta T \end{cases} \tag{4.28}$$

where t_0 marks the start of the impulse. Using this assumption, the envelope of the harmonics can be expressed as follows,

$$\text{Envelope} = \mathcal{F}\Big\{W(t)\Big\} = 2A\Big[\Delta T e^{(-i\omega(t_0+\Delta T/2)}\Big]\text{sinc}(\omega\Delta T) \tag{4.29}$$

Thus, the envelope of the harmonics in Figure 4.18b) approximately conforms to a sinc function, with some small discrepancies occurring as a result of the actual shape of the impulse and the double-impact phenomenon. Since the amplitude of the harmonics decays with increasing frequency, the 1-3 kHz region (highlighted in Figure 4.18b)) is identified as a suitable region in the spectrum for detecting the presence of stroke saturation, as this is well above the control bandwidth region. This frequency region also relates to the duration of the impacts, which is discussed in more detail in chapter 5.

Labworks FG-142 actuator

We now investigate the suspension and stroke saturation nonlinearities in the frequency domain by examining the spectra of two force-time responses ($V = 0.3$ Volts, $\omega = 30\pi$ rad/s and $V = 0.5$ Volts, $\omega = 30\pi$ rad/s) shown in Figure 4.14. These spectra are displayed in Figure 4.19.

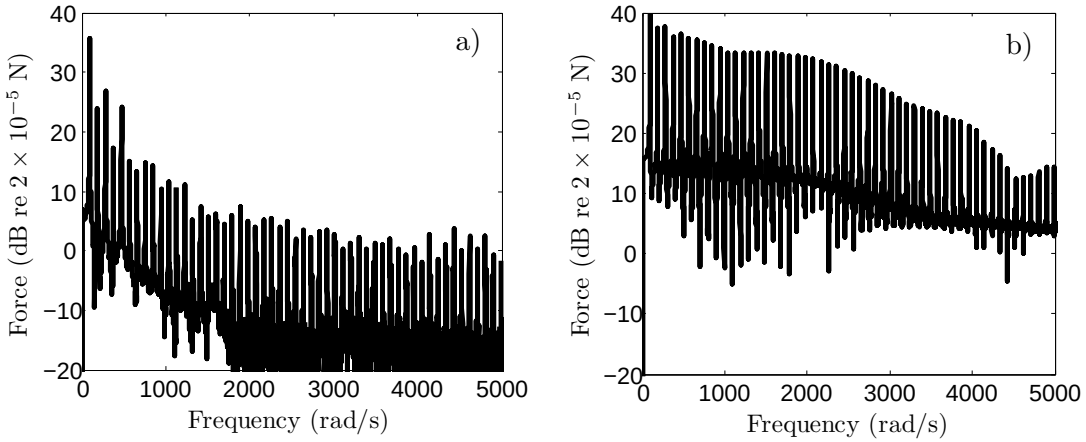

Figure 4.19: Spectral content of two force responses, for a) $\omega = 30$ rad/s, $V = 0.3$ Volts, and b) $\omega = 30$ rad/s, $V = 0.5$ Volts (see Figure 4.14).

Figure 4.19a) shows that the suspension nonlinearity manifests itself as a range of even-order harmonics that extend well into the upper frequencies due to the slow decrease in magnitude. This confirms that the suspension nonlinearity of this actuator is relatively strong in comparison with the Micromega IA-01 actuator, as shown in Figure 4.18a). Con-

versely, by comparing Figure 4.19b) with Figure 4.18b), it can be seen that the envelope of the harmonics does not conform to an appoximate sinc function, but the harmonics instead decay relatively quickly to a much lower magnitude. This suggests that the impulses cannot be modelled using the rectangular function expressed by Eq. 4.28, and the stroke saturation nonlinearity is relatively weak due to the softer end stops.

4.4.3 Force-Voltage FRFs

The next step is to analyse and compare the measured force-voltage FRFs of each actuator, which are displayed in Figures 4.20, 4.21, and 4.22 respectively. These figures demonstrate that each actuator behaves as a single-degree-of-freedom system up to the first higher-order resonance. The higher-order resonance is probably caused by the proof-mass rocking on the spring suspension, generating torsional motion. Additionally, the peak force resonance frequency appears to vary with excitation amplitude, thereby confirming that each actuator is weakly nonlinear.

Figure 4.20 shows that the Micromega IA-01 actuator exhibits a peak force resonance frequency of about 12 Hz and a higher-order resonance frequency of 3.8 kHz. It can be observed that the peak force resonance frequency shifts upwards as the excitation amplitude increases, even for excitation amplitudes beneath the saturation threshold ($V < 0.35$ Volts). This phenomenon suggests that the suspension nonlinearity is an amplitude-dependent hardening stiffness.

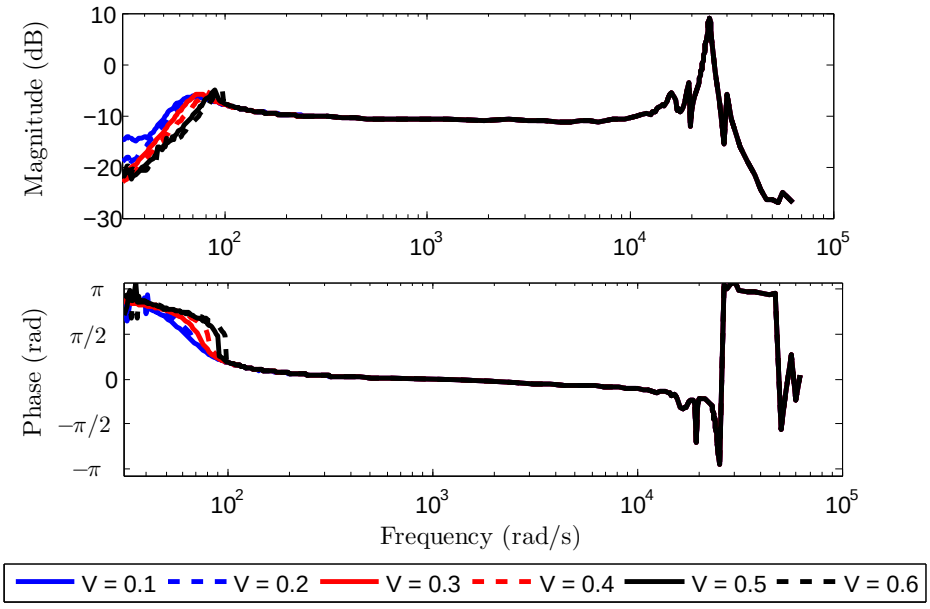

Figure 4.20: Force-voltage transfer functions of the Micromega IA-01 inertial actuator.

Once the saturation threshold is exceeded, the peak force resonance frequency increases further, exhibiting the jump phenomena at the highest excitation amplitudes. This shows that the actuator is susceptible to stroke saturation when the peak resonance frequency has increased sufficiently to encompass the relevant excitation frequency, which will occur if the excitation amplitude is large enough. When the excitation frequency is well above the peak force resonance frequency, the transfer functions are amplitude-invariant, such that the actuator behaves as a linear ideal force generator in this frequency region. Having said this, it is imperative to consider the excitation amplitude and the rise in the peak resonance frequency when assessing the validity of the ideal force generator assumption.

Figure 4.21 illustrates the transfer functions of the DataPhysics IV40 actuator, which reveals a peak force resonance frequency of 32.5 Hz and a higher-order resonance frequency of 3.2 kHz. A large force-to-voltage ratio (about 100 N/V) may be observed at the peak resonance, due to the small damping ratio. It is apparent that both the peak force resonance and the higher-order resonance reduce in frequency and increase in magnitude as the excitation frequency increases; this reveals that the actuator exhibits a weak softening stiffness nonlinearity in the suspension. Between the two resonances, the transfer functions are amplitude-invariant, and the actuator behaves as a linear ideal force generator. Since the softening nonlinearity reduces the peak resonance frequency, the validity of the ideal force generator assumption is not affected by the excitation amplitude.

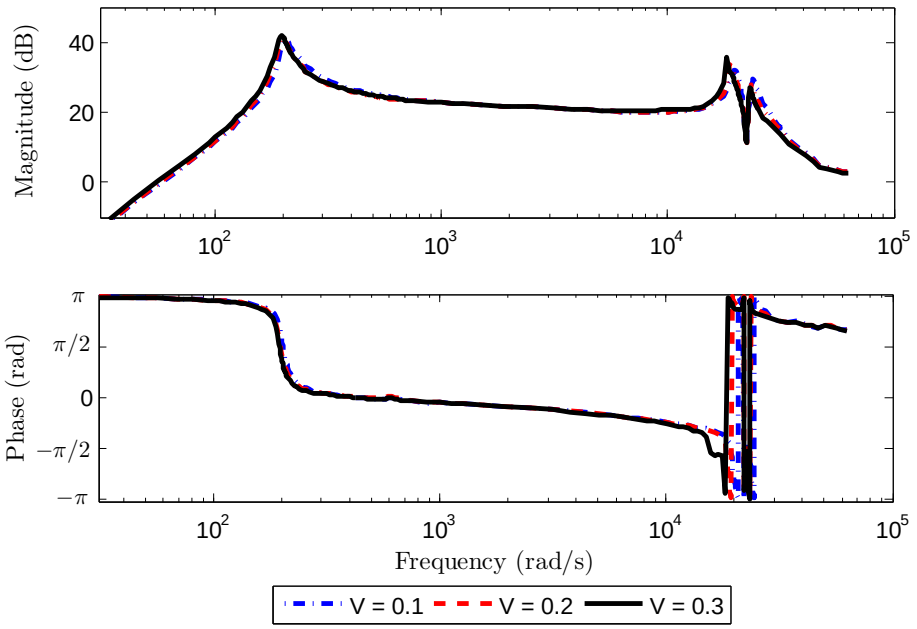

Figure 4.21: Force-voltage transfer functions of the DataPhysics IV40 inertial actuator.

The measured force-voltage FRFs of the Labworks FG-142 actuator, as shown in Figure 4.22, indicate that the actuator exhibits a highly damped peak force resonance frequency at about 45 Hz and a higher-order resonance frequency at 1.7 kHz. Above the peak force resonance, the actuator behaves as an ideal force generator. As the excitation amplitude increases, the peak force resonance frequency reduces significantly as a result of a strong softening stiffness nonlinearity in the suspension and the large damping ratio. This has the effect of increasing the ideal force generator bandwidth when the excitation amplitude is relatively large. However, the actuator also becomes more susceptible to stroke saturation, and so it is important to consider the excitation amplitude before assuming that the actuator will behave as an ideal force generator.

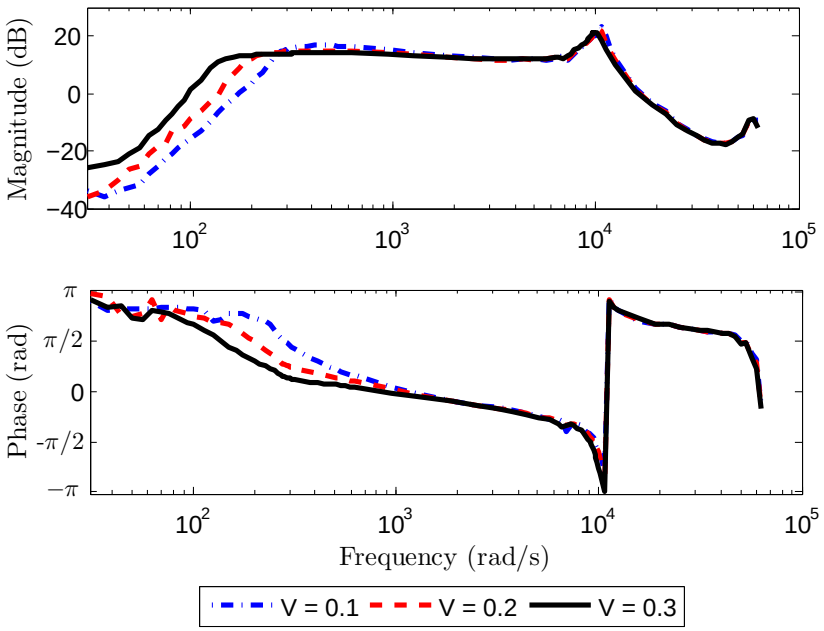

Figure 4.22: Force-voltage transfer functions of the Labworks FG-142 inertial actuator.

4.4.4 Displacement-Voltage FRFs

Now we examine the first-order displacement-voltage FRFs of each actuator, which are obtained from the equivalent force-time FRFs using Eq. 4.27. These figures are used to examine the peak resonance of each actuator in more detail and to compare the natural frequency with the peak force resonance frequency.

The transfer functions of the Micromega IA-01 actuator, as illustrated in Figure 4.23, indicate that the magnitude of the peak resonance frequency decreases with increasing excitation amplitude, whilst the peak resonance frequency rises. These characteristics are reminiscent of a hardening Duffing oscillator, which implies that the nonlinear suspension stiffness can be modelled using low-order polynomial terms. In addition, the linearised natural frequency of the actuator (8.7 Hz), is slightly lower than the peak force resonance frequency, due to the relatively high damping ratio of the actuator.

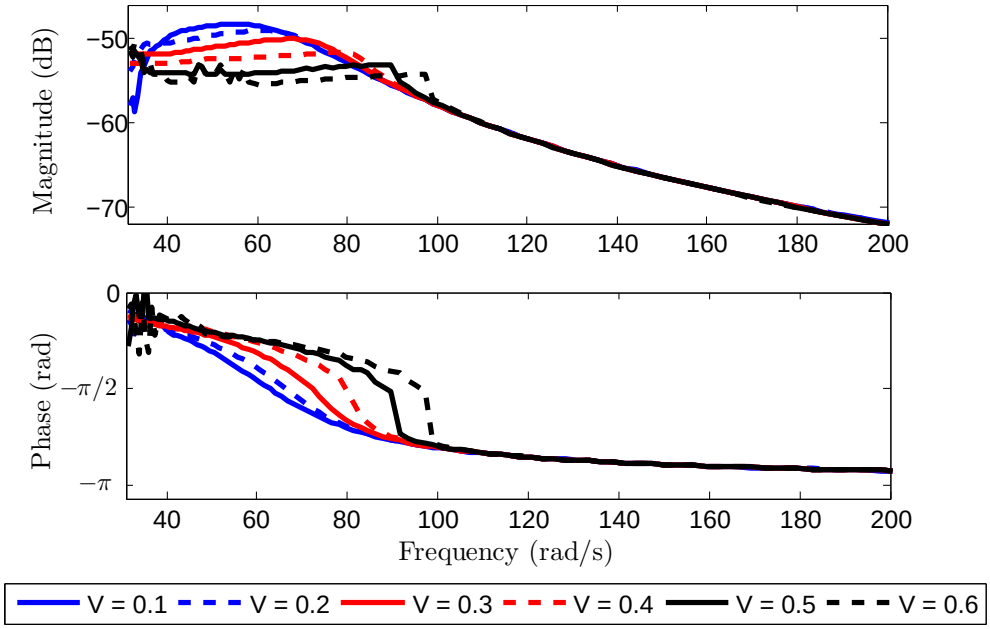

Figure 4.23: Displacement-voltage transfer functions of the Micromega IA-01 inertial actuator.

The displacement-voltage transfer functions of the DataPhysics IV40 inertial actuator, which are shown in Figure 4.24, confirm that the natural frequency of the actuator decreases with increasing excitation amplitude in a similar manner to a softening Duffing oscillator. Since the change in natural frequency is minor, it is apparent that the suspension nonlinearity is relatively weak, which indicates that the underlying linear dynamics of this actuator are dominant. The linearised natural frequency of the actuator (32.2 Hz) is almost identical to the peak force resonance frequency, due to the small inherent damping ratio.

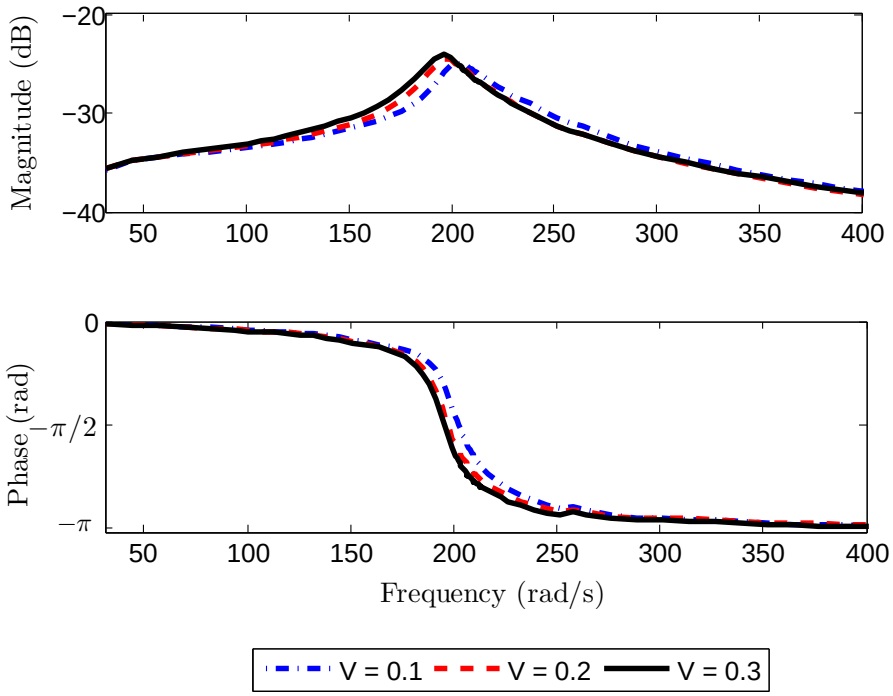

Figure 4.24: Displacement-voltage transfer functions of the DataPhysics IV40 inertial actuator.

Figure 4.25 shows the first-order displacement-voltage transfer functions of the Labworks FG-142 actuator. Here, it is apparent that the natural frequency of the actuator (about 22.3 Hz) is far lower than the peak force resonance frequency shown in Figure 4.22, which can be attributed to the large damping ratio. This has important implications for the presence of stroke saturation in this actuator, since the saturation threshold is determined by the proof-mass displacement rather than the inertial force.

By comparing Figures 4.22 and 4.25, it may be observed that the output force of the actuator is relatively small at the natural frequency. Therefore, the actuator may saturate for small force outputs when the excitation frequency is close to the natural frequency of the actuator. Conversely, the actuator may generate large force outputs without saturation occurring when the excitation frequency is close to or above the peak force resonance frequency. As a result, stroke saturation is less of a problem within the intended operating region, but care must be taken for excitation frequencies that are well below the peak force resonance frequency, as the actuator is most susceptible to stroke saturation in this frequency region.

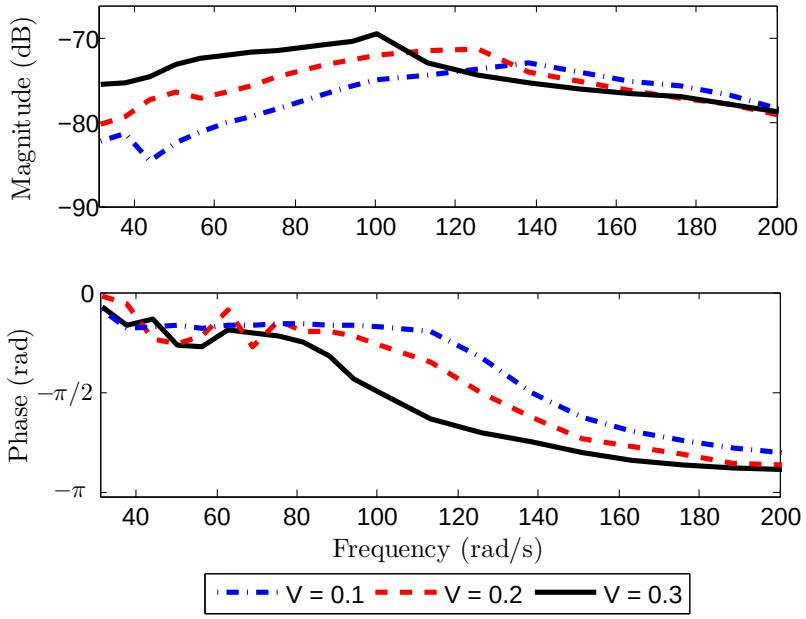

Figure 4.25: Displacement-voltage transfer functions of the Labworks FG-142 inertial actuator.

As the excitation amplitude increases, the natural frequency reduces and the magnitude of the peak resonance increases profoundly. This confirms that the actuator exhibits a strong softening stiffness nonlinearity, in addition to the stroke saturation phenomenon.

4.5 Discussion

Using the experimental results shown in the previous section, the dynamics of the three actuator types are now compared and discussed, focusing on the generalisation of the data to the majority of inertial actuators. The primary aim of the discussion is to expand upon the linear dynamics of the actuators, which are well-known from previous experimental analyses and manufacturer data, with the measured nonlinear actuator dynamics that are less well-considered, besides the effects of stroke saturation.

From the experimental data, it is apparent that each actuator under consideration can be described as a weakly nonlinear single-degree-of-freedom system within its intended operating region (frequencies beneath the first higher-order resonance frequency, no stroke saturation). Using this description, the following statements about the actuators used in the study can be made,

1. Each actuator behaves as an ideal force generator above the peak force resonance frequency [27], regardless of excitation amplitude. When the control bandwidth lies between the peak force resonance frequency and the first higher-order resonance, the actuator dynamics are optimal (linear, constant-gain, zero phase). This is the basis of modelling an inertial actuator as a linear single-degree-of-freedom system.
2. Each actuator exhibits a weak suspension stiffness nonlinearity that is particularly pronounced at or below the natural frequency. This observation suggests that all inertial actuators behaves as weakly nonlinear single-degree-of-freedom systems in their intended operating regions.
3. Each actuator has amplitude-dependent transfer functions, where the natural frequency is affected by the suspension nonlinearity. In most cases, the nonlinear effects are negligible above the peak force resonance frequency, and can therefore be ignored when assessing the actuator performance in its optimal frequency region. However, these nonlinearities often have a detrimental effect on the overall closed-loop stability, and the amplitude-dependent phase characteristics may cause phase compensation techniques to fail when high excitation amplitudes are considered.

Using these actuators as a representative sample, it is suggested that these statements can be generalised to the majority of inertial actuators, which may explain discrepancies in the predicted gain margin (estimated using linear control theory) and the actual gain margin observed in practice.

The primary benefits of the Micromega IA-01 inertial actuator are its low natural frequency and ability to be easily mounted horizontally to a supporting structure; however, the nonlinear dynamics of the actuator are detrimental to its performance. The nonlinear hardening suspension stiffness has the effect of introducing harmonic distortion in the force-time response signals, which increases the natural frequency of the actuator. This reduces the effective control bandwidth as the excitation amplitude increases. Furthermore, the hard end stops result in complex phenomena when stroke saturation occurs, including double-impacts, resonance effects, and a rich harmonic spectrum.

By analysing the results of the DataPhysics IV40 inertial actuator, it is evident that this actuator is particularly advantageous for control applications, due to a large force-to-voltage ratio and transduction coefficient, low inherent damping, a high degree of linearity, a softening stiffness nonlinearity, and the use of an external proof-mass. It is

difficult to observe the saturation characteristics of the actuator, since the saturation limit is determined by the matched amplifier. The only drawbacks are a relatively high natural frequency (which can be tuned), its relatively large weight, and its susceptibility to additional nonlinear phenomena, such as stiction, when mounted incorrectly.

The Labworks FG-142 inertial actuator features both the largest damping ratio and the strongest (softening) suspension nonlinearity, which results in a large difference between the natural frequency and the peak force resonance frequency. Therefore, the actuator is capable of delivering a relatively large force output with minimal risk of stroke saturation (since the nonlinear effects are concentrated around the natural frequency). One of the more remarkable characteristics of this actuator is the profound difference between the natural frequency and the peak force resonance frequency, which is a consequence of the large damping ratio and must be accounted for when assessing closed-loop stability. For large excitation amplitudes, the actuator exhibits stroke saturation phenomena in a similar manner to the Micromega IA-01 actuator (characteristic impulses), although the effect is less pronounced (harmonic spectrum is not as rich) due to the softer end stops.

4.6 Concluding remarks

In this study, the dynamics of three inertial actuators were examined for the purpose of observing nonlinear, amplitude-dependent effects in the force outputs, particularly with regards to saturation nonlinearities. This was achieved by measuring the force responses to a variety of monoharmonic excitation voltages and analysing the measurements in the time- and frequency-domains. Two of the actuators feature stroke saturation (Micromega IA-01 and Labworks FG-142), whereas the other one avoids stroke saturation through the use of an external proof-mass (DataPhysics IV40).

From the results, it is believed that most inertial actuators behave as weakly nonlinear single-degree-of-freedom systems within their intended operating regions, where the nonlinearities are negligible above the peak force resonance frequency and the actuator behaves as an ideal force generator. When the excitation amplitude exceeds the saturation threshold (stroke-saturated actuators), the actuator exhibits strongly nonlinear vibro-impact phenomena that results in the generation of large impulses in the force-time signals. The characteristics of stroke saturation appear to vary from actuator to actuator, depending on the inertia of the proof-mass and the rigidity of the end stops.

The primary limitation of the study is that the experimental data is mainly focused on the Micromega IA-01 inertial actuator, which is a key feature throughout this thesis. As a result, the data collected for the DataPhysics IV40 and Labworks FG-142 inertial actuators is relatively superficial, as a means of comparison with the Micromega IA-01 actuator. It is therefore recommended that a more extensive study of these two actuators is conducted for future work. Furthermore, the actuator responses to broadband excitation (random, swept sine, impulses etc.) are not considered in this study, and are worthy of further exploration.

Chapter 5

Identification and Modelling of Actuator Dynamics

5.1 Introduction

It was postulated in chapter 4 that the majority of inertial actuators behave as weakly nonlinear single-degree-of-freedom systems within their intended operating regions. For each case study, the effective control force that can be applied by these actuators is limited by saturation effects, either as a result of a finite stroke length or electronic clipping. In this chapter, the dynamics of the Micromega IA-01 inertial actuator are explored further, using identification techniques to devise a nonlinear single-degree-of-freedom model that is capable of accurately emulating these actuator dynamics. This requires the use of a variety of parameteric and non-parametric methods, such as inverse FRFs [125], peak resonance monitoring [126], and force-state mapping [109].

The first step is to specify the equations of motion of the actuator, according to the underlying linear dynamics, the suspension nonlinearities, and the saturation nonlinearities. By assuming that the nonlinearities are memoryless, with no hysteresis effects, the equations of motion of the actuator can be described using a discontinuous model,

$$g_a v(t) = \begin{cases} F_{lin}(\mathbf{x}) + F_{sus}(\mathbf{x}) + F_{sat,1}(\mathbf{x}) & y_p(t) > d_1 \\ F_{lin}(\mathbf{x}) + F_{sus}(\mathbf{x}) & d_2 \leq \ y_p(t) \leq d_1 \\ F_{lin}(\mathbf{x}) + F_{sus}(\mathbf{x}) + F_{sat,2}(\mathbf{x}) & y_p(t) < d_2 \end{cases} \tag{5.1}$$

where $F_{lin}(\mathbf{x})$ represents the underlying linear forces;

$F_{sus}(\mathbf{x})$ represents the nonlinear suspension forces;

d_1, d_2 represent the positive and negative stroke limits respectively;

$F_{sat,1}(\mathbf{x})$ and $F_{sat,2}(\mathbf{x})$ represent the saturation forces for positive and negative displacements respectively.

Since the actuator behaves as a single-degree-of-freedom system at low frequencies ($\omega < 1,000$ rad/s), $F_{lin}(\mathbf{x})$ is defined as,

$$F_{lin}(\mathbf{x}) = m_p\ddot{y}_p(t) + c_p\dot{y}_p(t) + k_{p,1}y_p(t) \tag{5.2}$$

such that $m_p, c_p, k_{p,1}$ are the parameters to be identified for $F_{lin}(\mathbf{x})$. The nonlinear force terms $F_{sus}(\mathbf{x})$, $F_{sat,1}(\mathbf{x})$, and $F_{sat,2}(\mathbf{x})$ are currently unknown, and their forms are estimated using intuition and the measurements made in chapter 4.

The presence of even-order harmonics in Figure 4.18, in conjunction with the rise in peak resonance frequency in Figure 4.20, suggest that the forces associated with the weak suspension nonlinearities can be modelled using low-order polynomial stiffness terms. Therefore, in Eq. 5.1, $F_{sus}(\mathbf{x})$ can be neglected when the voltage $v(t) = V\sin(\omega t)$ is relatively small ($V = 0.1$ Volts), such that the actuator behaviour can be approximated by the underlying linear dynamics. This enables the linear parameters of $F_{lin}(\mathbf{x})$ to be identified independently of $F_{sus}(\mathbf{x})$, $F_{sat,1}(\mathbf{x})$, and $F_{sat,2}(\mathbf{x})$.

The next step is to consider the actuator dynamics at higher excitation ampitudes ($0.1 < V < 0.35$ Volts), where the effects of the nonlinear suspension forces $F_{sus}(\mathbf{x})$ become more observable through harmonic distortion, yet the saturation thresholds d_1, d_2 are not exceeded. Since $F_{lin}(\mathbf{x})$ is known, the low-order polynomial terms of $F_{sus}(\mathbf{x})$ can be identified using peak resonance monitoring (which assesses the change in the peak resonance frequency as the excitation amplitude rises) and force-state mapping (which is used to illustrate the restoring force surface from the measured data). These weakly nonlinear forces, in conjunction with the underlying linear forces, comprise the actuator dynamics within the intended operating region.

At the highest excitation amplitudes ($V \geq 0.35$ Volts), the proof mass collides with the end stops, and the actuator dynamics become strongly nonlinear, resulting in large forces for $F_{sat,1}(\mathbf{x})$ and $F_{sat,2}(\mathbf{x})$ that change rapidly with time. Since stroke saturation is an impact phenomenon, the contact mechanics are typically described using a set

of impact parameters, such as the contact time, the coefficient of restitution, and the impulse magnitude [127]. These parameters dictate how the energy of the proof-mass is transferred and dissipated throughout the collision, and it is necessary to relate these terms to equivalent structural parameters before parametric identification can take place. This is achieved using a nonlinear viscoelastic model to describe the impact dynamics.

Using the identified parameters, the nonlinear actuator model is devised in Simulink for the purpose of simulating the actuator responses under various conditions. A comparison of the simulated results with the experimental measurements is then undertaken in the time- and frequency-domains, which confirms that the nonlinear model is capable of emulating the actuator dynamics with a high degree of accuracy.

5.2 Underlying linear dynamics

In this section, the parameters of the underlying linear forces $F_{lin}(\mathbf{x})$ are identified using least-squares optimisation for the inverse of the measured first-order displacement-voltage FRF, which is obtained in chapter 4 (see Figure 4.23). This is because the inverse FRF is generally much easier to analyse than the FRF itself [12], particularly for single-degree-of-freedom systems.

Preumont's derivation of the underlying linear force-voltage FRF of the actuator [19] is given in Eq. 4.11. By applying the displacement-force relation $Y(j\omega) = -m_p\omega^2 F(j\omega)$, the displacement-voltage FRF, denoted by $H_p(\omega)$, is expressed as,

$$H_p(j\omega) = \frac{Y(j\omega)}{V(j\omega)} = \frac{g_a}{k_{p,1} - m_p\omega^2 + jc_p\omega} \tag{5.3}$$

The inverse FRF of $H_p(j\omega)$, denoted by $R(j\omega)$, can therefore be written as,

$$R(j\omega) = \frac{1}{H_p(j\omega)} = \frac{k_{p,1} - m_p\omega^2}{g_a} + j\frac{c_p\omega}{g_a} \tag{5.4}$$

By considering the real and imaginary parts of Eq. 5.4 separately, the following equations appear,

$$\Re e\Big\{R(j\omega)\Big\} = \frac{k_{p,1} - m_p\omega^2}{g_a}, \qquad \Im m\Big\{R(j\omega)\Big\} = \frac{c_p\omega}{g_a} \tag{5.5}$$

Therefore, plotting $\Re e\Big\{R(j\omega)\Big\}$ against ω^2 should result in a straight line, with a gradient m_p/g_a and intercept $k_{p,1}/g_a$. Similarly, plotting $\Im m\Big\{R(j\omega)\Big\}$ against ω should yield a straight line with gradient c_p/g_a. Since the structural parameters $m_p, c_p, k_{p,1}$ are independent and linear, these parameters can be identified with respect to g_a by applying linear least-squares optimisation to the underlying linear inverse displacement-voltage FRF. In this case, an approximation of the underlying linear displacement-voltage FRF has been measured at $V = 0.1$ Volts in chapter 4, such that the nonlinear dynamics are negligible. By taking the inverse of this measured FRF and separating the real and imaginary components, the structural parameters are identified using the Moore-Penrose right pseudoinverse,

$$\mathbf{P_1} = g_a\mathbf{W^T}(\mathbf{WW^T})^{-\mathbf{1}}\mathbf{Re(R)}, \quad \mathbf{P_2} = g_a\mathbf{Z^T}(\mathbf{ZZ^T})^{-\mathbf{1}}\mathbf{Im(R)} \tag{5.6}$$

where $\mathbf{P_1}, \mathbf{P_2}$ are the structural parameters to be identified and $\mathbf{R}$ represents the measured inverse displacement-voltage FRF data,

$$\mathbf{P_1} = \begin{pmatrix} -m_p \\ k_{p,1} \end{pmatrix}, \mathbf{P_2} = c_p, \mathbf{W} = \begin{pmatrix} \omega_1^2 & 1 \\ \vdots & \vdots \\ \omega_N^2 & 1 \end{pmatrix}, \mathbf{Z} = \begin{pmatrix} \omega_1 \\ \vdots \\ \omega_N \end{pmatrix}, \mathbf{R} = \begin{pmatrix} R(j\omega_1) \\ \vdots \\ R(j\omega_N) \end{pmatrix} \tag{5.7}$$

N being the number of data points. Applying Eq. 5.6 yields the following values for $\mathbf{P_1}, \mathbf{P_2}$,

$$\mathbf{P_1} = \begin{pmatrix} -0.1066 \\ 401.6733 \end{pmatrix} g_a, \qquad \mathbf{P_2} = 4.346 g_a \tag{5.8}$$

The actuator gain g_a can be ascertained from the high-frequency asymptote of the measured force-voltage FRFs, which are shown in Figure 4.20 in chapter 4. Using these measured FRFs, the actuator gain is identified as $g_a \approx 0.3$. Therefore, the structural parameters are identified by applying this term to Eq. 5.8,

$$m_p = 0.032 \text{ kg}, \quad c_p = 1.3 \text{ Ns/m}, \quad k_{p,1} = 120.56 \text{ N/m} \tag{5.9}$$

where the identified value for m_p complies with manufacturer data [128]. A linear model of the inverse FRF is then obtained by substituting these parameters into Eq. 5.4.

A comparison between the optimised linear least-square-error (LSE) model of the inverse FRF and the measured experimental data in Eq. 5.7 is shown in Figures 5.1 and 5.2, using the real and imaginary components respectively. Furthermore, additional experimental data representing the inverse FRF, measured at the higher excitation amplitudes ($V = 0.3$ Volts and $V = 0.5$ Volts), is also included for the purpose of illustrating the distortion effects caused by the actuator nonlinearities.

In Figure 5.1, it is apparent that the optimised LSE model agrees well with the experimental data taken at $V = 0.1$ Volts. At the higher excitation voltages, the straight line becomes distorted near the peak resonance frequency of the actuator, due to the actuator nonlinearities. The distortion characteristics are similar to those of a hardening SDOF system, which indicates that the suspension nonlinearities and stroke saturation both increase the effective stiffness of the actuator.

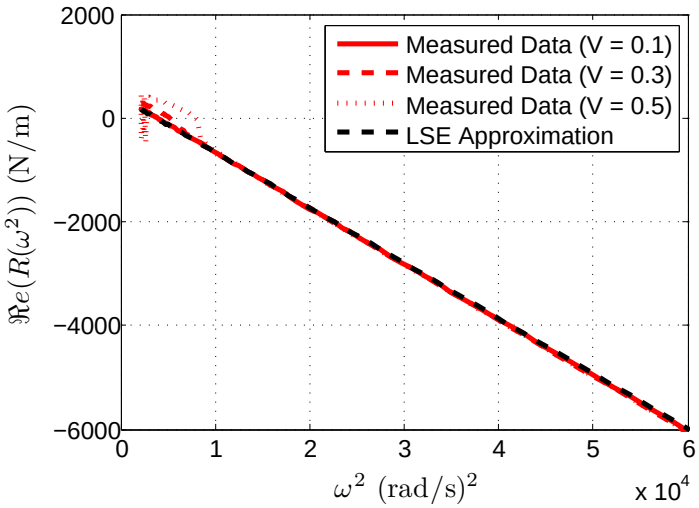

Figure 5.1: Comparison of real part of measured experimental data $R(j\omega)$ with the optimised LSE model given by the $\mathbf{P_1}$ parameters.

By examining Figure 5.2, a number of observations can be made about the apparent damping of the actuator. Firstly, it is apparent that the imaginary part of $R(j\omega)$ is not linear with ω, but instead deviates from the optimised LSE model when $\omega > 100$ rad/s. This phenomenon is amplitude-independent and is attributed to the magnetic inductance of the actuator through the term $G_e(s)$ in Eq. 4.5, which reduces the damping at higher frequencies by short-circuiting the effective damping provided by the counter-electromotive force. Since this phenomenon is only significant above the first natural

frequency of the actuator, where the actuator dynamics are governed by the mass law, the damping reduction is therefore negligible.

Secondly, there is little difference between the experimental data measured at $V = 0.1$ Volts and $V = 0.3$ Volts. Since the effects of the suspension nonlinearities can be observed at this latter excitation amplitude, this indicates that $F_{sus}(\mathbf{x})$ primarily affects the apparent stiffness, with negligible effect on the apparent damping.

Thirdly, nonlinear distortion occurs around the actuator peak resonance frequency at the highest excitation amplitude $V = 0.5$ Volts; this confirms that stroke saturation has the effect of increasing the apparent damping of the actuator, such that $F_{sat,1}(\mathbf{x})$, and $F_{sat,2}(\mathbf{x})$ have a combined effect on the total stiffness and damping.

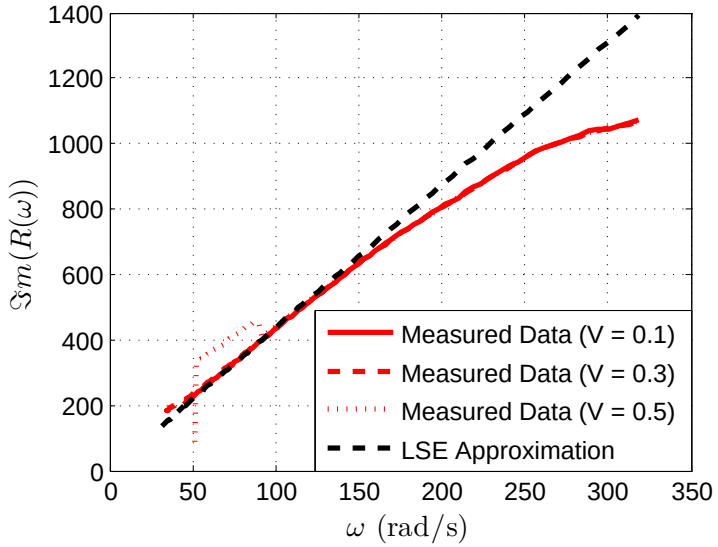

Figure 5.2: Comparison of imaginary part of measured experimental data $R(j\omega)$ with the optimised LSE model given by the $\mathbf{P_2}$ parameters.

In order to confirm that the structural parameters give an accurate representation of the underlying linear actuator dynamics, a model of the linear actuator force-voltage FRF is obtained by substituting the parameters in Eq. 5.9 into Eq. 4.11. A comparison of this model against the measured force-voltage FRF is shown in Figure 5.3. Here, it is apparent that the model agrees well with the measured data, thereby confirming that the linear structural parameters are correctly identified.

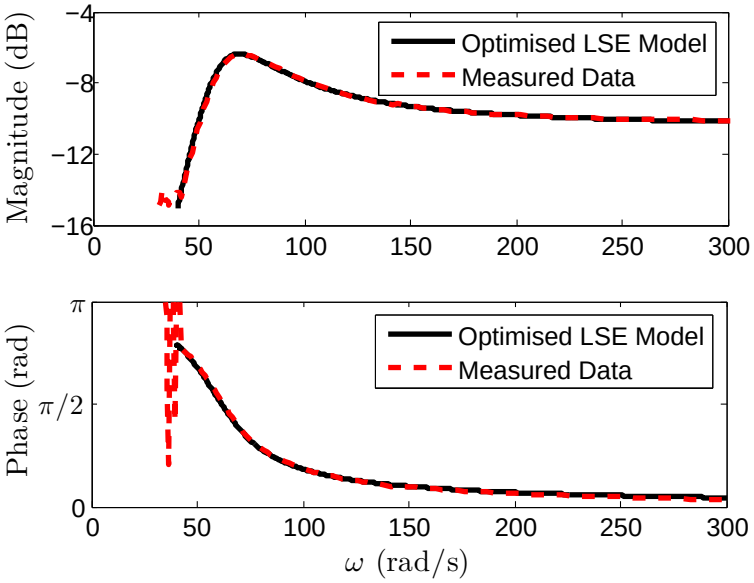

Figure 5.3: Bode plot comparison of the modelled and measured force-voltage FRFs.

5.3 Nonlinear suspension dynamics

Now that the underlying linear structural parameters are known, it is necessary to obtain the nonlinear structural parameters of the actuator, starting with the suspension nonlinearities. The excitation amplitude range of interest is increased to ensure that the nonlinear dynamics are observable in the measured data. In this section, we use two methods to identify the parameters associated with the suspension nonlinearities; the first method involves minimising the error between the predicted and measured peak resonance frequencies of the actuator as the excitation amplitude increases, and the second method utilises the force-state mapping approach developed by Masri and Caughey [109] to illustrate the restoring force as a function of displacement and velocity. In the latter case, curve-fitting techniques are applied to estimate the structural parameters from the restoring force curve.

First, we need to establish a function to represent $F_{sus}(\mathbf{x})$. It was shown in the previous section that the suspension nonlinearities increase the effective stiffness of the actuator at higher excitation amplitudes, with little effect on the damping. Thus, $F_{sus}(\mathbf{x})$ is a purely nonlinear function of $y_p(t)$. Furthermore, the presence of even-order harmonics in the force-time responses shown in chapter 4, in conjunction with the hardening effects on the peak resonance frequency, suggest that the suspension nonlinearities can be modelled

using a third-order polynomial of the form,

$$F_{sus}(\mathbf{x}) = k_{p,2}y_p^2(t) + k_{p,3}y_p^3(t) \tag{5.10}$$

In this expression, $k_{p,2}$ represents quadratic stiffness, which accounts for the even-order harmonics, and $k_{p,3}$ represents cubic stiffness, which accounts for the hardening effects. This indicates that the actuator behaves as an asymmetric Duffing oscillator within its intended operating region. It is well-known that even-order nonlinearities, such as quadratic nonlinearities, will introduce asymmetry into the system, thereby causing a DC offset in the displacement-time signals. The consequences of this DC offset are discussed in greater detail in section 5.4.

5.3.1 Peak resonance monitoring

Using the expression shown in Eq. 5.10, the aim is to identify the structural parameters $k_{p,2}, k_{p,3}$ associated with the suspension nonlinearities. In this case, the nonlinear parameters are determined using frequency monitoring, where the peak resonance frequency of the nonlinear system is analysed as the excitation amplitude increases, in order to assess how the effective stiffness of the system is changing. This method is popular in the aircraft industy, where normal mode testing is conducted on individual aircraft components for the purpose of detecting potential weaknesses [126]; the peak resonance frequencies are monitored as the excitation amplitude is increased, and the changes are attributed to particular nonlinearities, which may indicate structural damage.

Using the measured displacement-voltage FRFs, we can observe how the peak resonance frequency of the actuator increases with excitation amplitude from Figure 4.20 and Figure 4.23. This variation with excitation amplitude is governed by the nonlinear suspension forces $F_{sus}(\mathbf{x})$ when the proof-mass remains within the stroke limits. Using the dual-input describing function analysis shown in section 2.3.3, the first-order displacement-voltage transfer function of the actuator may be written as follows,

$$H_p(j\omega, Y_0, Y_1) = \frac{g_a}{k_{p,1} - m_p\omega^2 + jc_p\omega + N(Y_0, Y_1)} \tag{5.11}$$

where $N(Y_0, Y_1) = 2k_{p,2}Y_0 + 3k_{p,3}Y_0^2 + 0.75k_{p,3}Y_1^2$, is the describing function used to model the effects of the suspension nonlinearities. As $N(Y_0, Y_1)$ tends towards zero, $H_p(j\omega, Y_0, Y_1)$ tends towards the underlying linear transfer function given by Eq. 5.3.

By applying the solution $Y_0 \approx f[k_{p,1}, k_{p,2}, k_{p,3}, Y_1]$ obtained in section 2.3.3, the peak resonance frequency ω_p of the actuator can be determined using the describing function term,

$$\omega_p = \sqrt{\frac{k_{p,1}(1 - \frac{c_p^2}{2m_p k_{p,1}}) + 2k_{p,2} f[k_{p,1}, k_{p,2}, k_{p,3}, Y_1] + 3k_{p,3} f^2[k_{p,1}, k_{p,2}, k_{p,3}, Y_1] + 0.75k_{p,3} Y_1^2}{m_p}} \tag{5.12}$$

Since ω_p and Y_1 can be obtained from the measured data, the only unknowns in Eq. 5.12 are the nonlinear structural parameters $k_{p,2}$ and $k_{p,3}$. Since ω_p is a nonlinear function of $k_{p,2}, k_{p,3}$, it is necessary to utilise a nonlinear least-squares optimisation method to obtain these structural parameters. By rearranging Eq. 5.12, the error $\mathbf{E}$ between the estimated and measured apparent stiffness of the actuator is given by,

$$\mathbf{E} = \mathbf{A} - \mathbf{B}\mathbf{P_3} - z \tag{5.13}$$

where $\mathbf{A}$ utilises the measured ω_p values, $\mathbf{B}$ utilises the measured Y_1 values, and z is a constant,

$$\mathbf{A} = \begin{pmatrix} m_p \omega_{p,1}^2 \\ \vdots \\ m_p \omega_{p,M}^2 \end{pmatrix}, \mathbf{B} = \begin{pmatrix} 2f[k_{p,1}, k_{p,2}, k_{p,3}, Y_{1,1}] & 3f^2[k_{p,1}, k_{p,2}, k_{p,3}, Y_{1,1}] + 0.75k_{p,3} Y_{1,1}^2 \\ \vdots & \vdots \\ 2f[k_{p,1}, k_{p,2}, k_{p,3}, Y_{1,M}] & 3f^2[k_{p,1}, k_{p,2}, k_{p,3}, Y_{1,M}] + 0.75k_{p,3} Y_{1,M}^2 \end{pmatrix}, \tag{5.14}$$

$$\mathbf{P_3} = \begin{pmatrix} k_{p,2} \\ k_{p,3} \end{pmatrix}, z = \frac{2k_1 m_p - c_p^2}{2m_p}$$

M being the number of excitation amplitudes under consideration. Here, the excitation amplitudes considered range from $V = 0.1$ Volts to $V = 0.3$ Volts, increasing in increments of 0.05 Volts (see Table 4.1), such that $M = 5$. The cost function $\mathbf{J}(k_{p,2}, k_{p,3})$ to minimise is thus,

$$\mathbf{J}(k_{p,2}, k_{p,3}) = \mathbf{E^T E} \tag{5.15}$$

Using a suitable initial guess, the cost function is minimised by applying MATLAB's fmincon function, and the identified structural parameters are given as follows,

$$\mathbf{P_3} = \begin{pmatrix} k_{p,2} \\ k_{p,3} \end{pmatrix} = \begin{pmatrix} -9.86 \text{ x } 10^4 \\ 1.112 \text{ x } 10^8 \end{pmatrix} \tag{5.16}$$

such that the quadratic stiffness is negative and the cubic stiffness is positive and hardening. As a means of confirmation, the minimal region in the cost function is shown in Figure 5.4, where $\mathbf{J}(k_{p,2}, k_{p,3})$ is illustrated against $k_{p,2}$ and $k_{p,3}$.

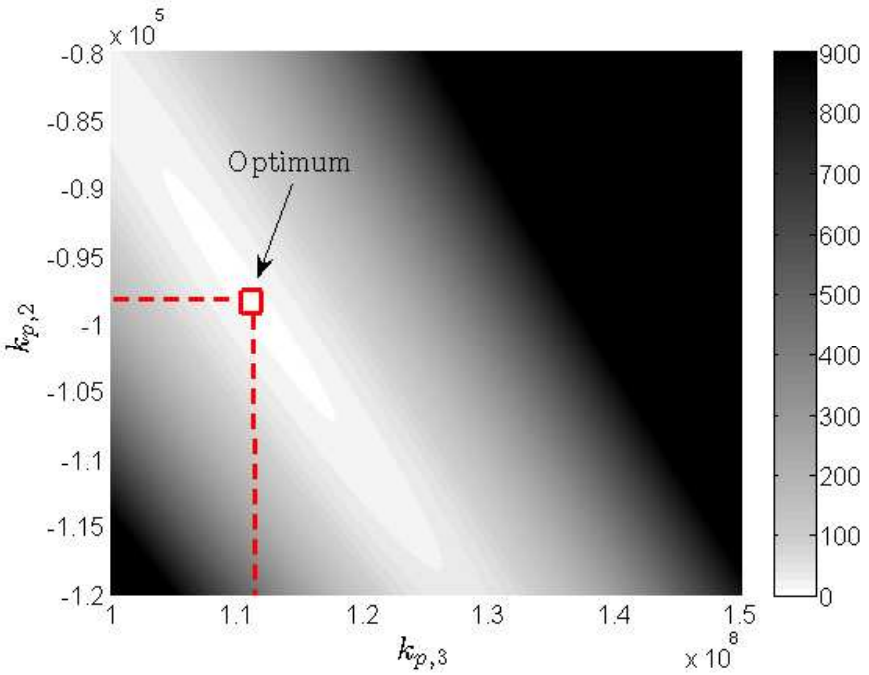

Figure 5.4: Variation of $\mathbf{J}(k_{p,2}, k_{p,3})$ against $k_{p,2}$ and $k_{p,3}$. The white area indicates the minimal region in the cost function.

It is worth noting that the minimum value of the cost function is $\mathbf{J}(k_{p,2}, k_{p,3}) \approx 10$ $(\text{rad/s})^2$. This corresponds to a total error of approximately 0.5 Hz, which is remarkably small, given the potential for discrepancies to occur from the finite frequency resolution in the measurements, the low-order polynomial approximations of the actuator response, and the estimations of the DC component Y_0.

Although the frequency monitoring approach provides an excellent means of estimating the nonlinear suspension parameters, it is impractical to apply this method to determine the stroke saturation dynamics, since it becomes very difficult to express the variation in the peak resonance frequency using analytical means. This difficulty can be overcome using the force-state mapping approach, which is explored in the next section.

5.3.2 Force-state mapping

The Masri-Caughey force-state mapping approach is a non-parametric method that utilises the measured data to illustrate the restoring force of the nonlinear system against the phase plane, thereby resulting in a three-dimensional restoring force surface. In order to implement this method, it is assumed that the actuator dynamics are memoryless and do not exhibit hysteresis, such that the behaviour conforms to the following generalised equation of motion,

$$m_p\ddot{y}_p(t) + f(\dot{y}_p(t), y_p(t)) = g_a v(t) \tag{5.17}$$

where $f(\dot{y}_p(t), y_p(t))$ is the *total* restoring force to the inertial force $m_p\ddot{y}_p(t)$, accounting for linear and nonlinear dynamics. Rearranging Eq. 5.17 yields,

$$f(\dot{y}_p(t), y_p(t)) = gv(t) - m_p\ddot{y}_p(t) \tag{5.18}$$

such that the restoring force surface is obtained from $m_p, \ddot{y}_p(t), g_a$ and $v(t)$, which are known from experimental data. The acceleration-time signals are integrated to yield the phase-plane variables $\dot{y}_p(t)$ and $y_p(t)$, and so the three-dimensional restoring force surface can be shown as a function of these states.

Since the excitation signal $v(t)$ is sinusoidal, the measured data is scattered in a circular pattern around the phase plane when a single excitation frequency or amplitude is used, which results in an unevenly distributed restoring force surface. To overcome this problem, the data is taken from the entire range of excitation frequencies and amplitudes used to measure the actuator dynamics, such that the restoring force surface covers a large number of circular patterns, and is therefore more evenly distributed. However, this approach involves the manipulation of a large amount of measured data, and is impractical if the entire time series is considered. Fortunately, we can take advantage of the repetition in the measured steady-state responses to shorten the duration of the time histories used for the restoring force surface, thereby reducing the amount of data. In this case, a one-second segment of measured data (i.e. 51,200 measurement points) was used for the entire range of excitation amplitudes and frequencies to obtain the restoring force surface. To ensure that the transient response of the actuator had decayed sufficiently, this one-second segment was taken five seconds after the start of the excitation signal. The resulting restoring force surface can be observed in Figure 5.5.

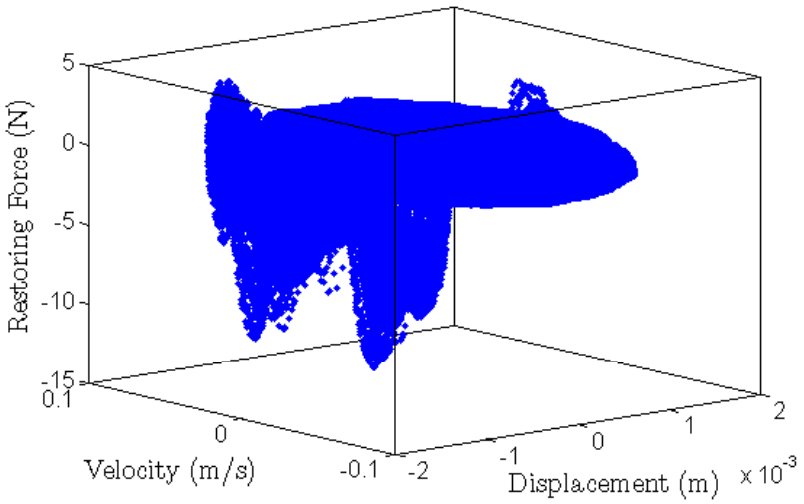

Figure 5.5: Restoring force surface of the inertial actuator, obtained using the full range of excitation frequencies and amplitudes used in chapter 4.

It is apparent in Figure 5.5 that the magnitude of the restoring force increases rapidly once the proof-mass displacement is sufficiently large in the negative direction, with a similar, less noticeable effect in the positive direction. These regions indicate the presence of stroke saturation, thereby illustrating that the forces associated with stroke saturation are far greater than the restoring forces of the actuator when the proof-mass is within its intended operating region.

In order to illustrate the relationship between the restoring force and proof-mass displacement in a clearer manner, the three-dimensional restoring force surface is reduced to two dimensions by defining a small velocity region close to the origin and removing all data that is outside this quasi-two-dimensional region. In other words, the data must satisfy the constraint $|\dot{y}_p(t)| < \epsilon$ for the two-dimensional representation of the restoring force against proof-mass displacement, as shown in Figure 5.6. Here, $\epsilon = 1$ x 10^{-5}. This technique is known as sectioning [12].

By ignoring the rapid increases in the restoring force at the displacement extremes, it is apparent in Figure 5.6 that the restoring force curve is similar to a polynomial function beneath the saturation threshold, thereby confirming that the low-order polynomial stiffness assumption is true. The nonlinear suspension parameters are then identified by applying a polynomial curve-fit model to the restoring force curve using MATLAB's cftool toolbox. This results in the following optimised parameters,

$$k_{p,2} = -8.2 \times 10^4 \text{ N/m}^2, \qquad k_{p,3} = 1.27 \times 10^8 \text{ N/m}^3 \tag{5.19}$$

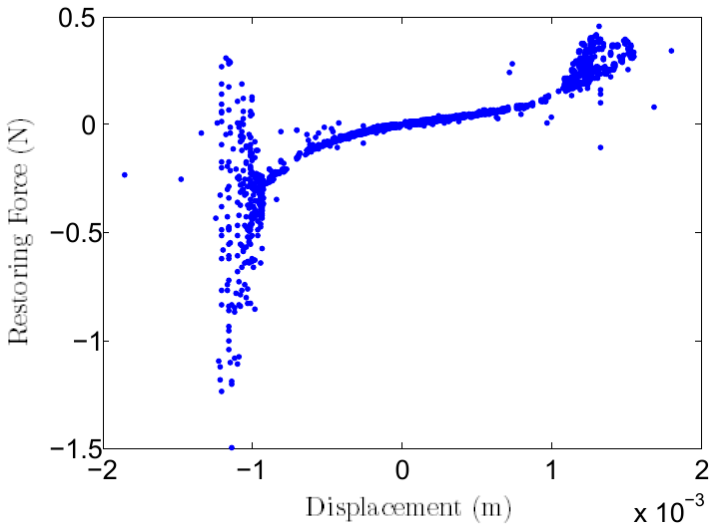

Figure 5.6: Restoring force of the inertial actuator against proof-mass displacement.

These structural parameters are remarkably consistent with those obtained with the frequency monitoring approach, as shown in Eq. 5.16, with the same signs and orders of magnitude. To compare the accuracy of these parameters, two polynomial models are obtained using both sets of parameters $k_{p,1}, k_{p,2}, k_{p,3}$, and are illustrated in Figure 5.7 alongside the restoring force curve. Here, both polynomial models are able to emulate the restoring force curve with a high degree of accuracy, yet the polynomial model obtained using the frequency monitoring approach gives a slightly better fit, and yields a more accurate model of the actuator. Therefore, the identified parameters shown in Eq. 5.16 are used to represent the nonlinear suspension stiffness.

Similarly, the relationship between the restoring force and the velocity of the proof-mass is obtained by applying the constraint $|y_p(t)| < \epsilon$, where $\epsilon = 1 \text{ x } 10^{-8}$, and removing all data outside this displacement region. The restoring force is shown against velocity in Figure 5.8, where it is apparent that the variation in the restoring force can be represented using a linear model. Using the linear damping parameter c_p as the proportionality constant in the model yields good agreement with the measured data. This confirms that the suspension nonlinearities primarily affect the apparent stiffness of the actuator without affecting the apparent damping.

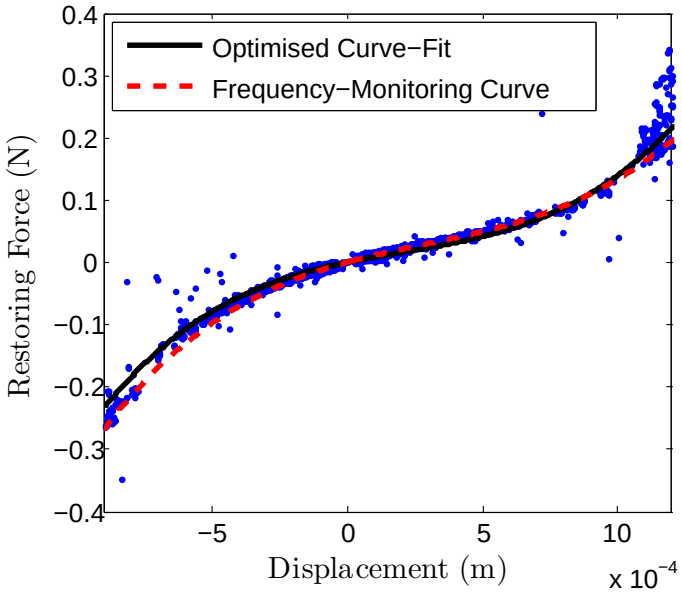

Figure 5.7: Restoring force of the inertial actuator against displacement amplitude (zoomed-in).

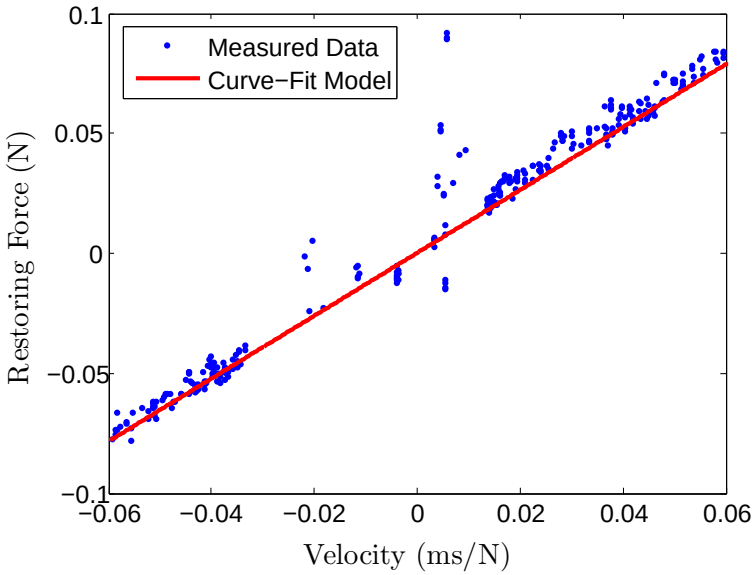

Figure 5.8: Restoring force of the inertial actuator against velocity.

5.3.3 Comparisons

By using the optimised structural parameters obtained in the previous section, the actuator model was constructed in Simulink for the purpose of simulating the force-time histories of the actuator. Several simulated force-time histories are compared with the equivalent measured signals in Figure 5.9, using Figures 4.5 and 4.6 in chapter 4 as the basis of comparison. In this figure, the lower excitation frequency $\omega = 16\pi$ rad/s is close to the peak resonance of the actuator, thereby resulting in significant harmonic distortion in the measured force-time histories. The simulations were conducted over a period of ten seconds using the fixed-step ode3 solver and a sample rate of 51.2 kHz.

It is evident from Figure 5.9 that there is excellent agreement between the simulated and measured force-time histories, thereby demonstrating that the actuator model is capable of emulating the characteristics of the harmonic distortion seen in Figure 5.9 by using the nonlinear suspension parameters. This confirms that the actuator behaves fundamentally as an asymmetrical Duffing oscillator within its intended operating region beneath the saturation threshold.

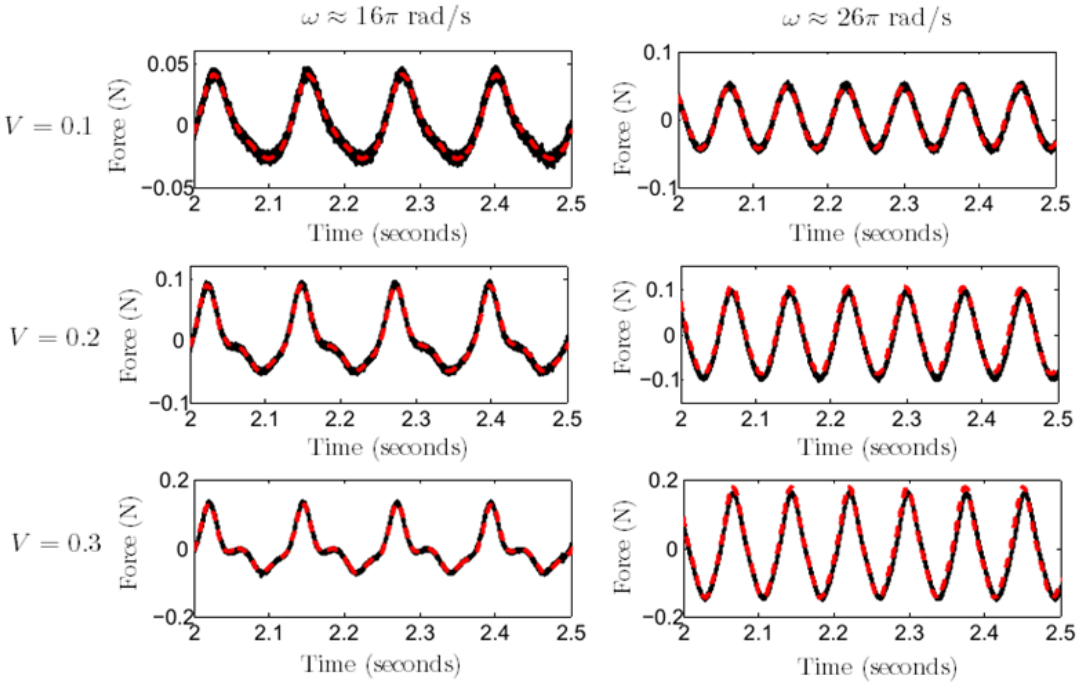

Figure 5.9: Comparison of the measured data in Figures 4.5 and 4.6 (solid black line) with equivalent simulated data (dashed red line), using the nonlinear actuator model.

5.4 Stroke saturation dynamics

By utilising the nonlinear actuator model identified in the previous section, the final step to is to determine the saturation forces $F_{sat,1}(\mathbf{x})$, $F_{sat,2}(\mathbf{x})$ and the stroke limits d_1, d_2, such that the model can account for the effects of stroke saturation. This is achieved by considering the impact parameters, such as the contact time, coefficient of restitution, and the peak magnitude, that can be obtained from the measured data. The primary difficulty with using this approach is establishing the relationship between the impact parameters and the equivalent structural parameters, which is not trivial unless the saturation model is very simple. Furthermore, the presence of multi-valued restoring force values at the displacement extremes in Figure 5.6 suggests that the actuator undergoes hysteresis during stroke saturation; it is believed that this can be attributed to a small increase in the stroke length during the first collision, as the momentum of the proof-mass is transferred to the end stop, resulting in a slight movement in the position of the end stop before it returns to its origin. Therefore, modelling the dynamics associated with stroke saturation is a more involved process than in the previous sections, with many assumptions, approximations, and compromises.

5.4.1 Saturation modelling

When modelling impact dynamics, it is typically assumed that the collisions are viscoelastic, where energy is transferred through elastic deformation and dissipated as sound, heat *etc.* through viscous deformation [129, 130]. Furthermore, it is also assumed that the end stop simply deforms and coalesces with the proof-mass during the collision. Provided that these assumptions hold, the impact dynamics may be described using a Kelvin-Voigt model [131, 132], where the elastic energy transfer is modelled using a spring and the viscous energy dissipation is modelled using a damper. In this manner, the additional spring rapidly increases the effective stiffness of the system once the stroke limit is reached, in order to prevent further extension of the proof-mass, and the damper dissipates energy according the the velocity of the proof-mass. This model is relatively simple, and is commonly used to represent impact between metallic surfaces or rigid bodies [133]. By assuming that these processes are independent of each other, the form of $F_{sat,1}(\mathbf{x})$, $F_{sat,2}(\mathbf{x})$ can be expressed as follows,

$$\begin{aligned} F_{sat,1}(\mathbf{x}) &= f[y_p(t) - d_1, k_{sat}](y_p(t) - d_1) + g[y_p(t) - d_1, c_{sat}]\dot{y}_p(t) \\ F_{sat,2}(\mathbf{x}) &= f[y_p(t) - d_2, k_{sat}](y_p(t) - d_2) + g[y_p(t) - d_2, c_{sat}]\dot{y}_p(t) \end{aligned} \tag{5.20}$$

where $f[y_p(t) - d_1, k_{sat}]$, $f[y_p(t) - d_2, k_{sat}]$ and $g[y_p(t) - d_1, c_{sat}]$, $g[y_p(t) - d_2, c_{sat}]$ are the equivalent stiffness and damping functions associated with the impacts respectively. An illustration of the Kelvin-Voigt model is shown in Figure 5.10, using the stiffness $k_0 = 0$ N/m and damping $c_0 = 0$ Ns/m to indicate that k_{sat} and c_{sat} are only applicable when the stroke limit is exceeded.

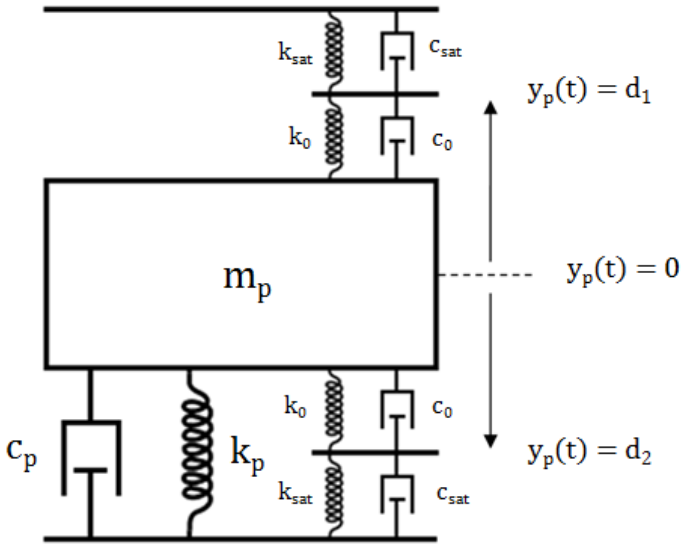

Figure 5.10: Mass-spring-damper model of the inertial actuator, with stiffness k_p and damping c_p, using a Kelvin-Voigt contact model [131].

The form of stiffness function $f[y_p(t) - d_{1,2}, k_{sat}]$ for stroke saturation has been of particular interest to researchers, where the types of functions considered include linear piecewise [134], high-order continuous polynomial [22], and hard clipping [31]. All of these functions are capable of emulating the general effects of stroke saturation by limiting the proof-mass displacement, resulting in the characteristic impulses in the force-time signals. However, by analysing the force-time signals shown in Figure 4.8, it is apparent that the stiffness function should be discontinuous, since a continuous model is not capable of sufficiently emulating the abruptness of the onset of stroke saturation. Furthermore, the velocity-time signals in Figure 4.9 indicate that a hard clipping model is a relatively simplistic approach

that does not truly represent a complex impact phenomenon such as stroke saturation. This confirms that a piecewise model, which does not exhibit these limitations, is a more suitable method for emulating the dynamics of stroke saturation, since this approach offers a means of describing the relationship between the impact parameters and the equivalent structural parameters.

Nagurka and Huang [75] presented a method for obtaining the equivalent structural parameters from the impact parameters using a simple piecewise linear mass-spring-damper model of a bouncing ball. Here, it was found that the piecewise linear functions yield a constant contact time $\Delta\mathrm{T}$ and coefficient of restitution ε, where the piecewise stiffness term k_d is inversely proportional to the squared contact time and the piecewise damping term c_d is proportional to the natural logarithm of the coefficient of restitution. The equations for these terms can be stated as,

$$k_d \approx m_d \left(\frac{\pi}{\Delta\mathrm{T}} \right)^2 \tag{5.21}$$

$$c_d = -\frac{2m_d}{\Delta\mathrm{T}} \ln(\varepsilon) \tag{5.22}$$

where m_d is defined as the combined mass of the proof mass and the end stops, assuming they coalesce during stroke saturation. This term can be simplified to $m_d \approx m_p$ if the mass of the end-stop is negligible in comparison to the proof mass.

First, we consider the optimisation of the piecewise stiffness function. By applying non-adhesive contact mechanical theory [130], a linear piecewise stiffness model is only valid if the normal restoring force applied by the end stop is proportional to the indentation depth $(y_p(t) - d_{1,2})$ of the proof-mass, which requires a constant conforming contact area between the colliding objects. Therefore, the function $f[y_p(t) - d_{1,2}, k_{sat}]$ depends on the geometry of the proof-mass and the end stop, and a nonlinear piecewise model becomes necessary if the contact area is non-conforming or significantly increases with the indentation depth. This may be assessed by examining the contact time of the measured force-time signals against the excitation amplitude and frequency; here, significant variations in the contact time indicate that the contact area is non-conforming, which necessitates the use of a nonlinear piecewise stiffness model. In this case, the relationship between the impact parameters and structural parameters is not obvious, and Eq. 5.21 serves as an approximation of k_d for small indentation depths.

An additional factor to consider is that the stiffness parameter k_d affects the magnitude of the impulses, F_{im} as well as the contact time. Assuming perfectly elastic collisions, it can be shown that k_p has inverse effects on each parameter; increasing k_p reduces ΔT, yet increases F_{im}, since the same amount of energy is transferred in a shorter period of time. This phenomenon can also be observed for viscoelastic collisions, where some of the collision energy is dissipated. It is therefore necessary to consider both of these impact parameters when optimising the stiffness function.

Next, we examine the linear piecewise damping term c_d in relation to the impact parameters. Eq. 5.22 highlights that including a non-zero c_d has the effect of reducing the contact time ΔT and the coefficient of restitution ε, which is unity when $c_d = 0$ and tends to zero as c_d tends to infinity. Additionally, the damping term also reduces the magnitude of the impulses, F_{im}, since less energy is transferred elastically as a result of dissipation. In theory, the damping term may be ascertained from the measured coefficient of restitution, which is a ratio of the relative separation velocity $\dot{y}_{sep}$ to the relative approach velocity $\dot{y}_{app}$ of the proof-mass and end stop,

$$\varepsilon = \frac{\dot{y}_{sep}}{\dot{y}_{app}} = -\frac{\dot{y}_{p,sep} + \dot{y}_{d,sep}}{\dot{y}_{p,app} - \dot{y}_{d,app}} \tag{5.23}$$

where $\dot{y}_{p,sep}, \dot{y}_{p,app}$ are the separation and approach velocities of the proof-mass and $\dot{y}_{d,sep}, \dot{y}_{d,app}$ are the separation and approach velocities of the end stop respectively. Since the proof-mass and end stop coalesce during the impact, it is assumed that the separation and approach velocities of the end stop are negligible in comparison with the proof-mass velocities. Therefore, $\dot{y}_{d,sep}, \dot{y}_{d,app}$ can be set to zero in Eq. 5.23, and the separation and approach velocities of the proof-mass are obtained from the velocity-time signals, as marked in Figure 4.9.

Having said this, there is an inherent difficulty with using the coefficient of restitution to obtain the damping term in this case; it is apparent in Figure 4.9 that the separation and approach velocities of the proof-mass have the same sign in some cases, particularly when double- or triple-impacts are present. As a consequence, the coefficient of retitution becomes negative, which is not physically realisable as it implies that either no collision occurs or the two bodies remain coalesced after the collision occurs. This suggests that the end stop initially moves away from its origin after the first collision, and then returns to the origin as a result of a restoring force, thereby causing an additional collision with

the proof-mass. Therefore, to ensure a positive coefficient of restitution, the end stops appear to exhibit their own internal dynamics, such that $\dot{y}_{d,sep}, \dot{y}_{d,app}$ are non-negligible; consequently, the true coefficient of restitution cannot be ascertained without knowledge of these velocities, and so ε is not a reliable impact parameter to use for optimisation purposes in this case.

Furthermore, there is another difficulty associated with modelling the energy dissipation of the collisions using a viscous damping model. In Figure 4.9, it can be seen that the velocity of the proof-mass $\dot{y}_p$ is typically very low over the duration of a collision, which means that little energy is dissipated if the saturation damping force is a function of $\dot{y}_{p,app}$. This is an additional limitation when the dynamics of the end stops are neglected, as the energy of the proof-mass is transferred to the end stop during the collision, where it is dissipated as sound and heat. By incorporating the end stop dynamics, the saturation damping force can be modelled as a function of the end stop velocity, since larger impacts result in greater velocities and energy dissipation.

Including the internal dynamics of the end stops requires the use of a three-degree-of-freedom actuator model, where one of the additional degrees-of-freedom only becomes active when saturation occurs. Since we desire a relatively simple actuator model for intuition purposes, the single-degree-of-freedom model is utilised to emulate the general impact dynamics at the expense of the more subtle characteristics of stroke saturation, such as the multiple collisions. Details of a possible three-degree-of-freedom actuator model are discussed further in Appendix D.

From this analysis, it is apparent that the use of a single-degree-of-freedom actuator model results in a significant compromise of the saturation dynamics, particularly with regards to the damping function $g[y_p(t) - d_{1,2}, c_{sat}]$. Since an accurate damping model cannot be obtained in this case, a relatively simple linear piecewise damping model is used as a compromise to control the magnitude of the impulses, in conjunction with the piecewise stiffness model. The piecewise stiffness function is identified by examining the contact time of the impulses in the measured force-time signals, and the parameters are optimised using the magnitude of the impulses. This requires knowledge of the stroke lengths d_1, d_2, which are obtained in the next section.

5.4.2 Stroke length

In order to ascertain the positive and negative stroke lengths, denoted by d_1 and d_2 respectively, it is necessary to consider the actuator bias caused by the non-central equilibrium position of the proof-mass and the DC offset associated with stroke saturation; these factors ensure that the negative stroke length d_2 is shorter than the positive stroke length d_1, such that the occurrence of stroke saturation is biased in the negative direction. This bias can be observed in the displacement-time signals in Figure 4.10 and the restoring force curve in Figure 5.7.

First, the total stroke length $d = |d_1| + |d_2|$ can be established by utilising the restoring force data shown in Figure 5.6. In this figure, stroke saturation manifests itself as a rapid increase in the magnitude of the restoring force at the positive and negative displacement extremes. Therefore, the total stroke length can be defined as the displacement region between these two extremes where stroke saturation occurs. This is shown in Figure 5.11, where it is apparent that the total stroke length is $d \approx 2.4$ mm.

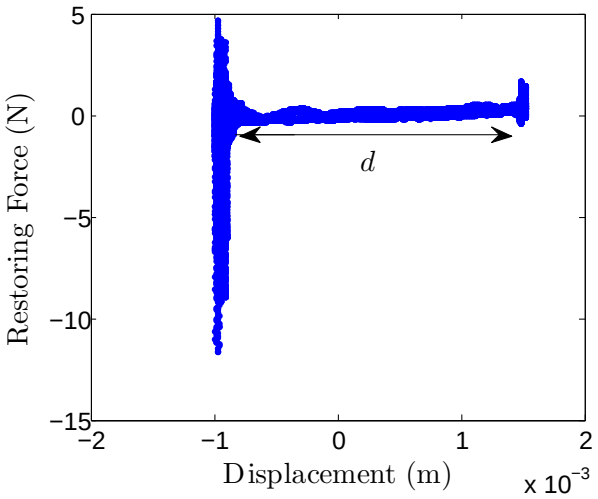

Figure 5.11: Restoring force of the proof-mass actuator against displacement amplitude, where double-sided stroke saturation occurs. The total stroke length d is shown as the region between the saturation limits.

The next step is to establish the negative stroke length, d_2, since the occurrence of stroke saturation is biased for negative displacements, and so there is a large amount of measured data where the proof-mass hits this end stop. In contrast, there are few examples in the measured data where stroke saturation occurs for positive displacements, and so it is more difficult to reliably ascertain the positive stroke length, d_1. Since the restoring

force is multi-valued in the stroke saturation regions, due to the end stop dynamics, the negative stroke length cannot be obtained with sufficient accuracy using Figure 5.11 alone, although it appears that d_2 is close to 1 mm.

Instead, it is necessary to estimate d_2 by utilising the Simulink actuator model to simulate the displacement-time signals, including the unmeasured DC offset, in conjunction with the measured force-time signals. In principle, this actuator model is only valid when the stroke limits are not exceeded in the measured displacement-time signals, and it is therefore important to establish the saturation bandwidth $\Delta\omega_{sat}$ (*i.e.* the range of frequencies over which stroke saturation occurs for a given excitation amplitude) of the actuator. The saturation bandwidth can be obtained from the kurtosis of the measured force-time signals, which is a statistical indicator used to describe the peakedness of the measured data.

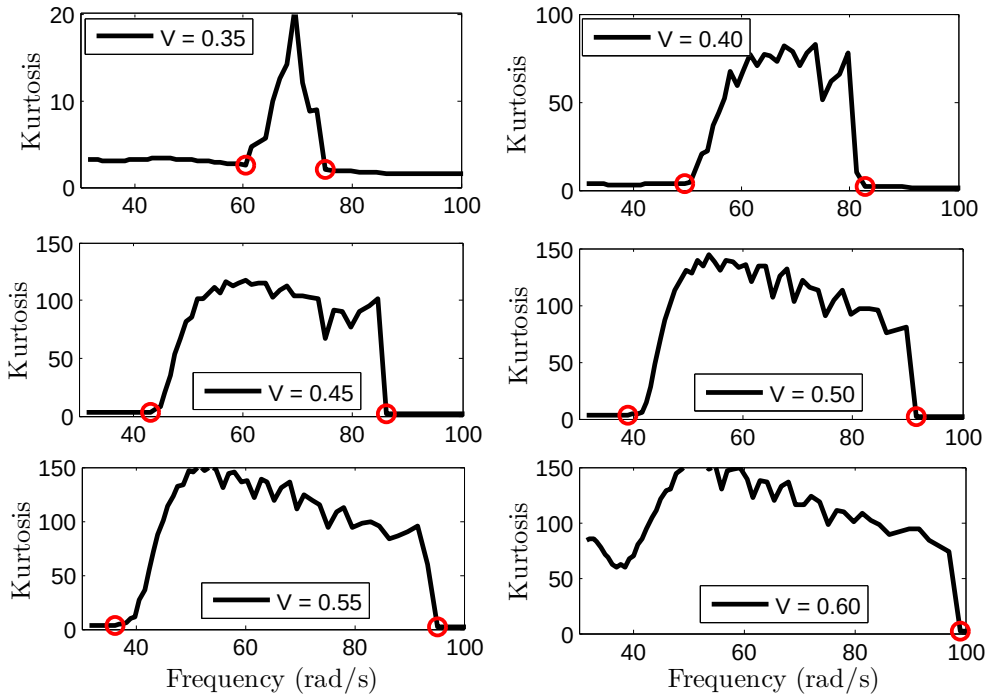

Figure 5.12: Kurtosis values of the force-time signals against excitation amplitude and frequency. The circles convey the saturation cut-on and cut-off frequencies.

Kurtosis is defined as follows,

$$\text{Kurtosis} = \frac{1}{N}\sum_{i=1}^{N}\left(\frac{f_p[i]-\mu}{\sigma}\right)^4 \tag{5.24}$$

where μ is the average and σ is the standard deviation of the measured force-time signal. The kurtosis of the measured signals is shown against the excitation frequency and amplitude in Figure 5.12. Here, the regions of increased kurtosis correspond to the presence of stroke saturation, and so it is apparent that the saturation bandwidth appears to increase with excitation amplitude. The cut-on and cut-off frequencies of the saturation bandwidth, denoted by $\omega_{sat,l}$ and $\omega_{sat,u}$, are also marked in Figure 5.12.

By utilising these measured cut-on and cut-off frequencies, it is reasonable to assume that the Simulink actuator model is valid when the excitation frequency is outside the saturation bandwidth defined for a given excitation amplitude. Therefore, the saturation threshold may be estimated by simulating the displacement-time signals of the actuator over a range of excitation frequencies and amplitudes close to the cut-on and cut-off frequencies, and examining the peak negative displacement amplitude at these frequencies.

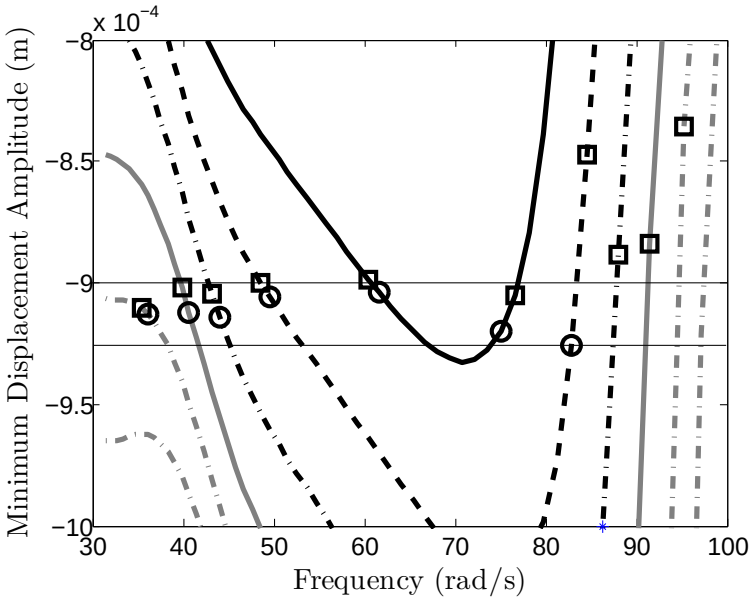

Figure 5.13: Minimum peak displacement amplitude in the simulated displacement-time signals for a variety of excitation amplitudes and frequencies. The cut-on and cut-off frequencies, where saturation occurs, are marked as circles, and the nearest excitation frequency, where stroke saturation does not occur, are maked as squares. These markings define the region for the saturation threshold d_2.

If this threshold is consistent with excitation amplitude, then it is reasonable to state that the threshold is d_2. This is illustrated in Figure 5.13, where it is shown that the peak negative displacement amplitude is relatively consistent at the cut-on frequency as the

excitation amplitude increases, ranging from -0.9 millimetres to -0.92 millimetres. This range is also covered in the cut-off frequencies, which exhibits large changes in amplitude as the excitation frequency varies slightly. By taking an average of this range of possible values, the negative stroke length is defined as $d_2 \approx -0.91$ millimetres. Since the total stroke length d and the negative stroke length d_2 are now known, the positive stroke length is estimated using $d_1 = d - |d_2| \approx 1.49$ millimetres.

5.4.3 Impact parameter optimisation

Now that the stroke limits d_1, d_2 are known, the remaining terms to be identified are the saturation forces $F_{sat,1}(\mathbf{x}), F_{sat,2}(\mathbf{x})$, which, in turn, are obtained from the stiffness and damping functions. As discussed in section 5.4.1, these terms can be identified from the contact time, the impulse magnitude, and the coefficient of restitution of the impulse that occur in the measured force-time signals. First, the contact time ΔT of the collisions is established from the force-time signals by measuring the time period of the impulses, where the proof-mass is in contact with one of the end stops. This is achieved by taking the finite difference of the force-time signal and setting a threshold for large gradients that correspond to stroke saturation. An example is shown in Figure 5.14.

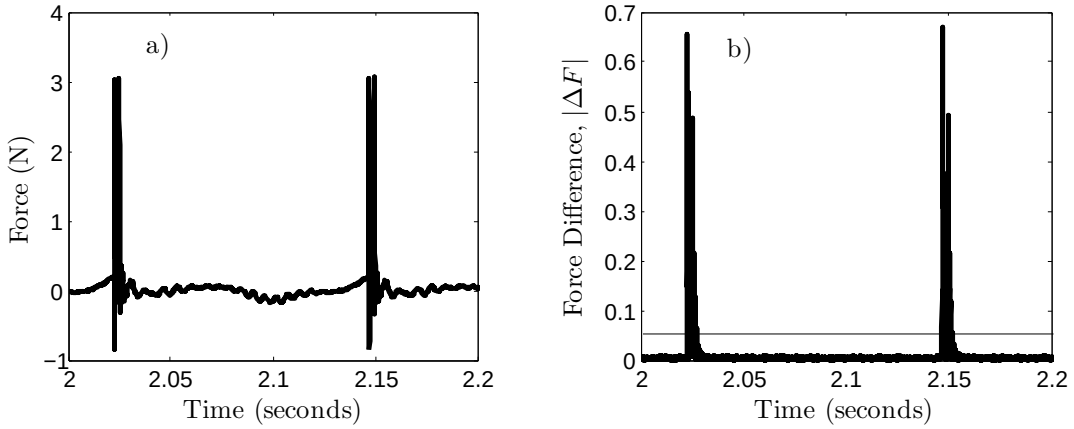

Figure 5.14: Example of the finite difference approach to detect the start and finish times of the impulses, where a) is the measured force-time signal for $V = 0.5$ Volts, $\omega = 50$ rad/s, and b) is the absolute forward finite difference of the force-time signal. A threshold is set at 0.05 for the detection of the impulses.

Figure 5.15a) illustrates the averaged contact time, $E[\Delta T]$, of the impulses for each measured force-time signal against excitation frequency and amplitude. In this figure, it is immediately apparent that the contact time decreases as the excitation amplitude and frequency increase, starting with a maximum of about 1 millisecond and tending towards a limiting value of about 0.4 milliseconds. Furthermore, the consistency of the impulses for each measured force-time signal is established from the relative unbiased standard deviation, denoted as RSD, where,

$$\text{RSD} = \frac{\sum_{n=1}^{N}(\Delta T_n - E[\Delta T])^2}{E[\Delta T](N-1)} \tag{5.25}$$

N being the number of impulses. The RSD parameter is shown against excitation amplitude and frequency in Figure 5.15b), ranging from $2-8\%$ of the total contact time. This indicates that the contact time of the impulses is consistent for each measured force-time signal, especially considering that the sample rate of 51.2 kHz corresponds to $2-5\%$ of the contact time.

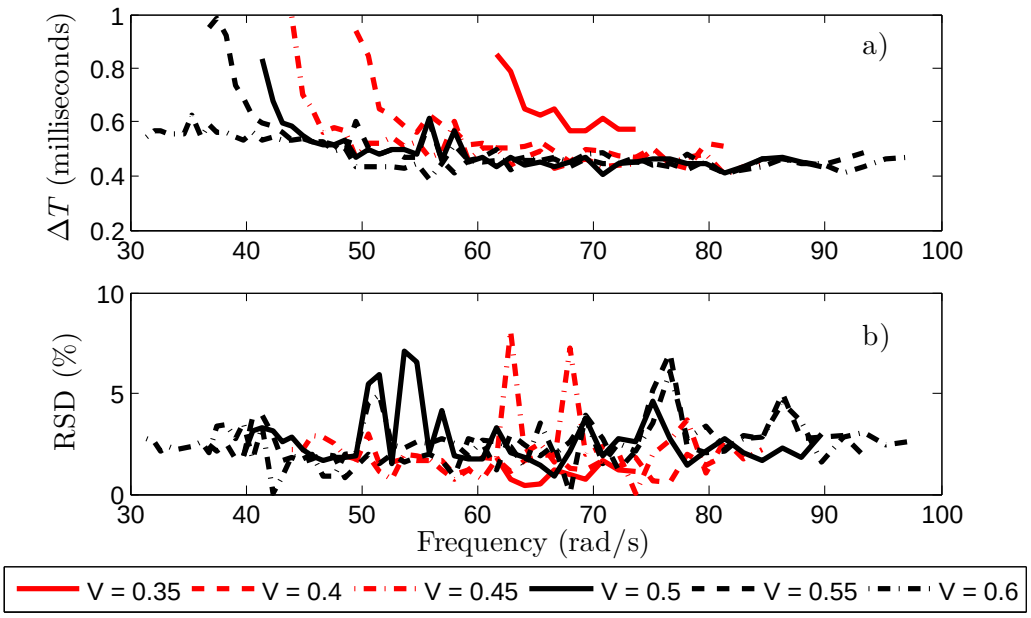

Figure 5.15: Impulse properties of the force-time histories, where a) is the average contact time, in milliseconds, and b) is the relative unbiased standard deviation.

As discussed earlier, the variability in the contact time indicates that the piecewise stiffness function $f[y_p(t) - d_{1,2}, k_{sat}]$ is not linear with the proof-mass displacement, since a linear relationship yields a constant contact time [75]. Therefore, it is necessary to consider a nonlinear piecewise stiffness model to emulate the dynamics of stroke saturation. A solution to this problem may be found by considering non-adhesive Hertzian contact theory [130, 135], where it is assumed that the contact between the proof-mass and the end stop is non-conforming, such that the contact area is small compared to the size of the two bodies. By modelling the collision of the proof-mass and the end stop as a contact beween a curved surface and a flat elastic half-space, the contact area increases with the indentation depth $(y_p(t) - d_{1,2})$, resulting in the following relationship between the restoring force F and the indentation depth [136],

$$F = k_{sat}(y_p(t) - d_{1,2})^{3/2} \tag{5.26}$$

This term can be used to represent the effective stiffness that is associated with stroke saturation [136].

Figure 5.16 illustrates the averaged coefficient of restitution $E[\varepsilon]$ against excitation amplitude and frequency, where ε is defined in Eq. 5.23. This parameter is obtained by applying the finite difference approach of the force-time signals to the measured velocity-time signals. As discussed earlier, it is evident that, in general, the coefficient of restitution falls rapidly with increasing excitation amplitude and frequency, resulting in negative values at higher amplitudes. This is because the end stop does not impart enough force to the proof-mass during the collision to change its direction upon separation. Therefore, it is very difficult to describe the energy dissipation mechanisms during the collision without considering the dynamics of the end stops.

Since it is impractical to use a single-degree-of-freedom model to emulate the energy dissipation processes during the collisions in detail, a relatively simplistic approach is taken to ensure that model is able to account for viscoelastic collisions, where the coefficient of restitution is less than unity. This allows the magnitude of the impulses to be controlled using both the stiffness and damping terms. Figure 5.2 shows that the effective damping appears to increase around the peak resonance frequency, and so a simple linear piecewise damping model is used to account for the effects of energy dissipation. In this model, the damping varies linearly with velocity, but the proportionality constant is determined by whether the proof-mass displacement exceeds the stroke limit.

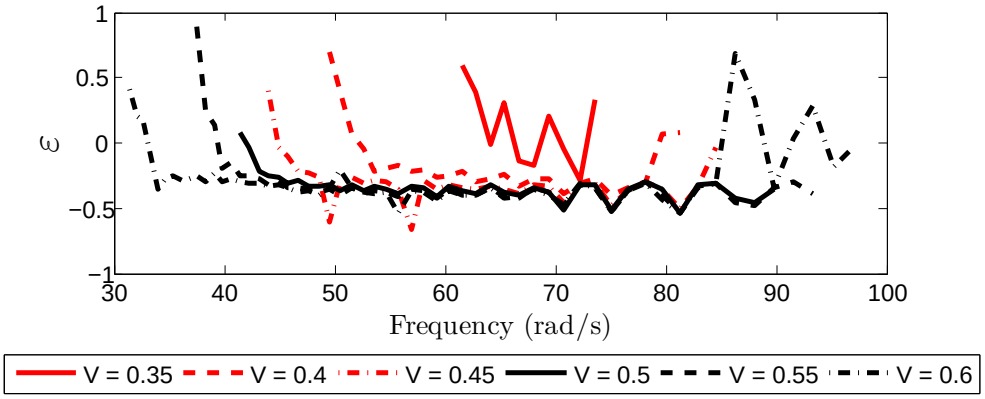

Figure 5.16: Average coefficient of restitution of the velocity-time signals against excitation amplitude and frequency.

Using the ascertained piecewise stiffness and damping functions, the saturation forces can therefore be described in the following form,

$$\begin{aligned} F_{sat,1}(\mathbf{x}) &= k_{sat}\sqrt{|y_p(t)-d_1|}(y_p(t)-d_1)+c_{sat}\dot{y}_p(t) \\ F_{sat,2}(\mathbf{x}) &= k_{sat}\sqrt{|y_p(t)-d_2|}(y_p(t)-d_2)+c_{sat}\dot{y}_p(t). \end{aligned} \tag{5.27}$$

such that $f[y_p(t)-d_{1,2},k_{sat}] = k_{sat}\sqrt{|y_p(t)-d_{1,2}|}$ and $g[y_p(t)-d_{1,2},c_{sat}] = c_{sat}$, where k_{sat} and c_{sat} are the saturation stiffness and damping parameters to be identified. The stiffness representation is modular to prevent complex restoring forces from occurring as a result of negative indentation depths.

Eq. 5.22 shows that the damping parameter c_{sat} is primarily dependent on the contact time and the coefficient of restitution, where ΔT is known from measured data. A coefficient of restitution of $\varepsilon = 0.7$ is specified as a reasonable degree of energy dissipation. By using the largest known contact time $\Delta T = 1$ millisecond, an estimate of c_{sat} is obtained using Eq. 5.22.

$$c_{sat} = -\frac{2\times 0.032}{0.001}\ln(0.7) \approx 20 \text{ Ns/m} \tag{5.28}$$

In this case, the damping parameter is reduced slightly to prevent impulse distortion in the simulated force-time signals, which may occur if the damping is too high. This identified parameter is thus a suitable compromise that results in a reduction of the magnitude of the impulses without distorting the impulses themselves.

In contrast, obtaining the stiffness parameter k_{sat} is not trivial, since the piecewise model is nonlinear and so Eq. 5.21 cannot be used to accurately estimate this term. Furthermore, there is a large degree of variability in the measured restoring force curve in Figure 5.6 when stroke saturation occurs, which also prevents an accurate estimation of k_{sat}. Instead, it is necessary to define a lower and upper limit for k_{sat}, which is then fine-tuned by simulating the force-time responses using the nonlinear actuator model in Simulink[1] and comparing the magnitude of the impulses with the measured signals.

First, a lower limit to k_{sat}, defined as $k_{sat,low}$, is found by applying the contact time $\Delta T = 1$ millisecond to Eq. 5.21, which is used as a linear approximation. Here, the lower limit is found to be $k_{sat,low} = 3.16 \times 10^5$ N/m$^{3/2}$. Next, the upper limit $k_{sat,up}$ is obtained by finding the largest gradient that fits the measured restoring force data shown in Figure 5.6, which is found to be $k_{sat,up} = 1 \times 10^8$ N/m$^{3/2}$. The k_{sat} parameter is then optimised using the magnitude of the impulses, which are obtained by filtering the force-time signals and finding the maximum force for each cycle. This process yields the following optimised k_{sat} parameter,

$$k_{sat} = 8 \times 10^7 \text{ N/m}^{3/2} \tag{5.29}$$

A comparison of the impulse magnitudes of the simulated and measured force-time signals, as shown in Figure 5.17, confirms that the full nonlinear actuator model, which accounts for stroke saturation, is able to predict the impulse magnitude with a high degree of accuracy. Additionally, the figure shows that the saturation bandwidth of the actuator is similar to that of the physical actuator, which indicates that the stroke lengths d_1, d_2 are also estimated correctly.

The simulated and measured restoring force curves are also compared with each other in Figure 5.18, and it appears that the agreement is reasonable, where the simulated restoring force curve follows a steep gradient, particularly for negative displacements. This indicates that the additional data points at larger displacement amplitudes correspond to double-impacts, where the end stop has moved slightly from the initial collision.

The next step is to compare the average contact time of the simulated force-time signals, as illustrated in Figure 5.19, with the equivalent measured contact times shown in Figure 5.15. Here, it is evident that the duration of the impulses in Figure 5.19 appear to decrease as the excitation amplitude or frequency increases, which is a key

[1]The full nonlinear actuator model, which accounts for stroke saturation, is shown in Appendix E

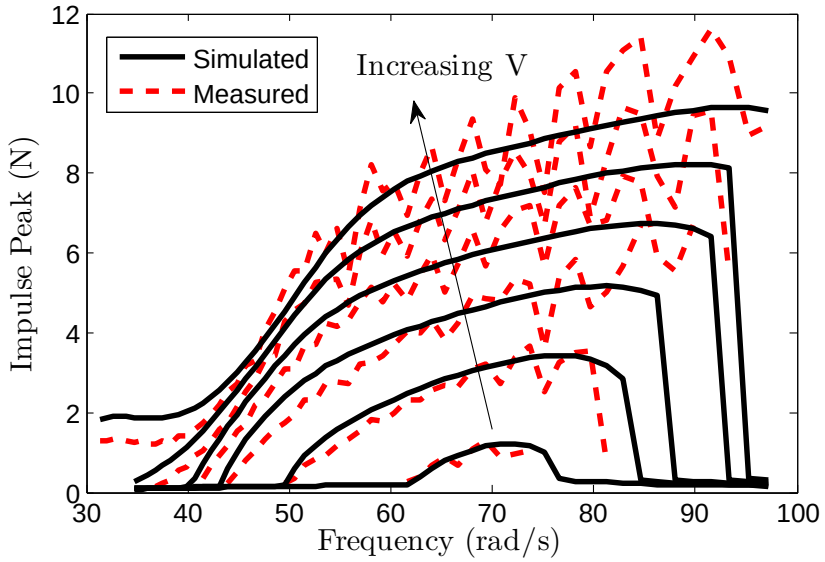

Figure 5.17: Comparison of the average peak magnitude of the impulses in the simulated and measured force time signals.

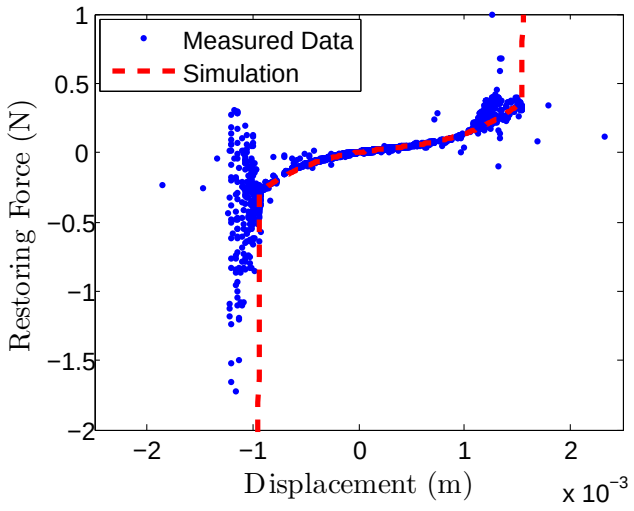

Figure 5.18: Simulated and measured restoring force curves against displacement.

characteristic of the measured contact times and confirms that the nonlinear piecewise model is reasonable. The simulated contact times, in general, are slightly longer than the measured contact times by a factor of $2-3$; since this corresponds to a similar order of magnitude, the accuracy of the simulated contact times is considered to be sufficient.

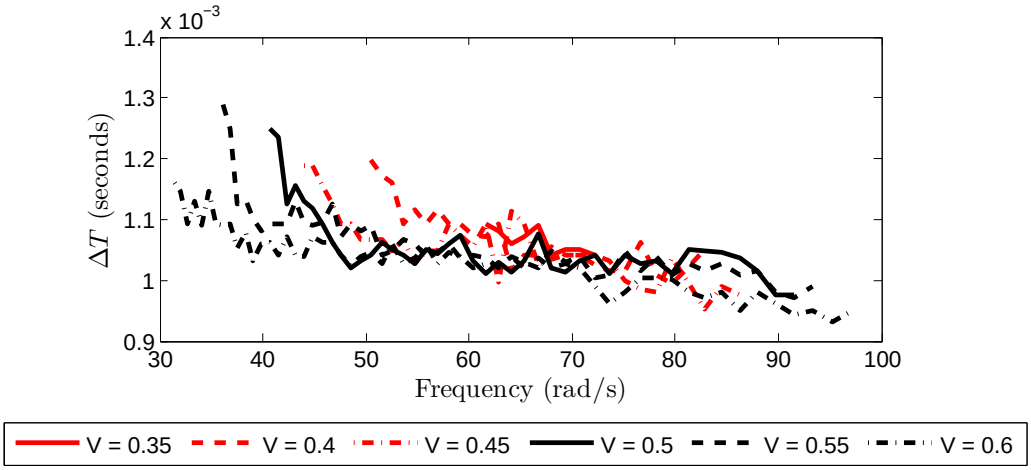

Figure 5.19: Average contact time of the impulses in the simulated force time signals against excitation frequency and amplitude.

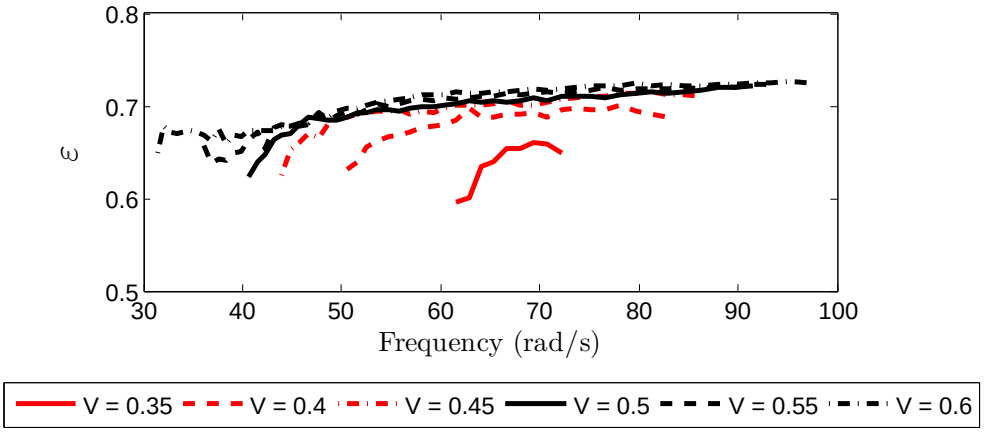

Figure 5.20: Average coefficient of restitution of the simulated velocity-time signals against excitation frequency and amplitude.

Finally, the average coefficients of restitution, obtained from the simulated velocity-time signals, are shown in Figure 5.20. In this figure, it is apparent that energy is dissipated during the collisions, as the coefficients of restitution start from a minimum value of 0.6 and tend towards a limiting value of about 0.7 as the excitation amplitude and frequency increases. The variation occurs as a result of the contact time, which reduces with the increases in excitation amplitude and frequency, thereby increasing the coefficient of restitution. These values indicate that the choice of damping parameter is reasonable, with a sufficient reduction in the coefficient of restitution without distorting the impulses in the force-time signals.

5.5 Comparisons of simulated and measured data

In order to ensure that the actuator model is able to simulate the dynamics of the physical actuator with a sufficient degree of accuracy, the simulated responses are compared directly with the measured responses, both in the time- and frequency-domains. The simulated signals are obtained in Simulink using the ode3 solver at a sample rate of 51.2 kHz.

First, the actuator model is used to simulate the force-time signals observed in Figure 4.7, and a comparison of the simulated and measured signals is shown in Figure 5.21. The main priorities in the comparison are to assess whether the presence of impulses in the simulated force-time signals is consistent with the measured force-time signals, and to examine the magnitudes of the impulses in the simulated signals, relative to the measured signals. It is apparent that the actuator model is able to accurately predict the onset of stroke saturation, which occurs in most of the measured force-time signals in Figure 5.21. Furthermore, there is good agreement between the magnitudes of the impulses in the simulated and measured force-time signals.

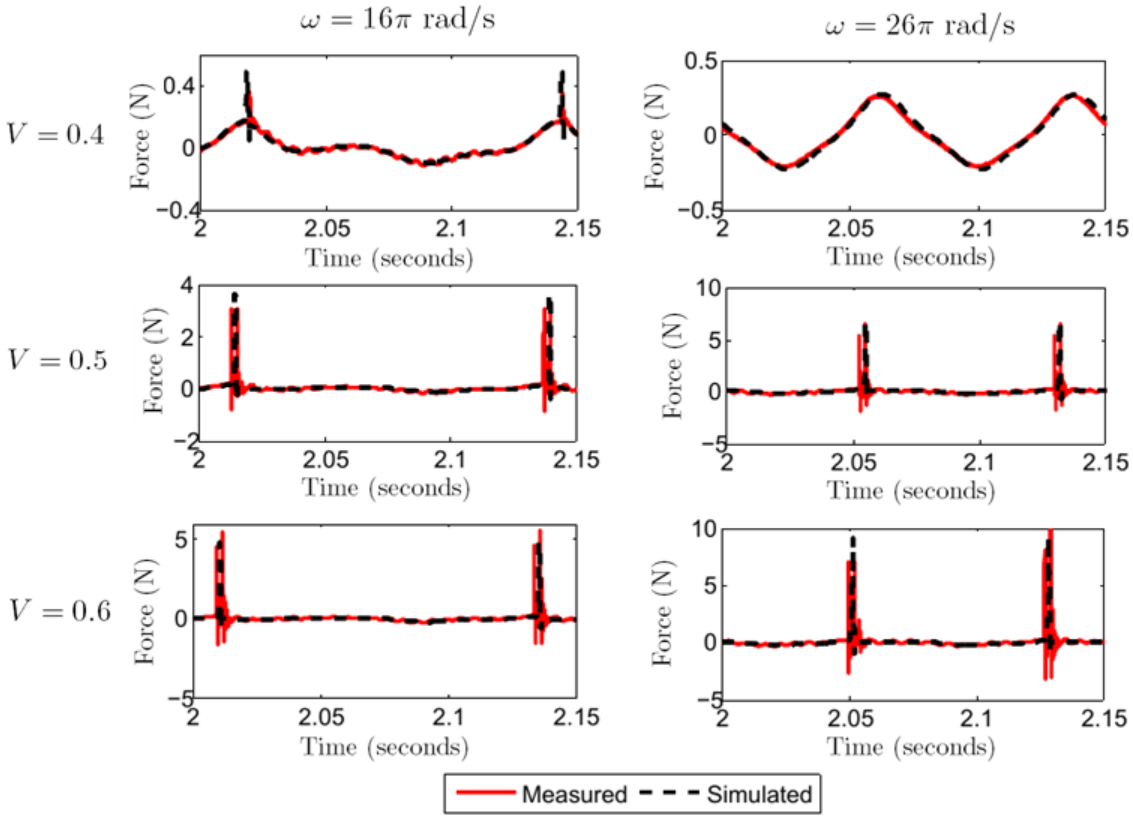

Figure 5.21: Comparison of simulated and measured force-time signals.

As discussed earlier, the actuator model fails to account for the more subtle characteristics of stroke saturation, such as the double-impacts and the high-frequency transients. However, these dynamics are relatively minor, and the simulated responses generated by the actuator model are otherwise excellent representations of the measured force-time signals.

Next, a frequency-domain comparison is undertaken on the simulated and measured first-order displacement-voltage FRFs, based on the experimental results shown in Figure 4.23. The simulated FRFs were obtained by simulating the steady-state displacement-time responses to sinusoidal voltage signals over the range of excitation amplitudes and frequencies used in chapter 4, and then applying the first-order stepped-sine approach. The comparison is illustrated in Figure 5.22.

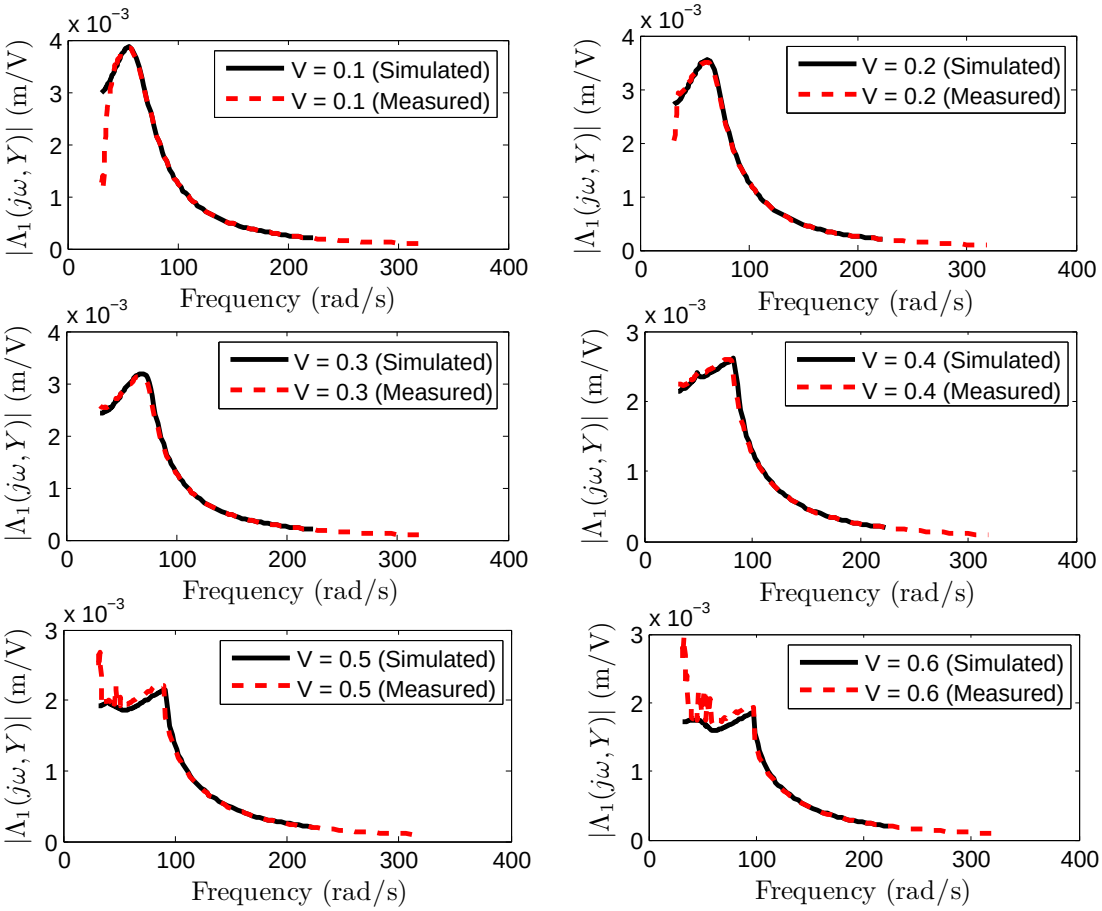

Figure 5.22: Comparison of simulated and measured first-order displacement-voltage FRFs (denoted by $\Lambda_1(j\omega, Y)$) of the actuator.

Since the first-order FRFs only reveal information about the steady-state displacement amplitude at the fundamental excitation frequency, the frequency-domain comparison is less detailed than the time-domain comparison, but it gives a more generalised overview on the accuracy of the actuator model. From Figure 5.22, it is apparent that the agreement between the simulated and measured FRFs is excellent over the entire excitation amplitude range, thereby confirming that the actuator model also works well in the frequency domain. The magnitude of the simulated FRFs appears to be slightly smaller than the measured FRFs around the peak resonance when the excitation amplitude is high, which infers that the saturation threshold d_2 is slightly underestimated. However, this discrepancy is very small, and can be neglected. More importantly, the peak resonance frequency of the simulated FRFs almost exactly match those of the measured FRFs, thereby indicating that the actuator model predicts the saturation bandwidth of the physical actuator with a high degree of accuracy.

5.6 Conclusions

In this chapter, a nonlinear single-degree-of-freedom actuator model was devised for the purpose of emulating the dynamics of a Micromega IA-01 inertial actuator, using the measured data from chapter 4. A variety of identification methods were utilised to create the model, based on the underlying linear dynamics, the weak nonlinear suspension dynamics, and the stroke saturation dynamics. The underlying linear dynamics were identified by applying linear least-squares optimisation to the inverse displacement-voltage FRFs.

The form of the nonlinear suspension dynamics was specified as a low-order polynomial stiffness function, and the parameters were identified by monitoring the peak resonance frequency and applying nonlinear least-squares optimisation. In addition, a force-state mapping approach was taken to identify the parameters by curve-fitting the restoring force curves; the identified parameters were consistent for both cases. It was found that the stroke saturation dynamics could be reasonably emulated using a nonlinear piecewise stiffness and linear piecewise damping model, and the parameters were optimised using the contact time, impulse magnitude, restoring force curve, and coefficient of restitution.

Using these optimised parameters, the actuator model was created in Simulink, and it was demonstrated using time- and frequency-domain comparisons that the model is capable of emulating the dynamics of the Micromega IA-01 inertial actuator with a high

degree of accuracy, particularly when the stroke limits are not exceeded and the actuator is operating within its intended region.

The primary limitations of the actuator model lie in the use of a simple single-degree-of-freedom system to emulate stroke saturation, which exhibits complex dynamic phenomena such as double- or triple-impacts and internal resonance effects. As a result, many compromises were required to estimate the parameters associated with stroke saturation, since this form of structural model is not directly applicable to the physical process. In particular, it was necessary to specify an alternative coefficient of restitution, as the measured coefficients obtained using the SDOF assumption are negative and unphysical.

These findings suggest that a more accurate model of stroke saturation may be obtained by utilising a three-degree-of-freedom system that accounts for the dynamics of the end stops. This type of model is capable of including the effects of double-impacts and internal resonances by considering the rebound of the end stop towards its original position. However, devising such a model is relatively complicated and requires knowledge of variables that may be difficult to measure, primarily the displacement of the end stop. Thus, there is plenty of scope for improving the actuator model and the emulation of impact dynamics in future work, especially with regards to the literature concerning the use of structural vibro-impact models for double- or triple-impact phenomena.

Chapter 6

Preliminary Analysis of an Actuator-Plate Configuration

6.1 Introduction

It has been demonstrated in previous chapters that a typical inertial actuator exhibits a weak stiffening nonlinearity, which can be modelled using low-order polynomials, and the well-known stroke saturation phenomenon, whose dynamics are emulated using a nonlinear piecewise stiffness model. Previous studies [22] have shown that these actuator nonlinearities may degrade the control performance by significantly reducing the closed-loop stability margin. It is therefore neccessary to investigate the destabilising effects of these nonlinearities and to devise a stabilising control law, based on the nonlinear analysis.

In this chapter, we present a case study of a typical SISO vibration control scenario, where a single Micromega IA-01 actuator is attached to a lightweight aluminium plate to provide active vibration suppression using velocity feedback control. An external disturbance, known as the primary force $f_p(t)$, is applied to the plate, and the actuator provides a secondary control force $f_s(t)$ to the structure to apply active damping to the first mode of the plate. The study focuses on the effects of actuator nonlinearities on the overall closed-loop stability margin, and considers potential strategies for stabilising the closed-loop system.

First, a preliminary analysis is conducted on the actuator-plate configuration, where the dynamics of the open-loop control path and the feedback controller are obtained with simulations and experimental measurements. Using monoharmonic excitation, a variety

of features are identified, including the number of plate modes in the control bandwidth, their effects with regards to the control path dynamics, and the presence of nonlinearities. Additionally, two types of feedback controllers are considered and their effects on the closed-loop stability are observed: the first is an ideal pure-gain feedback controller, whereas the second is a more practical controller that contains a digital integrator and two band-pass filters.

Next, a nonlinear two-degree-of-freedom Simulink model of the actuator-plate configuration is constructed, representing the actuator mode and the first plate mode. This model is used to simulate the time responses of the closed-loop system and to predict the stability margin, accounting for the actuator nonlinearities and the controller dynamics. Using Nyquist and Lyapunov analysis, it is demonstrated that the saturation nonlinearities reduce the gain margin significantly if the excitation amplitude is sufficiently large, whereas the suspension nonlinearities have a similar destabilising effect when larger feedback gains and smaller excitation amplitudes are considered. By applying Lyapunov's direct method, it is found that the actuator nonlinearities "exploit" regions of potential instability present in the underlying linear closed-loop system, which results in an increase in the total energy of the system as the proof-mass moves from one end stop to the other.

A saturation-dependent on-off control scheme is then designed to counteract this energy increase by deactivating the control signal when stroke saturation is detected. In order to achieve this, a saturation detection scheme is employed by placing an accelerometer on the actuator casing and monitoring the resulting acceleration signal. Alternatively, a gain-scheduling control scheme that increases the gain of a secondary control loop when saturation is detected is considered for the purpose of preventing stroke saturation. Further details on the implementation of this control scheme are given in Appendix F.

6.2 Control path analysis

6.2.1 Experimental setup

The Micromega IA-01 actuator was attached horizontally to a flexible aluminium plate via the PCB 208C01 force transducer, which was used to measure the relative force between the actuator and the plate. The control loop was generated by collocating a B&K Type 4375 accelerometer with the actuator on the plate, for the purpose of measuring the structural acceleration at this location. These force and acceleration signals were

conditioned using the PCB ICP conditioner and a B&K Type 2626 conditioning amplifier respectively. An illustration of the setup is shown in Figure 6.1.

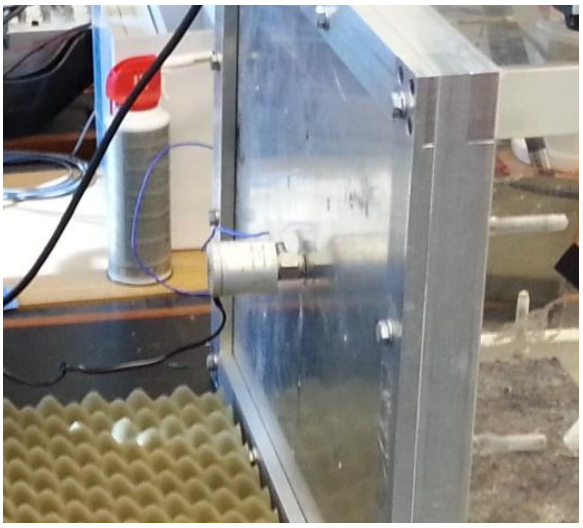

Figure 6.1: Illustration of the Micromega inertial actuator attached to the flexible plate.

The open-loop plant dynamics $H_s(s, Y)$, which is defined as the path between the control signal and the structural acceleration, determines the performance of the feedback controller and the overall closed-loop stability. These dynamics are obtained by applying monoharmonic input voltages to the actuator and measuring the resulting force-time and acceleration-time signals, denoted by $f_{rel}(t)$ and $\ddot{y}_s(t)$ respectively, where the sensitivities of the accelerometer and the conditioner are accounted for in Table 6.1. These measurements are taken over a period of ten seconds, using a relatively high sampling rate of 51.2 kHz to capture the effects of actuator saturation.

Table 6.1: Sensitivities of the accelerometer and conditioner.

Equipment	**Sensitivity,** T_s
B&K Type 4375 accelerometer	0.346 pC/ms^{-2}
B&K Type 2626 conditioner	0.102 V/ms^{-2}

The excitation frequency vector ranges from 30 rad/s to 1 krad/s, which is sufficient to capture the actuator mode and the first few structural resonances of the plate,

$$\omega(i) = \Big([\,30{:}10{:}60\ 65\ 70{:}2{:}80\ 85\ 90{:}10{:}190\ 195{:}5{:}240\ 250{:}10{:}700\ 705{:}5{:}720\ 730{:}10{:}1\mathrm{k}\,] \Big)$$

Furthermore, the nonlinear dynamics of the open-loop control path were captured using three voltage amplitude levels,

$$V = \Big[0.1 : 0.2 : 0.5\Big]$$

6.2.2 Open-loop plant dynamics

Force measurements

First, the measured force-time signals are analysed for the purpose of identifying the plate resonances and examining the nonlinear behaviour of the open-loop plant. As the force transducer is placed between the actuator and the plate, the force-time signals represent their coupled dynamics, and the nonlinear actuator dynamics are therefore easier to observe.

Illustrations of the measured input voltage-time signal, the force-time response signal, and the force spectrum, all obtained at $\omega = 75$ rad/s, are shown in Figure 6.2. Since the excitation frequency is close to the peak resonance of the actuator, we can clearly see the effects of the actuator nonlinearities on the force response through harmonic distortion. Moreover, the presence of impulses at the highest input voltage amplitude $V = 0.5$ indicates that the actuator is undergoing stroke saturation. This behaviour infers that the actuator dynamics are dominant in this frequency region, exhibiting the weak suspension nonlinearities and saturation dynamics observed in chapters 4 and 5.

As the excitation frequency rises above the natural frequency of the actuator, the harmonic distortion in the force-time signals becomes less apparent, and the open-loop plant behaves in an approximately linear manner. To demonstrate this, Figure 6.3 shows the measured signals obtained at $\omega = 190$ rad/s, which is close to the first natural frequency of the plate. The force-time signals exhibit a small degree of harmonic distortion, due to nonlinear coupling between the actuator and the plate, and weak nonlinearities in the plate itself. However, these harmonics are small enough in magnitude to be neglected.

The first-order force-voltage FRFs $H_f(j\omega, Y)$, which are ascertained uing the stepped-sine method, reveal important information about the number and prominence of the resonance modes in the frequency range of interest, as well as their susceptibility to nonlinear distortion. These measured FRFs, which are displayed in Figure 6.4, highlight

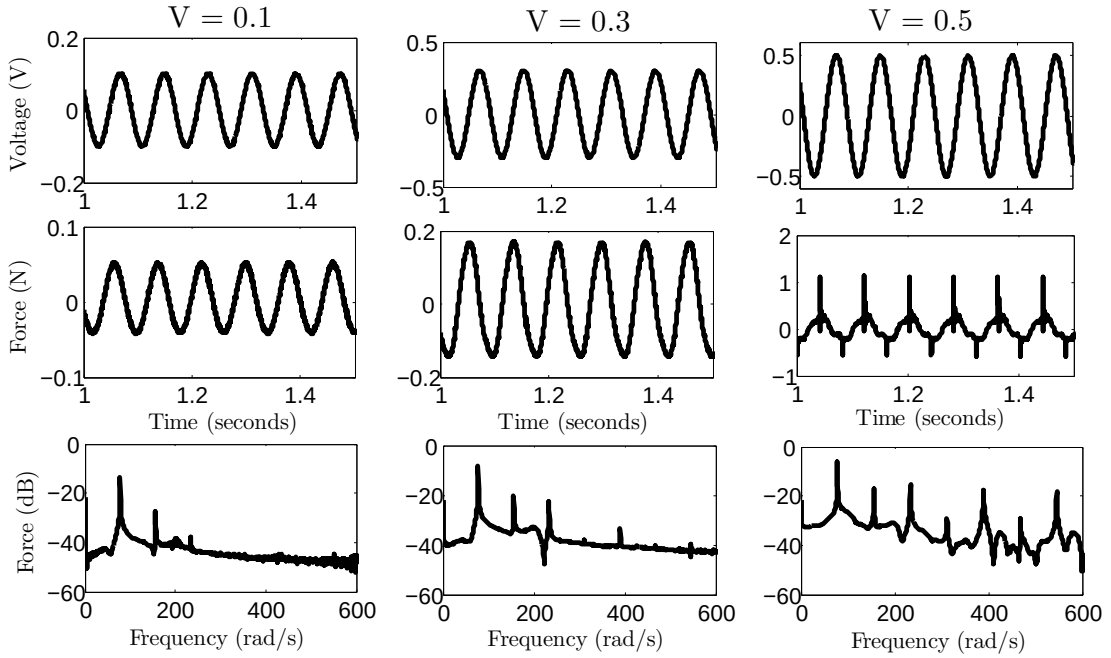

Figure 6.2: Voltage-time signals, force-time signals, and force-frequency spectrum for $\omega = 75$ rad/s.

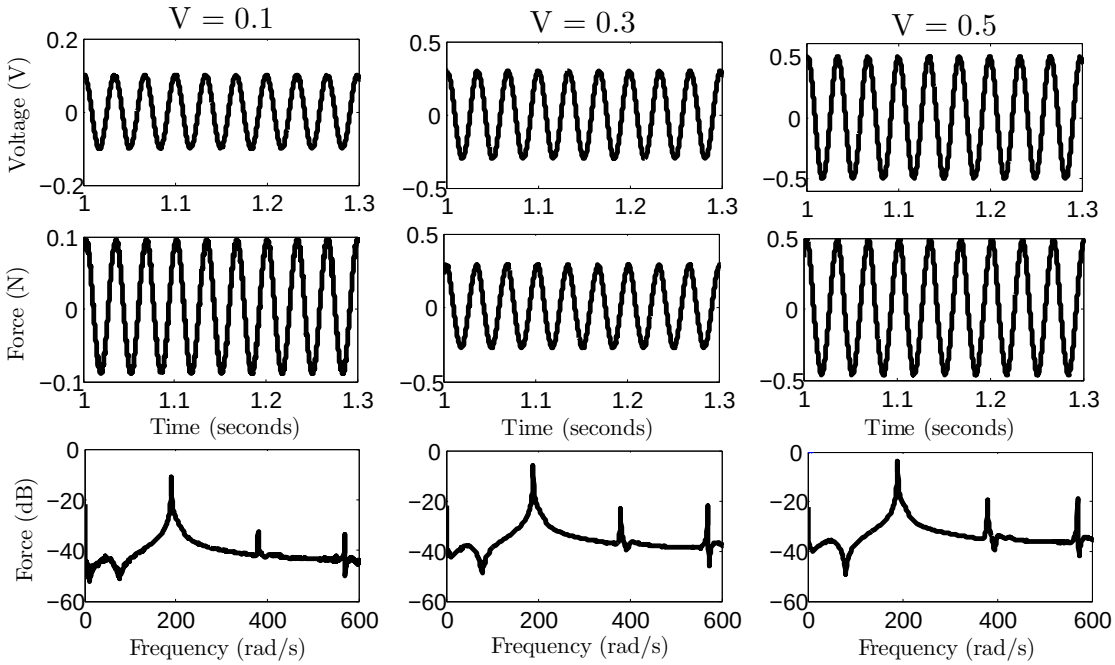

Figure 6.3: Voltage-time signals, force-time signals, and force-frequency spectrum for $\omega = 190$ rad/s.

the presence of five plate modes up to 1 krad/s, where the higher-order out-of-band modes start to become less prominent. The first few natural frequencies and mode shapes of the plate are estimated using a Kirchhoff model [137]; details can be found in Appendix G.

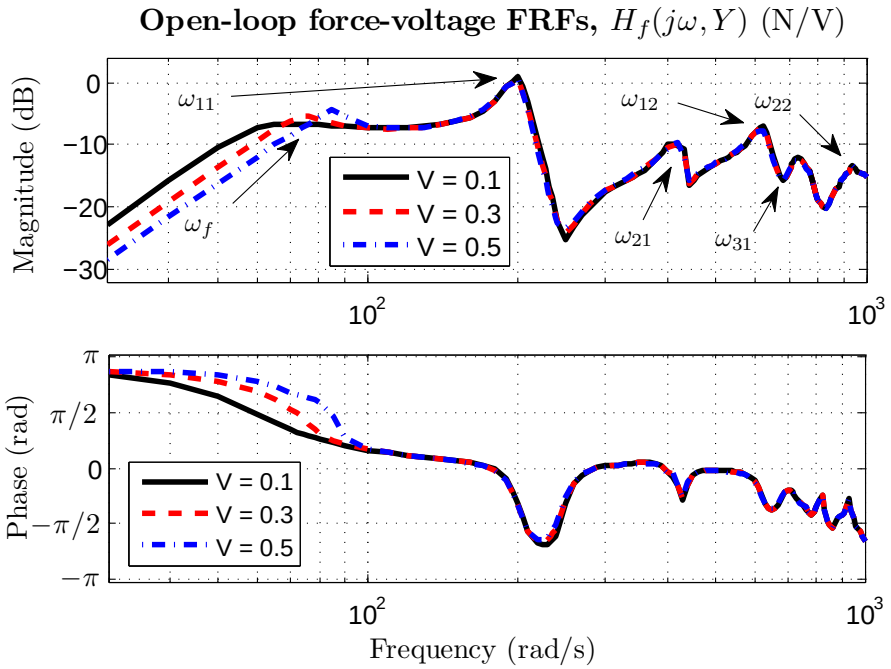

Figure 6.4: Magnitude and phase of the measured force-voltage FRFs.

The first peak resonance ($\omega_f \approx 60$ rad/s) represents the contribution to the response of the actuator mode. It should be noted that the stiffness of the plate will alter the frequency of this coupled resonant peak. Due to the nonlinearities in the actuator, this peak resonance frequency increases significantly as the input voltage amplitude rises, and exhibits the jump phenomenon at the highest excitation levels. The next mode ($\omega_{11} \approx 200$ rad/s) is the contribution of the first structural resonance of the plate, which is particularly prominent due to light structural damping. The frequency of this mode is well above the natural frequency of the actuator; this ensures that the coupling between the actuator and the plate is relatively weak in this region, such that the actuator behaves as an ideal force generator. Furthermore, this mode exhibits little variation with the input voltage level, and is therefore assumed to be amplitude-invariant.

Similar characteristics can be observed in the contribution of the second structural resonance of the plate ($\omega_{21} \approx 420$ rad/s). Conversely, the third plate mode ($\omega_{12} \approx 620$ rad/s) features a small degree of nonlinear damping, as the magnitude of the peak reso-

nance decreases with increasing excitation amplitude. At the upper end of the frequency range, the fourth and fifth plate modes (located at $\omega_{31} \approx 780$ rad/s and $\omega_{22} \approx 920$ rad/s respectively) are amplitude-invariant and indicate that the modes are starting to reduce in prominence.

Since we are primarily interested in controlling the first structural resonance of the plate, the weak nonlinearities observed in the higher-order modes are neglected, such that the plate dynamics are assumed to be approximately linear. In contrast, the strongly nonlinear actuator dynamics observed in the previous chapters are present in the actuator-plate configuration, and should therefore be taken into account when assessing the closed-loop stability.

Acceleration measurements

The acceleration-time signals measured by the accelerometer are now analysed in a similar manner to the force-time signals. These accelerometer signals represent the structural acceleration and are used as the output of the open-loop plant $H_s(j\omega, Y)$. Therefore, the closed-loop stability is primarily determined by the phase relationship between the voltage-time and the acceleration-time signals.

Figure 6.5 illustrates the voltage-time signal, the acceleration-time signal, and the acceleration spectrum measured at $\omega = 75$ rad/s. It is apparent in this figure that the harmonic distortion is more pronounced in the acceleration-time signals than the corresponding force-time signals. This is confirmed in the acceleration spectrum, where the amplitude of the second harmonic exceeds the fundamental amplitude at the higher excitation voltages. The stroke saturation phenomenon is also apparent in the acceleration-time signal at $V = 0.5$ Volts.

For the first plate mode, the measured voltage-time signal, acceleration-time signal, and acceleration spectrum measured at $\omega = 190$ rad/s are shown in Figure 6.6. Since this excitation frequency is close to the first resonance frequency of the plate, the acceleration-time signals are relatively large in amplitude, yet the degree of harmonic distortion is greatly reduced. In addition, the acceleration-time signals are almost totally out-of-phase with the voltage-time signals at this particular frequency, which can be attributed to the plate dynamics; this implies that the phase shift of the actuator is negligible at this frequency and confirms that the ideal force generator assumption is valid.

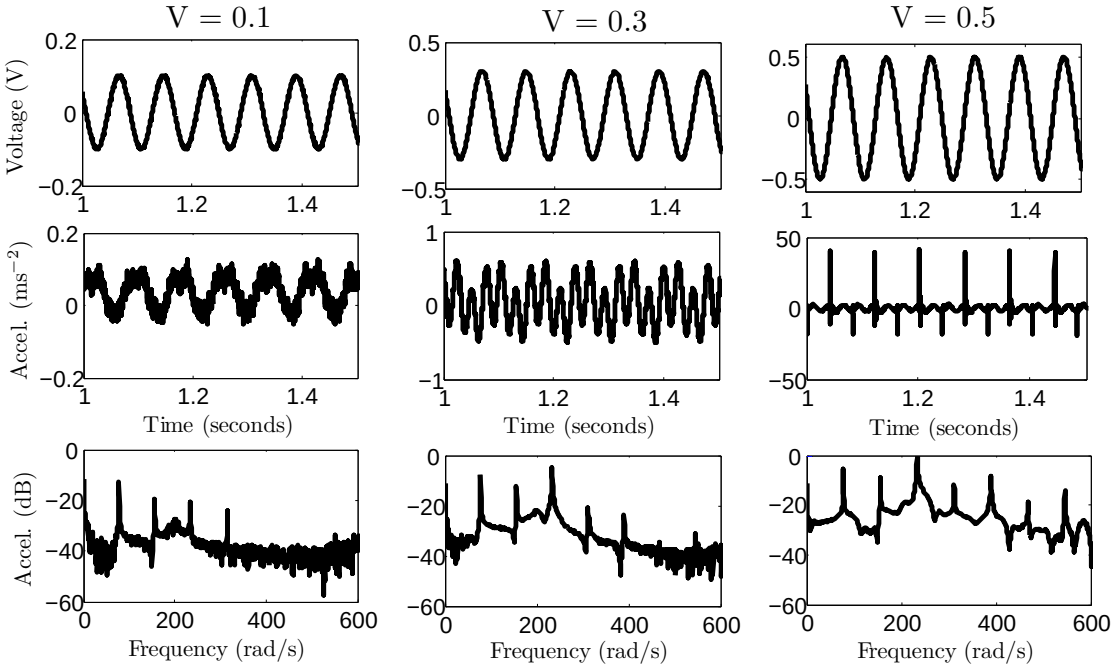

Figure 6.5: Voltage-time signals, acceleration-time signals, and acceleration-frequency spectrum for $\omega = 75$ rad/s.

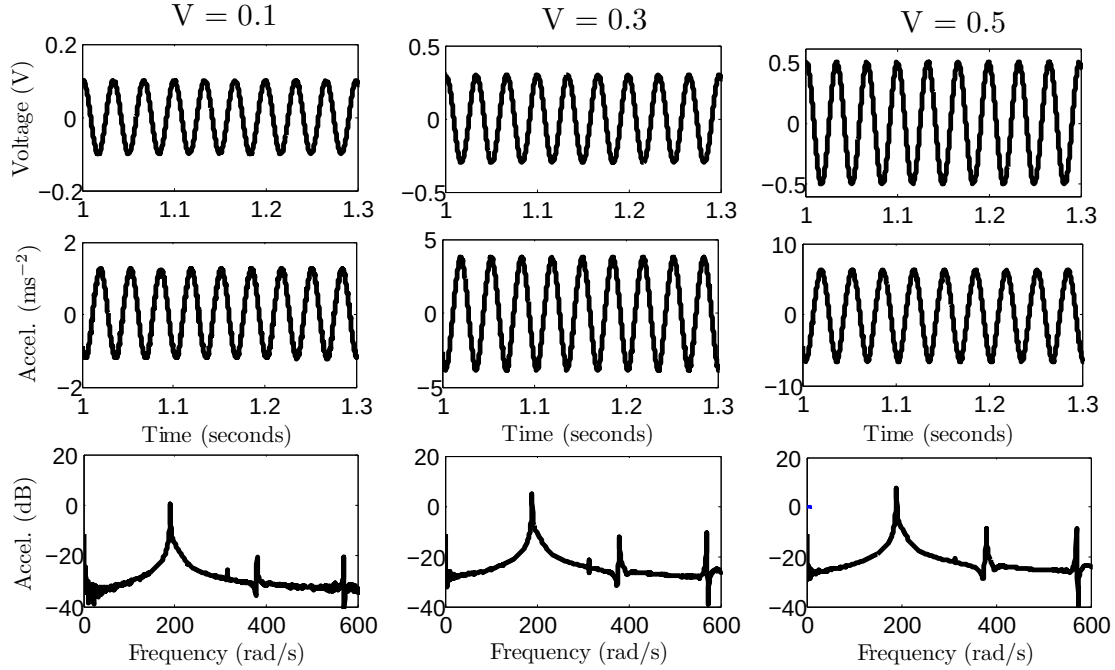

Figure 6.6: Voltage-time signals, acceleration-time signals, and acceleration-frequency spectrum for $\omega = 190$ rad/s.

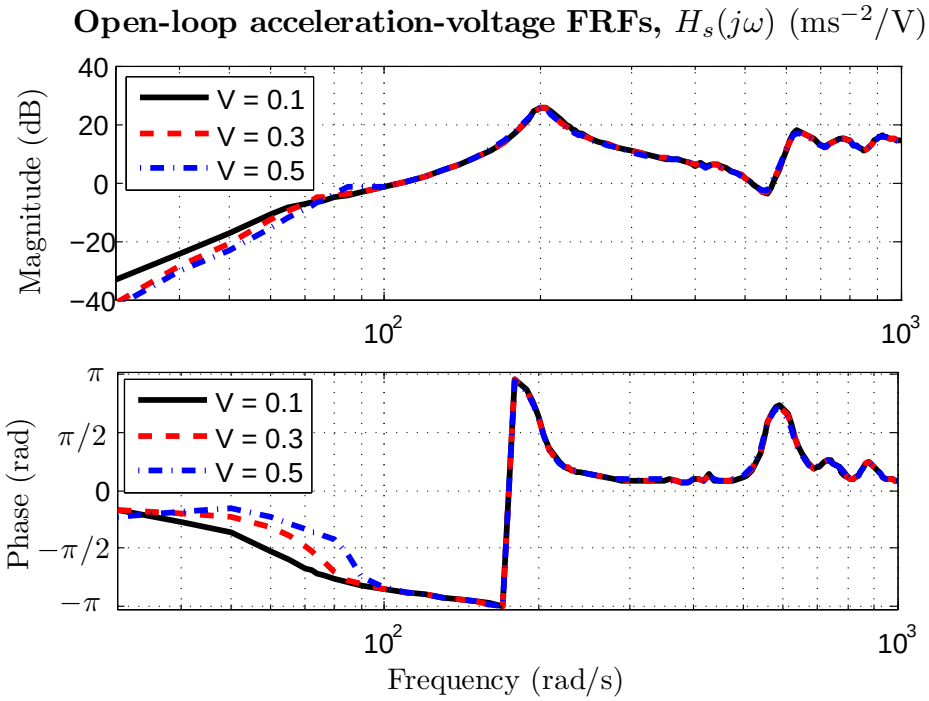

Figure 6.7: Magnitude and phase of the measured acceleration-voltage FRFs.

Using the stepped-sine method, the first-order acceleration-voltage FRFs, which represent the open-loop plant dynamics, are obtained from the measured voltage-time and acceleration-time signals. By comparing these FRFs with the measured force-voltage FRFs shown in Figure 6.4, it is evident that there are various features of interest for the open-loop plant dynamics. Firstly, the second plate mode ($\omega_{21} \approx 420$ rad/s) is unobservable, since the accelerometer is located at the centre of the plate. Therefore, this mode has little effect on the closed-loop stability.

Secondly, we can confirm that the first plate resonance is the dominant mode in the frequency range of interest, and therefore, we are primarily interested in ensuring that this mode is sufficiently controlled using velocity feedback control.

Thirdly, the actuator mode dominates the actuator-plate dynamics at low frequencies ($\omega < 100$ rad/s), where the plate provides a constant phase shift (π rad). In contrast, the amplitude and phase spectra are primarily dictated by the plate dynamics at high frequencies ($\omega \geq 100$ rad/s), where the actuator behaves as an ideal force generator.

Fourthly, the phase spectra in Figure 6.7 show that the higher-order modes lie in the same phase quadrant as the first plate mode, which indicates that the feedback control will have similar effects on all the plate modes in the frequency range of interest, provided that the dynamics of the controller are negligible in this frequency region.

6.2.3 Controller dynamics

In most practical vibration control applications, a digital controller is used to generate the control signal(s) from the structural acceleration signal(s), since these controllers offer a greater degree of flexibility with respect to their analogue counterparts. The dynamics of the controller are specified by $G(j\omega)$, which represents the transfer function between the generated control signal(s) and the input accelerometer signal(s).

By considering the use of velocity feedback control (VFC) to apply active damping to the first plate resonance, the simplest type of controller is linear and pure-gain. Here, the ideal controller dynamics may be expressed as,

$$G(j\omega) = \frac{h}{j\omega} \tag{6.1}$$

where h is the feedback gain. However, for practical reasons, it is necessary to consider additional processing elements in the controller. Firstly, a digital band-pass filter, with discrete transfer function $L(z)$, is applied to the accelerometer signal for the purpose of removing the DC offset to prevent drift and limiting the control bandwidth by attenuating the higher-order out-of-band plate modes. Secondly, the continuous-time integrator is replaced with an equivalent discrete-time model, denoted by $I(z)$. By implementing the band-pass filters before and after the integrator, the practical filtered controller dynamics can be described in the z-domain as follows,

$$G(z) = hL^2(z)I(z) \tag{6.2}$$

These two velocity feedback controllers (pure-gain and filtered) are directly implemented in Simulink using a time step $\Delta T = 0.0005$, which corresponds to a lower sampling rate of 2 kHz. The schematics are shown in Figure 6.8.

It is apparent that the combination of band-pass filters and integrator in Eq. 6.2 introduces additional poles and zeros to the open-loop control path $G(j\omega)H_s(j\omega)$, which results in phase shifts that may affect the closed-loop stability. The equivalent continuous-time transfer function of $G(z)$, denoted by $G(j\omega)$, may be obtained from Eq. 6.2 by considering the open-loop control path schematic given in Figure 6.9.

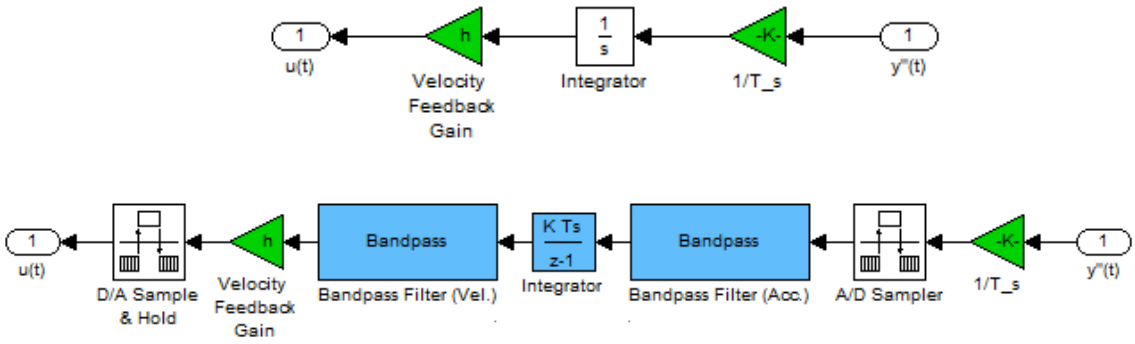

Figure 6.8: Illustration of the pure-gain velocity feedback controller (top) and the filtered velocity feedback controller used in practice (bottom). The additional gain $1/T_s$ compensates for the sensitivities of the accelerometer and conditioner.

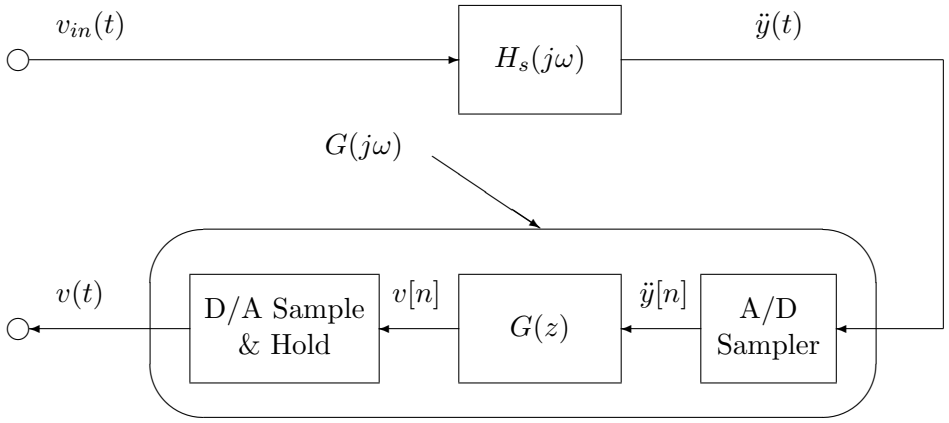

Figure 6.9: Schematic of the open-loop control path, including the plant dynamics, the discrete-time controller, and the equivalent continuous-time controller.

By using the first-order forward Euler method for integration, the dynamics of the discrete-time integrator can be simply written as follows,

$$I(z) = \frac{K\Delta T}{z-1} \tag{6.3}$$

where the gain K is given a value of unity. This discrete-time integrator has a single pole at $z = 1$, which is equivalent to the pole of the continuous-time integrator. In order to minimise the number of additional poles and zeros (and therefore the degree of phase shift in the control signal), the band-pass filter $L(z)$ is defined as a second-order IIR filter, such that the resulting phase shifts are minimised at the expense of a relatively slow rate of attenuation (3 dB per octave). The cutoff frequencies are specified at 38.6 rad/s and

1,930.2 rad/s respectively. Using a Butterworth filter design, the coefficients of the filter result in the following transfer function,

$$L(z) = \frac{0.3323(1 - z^{-2})}{1 - 1.3226z^{-1} + 0.354z^{-2}} \tag{6.4}$$

From Eq. 6.4, it is evident that the band-pass filter has two zeros at $z = -1$ and $z = 1$. The latter zero matches the integrator pole, thereby removing the DC offset through pole-zero cancellation. A Bode plot of the band-pass filter is given in Figure 6.10, which shows that the filter has little effect within the intended band-pass control region (as marked), whereas attenuation is achieved outside the band-pass region by means of a phase lead at low frequencies and a phase lag at high frequencies.

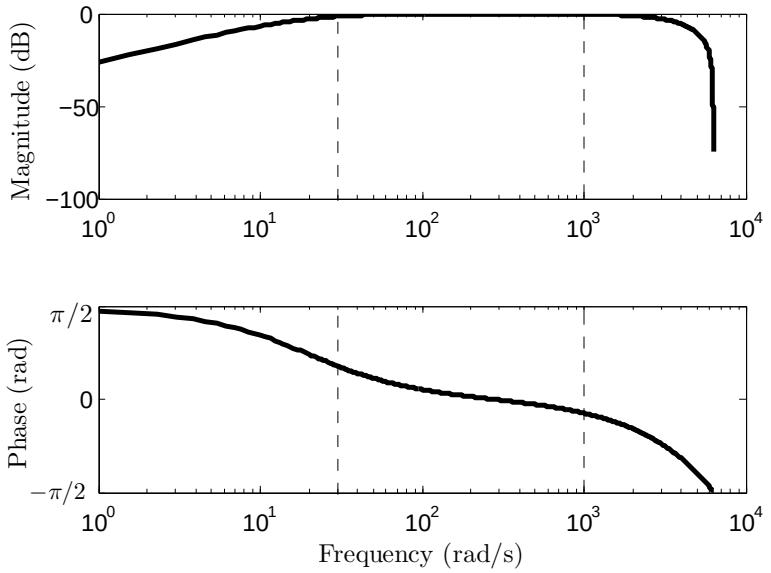

Figure 6.10: Bode plot of the band-pass filter used in the digital controller.

The continuous-time representation $G(s)$ may be obtained by applying Eqs. 6.3 and 6.4 to Eq. 6.2, and then using Tustin's approximation [138], where $z = \mathrm{e}^{s\Delta T}$,

$$G(s) \approx h\frac{0.13s^4 - 427.4s^3 + (4.79 \times 10^6)s^2 + 0.00007s + 0.026}{s^5 + 4370s^4 + (4.93 \times 10^6)s^3 + (3.67 \times 10^8)s^2 + (7.07 \times 10^9)s + 120.8} \tag{6.5}$$

The controller dynamics can then be expressed in the frequency-domain using $G(j\omega) = G(s = j\omega)$. Using this representation, the Bode plot of the open-loop control path dynamics $G(j\omega)H_s(j\omega)$ is ascertained by combining Eq. 6.5 or Eq. 6.1 with the measured

acceleration-voltage FRF (obtained at $V = 0.1$ Volts) in Figure 6.7. This Bode plot, which is shown in Figure 6.11, indicates that the phase spectrum undergoes a full 2π rad shift for both controllers as the excitation frequency increases, thereby revealing that the closed-loop system is conditionally stable. The inclusion of the band-pass filters has a profound effect on the phase spectrum in the low-frequency region, where the crossover frequency ω_c is increased from $\omega_c \approx 60$ rad/s to $\omega_c \approx 80$ rad/s due to the phase shift. This is a trade-off for ensuring that the DC and low-frequency components of the control signal are sufficiently attenuated with a low-order filter.

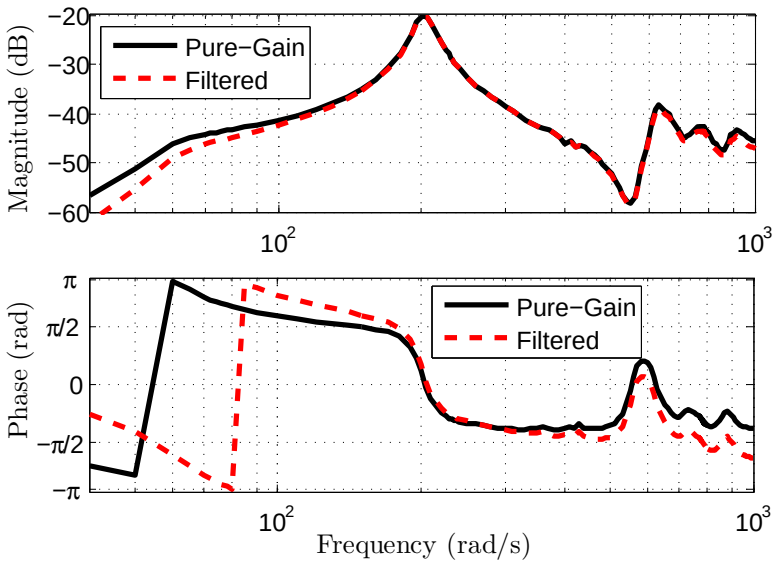

Figure 6.11: Bode plot of the open-loop control path $G(j\omega)H_s(j\omega)$ for $h = 1$.

6.3 System analysis and identification

Using the experimentally ascertained open-loop plant dynamics, the next step is to devise a model that is capable of emulating these dynamics. For this purpose, we utilise the nonlinear two-degree-of-freedom lumped parameter model established in chapter 4, where the structural mass is used to model the first plate resonance. A primary disturbance $f_p(t)$ is assumed to act directly on the structural mass, whereas the secondary electromotive force $f_e(t)$, which is proportional to the control signal $v(t)$ by a factor of g_a, is applied between the structural mass and the actuator proof-mass.

A state-space representation of the coupled actuator-plate dynamics is defined as follows,

$$\dot{\mathbf{x}} = \mathbf{f}(\mathbf{x}) + \mathbf{B_f} f_p(t) + \mathbf{B_e} v(t) \tag{6.6}$$

where,

$$\mathbf{f}(\mathbf{x}) = \begin{bmatrix} \dot{y}_s(t) \\ \dot{y}_p(t) \\ -\frac{1}{m_s}(c_s\dot{y}_s(t) - c_p\dot{y}_{rel}(t) + k_s y_s(t) - k_{p,1} y_{rel}(t) + F_{sus}(-y_{rel}) + F_{sat}(-y_{rel}) \\ -\frac{1}{m_p}(c_p\dot{y}_{rel}(t) + k_{p,1} y_{rel}(t) + F_{sus}(y_{rel}) + F_{sat}(y_{rel}) \end{bmatrix} \tag{6.7}$$

$$\mathbf{x} = \begin{bmatrix} y_s(t) \\ y_p(t) \\ \dot{y}_s(t) \\ \dot{y}_p(t) \end{bmatrix}, \mathbf{B_f} = \begin{bmatrix} 0 \\ 0 \\ 1/m_s \\ 0 \end{bmatrix}, \mathbf{B_e} = \begin{bmatrix} 0 \\ 0 \\ g_a/m_s \\ -g_a/m_p \end{bmatrix}$$

Here, the actuator nonlinearities are dependent on the relative displacement of the proof-mass and structural mass, denoted by $y_{rel} = y_p - y_s$. Using the identified nonlinear terms given by Eqs. 5.10 and 5.27,

$$F_{sus}(y_{rel}) = k_{p,2} y_{rel}^2 + k_{p,3} y_{rel}^3,$$

$$F_{sat}(y_{rel}) = \begin{cases} k_{sat}\sqrt{|y_{rel} - d_1|}(y_{rel} - d_1) + c_{sat}\dot{y}_{rel} & y_{rel} > d_1 \\ 0 & d_2 \leq \ y_{rel} \leq d_1 \\ k_{sat}\sqrt{|y_{rel} - d_2|}(y_{rel} - d_2) + c_{sat}\dot{y}_{rel} & y_{rel} < d_2 \end{cases} \tag{6.8}$$

If the excitation amplitude is sufficiently low, then the underlying linear dynamics are dominant, and $\mathbf{f}(\mathbf{x})$ may be approximated as $\mathbf{Ax}$, where $\mathbf{A}$ is defined as the open-loop state matrix,

$$\mathbf{A} = \begin{bmatrix} \mathbf{0} & \mathbf{I} \\ -\mathbf{M^{-1}K} & -\mathbf{M^{-1}C} \end{bmatrix} \tag{6.9}$$

Using this linear representation, we wish to apply curve-fitting to the measured FRFs for the purpose of obtaining the modal mass (m_s), damping (c_s), and stiffness (k_s) parameters of the plate structure. This is achieved using the first-order velocity-voltage FRF, denoted by $H_v(j\omega)$, which defines the linear structural velocity response to an actuator input voltage. The velocity-voltage FRF at $V = 0.1$ Volts may be simply obtained from the

equivalent acceleration-voltage FRF,

$$H_v(j\omega) = \frac{H_s(j\omega)}{j\omega} \tag{6.10}$$

The velocity-voltage transfer function may then be modelled using the following state-space representation,

$$\hat{H}_v(j\omega) = \mathbf{C_v}(j\omega\mathbf{I} - \mathbf{A})^{-1}\mathbf{B_e} \tag{6.11}$$

where,

$$\mathbf{C_v} = \begin{bmatrix} 0 & 0 & 1 & 0 \end{bmatrix} \tag{6.12}$$

We assume that the linear actuator parameters obtained in chapter 5 are sufficiently accurate to be directly applied to the state-space model. This leaves the modal parameters of the first plate resonance to be obtained by curve-fitting the model to the measured velocity-voltage FRF at $V = 0.1$ Volts. A nonlinear least-squares method is used to minimise the error between the measured and modelled velocity-voltage FRFs, which is used as the basis of the cost function $J(m_s, c_s, k_s)$,

$$J(m_s, c_s, k_s) = \left\| \hat{H}_v(j\omega, m_s, c_s, k_s) - H_v(j\omega) \right\| \tag{6.13}$$

By minimising $J(m_s, c_s, k_s)$ using MATLAB's fmincon function, the modal parameters of the first plate resonance are ascertained, and are shown in Table 6.2.

A comparison of the measured and modelled velocity-voltage FRFs for the underlying linear system is illustrated in Figure 6.12. The figure confirms that the lumped-parameter model is able to accurately simulate the underlying linear actuator-plate dynamics around the actuator peak resonance and the first plate resonance. This serves as justification for utilising the pre-determined values for $(m_p, k_{p,1}, c_p, g_a)$, as specified in the previous chapter.

The next step is to ensure that the lumped-parameter model is able to account for the nonlinear dynamics of the actuator-plate configuration, as illustrated in Figures 6.4 and 6.7. Since the plate dynamics are assumed to be linear, the structural parameters are kept constant, and the nonlinear behaviour is determined by the actuator nonlinearities, as shown in Eq. 6.8.

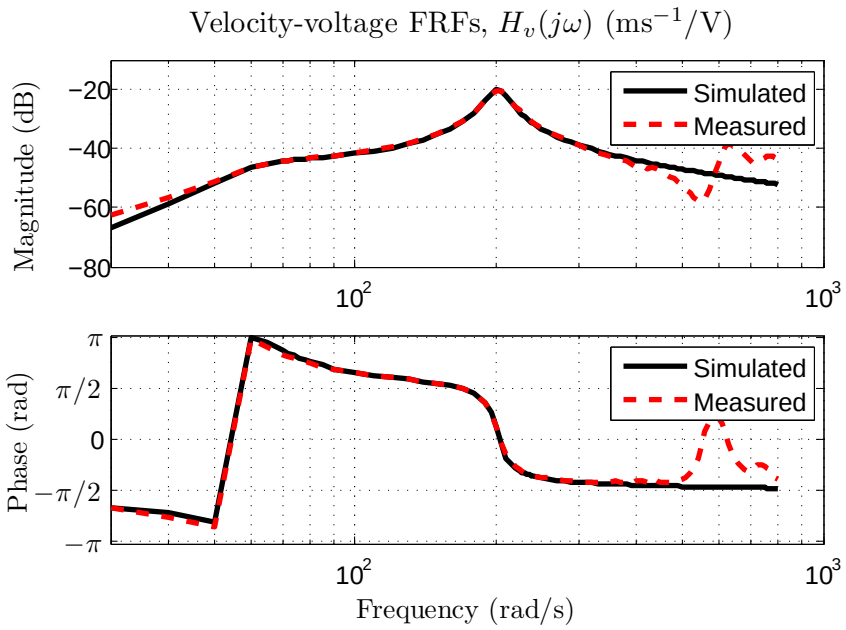

Figure 6.12: Bode plot of simulated and measured velocity-voltage FRF for V = 0.1 Volts

In this case, we cannot assume that the pre-determined parameter values of the actuator nonlinearities are accurate enough to be directly implemented in the model, since these parameters are affected by the mounting conditions. Instead, the nonlinear suspension parameters ($k_{p,2}$ and $k_{p,3}$) are modified slightly from their pre-determined values. It was found that the best results were achieved when these parameters were reduced to about two-thirds of their previous values. These new parameter values are given in Table 6.2.

Furthermore, the nonlinear saturation stiffness parameter k_{sat}, which is identified in chapter 5, is altered by a similar factor, such that the end stops are slightly softer. The modified parameter value is shown in Table 6.2. The pre-determined stroke lengths (d_1 and d_2) obtained in chapter 5 are implemented directly in the lumped-parameter model without modification, since these values are an intrinsic property of the actuator.

Using these parameter values, the nonlinear lumped-parameter model is constructed in Simulink for the purpose of simulating the structural velocity-time and displacement-time signals. By using monoharmonic excitation, the simulated velocity-voltage FRFs are obtained using the stepped sine method. Figures 6.13 and 6.14 show a comparison of the simulated first-order velocity-voltage FRFs, obtained at $V = 0.3$ and $V = 0.5$ Volts respectively, with the equivalent measured velocity-voltage FRFs. These illustra-

Table 6.2: Parameter values used in the model of the actuator-plate configuration.

Parameter	**Value**	**Parameter**	**Value**	**Parameter**	**Value**
m_s	0.162 kg	m_p	0.032 kg	g_a	0.3
c_s	1.7 Ns/m	c_p	1.3 Ns/m	d_1	1.49×10^{-3} m
k_s	6525.4 N/m	c_{sat}	20 Ns/m	d_2	-0.91×10^{-3} m
-	-	$k_{p,1}$	120.56 N/m	-	-
-	-	$k_{p,2}$	-4.93×10^4 N/m^2	-	-
-	-	$k_{p,3}$	7.41×10^7 N/m^3	-	-
-	-	k_{sat}	4.64×10^8 N/m$^{3/2}$	-	-

tions indicate that the model is able to emulate the first-order nonlinear dynamics of the actuator-plate configuration at the actuator mode and first plate resonance to a high degree of accuracy.

As a means of confirming that the lumped-parameter model also yields accurate responses in the time-domain, the acceleration-time signals[1] are simulated at $\omega = 80$ rad/s, using the excitation amplitudes $V = 0.3$ Volts and $V = 0.5$ Volts. In this frequency

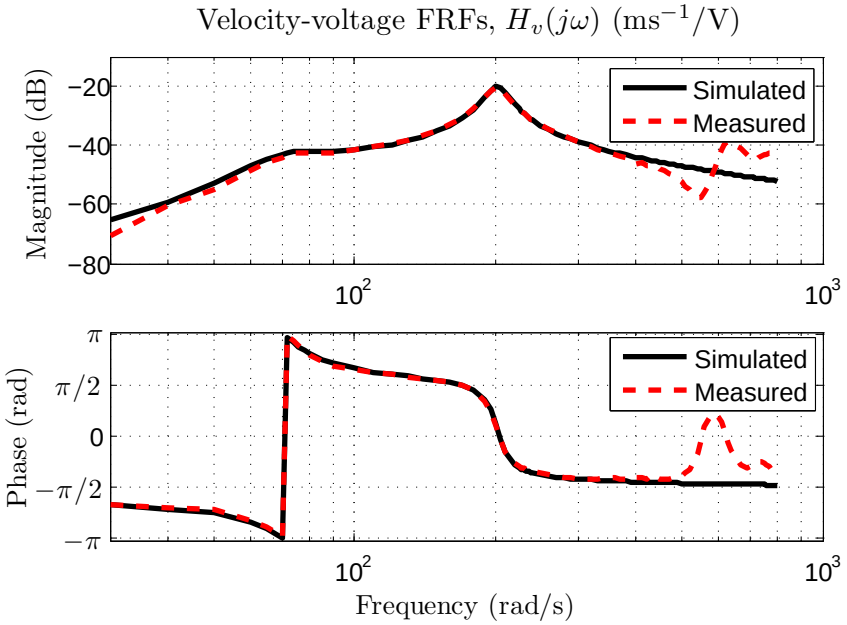

Figure 6.13: Bode plot of simulated and measured velocity-voltage FRF for V = 0.3 Volts

[1]The acceleration-time signals are chosen because they contain a relatively large degree of harmonic information. Due to the low-pass filtering effect of integration, a model that can reasonably simulate the acceleration-time signals will also be able to simulate the velocity-time and displacement-time signals.

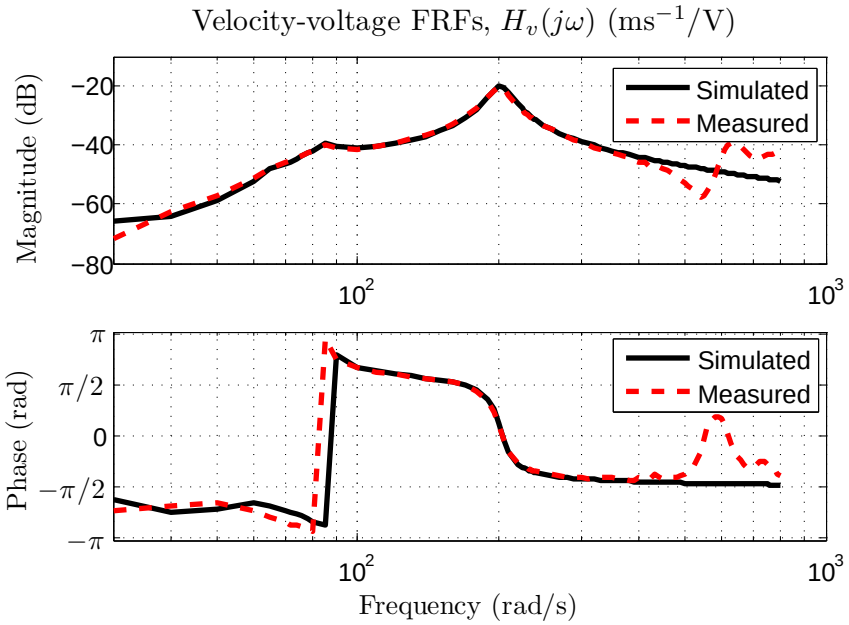

Figure 6.14: Bode plot of simulated and measured velocity-voltage FRF for V = 0.5 Volts

region, the nonlinear actuator dynamics dominate the system response, such that we can expect to observe the effects of the actuator nonlinearities. These simulated signals are then compared with the equivalent measured signals in the time- and frequency-domains, as shown in Figure 6.15.

At $V = 0.3$ Volts, harmonic distortion is apparent in both the simulated and measured time-domain signals. The two signals match closely, with some very minor discrepancies. This is not surprising, given that the actuator model is optimised for rigid block dynamics. Analysing the acceleration spectra confirms that the two signals are well-matched at the fundamental frequency, yet small discrepancies are present in the harmonics. These discrepancies are small enough to be neglected.

A similar comparison can be observed at $V = 0.5$ Volts, where impulses that are present in both of the time-domain signals indicates that stroke saturation is occurring. The magnitude of the impulses are well matched, yet the impulses observed in the simulated time-domain signal occur in the positive direction, whereas the impulses occur in both directions in the measured time-domain signal. This is because the proof-mass impacts with only one of the end-stops in the simulated time-domain signal. Again, the discrepancy may be attributed to the fact that the actuator stroke length is optimised for rigid block dynamics. Having said this, the lumped-parameter model is very sensitive to small changes in the excitation amplitude, and so this discrepancy is relatively minor.

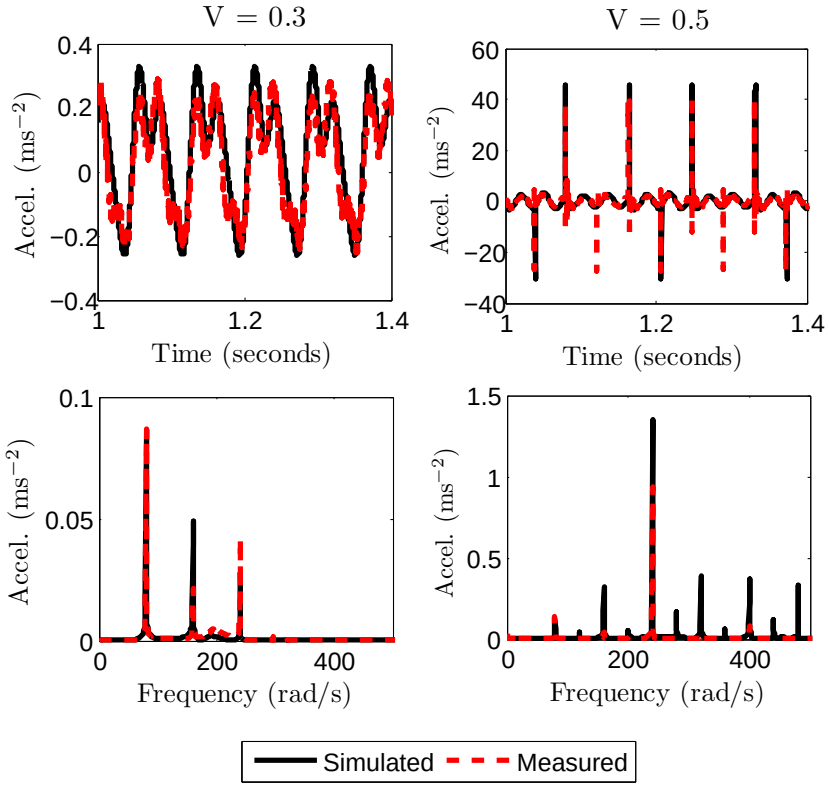

Figure 6.15: Comparison of simulated (solid line) and measured (dashed line) structural acceleration response in the time- and frequency-domains. The simulated signals are obtained in Simulink using the lumped-parameter model.

The acceleration spectra confirm that the response at the fundamental frequency is well-matched, with small discrepancies occurring at the harmonics. Again, these discrepancies are relatively minor, and can also be neglected.

To summarise, the identified lumped-parameter model is able to emulate the dynamics of the actuator-plate configuration with a sufficient degree of accuracy. The stability of the model is now analysed as a means of assessing the stability of the physical system.

6.4 Stability analysis

6.4.1 Root locus and linear Nyquist stability criterion

The underlying stability of the actuator-plate configuration is determined from the closed-loop poles, which may be found from the roots of the characteristic equation,

$$1 + G(j\omega)H_s(j\omega) = 0 \tag{6.14}$$

A model of the underlying linear acceleration-voltage transfer function is obtained from Eq. 6.11,

$$H_s(s) = \frac{1200s^4}{648s^4 + 38,325s^3 + (2.93 \times 10^7)s^2 + (1.09 \times 10^9)s + 9.8 \times 10^{10}} \tag{6.15}$$

By considering this model in conjunction with the pure-gain and filtered velocity feedback controllers given in Eqs. 6.1 and 6.5, the root locus of the open-loop control path $G(j\omega)H_s(j\omega)$ is ascertained for increasing feedback gain h, as shown in Figures 6.16a) and 6.16b). Here, it is apparent in the figures that the closed-loop actuator poles move to the right-hand side of the complex plane as the velocity feedback gain is increased, which confirms that the underlying linear closed-loop system is conditionally stable for both controller types. In Figure 6.16b), it can be seen that the bandpass filters introduce a complex conjugate zero pair on the right-hand side of the complex plane, which indicates that the phase of the control path is non-minimum.

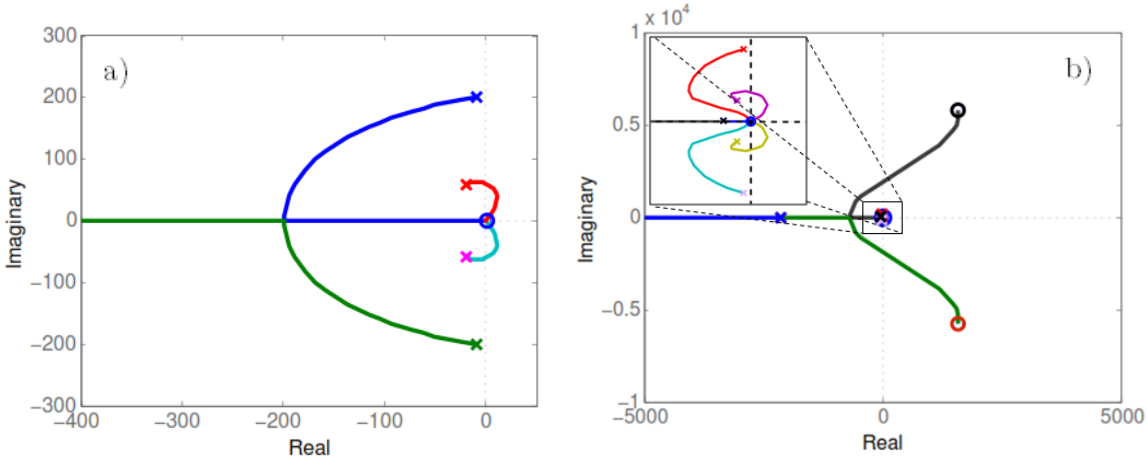

Figure 6.16: Root loci of closed-loop system, for the a) pure-gain controller and b) filtered controller (a zoomed-in view is shown around the origin).

As the feedback gain increases further, the root loci associated with the filters moves towards these zeros, thereby resulting in an additional pair of unstable closed-loop poles. This indicates that the dynamics of the filtered controller are detrimental to the stability of the closed-loop system. Having said this, the closed-loop actuator poles become unstable earlier than the poles of the filters, and so the actuator dynamics remain the primary cause of instability.

Using Cauchey's argument principle [139], the number of unstable poles Z for the closed-loop system (*i.e.* the number of zeros in Eq. 6.14 that lie in the right-hand complex plane) is equvialent to the sum of the number of clockwise encirclements N of the $(-1, j0)$ point made by the locus of $G(j\omega)H_s(j\omega)$ and the number of unstable open-loop poles P,

$$Z = N + P \tag{6.16}$$

The reduced Nyquist contour $\Gamma = j\omega, \omega = 0 \rightarrow \pm\infty$ rad/s is used to encompass the right-hand complex plane, such that the presence of unstable closed-loop poles is revealed by $G(\Gamma)H_s(\Gamma)$ encircling the $(-1, j0)$ point. Therefore, provided that the open-loop system is stable and the $(-1, 0)$ point is not clockwise encircled in the Nyquist plot of $G(j\omega)H_s(j\omega)$, the closed-loop system is also stable.

The absolute and relative stability of the closed-loop system is ascertained from the number of clockwise encirclements of the origin in the Nyquist plot of $G(j\omega)H_s(j\omega)$. If the origin is not encircled in a clockwise direction, then the closed-loop system is absolutely and unconditionally stable. However, if the origin is encircled at least once in the clockwise direction, with crossover frequency ω_c at the point $(-k, j0)$, $0 < k < 1$, then the closed-loop system is conditionally stable, with a gain margin $G_m = 1/k$. To ensure that the closed-loop stability is robust to small uncertainties and variations in the plant or controller dynamics, a gain margin of at least 10 dB is desirable.

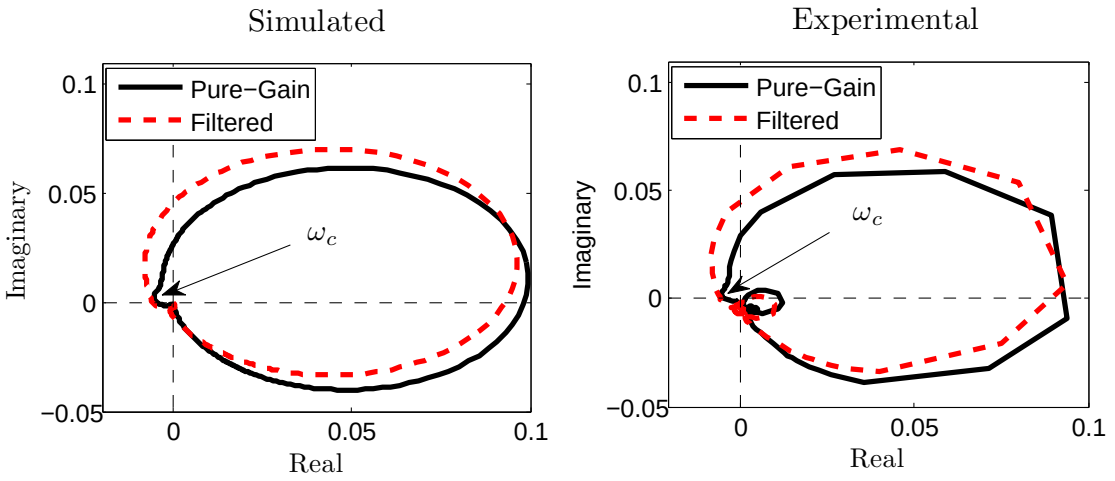

Figure 6.17: Nyquist plots of the open-loop control path when VFC is used. The additional encirclements in the experimental Nyquist plots are attributed to the higher-order plate modes.

As a means of comparison, we examine the Nyquist plots of $G(j\omega)H_s(j\omega)$ in Figure 6.17, where $H_s(j\omega)$ is either the model defined in Eq. 6.15 (simulated) or the measured acceleration-voltage FRF (experimental). Here, both controllers types are considered, and their effects on the Nyquist plots are observed, particularly with regards to the unmodelled higher-order modes. The gain margin G_m and crossover frequency ω_c of the closed-loop system is obtained for each Nyquist plot, and are shown in Table 6.3.

These Nyquist plots convey plenty of information on the aspects of the closed-loop stability, with three particularly noteworthy characteristics. Firstly, it is apparent that the closed-loop system is conditionally stable, regardless of the controller dynamics. The cut-off frequency ω_c is close to the actuator peak resonance frequency, which indicates that the actuator mode is amplified by the velocity feedback control, eventually destabilising the closed-loop system when the locus encircles the $(-1, j0)$ point. Secondly, the inclusion of filtering in the controller dynamics has the effect of reducing the gain margin and introducing an additional crossover frequency ($\omega_c = 1,911$ rad/s) at higher frequencies, which indicates that the closed-loop system is susceptible to high-frequency spillover. Since the gain margin at this crossover frequency ($h = 1,924$) is far greater than the gain margin of the actuator mode, this can be neglected. Thirdly, the higher-order unmodelled plate modes shown in Figure 6.17 primarily lie on the right-hand side of the Nyquist plot, which indicates that they will be attenuated by the velocity feedback control, albeit to a lesser degree.

Table 6.3: Gain margins of the closed-loop system. Once the control gain exceeds the value shown here, the $(-1, j0)$ point is encircled, and the closed-loop system becomes unstable.

Nyquist Plot	**Pure-gain controller**	**Filtered controller**
G_m (simulation)	$h = 216$	$h = 172.7$
G_m (experimental)	$h = 230.1$	$h = 172.9$
ω_c (simulation)	60 rad/s	82 rad/s
ω_c (experimental)	58 rad/s	81 rad/s

Comparing the gain margins and crossover frequencies of the simulated and experimental Nyquist plot indicates good agreement, particularly when the filtered controller dynamics are considered. This confirms that the state-space model is a sufficient representation of the underlying linear physical system.

The band-pass filters introduce a phase lead at low frequencies and a phase lag at high frequencies. The phase lead increases the crossover frequency around the actuator mode and reduces the gain margin by about $20 - 25$ %, whereas the phase lag shifts the higher-order out-of-band modes further to the left of the Nyquist plot. This renders the closed-loop system conditionally stable as a result of high-frequency spillover. Having said this, these modes are attenuated by the low-pass filter, and so the amplification of the actuator mode remains the primary cause of closed-loop instability.

As a means of confirmation, the roots of the characteristic equation $1 + G(s)H_s(s)$, defined as $\lambda(h)$, are found numerically as a function of the feedback gain h. The condition for stability is $\mathrm{Re}(\lambda(h)) < 0$. Figure 6.18 shows a comparison of the roots obtained for both types of controller dynamics. The figure shows that the stability condition is satisfied for feedback gains $h < G_m$, where the gain margins G_m are shown in Table 6.3. This confirms that the estimated gain margins are accurate for the underlying linear system.

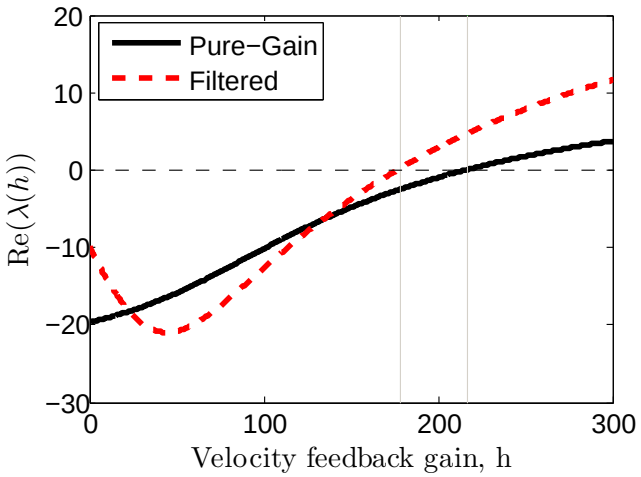

Figure 6.18: Roots of the characteristic equation against h for pure-gain and filtered controller dynamics. The gain margins stated in Table 6.3 are shown as solid grey lines, and it is apparent that the stability threshold is close to these values.

In order to demonstrate the effects of VFC on the time responses of the actuator-plate configuration, the Simulink model (illustrated in Appendix E) is modified to include the feedback loop using the parameters obtained in the previous section. For this example, the actuator nonlinearities are ignored. The closed-loop structural displacement (y_s), proof-mass displacement (y_p), and relative displacement (y_{rel}) responses to a 1 Newton impulse (of duration 1 millisecond) are simulated for three feedback gains using the Simulink model. These simulated signals are illustrated in Figure 6.19.

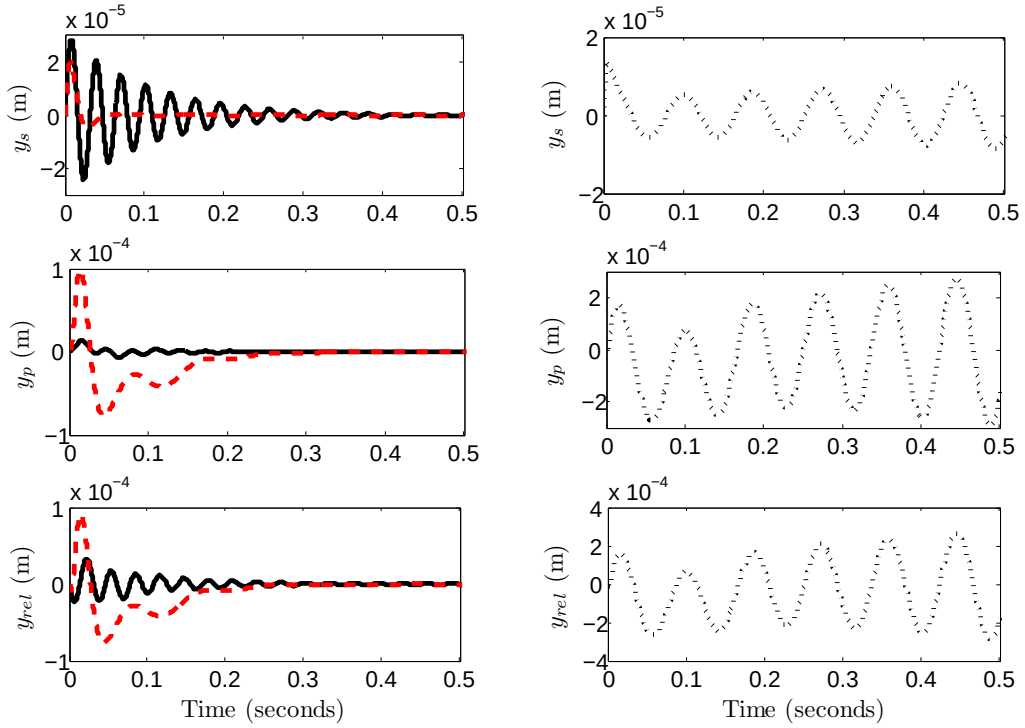

Figure 6.19: Structural time responses of the Simulink actuator-plate model to an impulsive input for control gains $h = 0$ (solid line), $h = 50$ (dashed line), and $h = 200$ (dotted line).

These time responses confirm the dynamic effects shown in the Nyquist plots in Figure 6.17. Initially, the open-loop impulse responses indicate that the structural displacement is relatively large, whereas the proof-mass displacement and relative displacement are small in amplitude. Applying VFC with a relatively small feedback gain ($h < G_m$) has the effect of attenuating the structural displacement whilst amplifying the proof-mass displacement and relative displacement. When the feedback gain is increased above the specified gain margin ($h > G_m$), the closed-loop system becomes unstable. The low-frequency oscillation is associated with the amplification of the actuator mode by the feedback controller, as shown in Figures 6.17 and 7.3.

Although the filters are detrimental to closed-loop stability, the effects are relatively minor, and a relatively large gain margin is retained. This ensures that it is possible to implement a considerable increase in the damping of the plate mode before instability occurs, provided that the displacements are very small and the assumption of linearity holds.

6.4.2 Nonlinear Nyquist stability and circle criteria

Now that the closed-loop stability of the underlying linear plant has been assessed, the effects of the actuator nonlinearities on the stability margin are analysed. From Eq. 6.8, it is evident that the actuator nonlinearities are dependent on the relative displacement of the actuator-plate configuration; we therefore consider an alternative state-space model in order to emulate the nonlinear system with a Lur'e representation. Since the controller is linear, we can account for its dynamic effects in the linear feedforward path, such that the actuator nonlinearities are exclusively used in the feedback path. This is achieved by modifying the linear state matrix $\mathbf{A}$, which is given by Eq. 6.9. By substituting $v(t) = -hsG(s)\mathbf{C_v}$ and $\mathbf{f}(\mathbf{x}) = \mathbf{Ax}$ into Eq. 6.6, the state matrix becomes $\mathbf{A_h}$ as a result of the feedback control, where,

$$\mathbf{A_h} = \mathbf{A} - hsG(s)\mathbf{B_e}\mathbf{C_v} \tag{6.17}$$

Using this modification, the closed-loop actuator-plate configuration can be modelled using the Lur'e representation shown in Figure 6.20. In this case, the state equations may be written as,

$$\dot{\mathbf{x}} = \mathbf{A_h}\mathbf{x} + \mathbf{B_p}f_p + \mathbf{B_n}\mathbf{u_{nl}}, \quad y_{rel} = \mathbf{C_{rel}}\mathbf{x}, \quad \mathbf{u_{nl}} = \mathbf{f_{nl}}(y_{rel}) \tag{6.18}$$

where,

$$\mathbf{B_n} = \begin{bmatrix} 0 & 0 \\ 0 & 0 \\ -\frac{1}{m_s} & \frac{1}{m_s} \\ -\frac{1}{m_p} & -\frac{1}{m_p} \end{bmatrix}, \mathbf{C_{rel}} = \begin{bmatrix} -1 & 1 & 0 & 0 \end{bmatrix}, \mathbf{f_{nl}}(y_{rel}) = \begin{bmatrix} k_{p,2}y_{rel}^2 \\ k_{p,3}y_{rel}^3 + F_{sat}(y_{rel}) \end{bmatrix} \tag{6.19}$$

Here, it is evident that the actuator-plate configuration is expressed as a *multi-input single-output* (MISO) system, where the actuator nonlinearities are subdivided into two independent inputs. The first input contains the even-order, asymmetric nonlinearities and the second input contains the odd-order, symmetric nonlinearities. This is because the function $F_{sus}(y_{rel})$ contains even-order and odd-order nonlinearities, and so there is no direct relation between $F_{sus}(y_{rel})$ and $F_{sus}(-y_{rel})$,

$$\begin{aligned} F_{sus}(y_{rel}) &= k_{p,2}y_{rel}^2 + k_{p,3}y_{rel}^3, \\ F_{sus}(-y_{rel}) &= k_{p,2}y_{rel}^2 - k_{p,3}y_{rel}^3 \neq \pm F_{sus}(y_{rel}) \end{aligned} \tag{6.20}$$

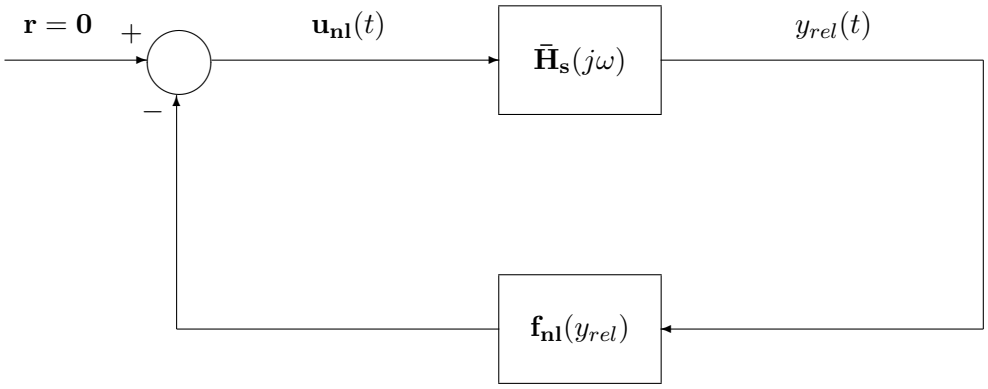

Figure 6.20: Lur'e representation of the actuator-plate configuration, where the linear closed-loop plant dynamics are included in the feedforward path, and the actuator nonlinearities are included in the feedback path.

The transfer function of the linear feedfoward path, denoted by $\bar{\mathbf{H}}_\mathbf{s}(j\omega)$, may be expressed as,

$$\bar{\mathbf{H}}_\mathbf{s}(j\omega) = \begin{bmatrix} \bar{H}_{s,1}(j\omega) & \bar{H}_{s,2}(j\omega) \end{bmatrix} = \mathbf{C_{rel}}(j\omega\mathbf{I} - \mathbf{A_h})^{-1}\mathbf{B_n} \tag{6.21}$$

Using these transfer functions, the occurrence of limit-cycle oscillations (LCO) may be predicted by replacing the actuator nonlinearities with their equivalent describing functions,

$$\mathbf{f_{nl}}(y_{rel}) \approx \mathbf{N}(y_{rel}) = \begin{bmatrix} N_1(y_{rel}) \\ N_2(y_{rel}) \end{bmatrix} \tag{6.22}$$

Using the nonlinear Nyquist criterion, the characteristic equation for LCO behaviour is,

$$1 + \bar{\mathbf{H}}_\mathbf{s}(j\omega)\mathbf{N}(y_{rel}) = 0 \tag{6.23}$$

and, with some abuse of notation, the condition for the existence of LCO behaviour is therefore,

$$N_1(y_{rel})\bar{H}_{s,1}(j\omega) + N_2(y_{rel})\bar{H}_{s,2}(j\omega) = -1 \tag{6.24}$$

Satisfying this condition is clearly more complicated than for the SISO case, due to the dependency of two terms. However, we can simplify the analysis by making a few statements,

1. A LCO has a particular amplitude Y_{rel} and frequency ω_c that must satisfy both terms.
2. Both terms of $\bar{\mathbf{H}}_{\mathbf{s}}(j\omega_c)$ should be purely real.
3. At least one term of $\bar{\mathbf{H}}_{\mathbf{s}}(j\omega_c)$ should be negative, since $\mathbf{N}(y_{rel}) > 0$.

These statements indicate that for a LCO to exist, the Nyquist plots of $H_{s,1}(j\omega)$ and $H_{s,2}(j\omega)$ should both cross the negative real axis at ω_c, which provides a suitable means of estimating the LCO frequency. Whilst it is possible to estimate the amplitude Y_{rel} of the LCO using the describing function representation, the accuracy of the estimation is poor as the sinusoidal assumption is invalid for the LCO. Instead, we consider the exact nonlinear functions $\mathbf{f_{nl}}(y_{rel})$ and use the circle criterion as a means of estimating the conditions for LCO behaviour. Since the relative displacement is bounded by actuator saturation, this provides a convenient means of providing a sector condition for the actuator nonlinearities.

It should be noted that this approach does not work well when the effects of actuator saturation are accounted for, as the sector condition varies greatly with small changes in y_{rel} when the stroke length is exceeded. However, the approach is very useful at predicting when the actuator-plate configuration will exhibit LCO behaviour before actuator saturation occurs, due to the suspension nonlinearities. In this case, the sector conditions for the nonlinearity are defined for $d_2 \leq y_{rel} \leq 0$, where d_2 is the negative stroke length and the largest displacement that may be considered before stroke saturation occurs. For the suspension nonlinearities, the sector conditions are as follows,

$$\begin{aligned} k_{p,2}y_{rel}^2 \Rightarrow 0 \leq k_{p,2}y_{rel} \leq k_{s1}, \quad k_{s1} = k_{p,2}d_2 \approx 44.86 \\ k_{p,3}y_{rel}^3 \Rightarrow 0 \leq k_{p,3}y_{rel}^2 \leq k_{s2}, \quad k_{s2} = k_{p,3}d_2^2 \approx 61.39 \end{aligned} \tag{6.25}$$

These sector conditions may be applied to the nonlinear system, in order to ascertain the closed-loop stability within the saturation boundaries.

The Nyquist plots of $H_{s,1}(j\omega)$ and $H_{s,2}(j\omega)$ respectively are show in Figures 6.21 (pure-gain controller dynamics) and 6.22 (filtered controller dynamics) as the feedback gain increases. In Figure 6.21a), it is evident that the negative real axis is always crossed, regardless of control gain. The point at which the negative real axis is crossed is relatively independent of the control gain. This is because open-loop systems with purely asymmetric nonlinearities tend to become unstable in one particular direction as the total energy becomes negative (*e.g.* the quadratic oscillator). In this case, open-loop instability is pre-

vented from occurring by the higher-order symmetric suspension nonlinearity. Therefore, the overall stability is primarily determined by the symmetric nonlinearities.

In Figure 6.21b), the Nyquist plots do not cross the negative real axis at the lower feedback gains $h = 0$ and $h = 10$. This indicates that the actuator-plate configuration is unconditionally stable when $h \leq 10$. Conversely, if $h > 10$, then it is apparent that the Nyquist plots cross the negative real axis, thereby satisfying the conditions for potential LCO behaviour in Eq. 6.24. The negative real axis crossing point varies strongly with the feedback gain, becoming increasingly negative as the feedback gain rises. This implies that the closed-loop system is more prone to instability for larger feedback gains, as expected.

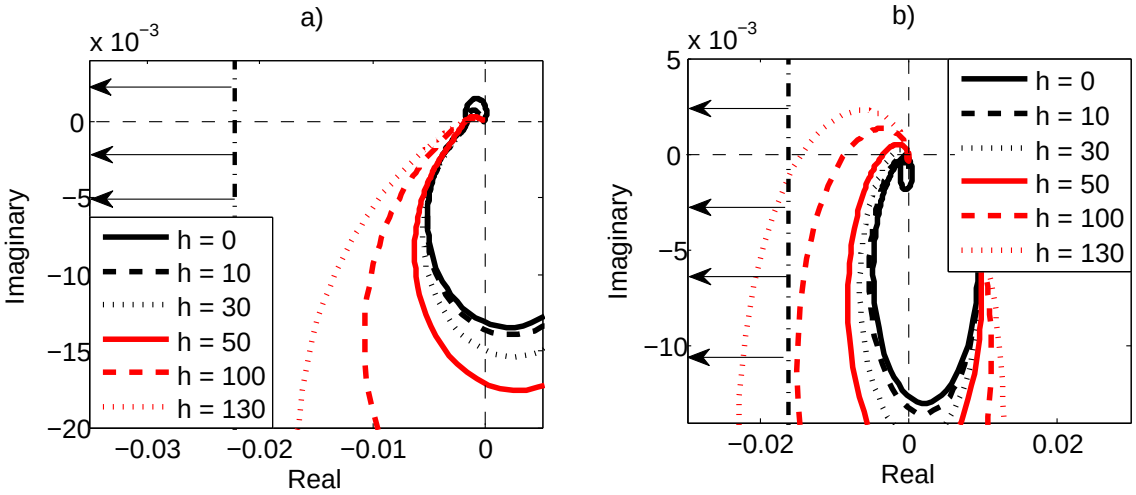

Figure 6.21: Simulated Nyquist plots of $H_{s,1}(j\omega)$ and $H_{s,2}(j\omega)$ for a variety of feedback gains and pure-gain controller dynamics. The instability regions (marked with arrows) is determined by the sector conditions $-1/k_{s1}$ and $-1/k_{s2}$.

The frequency of the negative real crossing point in Figures 6.21a) and 6.21b) varies weakly with the feedback gain, ranging from $\omega_c = 180$ rad/s ($h = 30$) to $\omega_c = 185$ rad/s ($h = 130$). The range of LCO frequencies corresponds to the first natural frequency $\omega_{p,c}$ of the structure when the two masses are rigidly connected; this is because the proof-mass coalesces with the structural mass for a significant period of the LCO as a result of saturation.

$$\omega_{p,c} = \sqrt{\frac{k_s}{m_s + m_p}} \approx 183 \text{ rad/s} \tag{6.26}$$

It is apparent in Figure 6.21a) that the boundary imposed by the circle criterion $(-1/k_{s1})$ is not crossed by the locus, which further implies that the asymmetric suspension nonlinearities have a relatively limited effect on the overall closed-loop stability. Conversely, the boundary $(-1/k_{s2})$ imposed in Figure 6.21b) is crossed in the range $100 < h < 130$. This suggests that the closed-loop system may tend to a LCO before the actuator stroke length is reached, due to the suspension nonlinearities, when the feedback gain is in this range, thereby reducing the closed-loop gain margin.

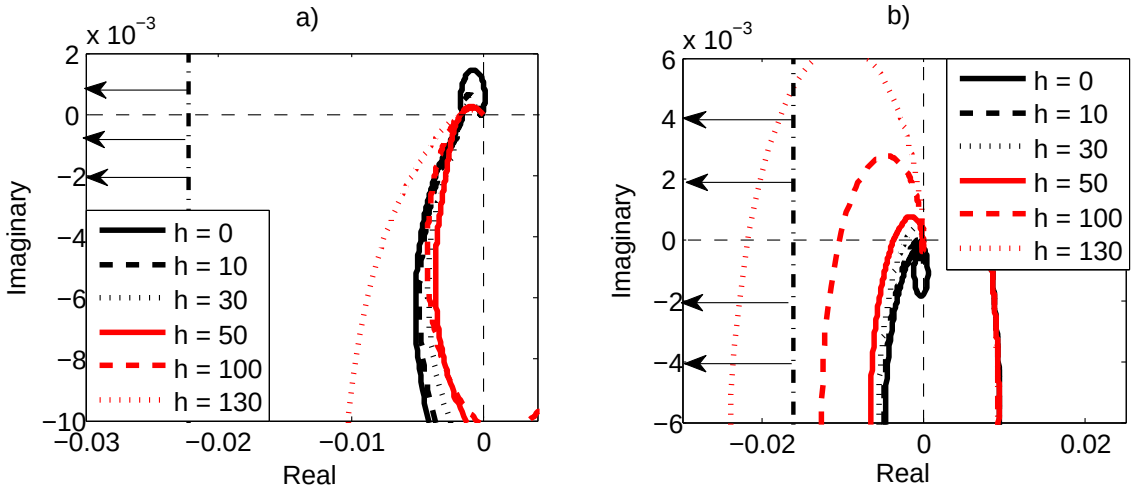

Figure 6.22: Simulated Nyquist plots of $H_{s,1}(j\omega)$ and $H_{s,2}(j\omega)$ for a variety of feedback gains and filtered controller dynamics. The instability regions (marked with arrows) is determined by the sector conditions $-1/k_{s1}$ and $-1/k_{s2}$.

Now, we examine the effects of the filtered controller dynamics on the Nyquist plots, which are shown in Figures 6.22a) and 6.22b). Here, it is apparent that the features described in Figures 6.21 and 6.21b) may also be observed in these figures, which indicates that the effects of the filters are relatively minor. The two key differences are as follows. Firstly, there is a very slight increase in the LCO frequency range as a result of the phase lead introduced by the filters, where $\omega_c = 182$ rad/s $(h = 30)$ to $\omega_c = 187$ rad/s $(h = 130)$. Practically, this increase is negligible. Secondly, the Nyquist plot obtained at $h = 130$ is well outside the boundary imposed by the circle criterion at the negative real axis crossing point, which indicates that the closed-loop system is more prone to instability when the effects of the filters are included in the Nyquist plot.

Using the Simulink model, the relative displacement-time response to a 6 Newton impulse, of duration 1 millisecond, is obtained using the feedback gain $h = 130$ for both types of controller dynamics. These time responses are shown alongside their respective

Fourier transforms in Figure 6.23. It is evident in both cases that the response tends to a LCO under these conditions, thereby confirming that the suspension nonlinearities are capable of reducing the closed-loop gain margin. The frequency of the LCO is 180 rad/s and 182 rad/s respectively, which matches the predictions made using the Nyquist plots. In addition, it can be seen that the time response becomes chaotic when the filter dynamics are included, similar to an experimentally measured LCO. This analysis confirms that the actuator nonlinearities are detrimental to the closed-loop stability by reducing the gain margin and introducing LCO behaviour to the actuator-plate configuration.

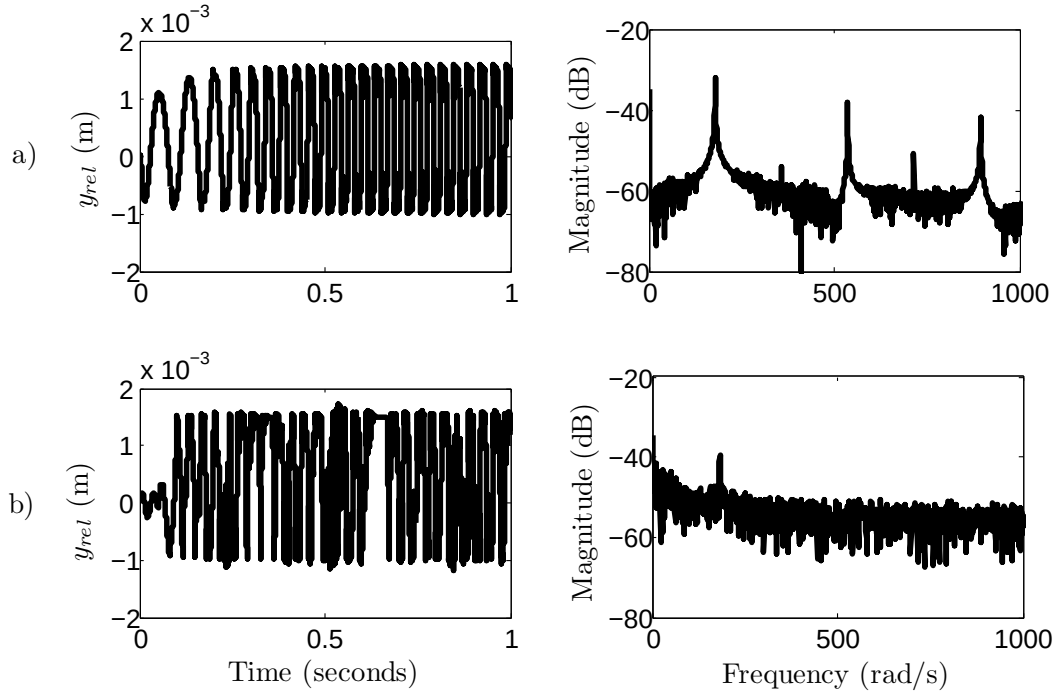

Figure 6.23: Simulated relative displacement response in the time- and frequency-domain, for a) pure-gain and b) filtered controller dynamics, with gain $h = 130$.

6.4.3 Lyapunov exponents

The effects of the actuator nonlinearities on the closed-loop stability margin are now investigated in more detail by considering each nonlinearity separately. By introducing the actuator nonlinearities, the closed-loop stability becomes dependent on the relative displacement amplitude as well as the feedback gain. This dependency can be analysed through the use of Lyapunov exponents. By including the velocity feedback dynamics in the state equations, the nonlinear closed-loop state vector, denoted by $\mathbf{f_c}(\mathbf{x})$, becomes,

$$\mathbf{f_c}(\mathbf{x}) = \mathbf{f}(\mathbf{x}) + \begin{bmatrix} 0 \\ 0 \\ \frac{1}{m_s}\big(g_a v(t)\big) \\ \frac{-1}{m_p}\big(g_a v(t)\big) \end{bmatrix}, \quad v(t) = -hsG(s)\dot{y}_s(t) \tag{6.27}$$

The Jacobian matrix of $\mathbf{f_c}(\mathbf{x})$, denoted by $\mathbf{J}(\mathbf{x})$, is given by,

$$\mathbf{J}(\mathbf{x}) = \begin{bmatrix} \mathbf{0} & \mathbf{I} \\ -\mathbf{M^{-1}}\Big(\mathbf{K} + \frac{\partial \mathbf{F_{nl}(x)}}{\partial \mathbf{x}}\Big) & -\mathbf{M^{-1}C_h} \end{bmatrix}\Bigg|_{\mathbf{x}=\mathbf{x_0}} \tag{6.28}$$

where,

$$\frac{\partial \mathbf{F_{nl}}(\mathbf{x})}{\partial \mathbf{x}} = \frac{\partial \mathbf{F_{sus}}(\mathbf{x})}{\partial \mathbf{x}} + \frac{\partial \mathbf{F_{sat}}(\mathbf{x})}{\partial \mathbf{x}} \tag{6.29}$$

represents the Jacobian matrices of the suspension nonlinearities and saturation nonlinearities respectively. These matrices are defined as,

$$\frac{\partial \mathbf{F_{sus}}(\mathbf{x})}{\partial \mathbf{x}} = \begin{bmatrix} -2k_{p,2}y_{rel} + 3k_{p,3}y_{rel}^2 & 2k_{p,2}y_{rel} - 3k_{p,3}y_{rel}^2 \\ -2k_{p,2}y_{rel} - 3k_{p,3}y_{rel}^2 & 2k_{p,2}y_{rel} + 3k_{p,3}y_{rel}^2 \end{bmatrix} \tag{6.30}$$

$$\frac{\partial \mathbf{F_{sat}}(\mathbf{x})}{\partial \mathbf{x}} = \begin{bmatrix} 1.5k_{sat}\sqrt{|y_{rel} - d_{1,2}|}(1 - d_{1,2}/y_{rel}) & -1.5k_{sat}\sqrt{|y_{rel} - d_{1,2}|}(1 - d_{1,2}/y_{rel}) \\ -1.5k_{sat}\sqrt{|y_{rel} - d_{1,2}|}(1 - d_{1,2}/y_{rel}) & 1.5k_{sat}\sqrt{|y_{rel} - d_{1,2}|}(1 - d_{1,2}/y_{rel}) \end{bmatrix} \tag{6.31}$$

Additionally, the damping matrix $\mathbf{C}$ is modified to $\mathbf{C_h}$ by the velocity feedback control, where,

$$\mathbf{C_h} = \mathbf{C} + \begin{bmatrix} g_a hsG(s) & 0 \\ -g_a hsG(s) & 0 \end{bmatrix} \tag{6.32}$$

The eigenvalues of the Jacobian matrix given by Eq. 6.28 may then be ascertained against the relative displacement y_{rel} and the feedback gain h as the Lyapunov exponents. In order to establish the relative influence of each actuator nonlinearity, the dynamics of the suspension nonlinearity and the saturation nonlinearity are considered separately before analysing the composite nonlinear system. These findings show that each actuator nonlinearity has a different influence on the closed-loop gain margin; the suspension nonlinearities have the greatest effect when large feedback gains and small excitation amplitudes are considered, whereas stroke saturation can destabilise the closed-loop system if the excitation amplitude is sufficiently large at smaller feedback gains.

Suspension Nonlinearities

To assess the effects of the suspension nonlineary on the closed-loop stability independently of the saturation nonlinearity, the Jacobian matrix given in Eq. 6.31 is neglected in $\mathbf{J}(\mathbf{x})$. The Lyapunov exponents of $\mathbf{J}(\mathbf{x})$, which are denoted by $\lambda(y_{rel}, h)$, are obtained for a variety of y_{rel} and h values, and their real parts are shown in Figure 6.24 for the filtered controller. Regions of instability are identified for specific displacements where the real part of the Lyapunov exponents is positive, where the response of the closed-loop system tends to increases away from the equilibrium position. The presence of these unstable regions indicates that the displacement response may tend towards a LCO if the closed-loop system is sufficiently excited.

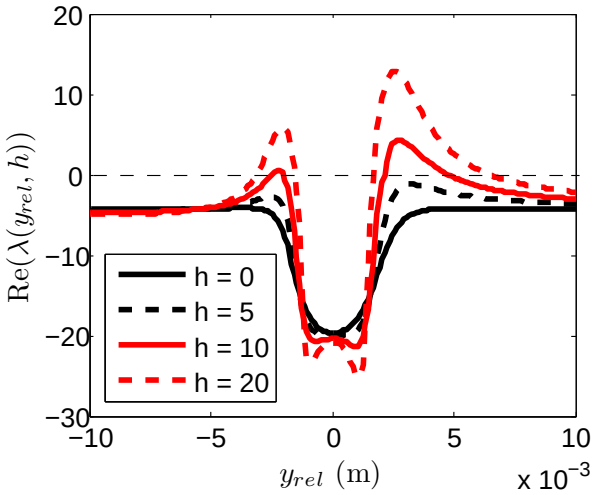

Figure 6.24: Real part of the Lyapunov exponents of $\mathbf{J}(\mathbf{x})$ against y_{rel} and h (filtered controller dynamics).

In Figure 6.24, it is apparent that the eigenvalues are asymmetrical around the equilibrium position as a result of the y_{rel}^2 term in the suspension nonlinearity. We can observe that regions of instability appear when $h > 10$, which are particularly pronounced for positive displacements due to the asymmetric nonlinear behaviour. This finding is consistent with the results obtained in the previous section. The regions of instability are relatively narrow and only occur at specific displacement amplitudes, which corresponds approximately to the amplitude(s) of the LCO. As the feedback gain increases, the regions of instability increase in prominence and width, thereby indicating that the closed-loop system becomes

more prone to instability. This confirms that the suspension nonlinearities, in conjunction with the filtered controller dynamics, are highly detrimental to the overall closed-loop stability.

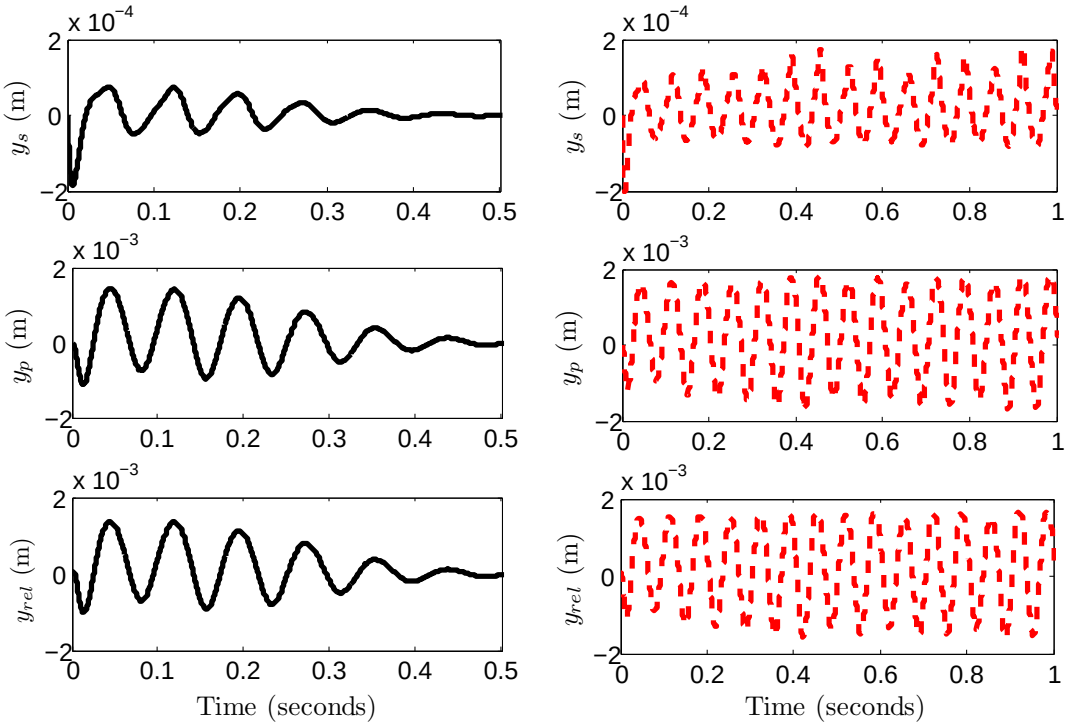

Figure 6.25: Displacement-time responses of the actuator-plate model to an impulsive input using $h = 100$, $F = 10$ N (solid line) and $F = 11$ N (dashed line).

In order to demonstrate the effects of the suspension nonlinearities on the closed-loop stability, several time-domain simulations are shown in Figure 6.25. These illustrations show the closed-loop displacement-time histories of the plate structure, the proof-mass, and their relative displacement, in response to a 10 Newton and 11 Newton impulse respectively. The feedback gain is fixed at $h = 100$, and the duration of the impulse is 1 millisecond.

Here, it can be seen that the system response is stable and tends to the equilibrium position when the smaller impulse is used, yet tends towards a LCO for the larger impulse. This indicates that closed-loop stability margin varies with the excitation amplitude level, where the threshold amplitude is relatively small for large feedback gains ($h \geq 100$). Furthermore, the frequency of the LCO is approximately equivalent to the actuator resonance, which highlights that the actuator mode remains the primary cause of instability.

Saturation nonlinearities

Next, we focus on the effects of stroke saturation on the closed-loop stability margin by neglecting the suspension nonlinearities in a similar manner to the previous case. Here, the actuator-plate configuration behaves as a linear system within the stroke limit (where the Jacobian matrix $\mathbf{J}(\mathbf{x})$ is equivalent to the closed-loop state matrix $\mathbf{A_h}$), whilst exhibiting nonlinear behaviour once the stroke limit is exceeded and stroke saturation occurs. The Lyapunov exponents of the Jacobian matrix are shown against y_{rel} and h in Figure 6.26 for the purpose of identifying the regions of instability associated with stroke saturation.

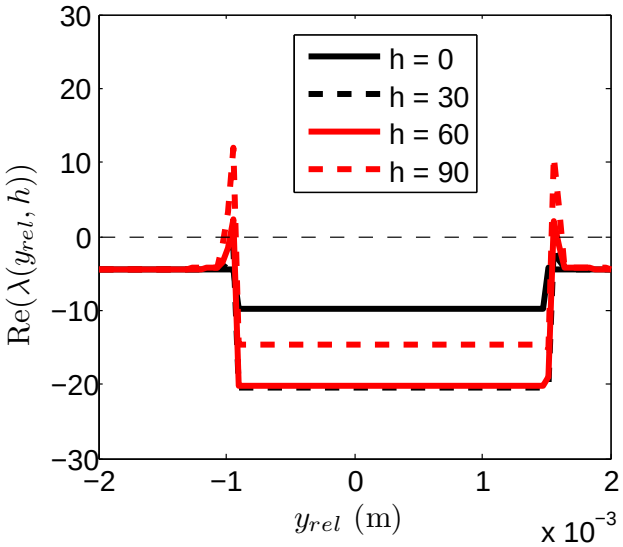

Figure 6.26: Real part of the Lyapunov exponents of $\mathbf{J}(\mathbf{x})$ against y_{rel} and h (filtered controller dynamics).

In Figure 6.26, we can identify three areas of interest. The first of these areas relates to the linear regime within the stroke limits ($d_2 < y_{rel} < d_1$), where the Lyapunov exponents are amplitude-invariant. The real part of these exponents is determined by the eigenvalues illustrated in Figure 6.18. The second area is close to the stroke limit and represents the maximum real value of the exponents, where the regions of instability lie. In these narrow regions, the Lyapunov exponents increase with the feedback gain, becoming positive when $h > 50$. It should be noted that the maximum value is reached when y_{rel} is slightly greater than the stroke limits, which suggests that stroke saturation only induces closed-loop instability once the proof-mass collides with the end stop with enough force to reach this region of potential instability and overcome the inherent damping.

The third area lies well beyond the stroke limits, where y_{rel} greatly exceeds $d_{1,2}$. At these displacement extremes, the real part of the exponents tend towards a negative constant that is independent of the displacement amplitude and the control gain. This region prevents the displacement response from reaching infinity when the closed-loop system becomes unstable. Therefore, the closed-loop response will tend to a LCO, where the frequency is approximately equivalent to Eq. 6.26.

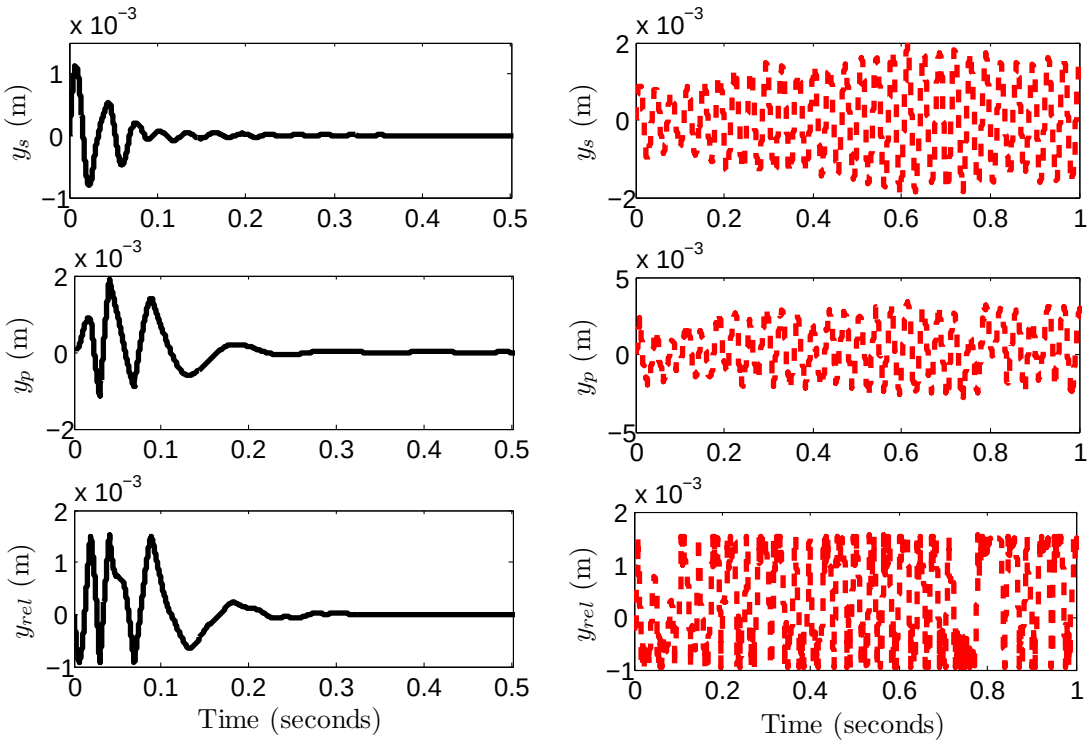

Figure 6.27: Displacement-time responses of the actuator-plate model to a 1 ms impulse of amplitude $F = 40$ N, including the open-loop response (solid line) and the closed-loop response (dashed line) for $h = 55$.

Using the Simulink model, a 1 millisecond impulse with a relatively large amplitude of 40 N was applied to the structural mass, and the resulting simulated displacement-time responses of the structural mass, the proof-mass, and their relative motion are shown in Figure 6.27. First, the displacement-time signals are simulated with no control, and it can be seen in the relative displacement-time signals that the amplitude of the impulse is sufficiently large for the proof mass to hit the end stops, thereby causing the actuator to saturate. Since the open-loop system is inherently stable, the proof-mass returns to the equilibrium position after hitting the end stops several times.

Next, the feedback gain $h = 55$ is applied to the velocity feedback loop, and the closed-loop displacement-time histories are simulated and illustrated in 6.27. Here, we can observe from the simulated signals that the closed-loop system is unstable and the relative displacement tends to a limit-cycle oscillation that is bounded by the stroke limits. This demonstrates that the occurrence of stroke saturation is sufficient to destabilise the closed-loop actuator-plate configuration for relatively small feedback gains, with a significant reduction of 72 % to the gain margin specified in Table 6.3.

Composite nonlinearities

In this section, we consider the dynamics of the composite nonlinear actuator-plate configuration, where both the suspension nonlinearities and saturation nonlinearities are included. In this case, the stability characteristics of the model are expected to represent the stability characteristics of the physical system, where the combined nonlinearities interact with each other.

The real Lyapunov exponents of the Jacobian matrix $\mathbf{J}(\mathbf{x})$, which are illustrated in Figure 6.28, exhibit characteristics of the isolated nonlinearities. For example, the real exponents initially increase as $|y_{rel}|$ rises, due to the suspension nonlinearities, and are abrutly halted once the stroke limit is reached, due to stroke saturation. This indicates that when the feedback gain is relatively small ($10 < h < 50$), the displacement bounds imposed by the stroke limits have the effect of stopping the real exponents from becoming positive, thereby negating the regions of instability observed in Figure 6.24. Therefore, stroke saturation initially *prevents* the suspension nonlinearities from destabilising the closed-loop system, which is possible if the displacement amplitude is much greater than the stroke length.

As h increases, however, a rapid increase in the real exponents can be seen around the stroke limit, and the regions of instability start to appear for $h > 50$. This indicates that stroke saturation may result in closed-loop destabilisation in this regime. As h increases further ($h > 60$), the real exponents become positive before the stroke limit is reached, which confirms that the suspension nonlinearities are capable of destabilising the closed-loop system, provided that the feedback gain is large.

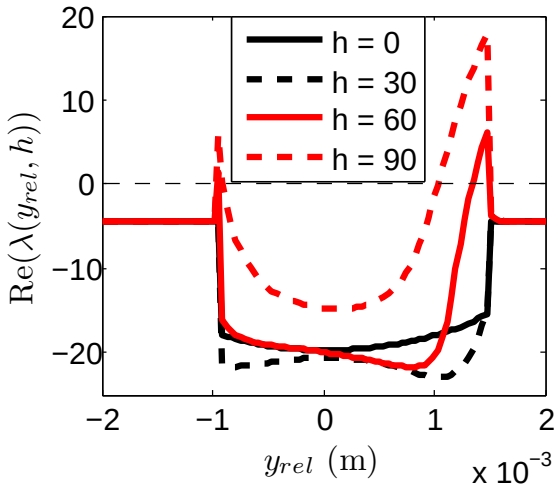

Figure 6.28: Real part of the Lyapunov exponents of $\mathbf{J}(\mathbf{x})$ against y_{rel} and h (filtered controller dynamics).

In order to compare the effects of the actuator nonlinearities on the closed-loop stability margin, a one millisecond impulse is applied to the structural mass in the Simulink model, and the smallest impulse amplitude F_{min} that results in a LCO is obtained using trial-and-error. The feedback gain is varied from $h = 60$ (where the closed-loop system may realistically become unstable) up to the linear gain margin $h = 175$. This procedure is applied to the isolated nonlinearities and the composite nonlinearities, resulting in three threshold amplitude curves that are shown in Figure 6.29. Using this comparison, we highlight several important factors regarding the stability of the composite system.

In Figure 6.29, it is apparent that the threshold amplitude is inversely proportional to the control gain for all cases, such that the closed-loop system is destabilised more easily as the feedback gain increases. We can also observe that there are three feedback regions of interest, where the first region lies at $60 < h < 100$, the second region is highlighted around $100 \leq h \leq 120$, and the third region represents the larger feedback gains up to the linear stability threshold $120 < h < 175$.

Within the first region, the stability of the closed-loop system is primarily dictated by stroke saturation, as observed in practice. There is also a minor contribution of the suspension nonlinearities, which slightly reduce the threshold amplitude required for instability.

Within the second highlighted region, all three threshold amplitudes are approximately equivalent, thereby indicating that both nonlinearities cause instability in this region.

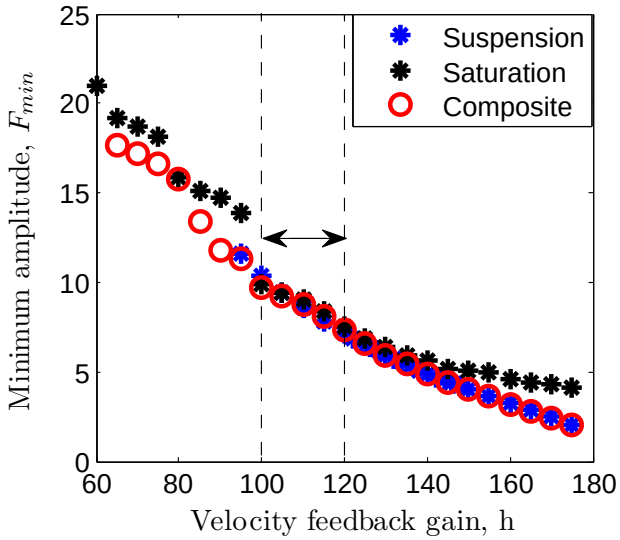

Figure 6.29: Threshold amplitude required for a 1 ms impulse to induce closed-loop instability, against the velocity feedback gain. The threshold of the system with either suspension or saturation is shown together with the composite results, which include both.

Within the third region, the stability of the closed-loop system is entirely determined by the suspension nonlinearities. Thus, the region $h > 120$ is highly unstable, and it is not sufficient to prevent stroke saturation as a means of ensuring closed-loop stability. Furthermore, the closed-loop system does not require a large excitation force to become unstable, and the background noise level may be sufficiently high to cause destabilisation. For these reasons, this unstable region should not be considered when applying VFC.

The displacement-time responses of the composite Simulink model to a 1 millisecond impulse are illustrated in Figure 6.30. First, a relatively small feedback gain $h = 60$ was used in conjunction with a large excitation amplitude ($F = 26$ N) to demonstrate the destabilising effects of stroke saturation. The control gain was then increased to $h = 130$ and a small excitation amplitude ($F = 5$ N) was applied to demonstrate that the suspension nonlinearities can render the closed-loop system unstable before the proof-mass hits the end stops. In this case, the LCO frequency initially corresponds to the actuator resonance and then tends to the coalesced frequency shown in Eq. 6.26.

These results suggest that the mechanisms for instability in the underlying linear closed-loop system remain the same for the nonlinear closed-loop system, where the controller deficiencies are accentuated by the actuator nonlinearities. It is apparent that these nonlinearities severely curtail the control performance that can be practically achieved with this controller.

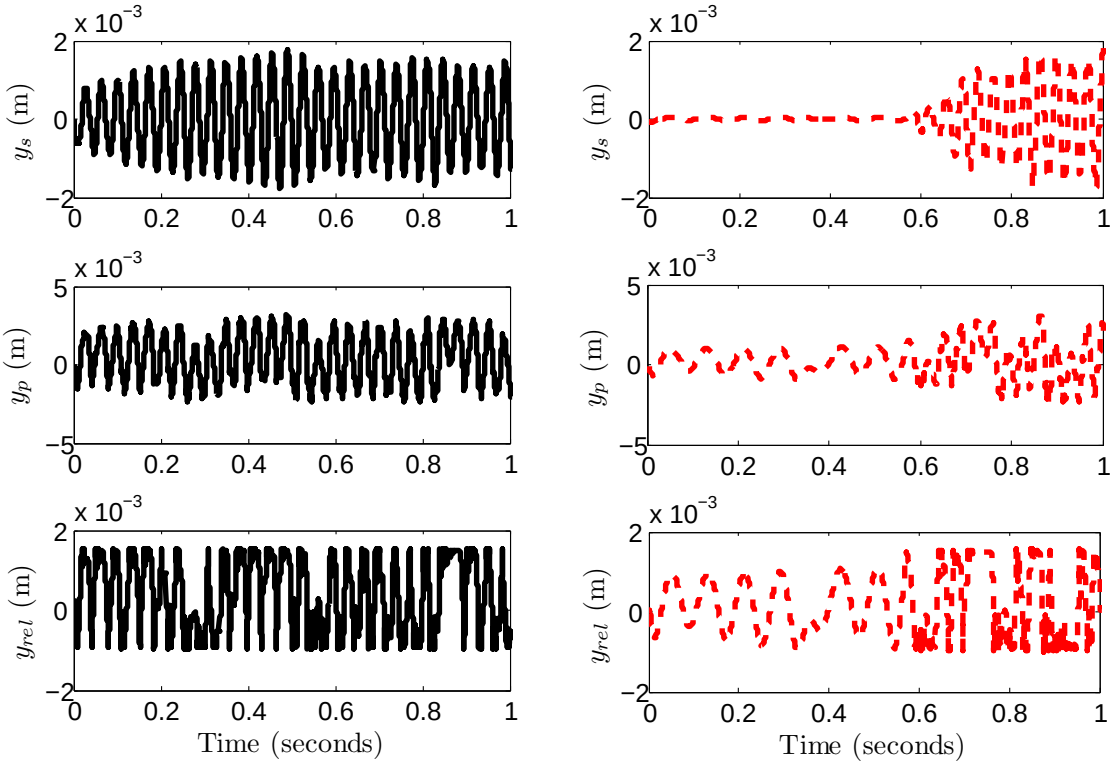

Figure 6.30: Displacement-time responses of the actuator-plate model to an impulsive input using $h = 60$, $F = 26$ N (solid line), and $h = 130$, $F = 5$ N (dashed line).

6.4.4 Causes of instability: Lyapunov's direct method

Now that the effects of the actuator nonlinearities on the closed-loop gain margin are known, the next step is to establish the causes of closed-loop destabilisation. From Eq. 6.32, we can observe that the velocity feedback control removes the symmetry of the damping matrix, thereby resulting in the non-collocated control forces that amplify the actuator mode. In order to devise an appropriate control law to prevent the resulting destabilisation of the closed-loop system, it is necessary to consider the underlying physical behaviour of the actuator-plate configuration. For this purpose, we utilise the total mechanical energy, denoted as $E(t)$, to provide physical intuition and to investigate the causes of destabilisation. The total mechanical energy is defined by the sum of the structural kinetic energy, $T_s(t)$, the proof-mass kinetic energy, $T_p(t)$, and the total potential energy, $U(t)$. The sum of $T_s(t)$ and $T_p(t)$ is the total kinetic energy, $T(t)$. Using the lumped parameter model, the expressions for these terms, with control, are as follows,

$$T_s(t) = m_s \int_0^t \ddot{y}_s(t)\dot{y}_s(t)\,dt = \frac{1}{2} m_s \dot{y}_s^2(t) \tag{6.33}$$

$$T_p(t) = m_p \int_0^t \ddot{y}_p(t)\dot{y}_p(t)dt = \frac{1}{2}m_p\dot{y}_p^2(t) \tag{6.34}$$

$$T(t) = \int_0^t \dot{\mathbf{y}}^{\mathbf{T}}\mathbf{M}\ddot{\mathbf{y}}dt = \frac{1}{2}m_s\dot{y}_s^2(t) + \frac{1}{2}m_p\dot{y}_p^2(t) \tag{6.35}$$

$$U(t) = \int_0^t \dot{\mathbf{y}}^{\mathbf{T}}\mathbf{K}\mathbf{y}dt + \int_0^y \mathbf{F_{nl}}(\mathbf{x})dy = \frac{1}{2}(k_s + g_a g)y_s^2(t) + \frac{1}{2}k_{p,1}y_{rel}^2(t) + U_{nl}(t) \tag{6.36}$$

where,

$$U_{nl}(t) = \begin{cases} \frac{1}{3}k_{p,2}y_{rel}^3(t) + \frac{1}{4}k_{p,3}y_{rel}^4(t) + \frac{2}{5}k_{sat}(y_{rel}(t) - d_1)^{\frac{5}{2}} & y_{rel}(t) > d_1 \\ \frac{1}{3}k_{p,2}y_{rel}^3(t) + \frac{1}{4}k_{p,3}y_{rel}^4(t) & d_2 \leq y_{rel}(t) \leq d_1 \\ \frac{1}{3}k_{p,2}y_{rel}^3(t) + \frac{1}{4}k_{p,3}y_{rel}^4(t) + \frac{2}{5}k_{sat}(-y_{rel}(t) + d_2)^{\frac{5}{2}} & y_{rel}(t) < d_2 \end{cases} \tag{6.37}$$

The total mechanical energy may be expressed as a Lyapunov candidate [52],

$$V(t) = \begin{bmatrix} \mathbf{K_{nl}}(\mathbf{x})/2 & \mathbf{0} \\ \mathbf{0} & \mathbf{M}/2 \end{bmatrix} = \mathbf{x}^{\mathbf{T}}\mathbf{P}\mathbf{x} \tag{6.38}$$

where,

$$\mathbf{K_{nl}}(\mathbf{x}) = \mathbf{K} + \mathbf{F_{sus}}(y_{rel})/y_{rel} + \mathbf{F_{sat}}(y_{rel})/y_{rel} \tag{6.39}$$

The change in energy with respect to time, $\dot{V}(t)$, is given by,

$$\dot{V}(t) = -\dot{\mathbf{y}}^{\mathbf{T}}\mathbf{C_h}\dot{\mathbf{y}} = \mathbf{x}^{\mathbf{T}}\mathbf{Q}\mathbf{x} \tag{6.40}$$

such that,

$$\mathbf{Q} = \begin{bmatrix} \mathbf{0} & \mathbf{0} \\ \mathbf{0} & \mathbf{C_h} \end{bmatrix} \tag{6.41}$$

It is apparent from Eqs. 6.38 and 6.41 that the total mechanical energy is dictated by the mass and stiffness matrices, whereas the change in energy is only affected by the damping matrix; therefore, the VFC has the effect of altering the $\mathbf{Q}$ matrix. In their current forms, Eqs. 6.38 and 6.41 are unsuitable for direct implementation as a Lyapunov candidate, since $\mathbf{Q}$ is a singular matrix. This problem can be alleviated with the introduction of a

small scaling parameter [140], denoted as $\epsilon > 0$, and redefining $\mathbf{P}$ and $\mathbf{Q}$ as,

$$\mathbf{P} = \begin{bmatrix} \mathbf{K_{nl}}(\mathbf{x}) & \epsilon\mathbf{M} \\ \epsilon\mathbf{M} & \mathbf{M} \end{bmatrix}, \mathbf{Q} = \begin{bmatrix} \epsilon\mathbf{K_{nl}}(\mathbf{x}) & \frac{1}{2}\epsilon\mathbf{C_h} \\ \frac{1}{2}\epsilon\mathbf{C_h} & \mathbf{C_h} - \epsilon\mathbf{M} \end{bmatrix} \tag{6.42}$$

As $\epsilon \to 0$, $\mathbf{P}(\mathbf{x})$ and $\mathbf{Q}(\mathbf{x})$ tend towards the original matrices shown in Eqs. 6.38 and 6.41. Therefore, by setting $\epsilon \approx 0$, Eq. 6.42 is almost equivalent to Eqs. 6.38 and 6.41, whilst ensuring $\mathbf{Q}$ is non-singular. Furthermore, it can be seen that $V(\mathbf{x}) = \mathbf{x^T P x} = \mathbf{0}$ and $\dot{V}(\mathbf{x}) = \mathbf{x^T Q x} = \mathbf{0}$ are satisfied only when $\mathbf{x} = \mathbf{0}$; this is a requirement of Lyapunov's direct method.

By focusing on the set $\mathbf{x} \in S_0$ $\{S_0 \subset \mathbb{R}^n \| S_0 \approx 0\}$ that is very close to the equilibrium position, the underlying linear dynamics are dominant and we can ignore the structural nonlinearities. In this case, it is a simple matter to show that $\mathbf{P} = \mathbf{P^T}$ and $\mathbf{Q} = \mathbf{Q^T}$ are positive-definite when no control is applied, which confirms that the open-loop system is locally asymptotically stable around the equilibrium position. By introducing VFC, the coupling between the actuator and the structure has the effect of disrupting the symmetry of $\mathbf{Q}$, such that it is no longer sufficient to check the eigenvalues for positive-definiteness. Instead, it is necessary to utilise Cholesky decomposition to determine the positive-definiteness of this matrix. Here, $\mathbf{Q}(h)$ is expressed[2] using the lower triangular matrix $\mathbf{L_Q}$ that satisfies $\mathbf{Q}(h) = \mathbf{L_Q^T L_Q}$. When $\mathbf{Q}(h)$ is positive-definite, the lower triangular matrix has non-negative diagonal terms; conversely, $\mathbf{L_Q}$ does not exist if $\mathbf{Q}(h)$ is not positive-definite [141].

Figure 6.31 show the primary diagonal terms of $\mathbf{L_Q}$ against h . Here, it is apparent that one of the diagonal terms reaches zero at $h \approx 3.25$, which indicates that $\mathbf{Q}$ loses its positive-definiteness when h exceeds this value. In this case, $\dot{V}(t)$ may become positive, thereby increasing the total mechanical energy, and so the global asymptotic stability of the closed-loop system can only be proved up to $h \approx 3.25$ using this Lyapunov function. This is inconsistent with the linear gain margin specified in Table 6.3, and indicates that the total mechanical energy is not an appropriate Lyapunov candidate for assessing the global closed-loop stability in this case. However, using $V(t)$ as a Lyapunov candidate shows that the total mechanical energy may increase over time without inducing closed-loop instability in the underlying linear system. This is demonstrated in Figure 6.32, where the total closed-loop mechanical energy in response to a 1 millisecond impulse of

[2]Assuming pure-gain feedback, $\mathbf{Q}$ is dependent on h, and so is denoted by $\mathbf{Q}(h)$ for this case.

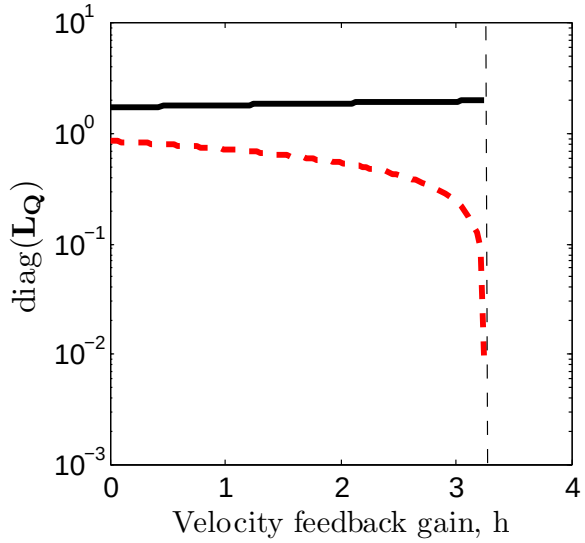

Figure 6.31: Diagonal terms of $\mathbf{L_Q}$ against h. The second term (dashed line) tends towards zero as h approaches 3.25.

20 Newtons, with a feedback gain $h = 80$, is shown against time. Here, it is apparent that whilst the total energy decays asymptotically towards zero, the feedback control is sufficient to increase the total energy at particular times, indicated as regions of potential instability. This phenomenon can be explained by the VFC loop, which has the effect of decreasing the vibration levels of the structure whilst increasing the vibration levels of the proof-mass. This is shown by the actuator kinetic energy in Figure 6.32.

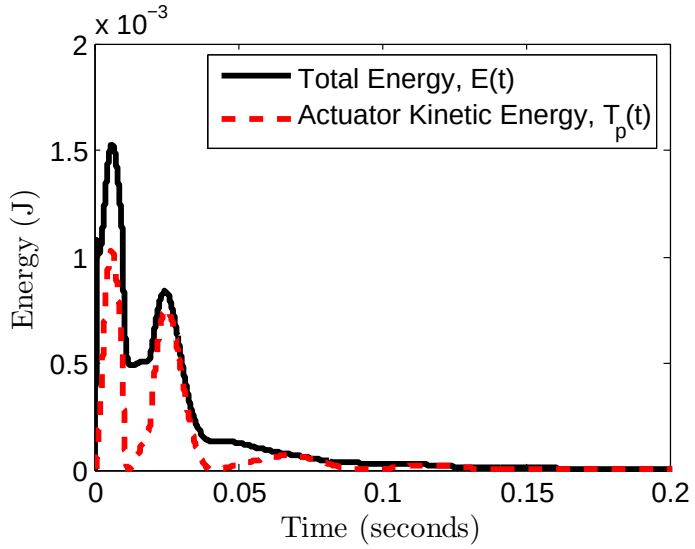

Figure 6.32: Total energy of the underlying linear closed-loop system against time.

Once we consider the actuator nonlinearities, it is evident that these regions of potential instability in the underlying linear system are the cause of closed-loop destabilisation; the actuator nonlinearities exploit the regions of potential instability, possibly resulting in LCO behaviour when $h > 50$. As a means of comparison with Figure 6.32, an illustration of the total closed-loop mechanical energy with the actuator nonlinearities is shown in Figure 6.33a), where it is apparent that the closed-loop system is unstable and has entered a limit-cycle oscillation.

The contributions of the kinetic and potential energies to the limit-cycle oscillation are highlighted in Figure 6.33b) within a short time span, and it is evident that there are several features of interest. Firstly, the stroke saturation phenomenon, as highlighted by the arrows, has the initial effect of reducing the total energy of the system. Since stroke saturation is modelled as a series of viscoelastic collisions, this energy is lost as heat and transferred as kinetic energy to the plate structure. Secondly, the total potential energy rises to a maximum once the impulses associated with stroke saturation have decayed, and the proof-mass prepares to move away from the end stop. Thirdly, the kinetic energy of the proof-mass rapidly increases as it moves, with the aid of the control signal, to the other end stop, thereby increasing the total mechanical energy of the closed-loop system and causing destabilisation. Therefore, we can determine from this analysis that stroke saturation destabilises the closed-loop system by accentuating the regions of potential instability already present in the underlying linear system.

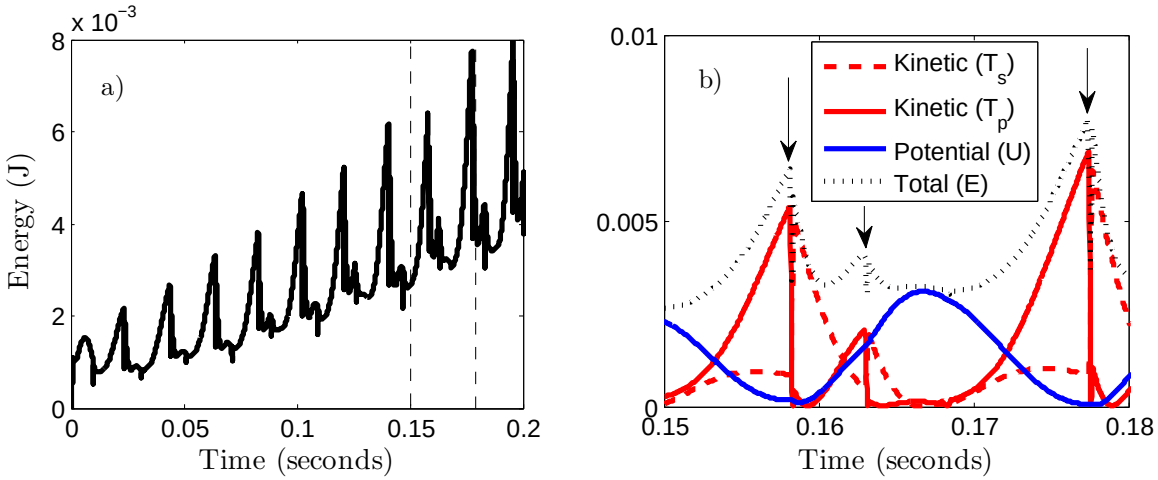

Figure 6.33: Illustration of a) the total energy of the closed-loop system, with actuator nonlinearities, against time, and b) a zoomed-in illustration showing the contribution of the kinetic and potential energies.

In order to establish the link between stroke saturation and the regions of potential instability, we compare the structural velocity with the total mechanical energy in Figure 6.34. This figure shows that when the proof-mass hits the end stops, as shown by the peaks in the total mechanical energy, the resulting impulses appear as spikes that are in phase with structural velocity; as a result, the magnitude of the control signal is greatly increased, which reduces the apparent damping of the actuator mode, as indicated by Baumann and Elliott [22]. This has the effect of increasing the kinetic energy of the proof-mass as it moves from one end stop to the other one, thereby exciting the regions of potential instability and destabilising the closed-loop system.

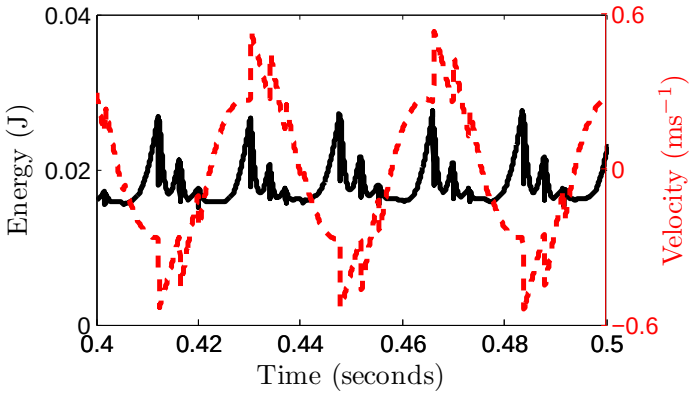

Figure 6.34: Simulated structural velocity signal in comparison with the total mechanical energy.

6.4.5 Stability criteria

From the analyses conducted in the previous sections, the following aspects of the closed-loop stability characteristics can be concluded,

1. The closed-loop system is, inherently, *conditionally stable* when VFC is applied, due to the amplification of the actuator mode. Including the controller dynamics in the control loop worsens the problem by reducing the gain margin.

2. Both the suspension nonlinearities and stroke saturation detrimentally affect closed-loop stability by reducing the gain margin; these effects are more pronounced with the inclusion of the controller dynamics.

3. Stroke saturation may destabilise the closed-loop system for relatively small feedback gains, whereas the suspension nonlinearities have a greater effect when the control gain is large and the excitation amplitude is small.

4. The nonlinearities destabilise the closed-loop system by exploiting regions of potential instability in the underlying linear closed-loop system. This demonstrates that these types of actuator nonlinearities only affect closed-loop stability the *underlying linear system* is conditionally stable. Therefore, the choice of controller is a crucial aspect in determining the effects of the actuator nonlinearities on closed-loop stability; an unconditionally stable closed-loop system, in principle, will remain stable regardless of these nonlinearities.

In order to verify these findings, a series of control experiments are conducted on the actuator-plate configuration in the next chapter, and the results are compared with these theoretical observations.

6.5 Control strategies for closed-loop stabilisation

6.5.1 Saturation detection scheme

In the previous section, it is shown that stroke saturation is capable of causing closed-loop destabilisation by significantly increasing the kinetic energy of the proof-mass as it moves through its stroke. A simple method for counteracting these destabilising effects is to devise a secondary control law when stroke saturation occurs; the closed-loop system then retains the original control law to increase the effective damping under normal operating conditions, whilst the secondary control prevents destabilisation from occurring as a result of stroke saturation.

In order to achieve this aim, it is necessary to detect the onset of stroke saturation in real-time using a knock detector, such that the controller may be switched between the two states. Knock detectors are frequently employed in the control of internal combustion engines [142, 143], for the purpose of improving efficiency and preventing engine damage. A well-established and low-cost procedure for detecting knock in these cases is to use data from accelerometer signals mounted near the combustion chambers, although care must be taken to prevent false detections resulting from high levels of parasitic noise.

By utilising a similar procedure, stroke saturation may be detected by placing a single accelerometer on the actuator casing and examining the signal for large impulses that are

attributed to the impacts. For this purpose, a Dytran 3035BG accelerometer was used to monitor the acceleration of the Micromega IA-01 actuator, and the resulting signal was conditioned by a Dytran 4102C signal conditioner. This is shown in Figure 6.35.

Figure 6.35: Illustration of an accelerometer mounted on an inertial actuator for stroke saturation monitoring.

To minimise the contributions of parasitic noise, the signal is band-pass filtered into the spectral region that corresponds to the frequency content of the impulses; a common procedure when applying knock detection [142, 143]. Since the duration of the impulses ranges from several hundred microseconds to approximately one millisecond, the spectral region of interest is approximately $1 - 3$ kHz, and a third-order band-pass filter is used to focus the accelerometer signal within this spectral region.

As a means of illustrating the abruptness of the onset of stroke saturation, a mono-harmonic input voltage, of frequency 75 rad/s, is applied directly to the inertial actuator, and the excitation amplitude is increased in increments of 0.01 Volts until the characteristic impulses appear in the filtered accelerometer signal. Figure 6.36 shows a comparison of various accelerometer signals obtained from $V = 0.4$ Volts to $V = 0.43$ Volts. At the smallest excitation amplitude, stroke saturation does not occur, and the filtered accelerometer signal comprises stationary background noise. However, as the excitation amplitude increases to 0.41 Volts, impulses start to appear in the accelerometer signal, which confirms the presence of stroke saturation. As the excitation amplitude increases further, it is apparent that these impulses greatly exceed the background noise level, and are relatively easy to distinguish. These illustrations demonstrate that the filtered accelerometer signal can be monitored to reliably detect stroke saturation.

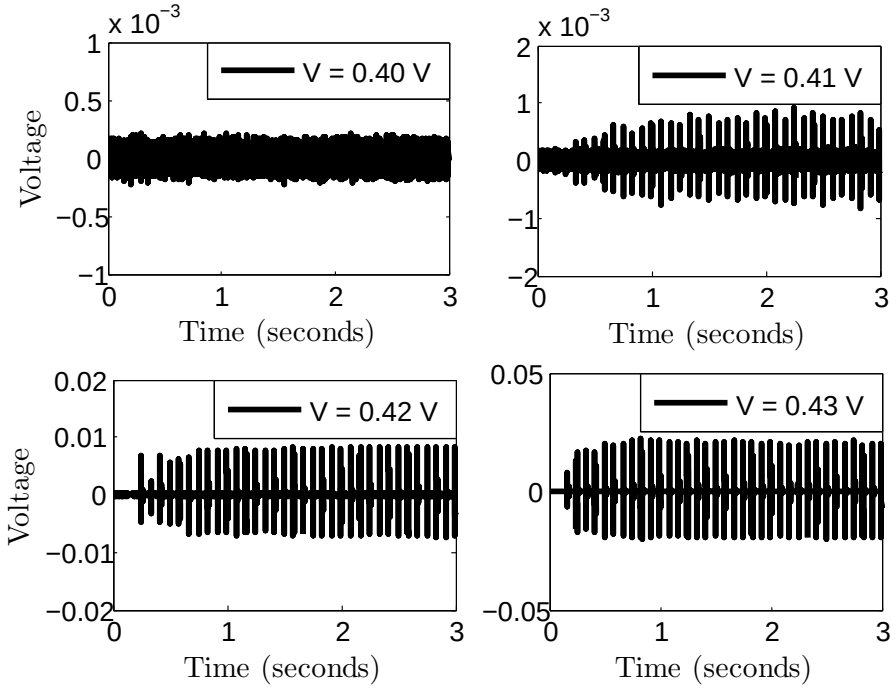

Figure 6.36: Measured accelerometer voltages obtained at similar excitation amplitudes.

Since the background noise level appears to be approximately stationary, we define a simple detection threshold, calibrated to $T_{dec} = 6 \times 10^{-4}$ Volts, that the filtered accelerometer signal, denoted by $v_{dec}(t)$, must exceed for stroke saturation to be detected. This detection threshold is used to create a binary detection signal, denoted by y_{dec}, that is unity when the threshold is exceeded and zero beneath the threshold,

$$y_{dec} = \begin{cases} 1 & |v_{dec}(t)| \geq T_{dec} \\ 0 & |v_{dec}(t)| < T_{dec} \end{cases} \tag{6.43}$$

Using this detection signal, the secondary, stabilising control law becomes active when stroke saturation is detected ($y_{dec} = 1$), whereas the original control law is retained under normal operating conditions ($y_{dec} = 0$).

To avoid the need for threshold calibration, a more rigorous approach for detecting stroke saturation is to monitor the kurtosis of the filtered accelerometer signal, given by Eq. 5.24. Since the kurtosis is determined by the pulse characteristics of the signal instead of amplitude variations, it is frequently employed in damage detection applications, such as detecting tooth faults in gears and defects in ball bearings [144, 145]. In the context of stroke saturation detection, monitoring the kurtosis may be advantageous in

an *in-situ* scenario, where parasitic noise is higher in level and is often non-stationary, as well as accounting for actuator-to-actuator variations without the need for threshold recalibration. However, calculating the kurtosis of a signal in real-time is complicated, and a detection threshold is used in this case for purposes of simplicity. A discussion of the potential application of kurtosis monitoring for the detection of stroke saturation is the subject of future work in chapter 8.

In order to prevent chattering, where y_{dec} switches rapidly between the two states when $v_{dec}(t) \approx T_{dec}$, a zero-order hold is utilised, such that y_{dec} is held at unity for a user-defined number of samples, denoted by N_τ, when stroke saturation is detected. This ensures that y_{dec} remains at unity for the whole duration of a stroke saturation event, such that the stabilising control law is active over this period.

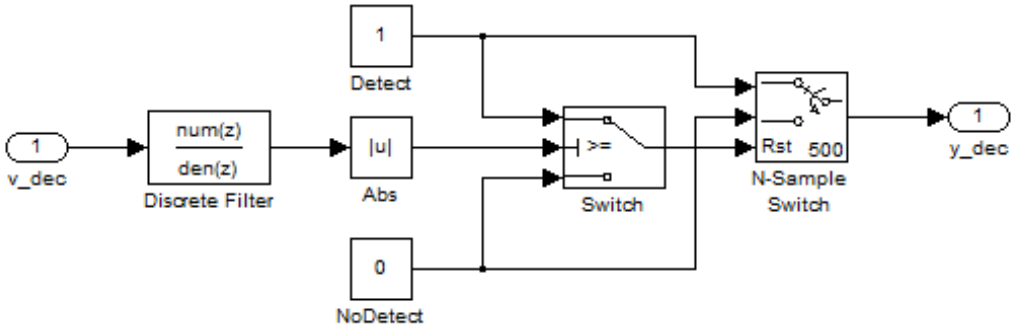

Figure 6.37: Illustration of the stroke saturation detection scheme in Simulink.

Figure 6.37 shows the implementation of the saturation detection scheme in Simulink. Using the accelerometer signal $v_{dec}(t)$ as the input, a third-order bandpass filter, with cut-off frequencies 1 kHz and 3 kHz respectively, is used to remove unnecessary frequency content. Next, a switch block is used to set the detection threshold, such that the output is unity above the threshold and zero below the threshold. Finally, an N-sample switch is utilised; here, the top port is triggered for 500 samples when the trigger port detects a non-zero sample (i.e. stroke saturation has been detected), whereas the middle port is used when the trigger is not active. The output is the binary detection signal y_{dec}. A comparison of an accelerometer signal v_{dec} and the resulting detection signal is shown in Figure 6.38, where it is apparent that the detection signal is unity when stroke saturation is present in v_{dec} and is zero elsewhere.

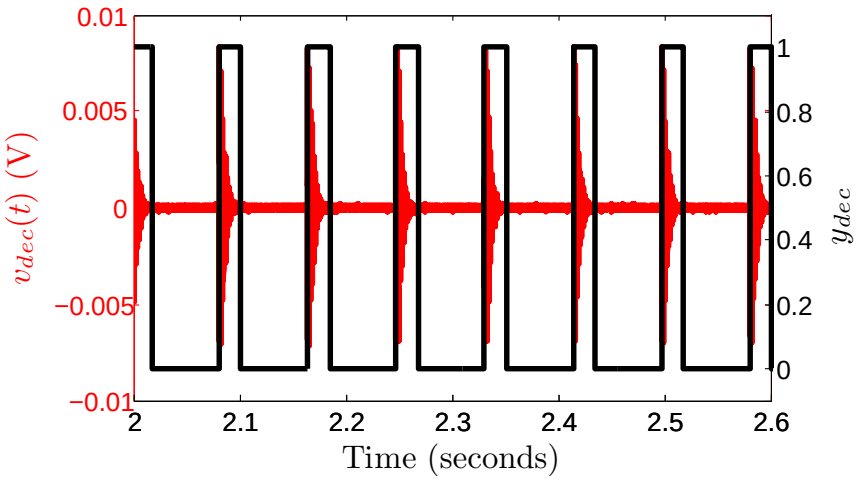

Figure 6.38: Illustration of the filtered accelerometer signal and the resulting detection signal.

6.5.2 Control deactivation

Since the open-loop system is globally asymptotically stable, one of the simplest possible control strategies, in principle, is to deactivate the feedback control when stroke saturation is detected, such that the increase in kinetic energy is prevented and the closed-loop system remains stable [141]. This strategy is a form of on-off control, and can be implemented relatively easily by using y_{dec} as a form of detection-dependent gain, denoted by h_{dec}, that is zero when stroke saturation is detected and unity under normal operating conditions,

$$h_{dec} = \begin{cases} 0 & y_{dec} = 1 \\ 1 & y_{dec} = 0 \end{cases} \tag{6.44}$$

In this manner, the secondary control law acts to reduce the control signal to zero when stroke saturation is detected, thereby stabilising the closed-loop system. The implementation of h_{dec} in Simulink is shown in Figure 6.39, and a demonstration of the application of control deactivation is shown in Figure 6.40, illustrating the filtered accelerometer signal and the resulting control signal obtained with h_{dec}.

Although the implementation of this control strategy is relatively simple, careful consideration is required for the achievement of the control objectives. Firstly, it is necessary to consider the deactivation period N_τ; if this time is too short, then the increase in kinetic energy remains sufficient to destabilise the closed-loop system, whereas an overly

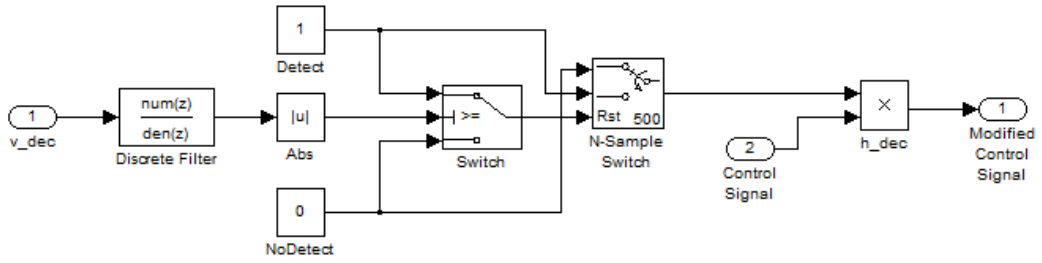

Figure 6.39: Illustration of the control deactivation scheme in Simulink. Notice that the top and middle ports in the N-sample switch block have been switched relative to Figure 6.37, in accordance with Eq. 6.44.

long deactivation period will prevent the closed-loop system being effectively controlled under normal operating conditions. Secondly, the primary aim of control deactivation is to prevent the kinetic energy of the proof-mass from increasing rapidly after stroke saturation has occurred, and so it is important to synchronise the control deactivation with the increase in kinetic energy. Since this occurs a short time after the proof-mass has hit the end stops, synchronisation may be achieved by choosing a sufficiently large N_τ that encompasses the duration of the stroke saturation period and the rise in kinetic energy levels. The benefits and drawbacks of this method is discussed in greater detail in the next chapter.

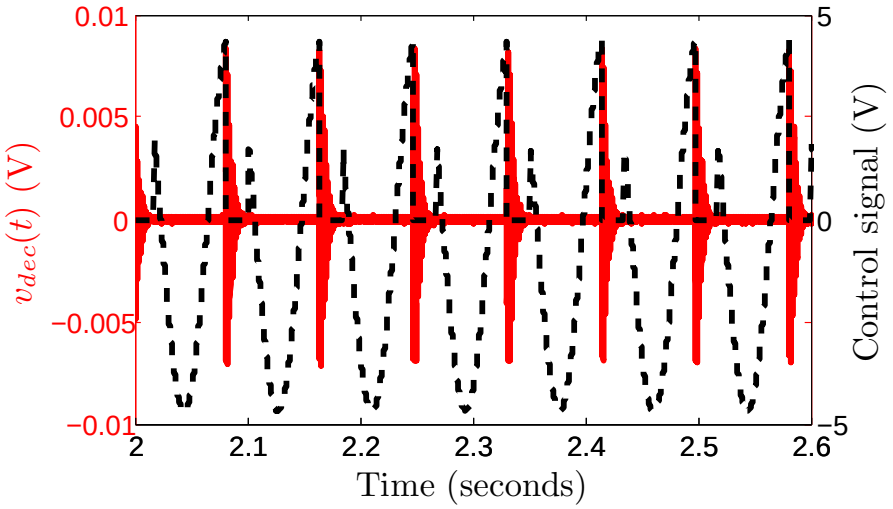

Figure 6.40: Illustration of the filtered accelerometer signal (solid line) and the resulting control signal (dashed line).

6.5.3 Gain scheduling

As an alternative means of controlling the inertial actuator, a simple gain scheduling approach can be taken to incrementally alter the gain of the feedback loop when stroke saturation occurs [146]. Since the primary control law of interest is on-off control deactivation, a brief overview of the gain scheduling approach is given in this section and a simple test of the control law being utilised in a practical application is provided in Appendix F.

Gain scheduling is advantageous for adaptive control purposes, and is commonly found in scenarios that utilise various interpolated linear models to control a nonlinear system [147], with applications in servo systems [148], nuclear reactors [149], and automobile engines [150]. In this case, the controller is used to steadily reduce the input excitation to the actuator until stroke saturation no longer occurs. This can be achieved by directly integrating the detection signal y_{dec} and using the resulting signal as the detection-dependent gain h_{dec}, which increases in magnitude when stroke saturation occurs. A Simulink schematic of this procedure is shown in Figure 6.41, using the accelerometer signal to detect saturation and to alter the gain h_{dec} used for the feedback loop.

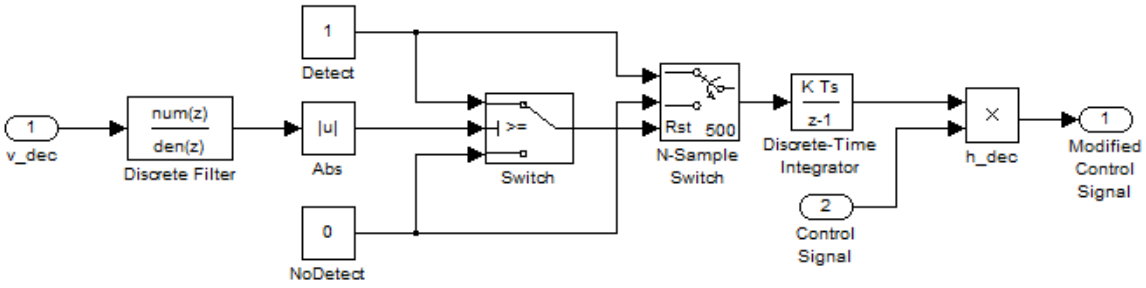

Figure 6.41: Illustration of the gain scheduling scheme in Simulink.

The use of this gain scheduling procedure is demonstrated in Figure 6.42, which shows the filtered accelerometer signal and the resulting detection-dependent gain. Here, it is apparent that the presence of stroke saturation in the accelerometer signal has the effect of incrementally increasing the gain associated with h_{dec}. The rate of increase in h_{dec} is dictated by the detection time N_τ and the feedback control gain h, which should therefore be carefully chosen to ensure that the controller is able to adapt quickly whilst retaining closed-loop stability. This is discussed further in Appendix F, which demonstrates the

use of the gain scheduling procedure to prevent stroke saturation in an inertial actuator on a rigid block.

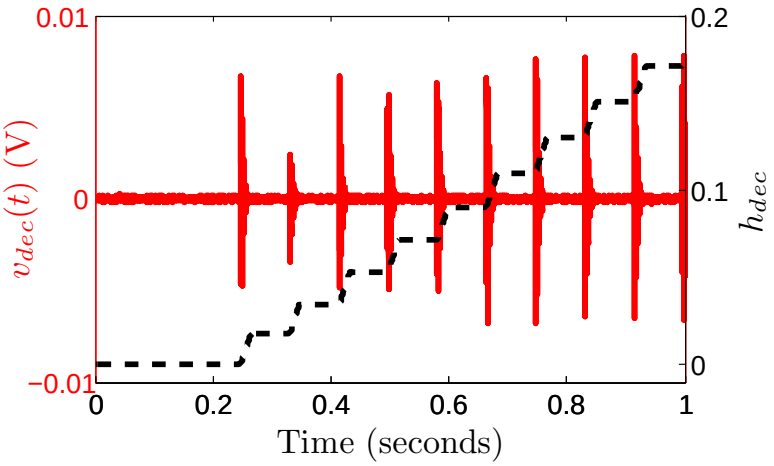

Figure 6.42: Illustration of the filtered accelerometer signal and the resulting detection-dependent gain.

6.6 Conclusions

In this chapter, the dynamics of a coupled actuator-plate configuration were measured in the time- and frequency-domains, using the structural acceleration as a means of providing SISO velocity feedback control. These measurements were used to devise a two-degree-of-freedom lumped parameter model that is capable of emulating the actuator nonlinearities, including the hardening suspension stiffness and stroke saturation.

An analysis on the closed-loop stability was carried out using the Nyquist criterion, circle criterion, and Lyapunov exponents. The analysis reveals that the underlying linear system is conditionally stable when VFC is used, due to the amplification of the actuator mode. It was found that the actuator nonlinearities are highly detrimental to the closed-loop stability, reducing the gain margin by up to 72 %. Furthermore, it appears that the actuator nonlinearities have different effects on closed-loop stability; stroke saturation is dominant for smaller feedback gains $50 < h < 100$ and large, impulsive inputs, whereas the suspension nonlinearities affect closed-loop stability for larger control gains ($h \geq 100$) and relatively small inputs. Including the dynamics of the band-pass filters in the digital controller has the effect of further reducing the gain margin for all cases.

The causes of closed-loop destabilisation were investigated using Lyapunov's direct method, and it was demonstrated that the total closed-loop mechanical energy of the underlying linear system is able to increase over time when $h > 3.25$, due to the kinetic energy of the actuator. This results in regions of potential instability that are utilised by the actuator nonlinearities to overcome the inherent damping of the actuator-plate configuration, thereby indicating that closed-loop destabilisation is a result of the controller performance as much as the nonlinearities themselves. For stroke saturation, it was found that the characteristic impulses are in-phase with the structural velocity, as predicted by Baumann and Elliott [22], thereby increasing the magnitude of the control force and destabilising the closed-loop system as the proof mass moves from one end stop to the other.

In order to stabilise the actuator-plate configuration, a nonlinear on-off control strategy is considered, where the control signal is deactivated for a short period of time when stroke saturation is detected. The performance of this nonlinear controller is investigated experimentally in the next chapter. Alternatively, a gain scheduling approach is considered for incrementally increasing the feedback gain of a secondary control loop when stroke saturation is detected. This is demonstrated experimentally in Appendix F.

Chapter 7

Experimental Control of an Actuator-Plate Configuration

7.1 Introduction

The preliminary analysis of the actuator-plate configuration conducted in chapter 6 suggests that the composite system will become conditionally stable once the velocity feedback loop is closed. Using the linear Nyquist stability criterion, the predicted linear gain margin is $h = 172.9$. However, by accounting for the actuator nonlinearities, the effective gain margin is reduced to approximately $h = 130$ as a result of the suspension nonlinearities. Moreover, the gain margin may be further reduced to $h = 50$ if stroke saturation occurs (due to an external shock, for example), which is a significant concern for ensuring closed-loop stability whilst achieving good control performance.

In this chapter, the predictions made in chapter 6 are verified experimentally by applying linear VFC to the physical actuator-plate configuration. The feedback loop is implemented in dSpace, ControlDesk and Simulink, which generates a control signal from the structural accelerometer signal. Using a variety of excitation sources (including sinusoidal excitation from a loudspeaker, impact excitation from a hammer, and background noise excitation), the structural acceleration response was measured in MATLAB, and the closed-loop stability characteristics are assessed. Reductions of up to 15 dB around the first plate resonance are possible before the predicted gain margin is reached ($h = 50$), with minor reductions also occurring at the third plate resonance. It was found that the effective gain margin of the physical system was in good agreement with the predictions

made using the lumped-parameter model, with much lower margins being observed in relation to the linear gain margin as a result of the actuator nonlinearities.

Next, the nonlinear on-off controller specified in the previous chapter is implemented on the actuator-plate configuration using simulations and experimental measurements. It is demonstrated that this on-off VFC scheme is capable of preventing stroke saturation from destabilising the closed-loop in most circumstances, provided that the control signal is deactivated for a sufficiently long period of time and the feedback gain is not too large. Since the on-off VFC scheme does not prevent the suspension nonlinearities from destabilising the closed-loop, it is important that the feedback gain does not exceed the effective gain margin imposed by the suspension nonlinearities. By ensuring that stroke saturation cannot destabilise the closed-loop system, larger feedback gains can be used, and the maximum possible attenuation around the first plate resonance is increased from 15 dB to 22 dB.

7.2 Implementation of velocity feedback control

7.2.1 Experimental setup

An active velocity feedback control loop is applied to the experimental actuator-plate configuration detailed in the previous chapter as a means of improving the vibration performance of the plate structure. The feedback loop is implemented using a dSpace DS1103 PPC Controller Board for real-time I/O processing at a sample rate of 2 kHz (the accelerometer signal is the input and the control signal is the output), and the digital controller is designed in Simulink using the integrator and filter schematic shown in Figure E.15, Appendix E.

The primary force $f_p(t)$ is applied directly to the plate structure using various sources, including a moving-coil loudspeaker and an impact testing hammer, for the purpose of assessing the response of the plate structure to different types of excitation. The structural acceleration is monitored by the B&K Type 4375 accelerometer, and the resulting acceleration-time signal is passed through the digital controller to generate the control signal. This control signal is then amplified by the Micromega Dynamics Rack-04-45N prior to driving the actuator in order to provide the secondary control force $f_s(t)$ to the plate structure. A block diagram of the closed-loop system is shown in Figure 7.1.

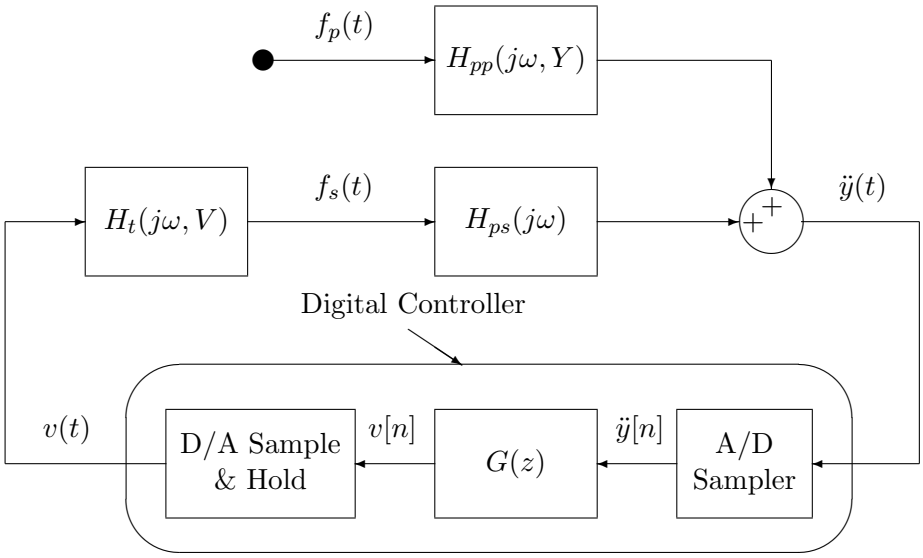

Figure 7.1: Block diagram of the practical implementation of the feedback loop, where $H_{pp}(j\omega, Y)$ and $H_{ps}(j\omega)$ represents the open-loop force-acceleration transfer functions for the primary and secondary forces respectively. The A/D and D/A Sample and Hold blocks relate to the dSpace Controller Board, and $G(z)$ describes the digital controller in Simulink and ControlDesk. The control signal $v(t)$ is converted to the secondary control force $f_s(t)$ transmitted to the structure from the free-velocity actuator transfer function $H_t(j\omega, V)$ described in chapter 4.

Using the SISO feedback loop to provide VFC, the performance of the controller is assessed by measuring the acceleration-time responses of the plate structure and analysing the closed-loop dynamics with regards to performance and stability. First, the plate is excited using tonal excitation, and the time histories of the accelerometer signals and source voltages are measured over a range of frequencies and feedback gains. The first-order closed-loop acceleration-voltage FRFs, which are defined as $\hat{H}_s(j\omega, V)$ between the accelerometer signals and source voltages, are ascertained from the measured time histories, and illustrate that the control loop is increasing the effective damping. Next, the plate is subjected to impulsive excitation, and the measured acceleration-time responses are used to assess the controller performance and stability characteristics with regards to the theoretical observations made using the Simulink model. Finally, the free acceleration-time response of the closed-loop system is measured with no input excitation to establish the stability limits of the closed-loop system.

7.2.2 Response to tonal excitation

In this experiment, a moving-coil loudspeaker was used to provide tonal excitation to the plate structure using vibro-acoustic transmission, as shown in Figure 7.2. Monoharmonic source voltage signals, denoted by $v(t)$, were generated in MATLAB at 0.7 Volts, ranging from 30 rad/s to 800 rad/s. The National Instruments NI-cRIO-9239 I/O module was used for data acquisition and ADA conversion, using a sample rate of 51.2 kHz to measure $v(t)$ and $\ddot{y}(t)$ over a period of ten seconds. The source voltages are amplified by a HH Electronics V200 Mos Fet power amplifier prior to driving the loudspeaker. Therefore, the primary force $f_p(t)$ comprises the dynamics of the power amplifier, the loudspeaker, and the vibro-acoustic transmission path. This means that these dynamics are also included in the measured FRFs.

It is assumed that the power amplifier acts as a pure gain over the frequency range of interest, and therefore has relatively little effect on the characteristics of the transfer function. In contrast, the moving-coil loudspeaker dynamics are strongly dependent on frequency, particularly when the excitation frequency is below the first loudspeaker resonance frequency, since the power output falls significantly in this region. In this case, the first resonance frequencies of the actuator and plate lie below the first resonance frequency of most moving-coil loudspeakers. To overcome this difficulty, a relatively large driver, with a cone size of approximately 17 inches, was chosen to ensure that the plate would be excited sufficiently at the lowest frequencies under consideration.

Furthermore, loudspeakers are particularly susceptible to harmonic distortion at low frequencies, as the cone excursions are large enough to move the suspension system into its nonlinear regime, resulting in dynamic behaviour similar to that of a Duffing oscillator [68]. For this reason, the driving input voltages to the loudspeaker are kept relatively low, such that the actuator-plate system is excited in its linear regime. This ensures that the superposition principle may be applied and each harmonic loading element may be considered separately.

Initially, the first-order acceleration-voltage transfer functions are obtained using the actuator-plate model in Simulink as a means of comparison. These transfer functions (illustrated in Figure 7.3), which are defined between the primary force $f_p(t) = F_p \sin(\omega t)$ and the structural acceleration $\ddot{y}(t) \approx -\omega^2 Y \sin(\omega t)$, are ascertained using stepped sine excitation. A relatively low excitation amplitude $F_p = 0.7$ N was used to excite the actuator-plate model, such that the acceleration signals are approximately sinusoidal.

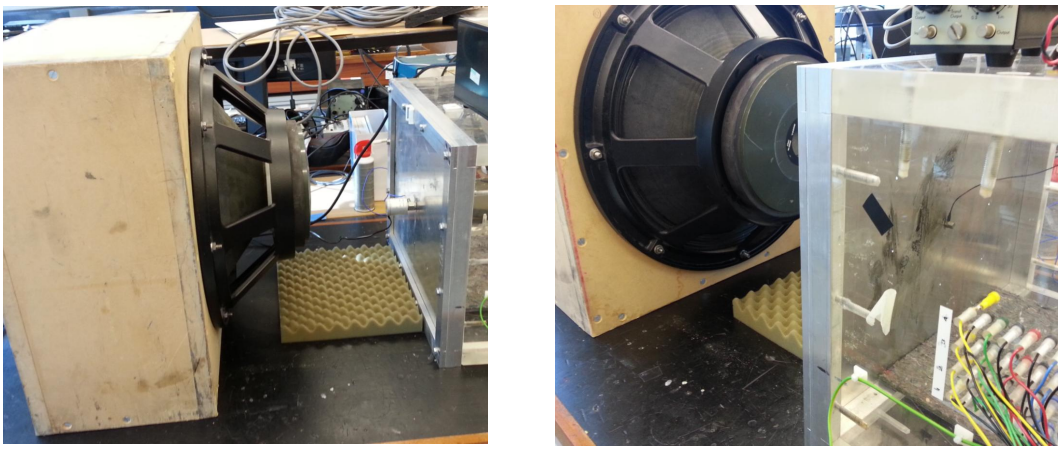

Figure 7.2: Illustration of the experimental setup, including the loudspeaker, the plate structure, and the collocated sensor-actuator configuration.

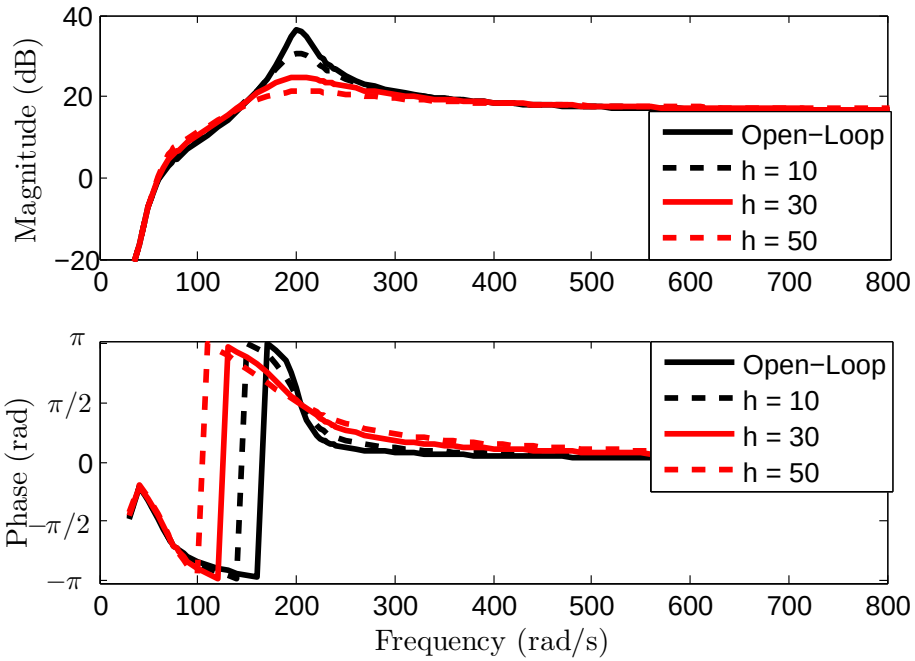

Figure 7.3: Open-loop and closed-loop VFC acceleration-voltage FRFs obtained using the Simulink model.

The open-loop transfer function indicates the presence of the actuator mode at 75 rad/s and the plate mode at 200 rad/s, as expected. The closed-loop transfer functions are obtained using various feedback gains up to the stability limit. Here, we can observe that the VFC loop increases the effective damping of the plate mode, resulting in reductions of up to 15 dB at the peak resonance frequency as the feedback gain is increased. In

contrast, the actuator mode is amplified by the VFC loop, such that the effective damping is reduced in this frequency region. We can also observe that the change in phase at the plate mode becomes more gradual as the feedback gain is increased; another indication that the effective damping is increased.

Now, we assess the effects of the VFC loop when applied to the physical plate structure. First, the loudspeaker is used to provide tonal excitation at the first plate resonance (200 rad/s), and an illustration of the measured open-loop and closed-loop acceleration-time responses is shown in Figure 7.4a), using a feedback gain $h = 30$. It is immediately apparent that the closed-loop response is much smaller than the open-loop response, thereby confirming that attenuation occurs around the first plate resonance. Whilst the open-loop acceleration response is quasi-sinusoidal, higher-order harmonics and noise can also be observed in the Fourier transform of this signal, as illustrated in 7.4b). Since the plate structure exhibits little harmonic distortion at this excitation frequency (as shown in the acceleration responses in Figure 6.6) these additional harmonics can be attributed to the nonlinear loudspeaker dynamics rather than being an intrinsic property of the system.

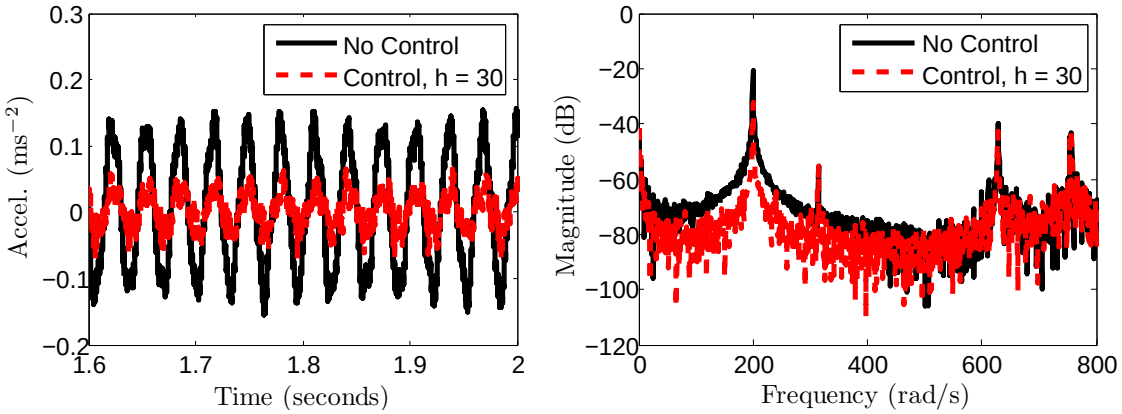

Figure 7.4: Acceleration-time and acceleration-frequency response of the plate structure to tonal excitation at 200 rad/s using VFC.

Although the closed-loop acceleration response is greatly reduced at the fundamental excitation frequency, the higher-order harmonics and noise components are relatively unaffected, since the VFC loop has little effect in these higher-frequency regions. Analysing the Fourier transform of the closed-loop signal with regards to the open-loop signal confirms that the VFC loop reduces the acceleration response at the fundamental excitation frequency by 12 dB, whilst the harmonic responses remain unattenuated. Therefore, the

closed-loop acceleration response exhibits a greater degree of harmonic distortion as a result of a lack of harmonic control in relation to the fundamental excitation frequency, which is well-controlled.

By measuring the acceleration-time responses over the specified frequency range, the first-order acceleration-voltage transfer functions of the plate structure are obtained and shown in Figure 7.5. Unlike in Figure 7.3, the source voltages are obtained by directly measuring $v(t)$ from the NI modules, as the primary force $f_p(t)$ is difficult to measure accurately. Since the dynamics of the power amplifier, the loudspeaker, and the vibro-acoustic transmission path are included in these transfer function, there is a greater degree of variation in comparison with the transfer functions shown in Figure 7.3. It is evident from these transfer functions that the magnitude falls significantly when the excitation frequency is less than 400 rad/s; this can be attributed to the roll-off in the loudspeaker frequency response as the power output reduces. Furthermore, we can observe the presence of the higher-order plate modes at 420 rad/s, 620 rad/s, and 780 rad/s, which are not accounted for in the actuator-plate model.

Despite these differences, it is apparent that the effects of the VFC loop are consistent with Figure 7.3; the effective damping of the first plate mode is increased, resulting in attenuation of up to 15 dB at the first plate resonance, whereas there is a reduction in the effective damping of the actuator mode. In addition, the higher-order plate modes are either attenuated (e.g. 620 rad/s) or unaffected by the VFC loop. These results show that the first plate mode is damped to a reasonable degree once the predicted stability limit is reached.

Whilst it has been demonstrated that VFC is capable of controlling the first plate mode by increasing the effective damping, there is a danger of the closed-loop system becoming unstable when $h > 50$. To illustrate this, the closed-loop acceleration response to tonal excitation at 200 rad/s is shown in Figure 7.6, using a large feedback gain $h = 100$. In this case, the response tends to a quasi-random LCO, thereby indicating that the closed-loop system is unstable. This confirms that the gain margin of the physical closed-loop system is smaller than the predicted linear gain margin.

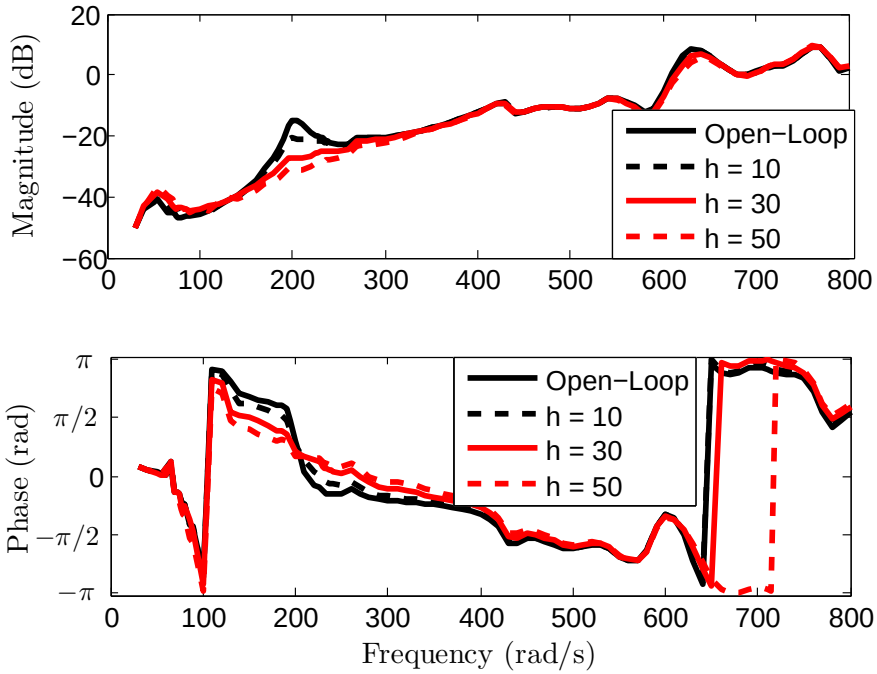

Figure 7.5: Open-loop and closed-loop VFC acceleration-voltage FRFs obtained from the physical system.

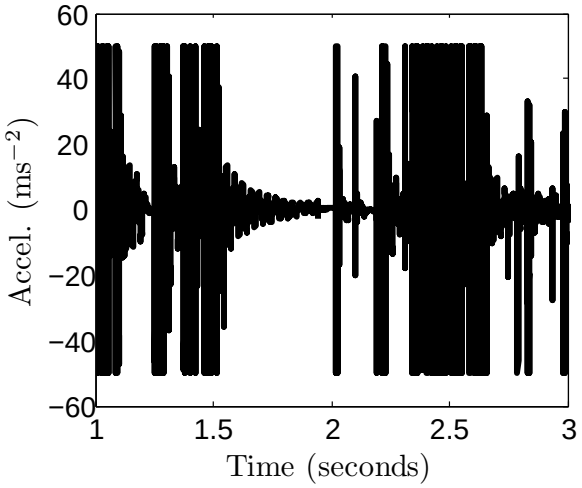

Figure 7.6: Closed-loop acceleration-time response of the plate structure to tonal excitation at 200 rad/s. The feedback gain is $h = 100$, which is well above the critical level $h = 50$.

An illustration of a velocity-time response (obtained by integrating the acceleration-time signal) is shown in Figure 7.7, where the impulses that are attributed to stroke saturation appear in-phase with the velocity signal. This confirms the predictions made by Baumann and Elliott [22] that stroke saturation increases the magnitude of the control signal.

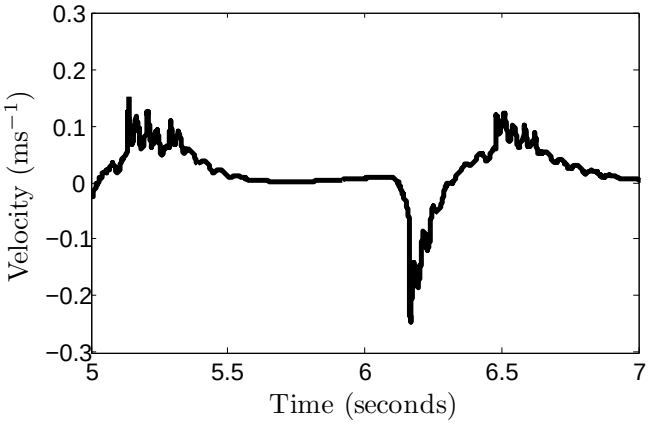

Figure 7.7: Measured structural velocity signal, including the effects of stroke saturation.

7.2.3 Response to impulsive excitation

In this section, we examine the closed-loop dynamics of the plate structure when excited by an impulse, applied using an impact testing hammer, as a means of comparison with the theoretical predictions. It is shown that the closed-loop system is particularly prone to instability when subjected to large, impulsive forces, since the proof-mass actuator is likely to saturate.

Using the VFC loop, the impulse responses of the plate structure for increasing feedback gains are illustrated in Figure 7.8. Here, we can see that when no control is applied ($h = 0$), the impulse response decays sinusoidally to the equilibrium position. However, once the VFC loop is introduced ($h = 10$), the actuator saturates several times before decaying to the equilibrium position, due to the greater energy levels in the proof-mass. This problem becomes more pronounced when the feedback gain is further increased ($h = 30$), where the actuator saturates over a period of several hundred milliseconds, thereby resulting in a less desirable impulse response of greater magnitude and duration. Once the feedback gain reaches the predicted stability limit ($h = 50$), the actuator saturates over a period of two seconds in the manner of a limit-cycle oscillation, and the closed-loop system is close to instability. These results show that the VFC loop has the effect of improving the plate dynamics when tonal excitation is used, whilst worsening the plate dynamics when impulsive excitation is used.

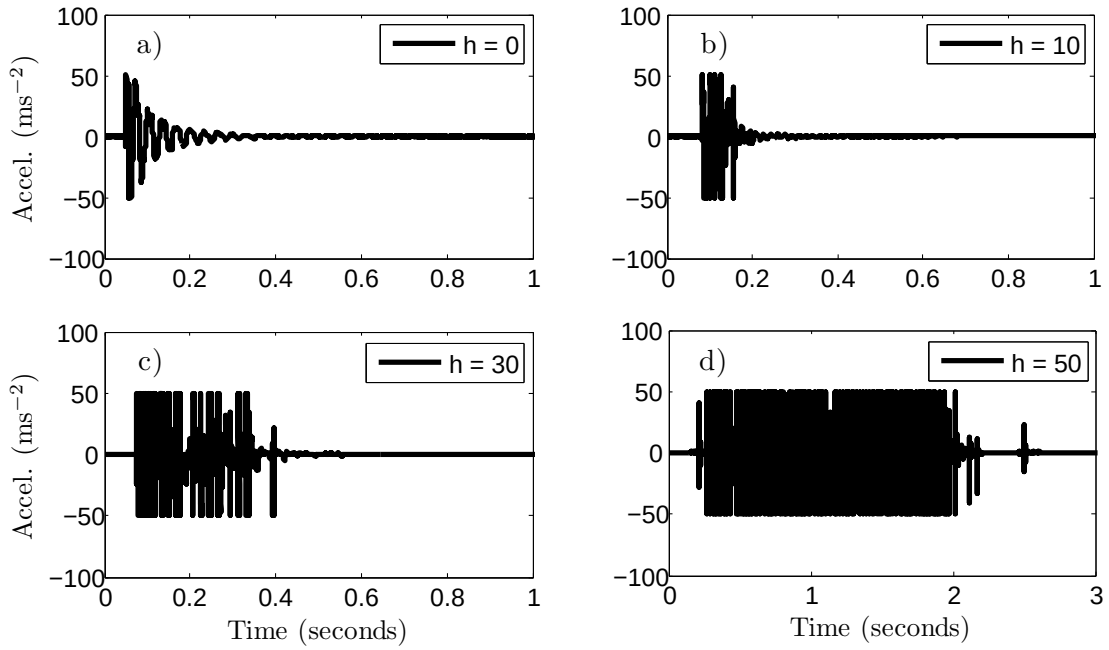

Figure 7.8: Acceleration responses to impulsive excitation using VFC, for a) $h = 0$, b) $h = 10$, c) $h = 30$, d) $h = 50$. The magnitude of the impulses is sufficient to cause voltage saturation at the data acquisition stage, which was unavoidable.

To assess the frequency of the oscillations observed in Figure 7.8, the Fourier transforms of each signal is taken using a Hanning window, and are shown in Figure 7.9. Initially ($h = 0$), the response decays with frequency $\omega_c = 194$ rad/s, which corresponds approximately to the frequency of the first plate mode. As the feedback gain increases, however, the frequency of the oscillations reduce to $\omega_c \approx 180$ rad/s for $h = 10$ and $\omega_c \approx 160$ rad/s for $h = 30, 50$ as the proof-mass coalesces with the first modal mass of the structure during saturation. The discrepancy between the predicted LCO frequency ($\omega_c = 183$ rad/s) and the lowest frequency of the measured oscillations ($\omega_c = 160$ rad/s) is 13.8 %, which is reasonable and confirms that the closed-loop system is tending towards LCO behaviour. The cause of the discrepancy is thought to occur from slight underestimations in the combined masses of the proof-mass and the first modal mass, since the plate does not behave exactly as a linear single-degree-of-freedom system.

Using the Simulink model, it was predicted that it becomes possible to destabilise the closed-loop system once the feedback gain exceeds $h = 50$, as shown in Figure 6.29. This is confirmed in Figure 7.10, which illustrates the impulse response of the plate structure for the feedback gain $h = 60$. Here, the impulse response tends to a self-sustaining

LCO, and the closed-loop system is now unstable. Thus, the theoretical gain margin is a reliable indication for predicting when stroke saturation will destabilise the closed-loop system when a sufficiently large impulsive input is provided. The frequency of the LCO is $\omega_c \approx 160$, which is consistent with Figure 7.9.

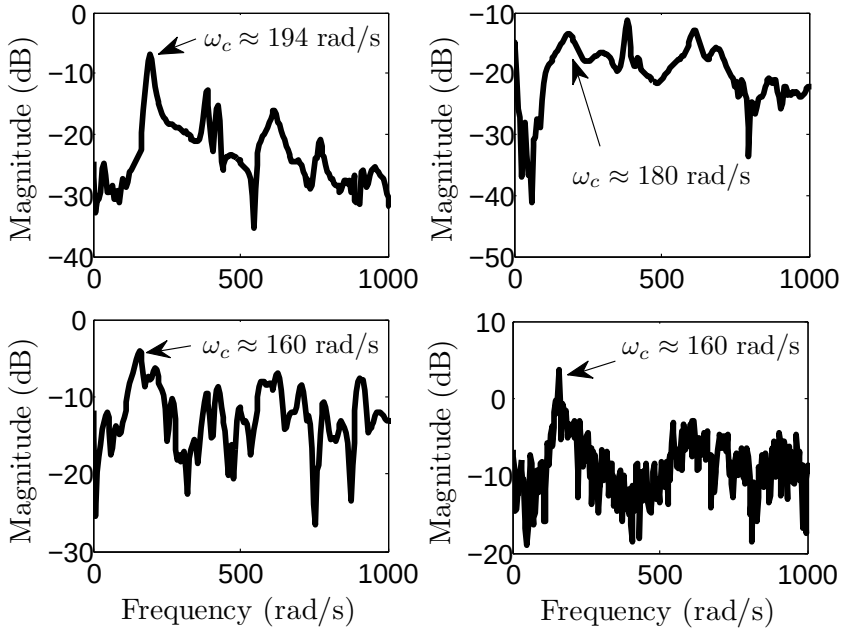

Figure 7.9: Fourier transforms of the acceleration-time signals shown in Figure 7.8.

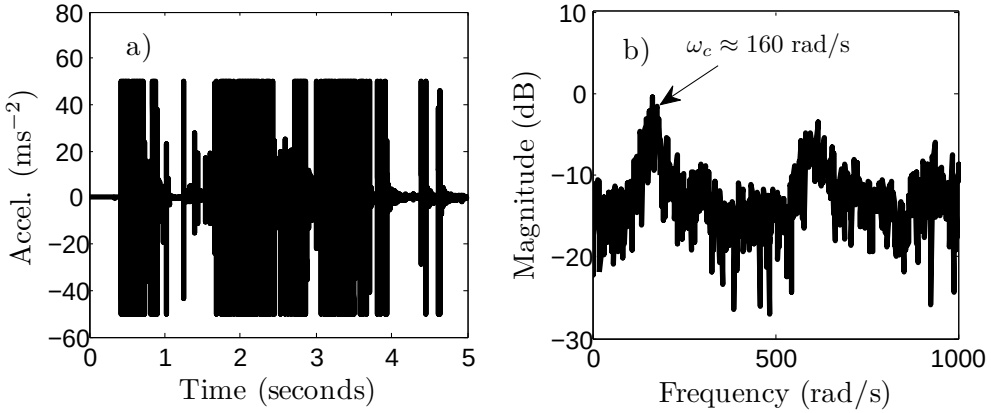

Figure 7.10: Unstable acceleration response to impulsive excitation using VFC, where $h = 60$, in the a) time-domain and b) frequency-domain.

7.2.4 Free response

Since the closed-loop stability limits to large, impulsive forces have now been established, the next step is to ascertain the effective stability margin when no input is considered. In the absence of stroke saturation, we expect the stability limits to be dictated by the suspension nonlinearities. To confirm that this is the case, we must observe some differences in the way that linear and nonlinear systems become unstable.

First, we apply positive VFC to the plate structure, such that the control loop reduces the effective damping at the first plate mode. Since the actuator-plate configuration is approximately linear at the crossover frequency (200 rad/s), the stability limit is determined by the linear gain margin at the first plate mode, and the actuator nonlinearities have a negligible effect on the overall stability. The linear gain margin is predicted from the Nyquist plots in Figure 6.17 as $h \approx 11$. This corresponds well with the physical system, which becomes unstable when the feedback gain exceeds this value.

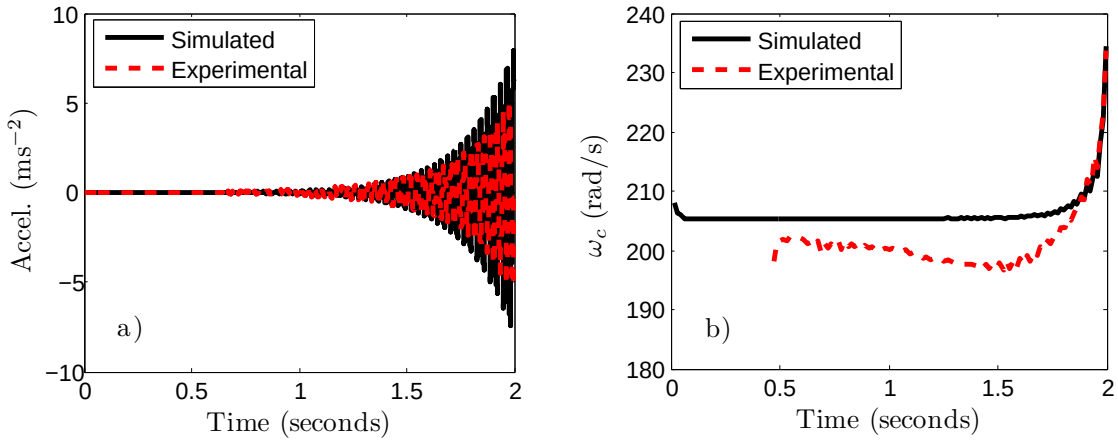

Figure 7.11: Unstable acceleration response for positive feedback control a) acceleration-time histories and b) frequency of acceleration-time histories over time.

A comparison of the simulated and measured acceleration-time signals, with positive feedback gain $h = 15$ and no external forcing, is shown in Figure 7.11a). Here, it is apparent that there is good agreement between the Simulink model and the physical system, which are both unstable. Since the responses immediately increase sinusoidally, it is apparent that the underlying linear system is the cause of instability. In addition, a zero crossing detection is used to ascertain the frequency of the sinusoids over time to establish the variation in the resonance frequency as the amplitude rises. This is shown

in Figure 7.11b). Again, there is relatively good agreement between the simulated and measured signals, with an initial frequency that approximately matches the first plate resonance frequency, as expected. As the amplitude rises, however, in both cases, the frequency of the sinusoids increases up to a factor of approximately 15%, due to the suspension nonlinearities in the actuator and weak nonlinearities in the plate structure.

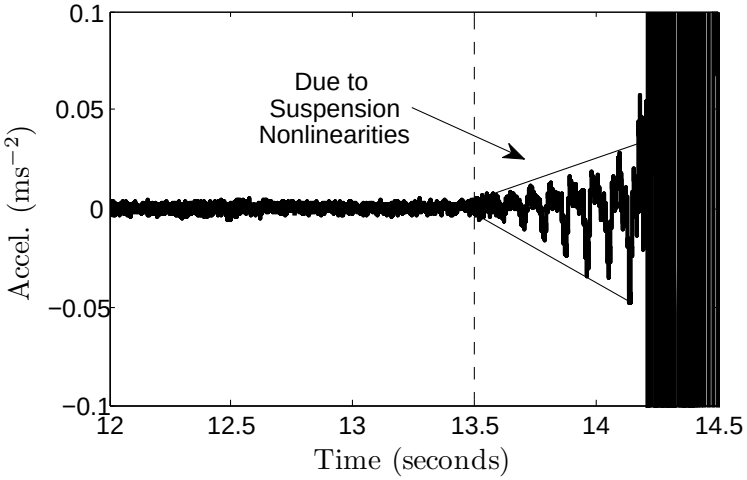

Figure 7.12: Unstable acceleration response using VFC, with feedback gain $h = 130$.

Next, the negative VFC loop is considered again, for the purpose of assessing the effects of the actuator suspension nonlinearities on the overall closed-loop stability, with regards to the theoretical predictions made in the previous chapter. Figure 7.12 shows the acceleration-time response, with no excitation, for the feedback gain $h = 90$ at $t = 0$, $h = 110$ at $t > 5$ seconds, and $h = 130$ at $t > 10$ seconds. During the first ten seconds, the closed-loop system is stable (not shown in Figure 7.12). However, at approximately 13.5 seconds, it is apparent that the system response exhibits growing periodic oscillations, which last for several hundred milliseconds until the actuator saturates and the closed-loop system enters a limit-cycle oscillation. This indicates that the closed-loop system becomes unstable before the actuator saturation occurs, and so the cause of instability relates either to the underlying linear system or the actuator suspension nonlinearities.

There are several reasons to believe that the actuator suspension nonlinearities are the cause of instability in this case. Firstly, the growing periodic oscillations in Figure 7.12 contain a significant degree of harmonic distortion, unlike the sinusoidal oscillations shown in Figure 7.11. The fundamental frequency of the periodic oscillations is approximately 70

rad/s, and so the harmonic distortion in the oscillations can be attributed to the actuator suspension nonlinearities.

Secondly, it is apparent that several seconds pass in Figure 7.12 before the growing periodic oscillations start to occur; this is a key feature of an unstable nonlinear system, which requires the response amplitude is sufficiently large to induce instability. In contrast, the response of an inherently unstable linear system will grow immediately away from the equilibrium position, as illustrated in Figure 7.11a). In other words, the nonlinear system does not become unstable until the background noise level is high enough at 13.5 seconds.

Thirdly, the feedback gain $h = 130$ lies within the unstable region identified in Figure 6.29 (for $h > 120$) where the suspension nonlinearities are considered to be the dominant cause of instability in the simulations. This suggests that the actuator suspension nonlinearities have a profound effect on the closed-loop stability margin by reducing the effective gain margin up to approximately 35 % from $h = 175.7$ to $h \approx 130$. In addition, the results demonstrate that the Simulink model is able to reliably predict the closed-loop stability limits when VFC is used.

7.2.5 Discussion

From the results obtained in this section, the following conclusions about the physical actuator-plate configuration are drawn,

1. The first plate mode can be effectively controlled using VFC to increase the apparent damping. It was found that reductions of up to 15 dB are possible at the peak resonance frequency before the stability limits are reached.

2. The actuator mode is affected by the VFC loop, which reduces its apparent damping. These findings are consistent with the theoretical predictions.

3. The impulse response of the plate structure is worsened by VFC, due to actuator saturation becoming more pronounced as the feedback gain increases. This eventually destabilises the closed-loop system.

4. It was confirmed that the closed-loop system may become unstable for control gains that are smaller than the linear gain margin when an impulsive input is applied. Using VFC, the stability limits of the physical system are consistent with the predicted stability limits made using the Simulink model.

5. It was confirmed that the suspension nonlinearities are capable of destabilising the closed-loop system for feedback gains that are consistent with the predictions made using the Simulink model. Thus, the Simulink model may be used to reliably predict the closed-loop stability of the physical system. Having said this, it should be noted that these results only confirm the reliability of predicting the stability limits, and the Simulink model may not be reliable at predicting the closed-loop stability for a particular operating condition.

Having established that stroke saturation is capable of greatly reducing the closed-loop stability margin, the next step is to implement the on-off VFC scheme specified in the previous chapter for the purpose of stabilising the closed-loop system. This is explored in the next section.

7.3 Stabilisation of actuator-plate configuration

In this section, we consider the application of detection-dependent control to the problem of stabilising the closed-loop actuator-plate configuration under the conditions of stroke saturation [141]. It was established in sections 6.4 and 7.2 that large spikes appear in-phase with the structural velocity when stroke saturation occurs, thereby greatly increasing the magnitude of the control signal. This has the effect of increasing the kinetic energy of the proof-mass as it moves rapidly from one end stop to the other, and results in closed-loop destabilisation by exploiting regions of potential instability that are already present in the underlying linear system.

Using the control deactivation scheme presented in section 6.5, the closed-loop system may, in principle, be stabilised by deactivating the control signal during the so-called "destabilisation period", which occurs after the onset of stroke saturation. In this manner, the control signal is deactivated for N_τ samples immediately after stroke saturation is detected, such that no control is applied when the proof-mass is moving within its stroke. This prevents the increase in total mechanical energy, and so the closed-loop system remains stable. This is referred to as on-off VFC.

The destabilisation period includes the duration of stroke saturation (where the magnitude of the control signal increases) and the subsequent duration of the proof-mass moving through its stroke (where the rise in total mechanical energy occurs). Therefore, it is necessary to ensure that the deactivation period N_τ is sufficiently long to cover both

these time periods whilst ensuring it is small enough to retain good control performance under normal operating conditions.

7.3.1 Simulations

The control deactivation scheme, as shown in Figure 6.39, was applied to the Simulink model (neglecting suspension nonlinearities) for the purpose of examining the effects of the detection-dependent controller on the simulated time histories and stability characteristics. In order to implement the control deactivation scheme, the velocity feedback loop shown in Figure E.15, Appendix E was modified to accommodate the detection-dependent elements. Since the detection of stroke saturation requires the use of a high sample rate (51.2 kHz), it was important to ensure that the detection procedure is applied *after* the control signal is generated. Furthermore, a unit delay is applied to the detection signal to prevent the occurrence of an algebraic loop in the Simulink model. Since the sample rate is high, relative to the dynamics of the actuator-plate configuration, this delay has a negligible effect on the synchronisation of the deactivated control signal with the destabilisation period. See Appendix E for schematic details.

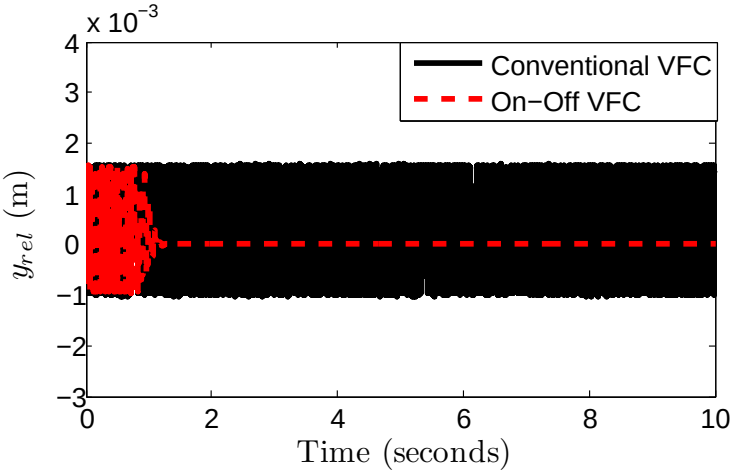

Figure 7.13: Closed-loop response to impulsive excitation for $h = 80$ using conventional VFC and on-off VFC.

Using this modified Simulink model, the control deactivation procedure is demonstrated by simulating the time histories of the relative displacement signal, $y_{rel}(t)$, in response to an impulse of amplitude 50 N and duration of one millisecond, where the feedback gain is $h = 80$. These time histories are simulated using the fixed-step ode3 solver at a sample

rate of 51.2 kHz. It is shown in Figure 6.29 that, under these conditions, the magnitude of the impulsive input is sufficient to destabilise the closed-loop system when conventional VFC is used; this is confirmed in Figure 7.13, as $y_{rel}(t)$ tends to a limit cycle oscillation.

In order to stabilise the closed-loop system for this particular case, we apply the on-off VFC procedure, using a relatively large detection threshold ($T_{dec} = 0.2$ Volts) and setting the deactivation period $N_\tau = 500$ samples (about 10 milliseconds). By simulating the resulting time history of $y_{rel}(t)$, it is also apparent in Figure 7.13 that the response tends towards the equilibrium point after approximately 800 milliseconds, thereby indicating that the closed-loop system is stable.

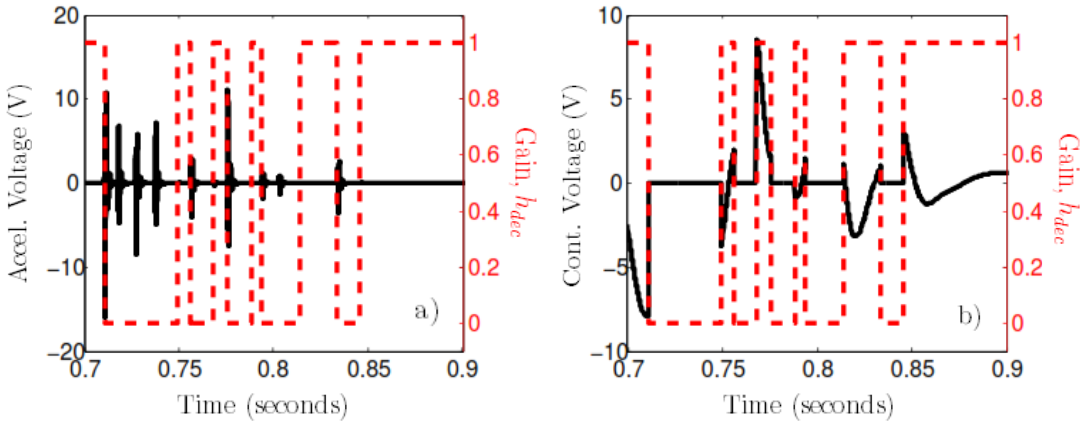

Figure 7.14: Simulations of a) the filtered acceleration signal (solid line) and h_{dec} (dashed line), and b) the control signal (solid line) and h_{dec} (dashed line).

The effects of the on-off controller are illustrated in Figures 7.14a) and 7.14b), where Figure 7.14a) shows the detection-dependent gain h_{dec} in relation to the filtered acceleration signal, and Figure 7.14b) shows the effects of h_{dec} on the control signal. Figure 7.14a) is similar in nature to Figure 6.40, and shows that h_{dec} is set to zero when impulses appear in the filtered acceleration signal, until after 0.85 seconds, where the impulses cease to occur. Figure 7.14b) indicates that the control signal becomes zero whenever saturation is detected and h_{dec} is zero. This enables the closed-loop response to eventually tend towards the equilibrium position. However, it should be noted that once the deactivation period is over and the controller is reactivated, large shocks may appear in the control signal, due to the non-zero velocity of the structure and the discontinuous nature of the controller. When this happens, the control signal increases the velocity of the proof-mass, thereby increasing its kinetic energy in a similar manner to the destabilising effects of

stroke saturation, as discussed previously.

An illustration of this phenomenon is given by Figure 7.15, which shows a comparison of the total mechanical energy, $E(t)$, the kinetic energy of the proof-mass, $T_p(t)$, and the detection-dependent control gain, h_{dec}. Here, it is apparent that $E(t)$ and $T_p(t)$ both decrease during deactivation periods $h_{dec} = 0$; this is expected, since the system is effectively open-loop during these periods. However, it can be seen that when the controller is reactivated ($h_{dec} = 1$), the kinetic energy of the proof-mass tends to rise significantly, causing a temporary increase in the total mechanical energy until the proof-mass hits the end stops, stroke saturation occurs, and the controller is deactivated again.

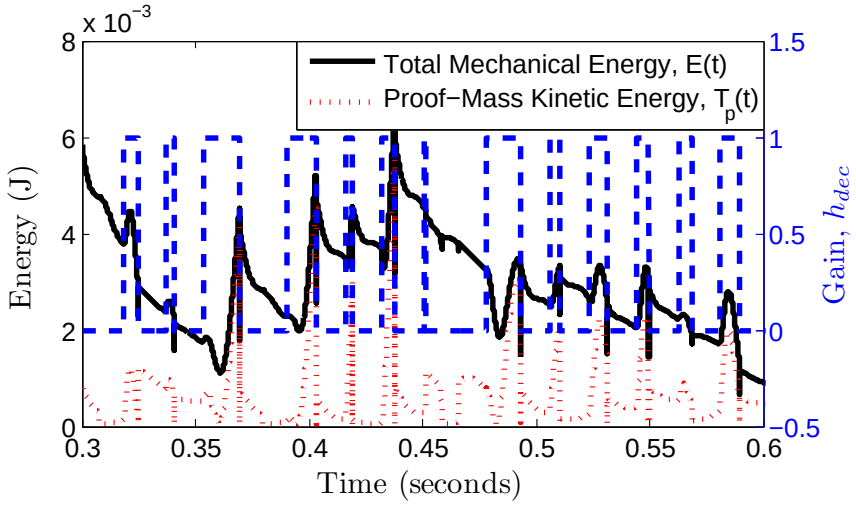

Figure 7.15: Simulations of $E(t)$ (solid line) and $T_p(t)$ (dotted line) in comparison with h_{dec} (dashed line).

In this case, the increases in $E(t)$ are not a concern regarding stability, as the closed-loop system is stabilised after 800 milliseconds. However, the closed-loop stabilisation is delayed by this phenomenon, resulting in multiple occurrences of stroke saturation before the closed-loop response tends to the equilibrium point. More importantly, this phenomenon may prevent the stabilisation of the closed-loop system when more severe operating conditions are considered, such as a larger feedback control gain. This is demonstrated in Figure 7.16a), where the control gain is increased to $h = 100$, and it is apparent that the closed-loop system is no longer stable.

One particular solution to this problem is to consider increasing the deactivation period N_τ, such that the system remains in the stable open-loop phase for longer periods of time. Figure 7.16b) shows the simulated responses of the closed-loop when the deac-

tivation period is increased to $N_\tau = 600$ samples and $N_\tau = 2,000$ samples respectively, for the control gain $h = 100$. In this figure, it is apparent that the closed-loop system is stabilised for both cases; when $N_\tau = 600$ samples, stabilisation occurs at $t \approx 5$ seconds, which is still a relatively long unstable period. However, for the larger deactivation period, the closed-loop is stabilised after a much shorter duration of 300 milliseconds, thereby indicating that a larger value for N_τ results in a more stable closed-loop system.

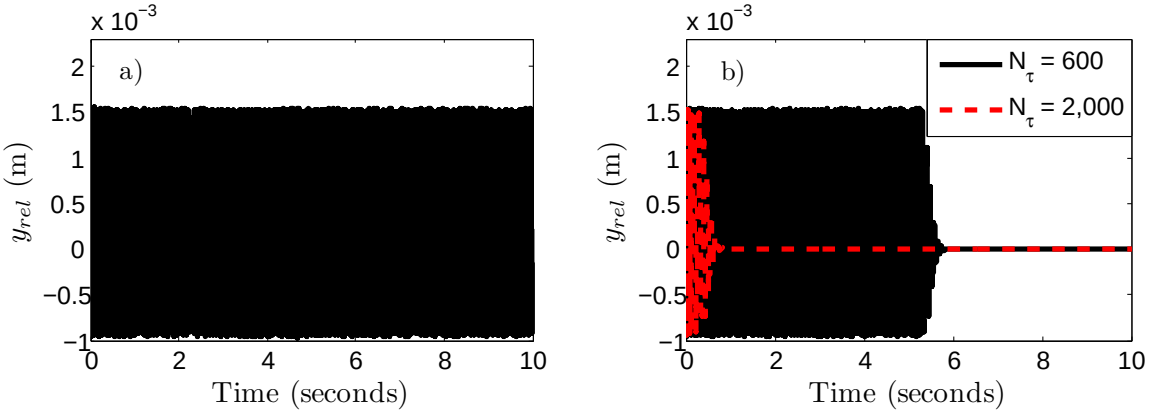

Figure 7.16: Closed-loop response to impulsive excitation using on-off VFC for a) $N_\tau = 500$ samples and b) $N_\tau = 600$ samples and $N_\tau = 2,000$ samples.

These results infer that the deactivation period required for stabilisation is dependent on the feedback control gain, since the closed-loop system is more prone to destabilisation when the control gain is higher. In order to illustrate this dependency, the minimum deactivation period required for stabilising the closed-loop system (in response to an impulse of magnitude 50 N and duration 1 millisecond) is ascertained using trial-and-error for a specified control gain, ranging from $h = 60$ to $h = 160$. The results are shown in Figure 7.17, which indicates that N_τ increases significantly when the feedback gain rises above $h = 80$, resulting in a doubling of N_τ as the feedback gain reaches $h = 160$.

It should be noted that the minimum values for N_τ specified in Figure 7.17 are also weakly dependent on the amplitude of the impulse excitation, where slightly larger values of N_τ are required as the amplitude increases. Therefore, the chosen deactivation period should be well above the minimum values in Figure 7.17, to ensure closed-loop stability. Several of these minimum-valued deactivation periods are confirmed in Figure 7.18, which shows the simulated closed-loop response for numerous control gains whilst utilising these deactivation periods. For these cases, we can observe that whilst the closed-loop system is unstable over a period of several seconds, due to N_τ being set to a minimum, all the re-

sponses eventually decay to the equilibrium position. This demonstrates the applicability of on-off VFC for ensuring closed-loop stabilisation.

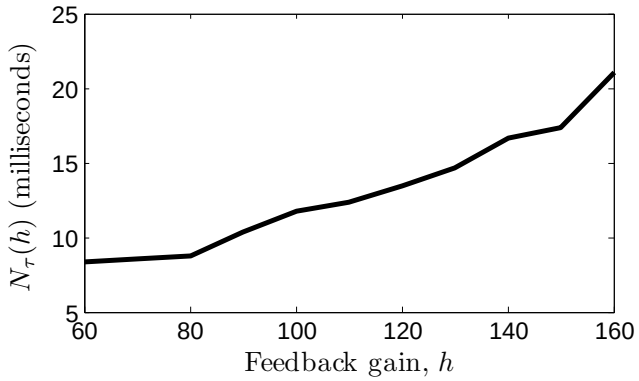

Figure 7.17: Illustration of minimum delay in on-off controller required for closed-loop stabilisation against h (simulations).

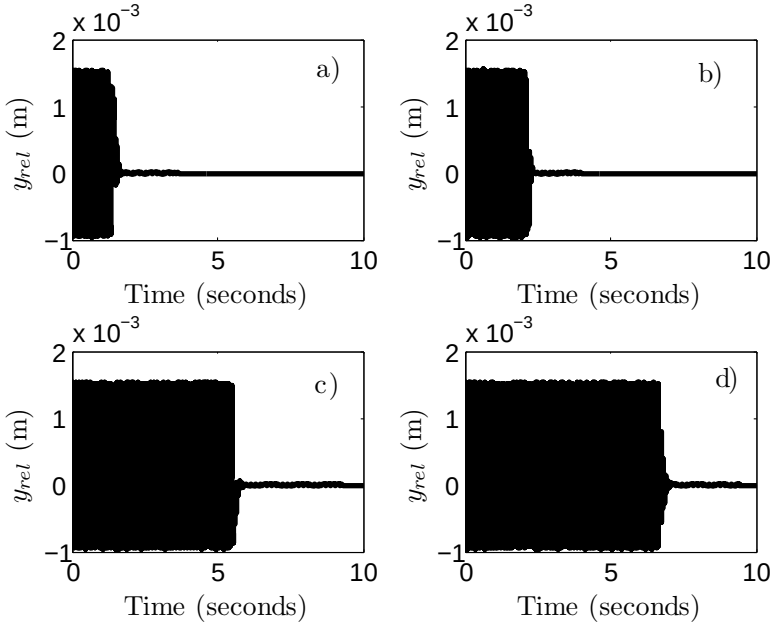

Figure 7.18: Closed-loop responses for a) $h = 70$, $N_\tau = 430$ samples, b) $h = 90$, $N_\tau = 530$ samples, c) $h = 110$, $N_\tau = 630$ samples, and d) $h = 130$, $N_\tau = 750$ samples.

7.3.2 Experiments

The on-off VFC controller is now applied to the physical actuator-plate configuration for the purpose of preventing closed-loop destabilisation as a result of stroke saturation. It was shown in section 7.2 that the closed-loop system becomes susceptible to destabilisation for $h > 50$ when conventional VFC is used, and so the aim of applying on-off VFC is to increase the stability limit of the closed-loop system.

In order to implement the on-off VFC scheme the experimental setup described in section 7.1 is modified by placing a Dytran 3035BG accelerometer on the actuator casing, which was connected to the dSpace DS1103 PPC Controller Board via a Dytran 4102C Signal Conditioner for saturation detection purposes. This setup is shown in Figure 7.19.

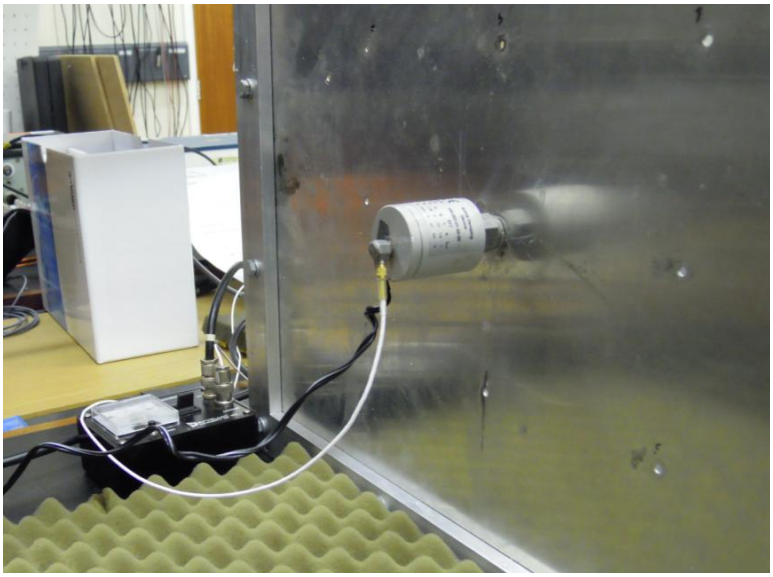

Figure 7.19: Illustration of the actuator-plate setup, including the accelerometer used for saturation detection.

Similarly, the velocity feedback controller implemented in Simulink is modified to account for saturation detection by including the aforementioned detection block in the control path. The sample rate is 40 kHz, with the velocity signal being temporarily downsampled to 2 kHz for filtering and integration purposes, and the detection threshold is set to $T_{dec} = 10^{-3}$ Volts. A schematic of the modified Simulink controller is illustrated in Figure 7.20.

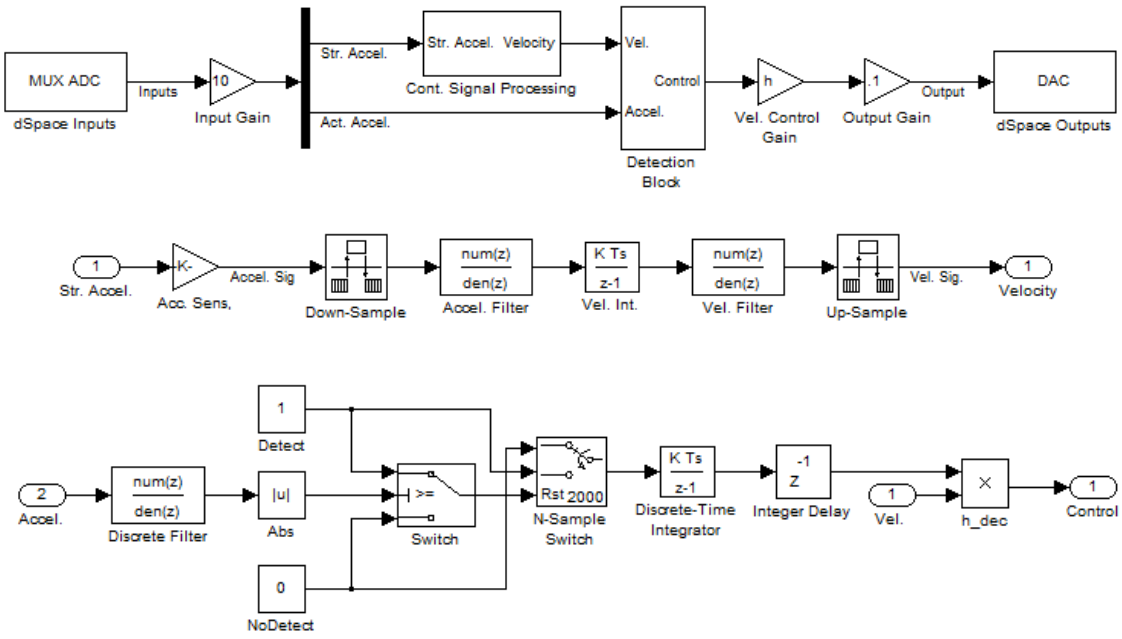

Figure 7.20: Schematic of the on-off velocity feedback controller in Simulink, including the primary control path, the control signal processing block, and the detection block.

In order to compare the effects of conventional VFC and on-off VFC, we apply an impulsive force to the plate structure using an impact testing hammer, and we assess the closed-loop acceleration response for the control gain $h = 60$, using a deactivation period $N_\tau = 2,000$ samples (about 40 milliseconds) for on-off VFC. It was demonstrated in Figure 7.10 that the specified control gain is sufficient to potentially destabilise the closed-loop system when an impulsive force is used. This is confirmed in Figure 7.21a), which illustrates the quasi-random LCO acceleration response when conventional VFC is used. In contrast, Figure 7.21b) shows that the amplitude of the impulses in the acceleration response is greatly reduced when on-off VFC is used, eventually decaying to the equilibrium position. This demonstrates that on-off VFC control has the capability of stabilising the closed-loop system in a particular control scenario where the application of conventional VFC results in closed-loop destabilisation.

A closer examination of the closed-loop response using on-off VFC is shown over a shorter time period ($t = 0.4 - 0.5$ seconds) in Figure 7.22, where the acceleration signal is compared with the filtered detection signal, the detection-dependent gain h_{dec}, and the control signal. In Figure 7.22a), it is apparent that impulses occur quasi-periodically

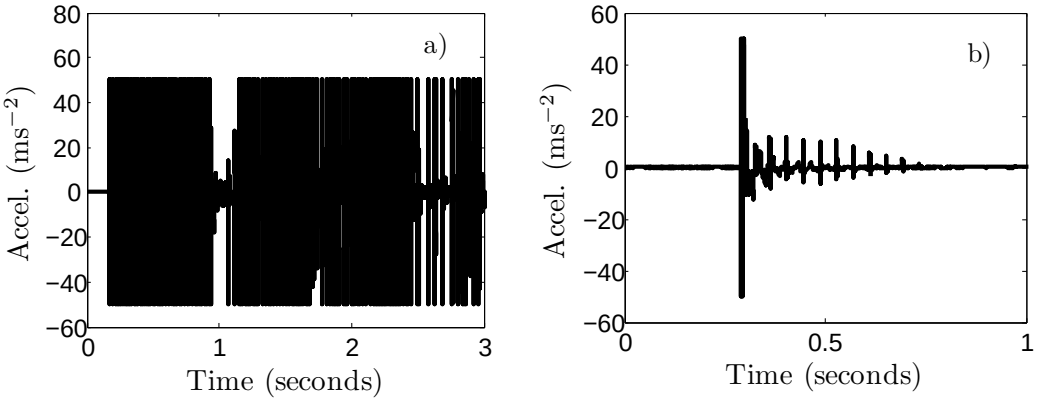

Figure 7.21: Acceleration responses to an impulsive input for $h = 60$, using a) conventional VFC and b) on-off VFC.

in both the acceleration response and the filtered detection signal as a result of stroke saturation. An explanation for this phenomenon is shown in Figure 7.22b) and Figure 7.22c). In Figure 7.22b), it can be seen that the impulses occur when the controller is reactivated, which infers that the controller causes stroke saturation at the time of reactivation. Since this results in control deactivation, the controller is only active for relatively short periods of time.

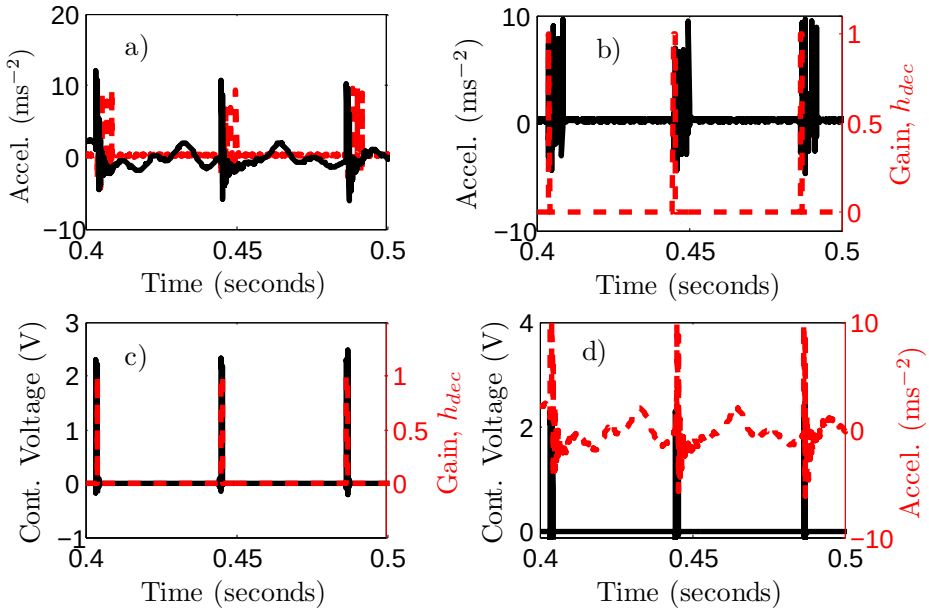

Figure 7.22: Comparison of a) acceleration and detection signals, b) detection signal and h_{dec}, c) control signal and h_{dec}, and d) control and acceleration signals.

Furthermore, Figure 7.22c) shows that magnitude of the control signal is relatively high when the controller is reactivated, which, in conjunction with the abruptness of the reactivation, results in a large, impulsive force being imparted to the actuator-plate configuration. This causes stroke saturation to occur again. It is apparent in Figure 7.21b) that this cycle is repeated numerous times until the amplitude of the impulses is sufficiently small to break the cycle and stabilise the closed-loop system. These findings are in agreement with the simulated results, demonstrating that the closed-loop system is eventually stabilised after a delay imposed by this phenomenon. Finally, we can observe in Figure 7.22d) that the structural acceleration becomes approximately time-harmonic when the controller is switched off in response to the impulses.

Now, we investigate the effects of the deactivation period N_τ on the stability of the closed-loop system. For this case, we increase the feedback gain to $h = 100$, such that the closed-loop system is more susceptible to destabilisation from stroke saturation. First, the gain of the filtered detection signal is set to zero, resulting in a conventional VFC loop. Next, an impulsive input is applied to the plate structure, and the closed-loop system is allowed to become unstable for several seconds until the detection gain is reset and the controller starts to apply on-off VFC.

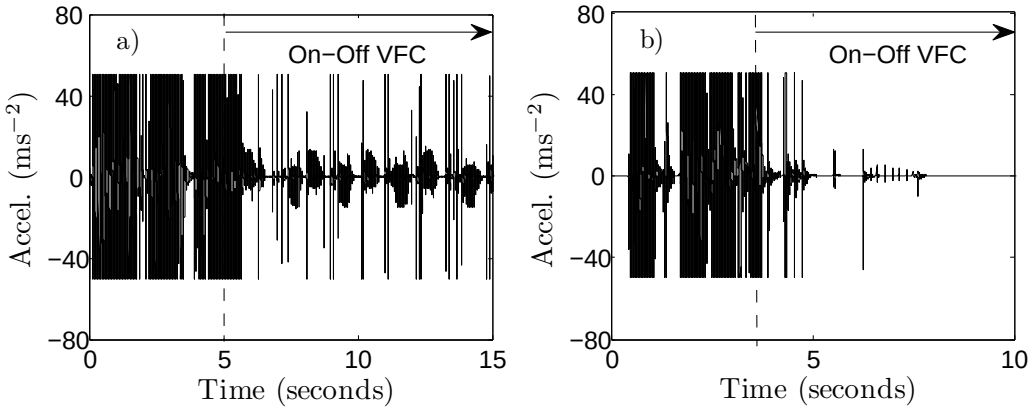

Figure 7.23: Closed-loop acceleration responses for $h = 100$ using on-off VFC, where N_τ is a) 1,500 samples, and b) 7,000 samples.

Figure 7.23a) shows the acceleration response of the structure when the deactivation period is specified as $N_\tau = 1,500$ samples (about 30 milliseconds). In this illustration, it is apparent that whilst the amplitude of the impulses is greatly reduced by the on-

off VFC, the closed-loop system is still unstable, and exhibts resonance effects after the impulses have occurs. This shows that the deactivation period is insufficient to prevent the impulses in the control signal from destabilising the closed-loop system when the controller is reactivated.

In order to ensure closed-loop stability, the procedure is repeated using a deactivation period $N_\tau = 7,000$ samples (about 137 milliseconds). The resulting acceleration response, which is shown in Figure 7.23b), shows that the unstable closed-loop system returns to the equilibrium position a few seconds after on-off VFC is activated, thereby indicating that the closed-loop system is stabilised as a result of the longer deactivation period.

The relationship between the deactivation period and the feedback gain is investigated further by measuring the closed-loop acceleration response for a specified h and establishing the minimum value of N_τ required to stabilise the closed-loop system, in a similar manner to Figure 7.17. The results are shown in Figure 7.24, where the feedback gains range from $h = 60$ to $h = 130$, up to the stability limit imposed by the suspension nonlinearities.

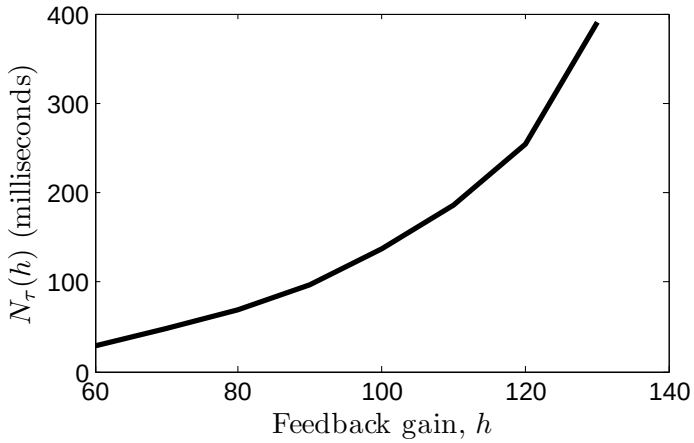

Figure 7.24: Illustration of minimum delay in on-off controller required for closed-loop stabilisation against h (experimental).

By comparing Figure 7.24 with Figure 7.17, it is apparent that in both cases, the deactivation period rises significantly as the control gain increases, which confirms that the closed-loop system requires a longer period in the open-loop phase to prevent destabilisation at higher gains. However, there are also a few noteworthy differences in the two figures. Firstly, the duration of the deactivation periods is far longer in Figure 7.24, up to a factor of 20, in comparison with Figure 7.17. This shows that the experimental

setup requires a longer deactivation period than suggested by the predictions made using the simulations. Secondly, the deactivation period increases more rapidly in Figure 7.24, which indicates that the closed-loop system becomes increasingly difficult to stabilise when the control gain is large ($h > 100$).

Thirdly, the control gain $h = 130$ in Figure 7.24 is determined as the limit to the performance of the controller, since the closed-loop system cannot be stabilised using on-off VFC when $h > 130$. In fact, this phenomenon also occurs at $h = 130$ if a sufficiently long period of time is allowed to pass, and so, the stability limit is set at $h = 120$. Therefore, we can determine from this analysis that the stability limit imposed by the suspension nonlinearities is still applicable for on-off VFC, and a different control law, such as an inverse describing function procedure [151], should be considered if one wishes to increase the stability limit above $h = 120$.

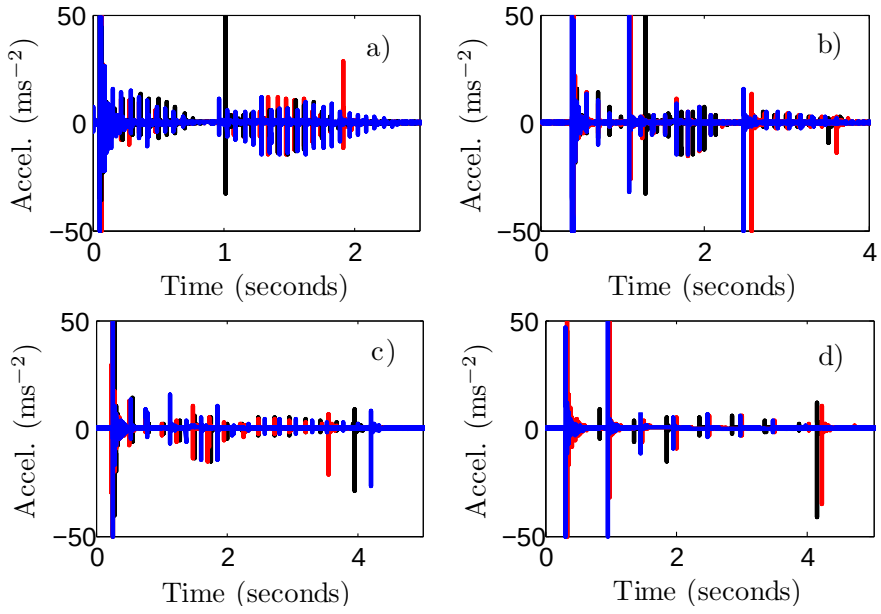

Figure 7.25: Closed-loop acceleration responses for a) $h = 70$, $N_\tau = 2,500$ samples, b) $h = 90$, $N_\tau = 5,000$ samples, c) $h = 110$, $N_\tau = 9,000$ samples, and d) $h = 130$, $N_\tau = 20,000$ samples.

In order to illustrate the effects of these various deactivation periods on the closed-loop system, several acceleration responses to an impulsive input are shown in Figure 7.25 using a variety of control gains ranging from $h = 70$ to $h = 130$. In each case, the deactivation period is chosen near the minimum value specified in Figure 7.24, and the procedure is repeated three times to demonstrate that the closed-loop system is stable. It

is apparent in these figures that the impulse response increases in duration as N_τ becomes larger, since the controller is switched off for longer periods of time and the impulses are spread further apart. Nevertheless, the figures demonstrate that the on-off controller is capable of increasing the stability limit from $h = 50$ to $h = 120$, which is considered to be sufficient for this thesis.

From the previous analyses, it is apparent that N_τ should either vary with the feedback gain or a value for N_τ should be specified that is a suitable compromise for as large a range of control gains as possible. The latter approach is deemed to be more suitable for practical applications, and so the deactivation period is specified as $N_\tau = 9,000$ samples, which is approximately 176 milliseconds. This value is sufficient to ensure closed-loop stability up to $h \approx 110$. However, it is also important to confirm that the closed-loop acceleration response is not unduly affected by the on-off VFC when N_τ is relatively large. Ideally, the on-off VFC should improve the impulse response in relation to conventional VFC by shortening the magnitude and duration when possible.

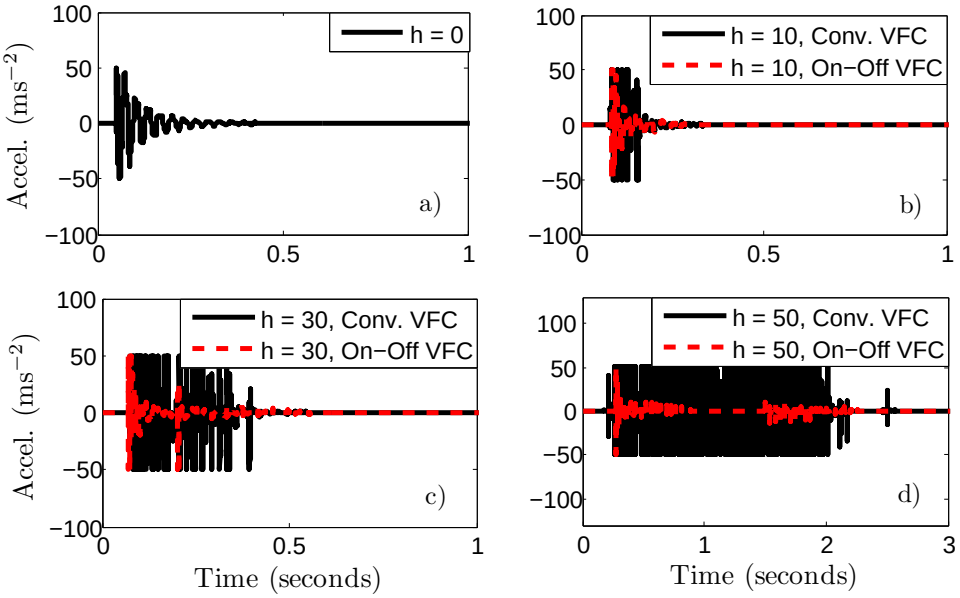

Figure 7.26: Comparison of closed-loop acceleration responses obtained using conventional VFC and on-off VFC for a) $h = 0$, b) $h = 10$, c) $h = 30$, and d) $h = 50$.

In section 7.2, the closed-loop acceleration response to an impulsive input using conventional VFC is measured for a number of control gains. These responses are shown in Figure 7.8. It was observed that increasing the feedback gain had the effect of worsening the acceleration response by increasing its magnitude and duration. This procedure was

repeated using on-off VFC, and the resulting measurements are shown in Figure 7.26 for the purpose of comparison with the results in Figure 7.8.

These figures show that the on-off VFC greatly improves the acceleration responses in relation to conventional VFC by reducing the magnitude of the impulsive shocks over time. There is little effect on the duration of the acceleration responses, as the impulses associated with the on-off VFC are relatively far apart as a result of the large deactivation period. Nevertheless, stroke saturation occurs less frequently and less severely in comparison with conventional VFC, and therefore, the application of on-off VFC is beneficial to the controller performance, as well as increasing the stability limit.

As a final means of confirmation that the on-off VFC is capable of increasing the stability limit of the closed-loop system, the acceleration-voltage transfer functions of the actuator-plate configuration are obtained using stepped-sine excitation with feedback gains $h = 0$ and $h = 100$. It was established in section 7.2. that $h = 100$ is well beyond the stability limit when conventional VFC is used. Therefore, the time histories are measured over a duration of 15 seconds to allow for the occurrence of stroke saturation. In the event of stroke saturation, the closed-loop system is stabilised, and the response tends to the steady-state solution required to obtain the transfer functions.

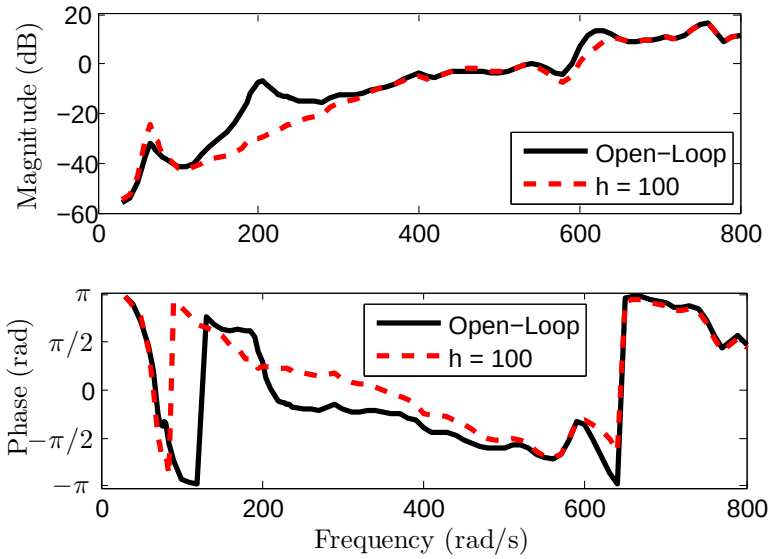

Figure 7.27: Magnitude and phase of open-loop and closed-loop acceleration-voltage transfer functions obtained using on-off VFC.

Figure 7.27 shows a comparison of these two measured transfer functions. Here, we can observe that the on-off VFC has similar effects to conventional VFC when tonal excitation is utilised, resulting in an 22 dB reduction at the first plate resonance ($\omega = 200$ rad/s), a minor reduction at the third plate resonance ($\omega = 620$ rad/s), and an amplification of the actuator mode at $\omega = 75$ rad/s. The damping effects of the controller are more pronounced in relation to conventional VFC, since the stability limits prevent this degree of control from being utilised in Figure 7.5. Therefore, utilising on-off VFC instead of conventional VFC can improve closed-loop performance by increasing the possible amount of effective damping, in addition to improving the closed-loop impulse response.

7.4 Conclusions

When conventional VFC is applied to the experimental actuator-plate configuration, it was demonstrated that the control loop improves the closed-loop response to tonal excitation whilst worsening the closed-loop response to impulsive excitation. It was found that the closed-loop system may be destabilised for control gains that are far smaller than the predicted linear gain margin predicted. The gain margins $h = 50$ and $h = 130$ for stroke saturation and the suspension nonlinearities respectively were ascertained from the experimental setup, which agree well with the theoretical predictions. In addition, the destabilising effects of the suspension nonlinearities was confirmed by setting the feedback gain to $h = 130$ and allowing several seconds to pass before the closed-loop system became unstable.

In order to stabilise the closed-loop system, a nonlinear on-off VFC scheme was implemented. This control scheme involves deactivating the control signal when stroke saturation is detected, such that the rise in energy levels is avoided. It was demonstrated using simulations and experimental measurements that the on-off VFC scheme is capable of preventing stroke saturation from destabilising the closed-loop system, provided that the deactivation period is sufficiently long. Additionally, the on-off VFC scheme, if used properly, offers several advantages over conventional VFC by increasing the stability limit from $h = 50$ to $h = 120$ and reducing the amplitude of the impulsive shocks caused by stroke saturation. Therefore, the on-off VFC scheme appears to offer a promising means of improving controller performance and stability in relation to conventional VFC.

Having said this, the findings also reveal a number of limitations to the on-off VFC scheme. Firstly, it is not effective at preventing closed-loop destabilisation for $h \geq 130$, where the suspension nonlinearities of the actuator are capable of inducing closed-loop instability.

Secondly, the closed-loop system becomes increasingly difficult to stabilise as the feedback gain approaches the stability limit, with no guarantee that the closed-loop system will remain stable over time.

Thirdly, the abrupt nature of the controller results in large, quasi-impulsive control signals when the controller is reactivated and subsequently deactivated as a result of stroke saturation. This phenomenon is detrimental to the stability of the closed-loop system, as it delays the acceleration response from returning to the equilibrium position and may destabilise the closed-loop system if the deactivation period is not sufficiently long.

Fourthly, the dynamics of the controller are extremely complex when on-off VFC is utilised, and it is difficult to develop a rigorous proof of closed-loop stability, particularly for MIMO control systems, where this control scheme has yet to be tested.

In order to overcome these deficiencies, it is proposed that the on-off VFC scheme is utilised in conjunction with the gain scheduling scheme outlined in chapter 6, where the control gain takes a finite period of time to increase from zero to its original value once the controller is reactivated. In this manner, the control signal is allowed to incrementally increase to normal operating conditions when controller reactivation occurs, thereby avoiding the observed quasi-impulsive control forces. This is a subject of ongoing research.

Chapter 8

Conclusions

8.1 Conclusions and suggestions for future work

This chapter summarises the results of the research undertaken in this doctoral thesis, which investigates the application of active feedback control for structures and plants that are inherently nonlinear. The primary aims and objectives are to analyse the effects of actuator nonlinearities on the closed-loop structural stability and to prevent destabilisation through the use of a nonlinear control law.

The linear Sherman-Morrison receptance method was expanded to single-degree-of-freedom structures with relatively simple nonlinearities using describing function and Volterra series representations. Applying the receptance method to nonlinear systems presents numerous challenges, since the poles are dependent on the response amplitude of the system undergoing control. By considering an exemplary Duffing oscillator, the poles were reassigned with displacement and velocity feedback control using an iterative scheme, where the feedback gains and open-loop pseudo-receptances are updated until convergence occurs. It was found that a describing function representation gives accurate results, provided that the structural parameters are known. Alternatively, the assignment may be conducted using measured pseudo-receptances and a Volterra series representation, which works well if the nonlinearities are relatively weak.

The primary benefit of applying the iterative receptance method to a nonlinear structure is a potential reduction in control effort when assigning the poles, relative to the non-iterative method. This is because the non-iterative approach requires the closed-loop dynamics to be sufficiently linear for accurate assignment, which may require a large control effort if the open-loop structure is strongly nonlinear. In contrast, the iterative

approach accounts for the nonlinear effects, and there is no need to assume that the underlying linear dynamics are dominant.

An experimental analysis and identification procedure was conducted on a single Micromega IA-01 inertial actuator for the purpose of investigating the effects of its nonlinear dynamics on the force outputs. The force-voltage dynamics of the actuator were examined by measuring the force responses to a variety of sinusoidal input voltages, and the first-order force-voltage pseudo-receptances were obtained. Using these measurements, the linear and nonlinear dynamics of the actuator were identified using inverse FRFs, peak resonance monitoring, the restoring force surface, and Hertzian contact theory. These results were then compared and verified with additional measurements on a DataPhysics IV40 actuator and Labworks FG-142 actuator.

The findings of this research reveal that it is likely for inertial actuators to behave as weakly nonlinear single-degree-of-freedom systems within their intended operating region, due to weak stiffening nonlinearities in the suspension. Once the proof-mass displacement becomes stroke-saturated, the inertial actuators exhibit strongly nonlinear vibro-impact dynamics that introduces large impulses in the force outputs. One exception is the DataPhysics IV40 actuator, which does not undergo stroke saturation due to the external proof-mass; however, the force response becomes saturated by the amplifier if the input voltage is sufficiently large.

Whilst the identification procedure was relatively straightforward for the linear and weakly nonlinear suspension dynamics, there were considerable difficulties with applying these identification methods to the stroke-saturated actuator dynamics; this is because the actuator exhibits complex dynamic phenomena during stroke saturation, such as double-impacts, high-frequency resonance effects, and force hysteresis. A nonlinear piecewise model was used to account for the variations in the impact parameters, such as the contact time and coefficient of restitution, which was able to model the effects of stroke saturation with a reasonable degree of accuracy.

To assess the effects of actuator nonlinearities on closed-loop stability, the Micromega IA-01 actuator was attached to a flexible plate structure with a single collocated accelerometer to provide velocity feedback control. The open-loop plant dynamics (between the actuator input and sensor output) were measured experimentally, and a simple linear single-degree-of-freedom model was identified for the purpose of representing the first plate resonance. A nonlinear coupled actuator-plate configuration was obtained by ap-

plying the identified actuator model to the plate model. The closed-loop stability of the resulting Simulink model was assessed using a variety of linear and nonlinear methods, which was verified experimentally by closing the control loop of the physical actuator-plate configuration using a dSpace digital controller.

The findings show that the actuator nonlinearities destabilise the closed-loop system by exploiting regions of potential instability that are already present in the underlying linear system, which occur as the proof-mass moves from one end stop to the other. The effects of destabilisation are particularly severe when stroke saturation occurs, resulting in a 72 % reduction of the gain margin. This is because the impulses associated with stroke saturation greatly increase the magnitude of the control signal, thereby reducing the effective damping of the actuator mode. The destabilising effects of the suspension nonlinearities are less pronounced, but are still capable of significantly reducing the gain margin by about 30 % within the intended operating region of the actuator. It is therefore of vital importance to account for these weak suspension nonlinearities in the actuator when predicting the stability margin of the closed-loop system.

It was demonstrated that the actuator nonlinearities do not intrinsically cause closed-loop destabilisation, but instead exploit flaws in the controller design that enable the underlying linear closed-loop system to become unstable. Therefore, the effects of the actuator nonlinearities are strongly dependent on the design of the controller. In this case, the velocity feedback controller amplifies the actuator mode, which results in poor control performance when uncompensated. Practically, almost all closed-loop systems are conditionally stable due to the effects of signal processing in the controller, and so the actuator nonlinearities will almost always affect the closed-loop stability; however, the effects of these nonlinearities could be mitigated with an appropriate choice of controller.

A nonlinear on-off control law was developed for the purpose of preventing closed-loop destabilisation when stroke saturation occurs. This control methods utilises an accelerometer as a means of knock detection, within the spectral region of the impulses associated with stroke saturation. If stroke saturation is detected, then the control loop is temporarily deactivated to stabilise the closed-loop system.

The simulations and experimental results demonstrate that this nonlinear control law is capable of providing closed-loop stability and improving the system response to impulsive excitation, provided that the control loop is deactivated for a sufficiently long period of time and the feedback gain is not too large. The primary disadvantage of the

on-off control scheme is the presence of quasi-impulsive control forces that occur when the control loop is reactivated, which is independent of the deactivation period and reduces the efficiency of the controller. This problem could possibly be overcome using a gain-scheduling approach in conjunction with the on-off control law, where the feedback gain increases incrementally when the control signal is reactivated.

8.2 Directions for future work

Whilst the results presented in this doctoral thesis give promising insights into the complex and challenging discipline of controlling nonlinear vibrations, there is plenty of scope for improvements and developments in this area. Based on the findings and discussions of this thesis, the following section highlights potential areas of exploration to be undertaken as future work.

1. Extension of the iterative Sherman-Morrison receptance method. Further research into this iterative approach is necessary to increase its current usability. This may include: using alternative representations, such as NOFRF modelling, that may be described using measured receptances and give accurate results for strong nonlinearities, examining the convergence properties of the iterations and its robustness to errors, and extending the method to accommodate nonlinear systems with multiple-degrees-of-freedom.

2. Dynamic analysis of other actuator types. The experimental analysis covers several types of inertial actuators, and should include other actuators (hydraulic, pneumatic, piezo *etc.*) to account for the different types of saturation effects. Furthermore, the dynamics of the inertial actuators may be investigated further by considering other common types of excitation, including random, impulsive, swept sine, and dual sine inputs.

3. Modelling of complex impact dynamics. Whilst the nonlinear single-degree-of-freedom actuator model is sufficient to emulate the impact dynamics for the purposes of this thesis, it is not capable of modelling the more subtle and complex impact phenomena, particularly the double- and triple-impacts. In order to model these complex dynamic effects, it is necessary to consider each end stop as an independent degree-of-freedom to the proof-mass, which requires the use of a three-

degree-of-freedom model. Obtaining experimental data for this type of model is difficult, since the dynamics of the proof-mass and end stops must be ascertained independently of each other. Moreover, the literature in this area is relatively limited, particularly with regards to modelling double-impact phenomena with equivalent structural parameters, and further research on this topic may yield interesting results.

4. Use of kurtosis to detect saturation. Whilst the simple detection threshold value set up in chapters 6 and 7 is adequate in a controlled environment, it is not suitable for use in practical applications where parasitic noise is typically non-stationary. A more reliable and consistent method for detecting stroke saturation would be to monitor the kurtosis of the filtered acceleration signal, which shows the "peakedness" of the signal. High kurtosis values would indicate the presence of stroke saturation, regardless of the amplitude of the acceleration signal. The primary difficulty with monitoring kurtosis in real-time is obtaining an appropriate sample of the acceleration data, since it is a statistical method. This may require a short delay for the kurtosis to be monitored accurately, and is more complicated to set up in Simulink than a simple detection threshold. Having said this, these problems should be overcome without much difficulty.

5. Alternative control laws for stabilisation. Whilst the on-off VFC scheme is capable of preventing stroke saturation from destabilising the closed-loop system, it is not particularly efficient at doing so, due to the quasi-impulsive effects that occur as a result of the strong discontinuities. The control law may potentially be improved by considering the implementation of the gain-scheduling approach in conjunction with the on-off VFC scheme, where the feedback gain is increased incrementally to its original value once stroke saturation has been detected and the control loop is deactivated. This approach should result in a more gradual change in the closed-loop dynamics once the control loop is reactivated, thereby preventing the quasi-impulsive chattering effects from occurring.

6. Stabilisation for MIMO control systems. Although it has been demonstrated that the on-off VFC scheme prevents closed-loop destabilisation in SISO control systems, preventing destabilisation in MIMO control systems is a much more challenging endeavour, since each control loop is susceptible to instability from other control

loops. The extension of the control scheme to MIMO systems, with multiple inertial actuators, is also necessary to ensure its usability in practical applications.

7. Destabilising effects of other actuator types. The Micromega IA-01 inertial actuator features hardening nonlinearities that increase the peak resonance frequency as the excitation amplitude rises. This has the effect of reducing the closed-loop stability margin, since the control bandwidth decreases with increasing excitation amplitude. Conversely, the Labworks FG-142 inertial actuator features softening nonlinearities that decrease the peak resonance frequency as the excitation amplitude rises, thereby increasing the control bandwidth. It would be interesting to consider a similar velocity feedback experiment using this actuator and investigating the conditions for destabilisation. It is expected that this type of actuator is less susceptible to closed-loop destabilisation as a result of the softening nonlinearities.

Appendix A

Proof of Unique Solution for an Asymmetric Duffing Oscillator

The amplitude of the DC displacement component of an asymmetric Duffing oscillator is determined by the following cubic equation,

$$k_3 Y_0^3 + k_2 Y_0^2 + (k_1 + 1.5 k_3 Y_1^2) Y_0 + 0.5 k_2 Y_1^2 = 0 \tag{A.1}$$

Since the equation is cubic in Y_0, there are three possible solutions that satisfy Eq. A.1. However, the solutions must be real in order to be physically realisable; this is determined by the discriminant Δ. If Δ can be shown to be negative for all possible cases, then a single solution for Y_0 may be obtained for Eq. A.1.

A linear transformation is applied to the cubic equation by dividing each coefficient by k_3 and substituting $Y_0 = z + k_2/3k_3$. This results in the following expression,

$$z^3 + pz + q = 0 \tag{A.2}$$

where,

$$p = \frac{k_1}{k_3} + \frac{3}{2} Y_1^2, q = \frac{2k_2^3}{27k_3^3} - \frac{k_2(k_1 + 1.5 k_3 Y_1^2)}{3k_3^2} + \frac{k_2 Y_1^2}{2k_3} \tag{A.3}$$

The discriminant of this cubic equation is simply,

$$\Delta = -4p^3 - 27q^2 \tag{A.4}$$

Therefore, a sufficient condition for ensuring $\Delta < 0$ is $p > 0$, which is expanded as,

$$\frac{k_1}{k_3} + \frac{3}{2}Y_1^2 > 0 \tag{A.5}$$

This condition is clearly satisfied if $k_1, k_3 > 0$, which is true for our particular example of a hardening Duffing oscillator. This proves that there is a unique solution for Y_0 when Eq. A.1 is solved.

Appendix B

Equipment Dynamics

In order to assess the effects of the equipment dynamics on the experimental results, the input-output transfer functions of the ADA converter, the Micromega power amplifier, and the PCB Signal Conditioner are recorded using the stepped-sine method. The transfer function of the ADA converter is defined between the specified input signal $v[n]$ and the recorded signal $v_v[n]$, as shown in Figure 4.2. The amplitude and frequency range of the input signals is $V = 0.1$ Volts and $\omega = 10\pi \rightarrow 100\pi$ rad/s respectively. It is apparent from the transfer function (shown in Figure B.1) that the gain of the ADA converter is approximately unity and the phase linearly increases with frequency. Since the measured signals $v_v[n]$ are passed twice through the ADA converter, this corresponds to a pure delay of about 800 microseconds.

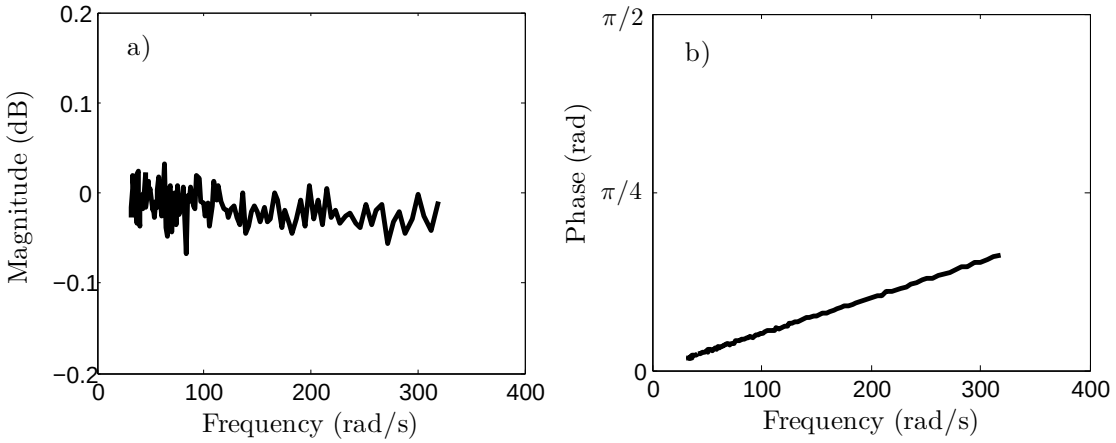

Figure B.1: Transfer function of the National Instruments ADA converter, with a) magnitude and b) phase.

Assessing the dynamics of the amplifier between $v(t)$ and $v_e(t)$ is slightly more complicated as the output voltage is dependent on the load impedence of the actuator. To avoid issues with the effects of counter-electromotive and inductive forces, the actuator was replaced with an equivalent 3 Ohm resistor to approximate the actuator load impedence at low frequencies. The measured transfer function, as shown in Figure B.2, confirms that the amplifier behaves as a pure gain (11 dB) in the frequency region of interest.

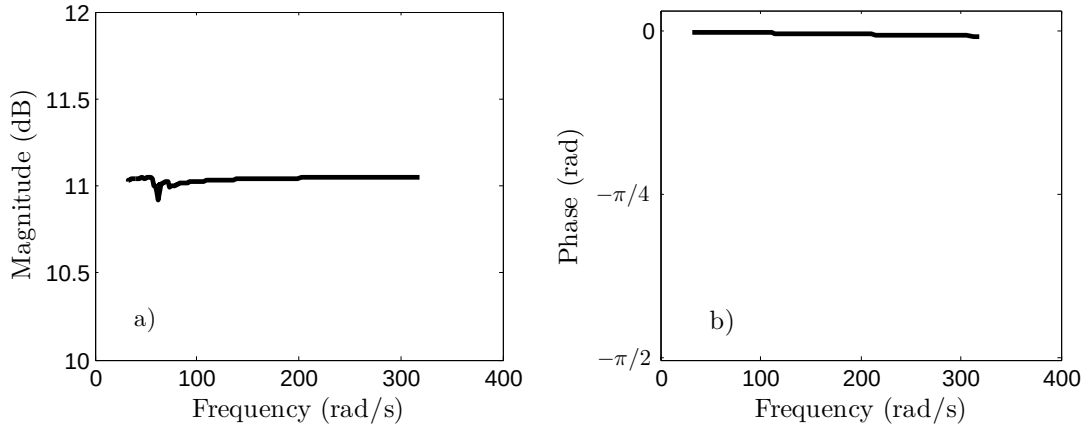

Figure B.2: Transfer function of the Micromega Dynamics Rack-04-45N amplifier, with a) magnitude and b) phase.

Finally, the transfer function of the PCB conditioner (between $\hat{v}_f(t)$ and $v_f(t)$) is measured using the stepped-sine excitation and illustrated in Figure B.3. Here, it is apparent that the gain of the conditioner is approximately frequency-independent, and tends to a value that is sufficiently close to unity to negate any small discrepancies. In addition, the change in phase is negligible in the frequency region of interest.

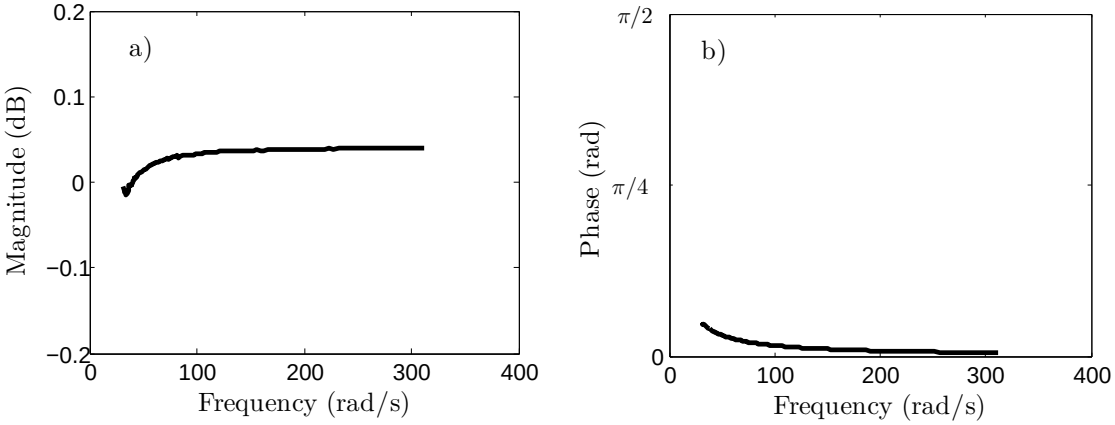

Figure B.3: Transfer function of the PCB ICP Sensor Signal Conditioner Model 480B10, with a) magnitude and b) phase.

Appendix C

Ribeiro Filtering

In chapter 4, it is necessary to filter the measured time-domain signals to remove the DC offset and facilitate integration. Since these signals are recorded with a high sampling rate (51.2 kHz), it is difficult to design a digital high-pass filter that provides sufficient attentuation of low frequencies without affecting the desired frequency components (as low as 5 Hz). This problem may be overcome by applying a filter in the frequency domain to provide a greater amount of control of the filtering process. First, the Fourier transform of the original time-domain signal $\bar{f}(t)$ is taken, and the spectral components $\bar{F}(j\omega)$ are revealed. Next, the low-frequency components that are beneath the fundamental excitation frequency are attenuated or removed by defining an alternative set of numeric values in this frequency range, repeating at the other end of the spectrum to ensure symmetry. Since we have a set of n discrete frequencies, the cutoff frequency for attenuation (ω_c) is denoted by the index number c, and the filtered spectrum may be split as follows,

$$F(j\omega) = \Big[Z(j\omega(S_c)) \quad \bar{F}(j\omega(S_i)) \quad Z^*(j\omega(S_n)) \Big] \tag{C.1}$$

where the sets $S_c = \Big[1:1:c \Big]$, $S_i = \Big[c+1:1:n-c \Big]$, $S_n = \Big[n+1-c:1:n \Big]$ denote the relevant frequency ranges, $Z(j\omega(S_c))$ is a user-defined tapering function designed to attenuate the low-frequency components, and $Z^*(j\omega(S_n))$ is the complex conjugate at the upper end of the spectrum. The inverse Fourier transform of the filtered spectrum is then taken, and its real part is used to obtain the filtered time-domain signal, to prevent complex values from occurring due to numerical roundoff errors. This approach, known as Ribeiro filtering [121], is demonstrated in Fig. C.1.

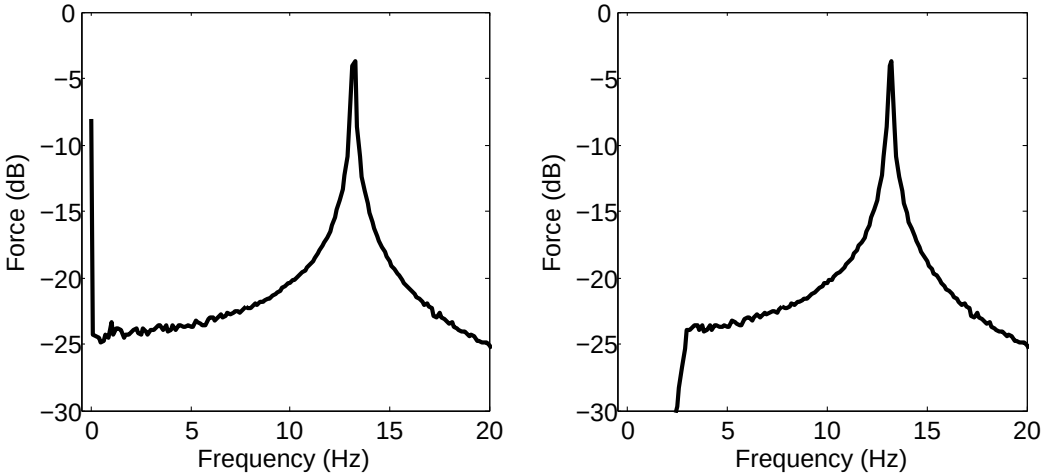

Figure C.1: Spectra of a) unfiltered force-time signal and b) filtered force-time signal. The DC component present in the unfiltered signal is removed using Ribeiro filtering.

For this procedure, it is important to ensure that the cutoff frequency and tapering function are carefully chosen for the filtering to be effective. In this case, the cutoff frequency was chosen to be 3 Hz. Although it is possible to implement brickwall filtering by setting $Z(j\omega(S_n)) = 0$, this results in intermodulation distortion in the time-domain signal, due to the duality principle between a rectangular function and a sinc function [152]. In order to minimise these problematic effects, the function is gradually tapered towards zero below the cutoff frequency. In this case, an exponential tapering function is chosen of the form,

$$Z(j\omega) = C \cdot 10^{M\omega} \tag{C.2}$$

where C, M are the user-defined coefficients of the tapering function. We then specify the constraints,

$$Z(0) = C = 10^{-10}, \qquad Z(j\omega_c) = C \cdot 10^{M\omega_c} = \bar{F}(j\omega_c) \tag{C.3}$$

such that the DC component is attenuated by 100 dB and the tapering value is equivalent to the unfiltered spectrum at the cutoff frequency. By splitting M into real and imaginary components M_R and M_I, such that $M = M_R + jM_I$, additional constraints are formulated,

$$C \cdot 10^{M_R\omega_c} = |\bar{F}(j\omega_c)|, \qquad 10^{jM_I\omega_c} = \mathrm{e}^{j\angle\bar{F}(j\omega_c)} \tag{C.4}$$

Rearranging the equations results in the obtained coefficients $M_R = 0.40$ and $M_I = 0.066$, which are then applied to the tapering function to perform the necessary filtering.

Appendix D

Potential MDOF Actuator Model with End Stop Dynamics

In chapter 4, it was observed that complex saturation phenomena occur when the excitation amplitude is particularly high, including double impacts and internal resonances. By analysing the velocity-time signals in Fig. 4.9, it is apparent that the double impacts occur because the initial collision is not sufficient to halt the proof-mass and change its direction, thereby necessating another collision. This phenomenon can only occur if the end stops are non-rigid and exhibit their own internal dynamics. These internal dynamics are not accounted for in the single-degree-of-freedom model; consequently, the coefficient of restitution becomes negative, which is impractical.

When double and triple impacts occur, the initial contact results in the proof-mass and the end stop moving away from the equilibrium point, with the end stop moving at a greater velocity than the proof-mass. However, the effective stiffness of the end stop counteracts its inertia and forces the end stop back to its equilibrium position, thereby setting up another collision with the proof-mass. This explanation is confirmed by the hysteresis observed in the restoring force data, where the secondary impact appears to occur at a greater displacement amplitude than the initial impact.

These dynamic effects may possibly be emulated using a three-degree-of-freedom model, where one the outer two degrees-of-freedom (the end stops) becomes coupled to the centre degree-of-freedom (the proof mass) during a collision. This enables the double and triple impact phenomenon to occur as a result of the end stop mass rebounding onto the proof-mass, provided that the model parameters are chosen carefully. An illustration

of this model is shown in Fig. D.1.

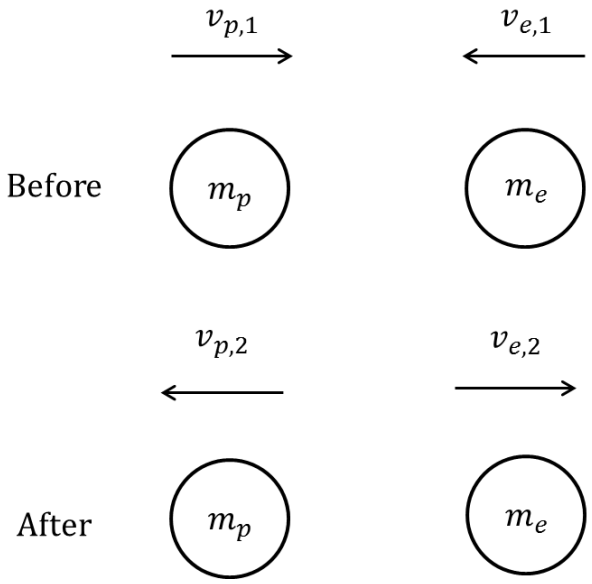

Figure D.1: Representation of the collisions between the proof-mass and the end stop.

Furthermore, including the dynamics of the end stops in the actuator model is advantageous for modelling the internal resonances associated with the collision, which are very prominent at high excitation amplitude levels. An example of this phenomenon is shown in Fig. D.2, where the resonance shown as a peak at 6.5 kHz in the spectrum.

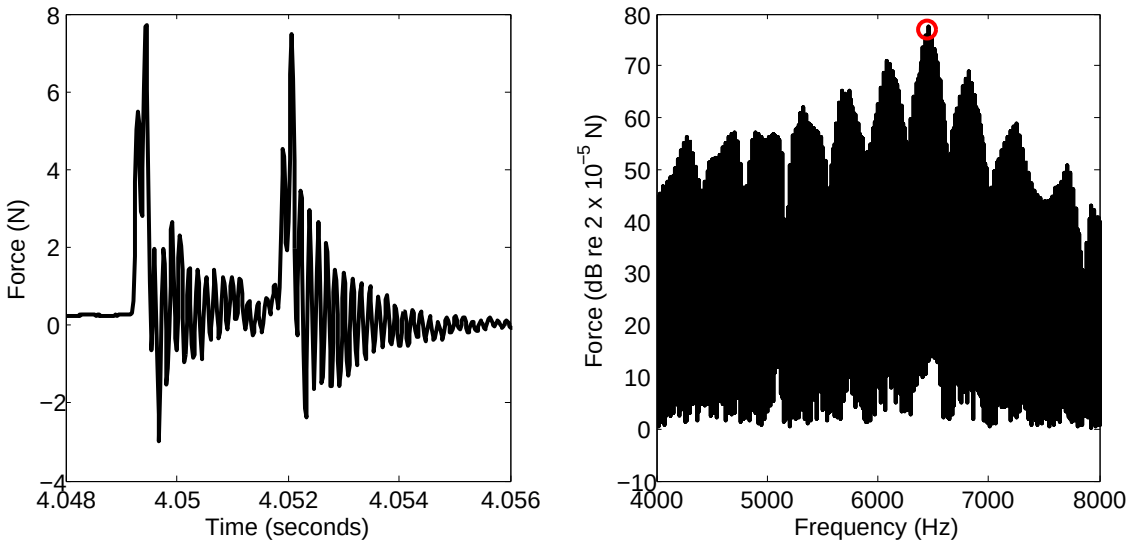

Figure D.2: Illustration of (a) high-frequency oscillations that occurs in one of the force-times during and after collisions, and (b) the spectra of the force-time signal, where the peak at 6.5 kHz is marked as a circle.

The primary difficulty of using the three-degree-of-freedom is to identify the mass, stiffness, and damping parameters associated with the end stops. This requires the measurement of the end stop states independently of the proof-mass states, which may be difficult to achieve in practice. The effective stiffness of the end stop may be estimated from the internal resonances shown in Figure D.2, which occur around 6.5 kHz. The end stop stiffness is independent of the stiffness associated with the collision, which dicates the impact duration. Furthermore, there is relatively little literature on the subject of emulating double impacts with a lumped-parameter model, and is a subject worthy of further interest.

Appendix E

Simulink Modelling

The following illustrations represent the Simulink models of the actuator, as identified in chapter 5, and the actuator-plate configuration used in chapter 6.

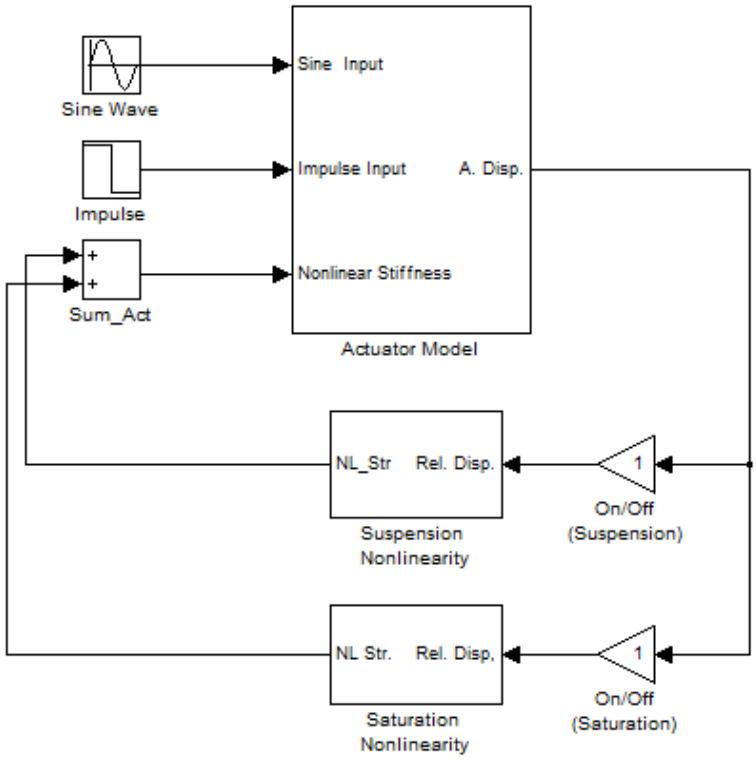

Figure E.1: Schematic of the overall actuator model in chapter 5, including the suspension and saturation nonlinearities, the underlying actuator model, and the sine and impulsive inputs.

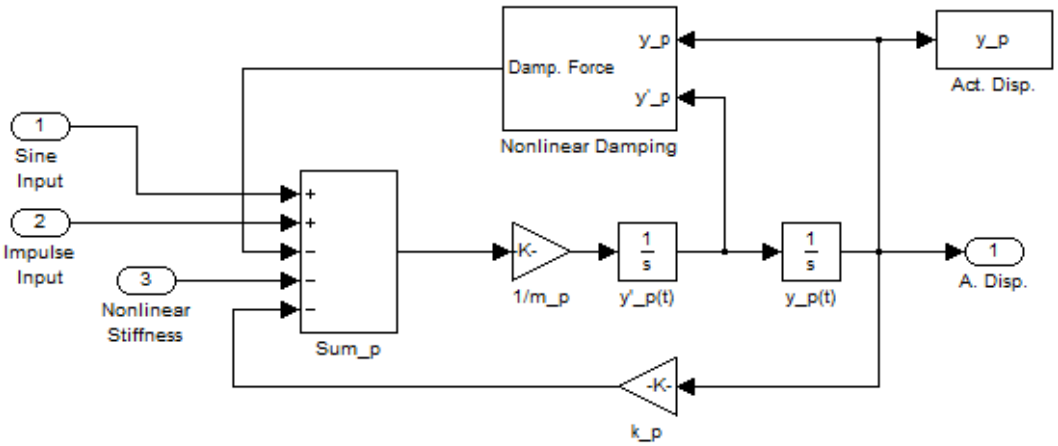

Figure E.2: Schematic of the underlying actuator model, including the linear mass and stiffness terms and the nonlinear damping term.

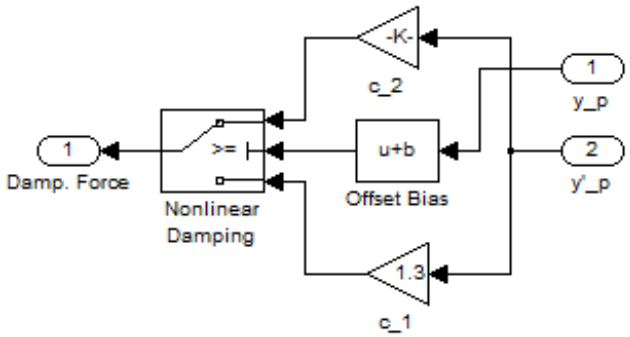

Figure E.3: Schematic of the nonlinear damping block. Here, the damping coefficient increases when the actuator displacement exceeds the stroke length.

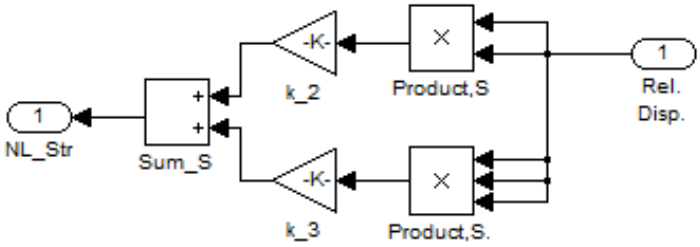

Figure E.4: Schematic of the suspension nonlinearity block used for the actuator model.

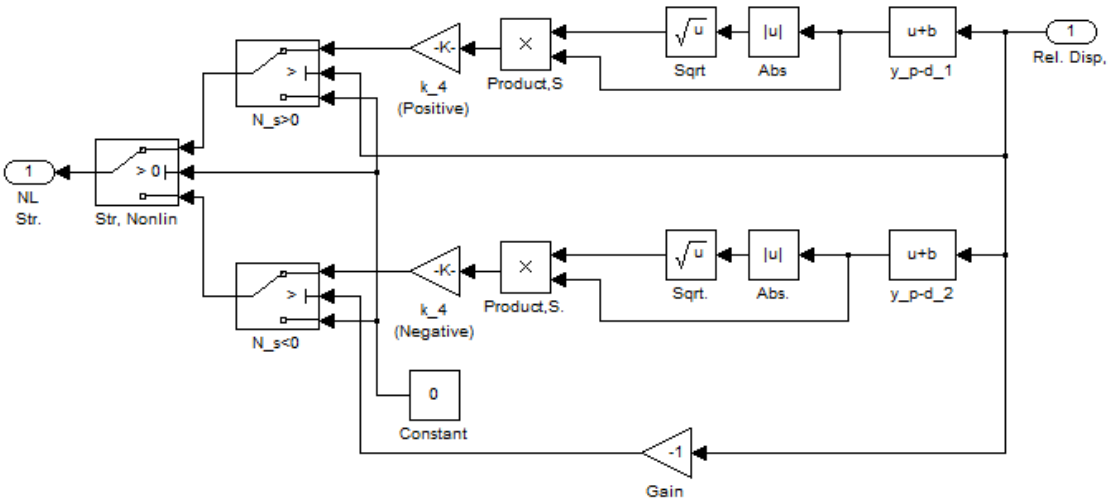

Figure E.5: Schematic of the saturation nonlinearity block used for the actuator model. Two independent paths are used to account for the asymmetry in the positive and negative directions. The bias of the relevant blocks are $-d_1$ and $-d_2$. The thresholds of the N_s > 0 and N_s < 0 switches are d_1 and d_2 respectively, and the threshold of the Str. Nonlin block is zero, in order to switch between positive and negative displacements.

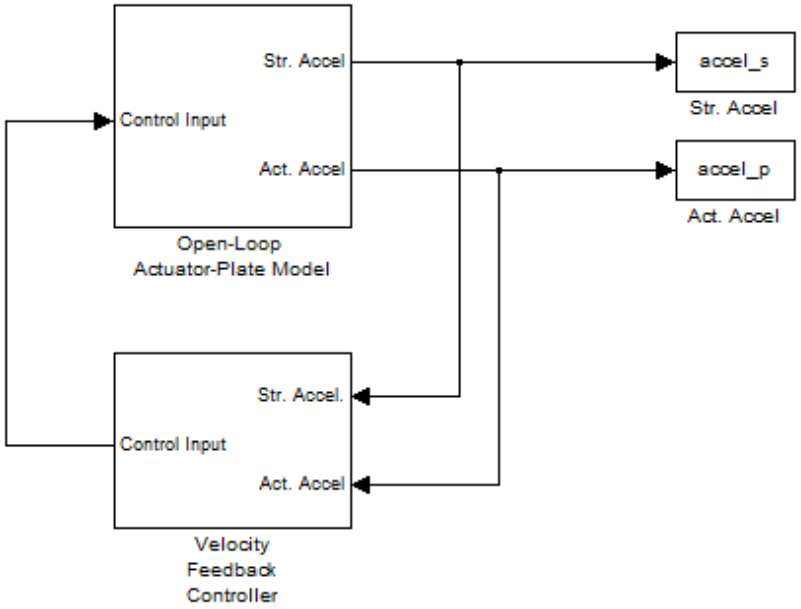

Figure E.6: Schematic of the overall closed-loop actuator-plate configuration in chapter 6, including the velocity feedback controller and the open-loop actuator-plate model.

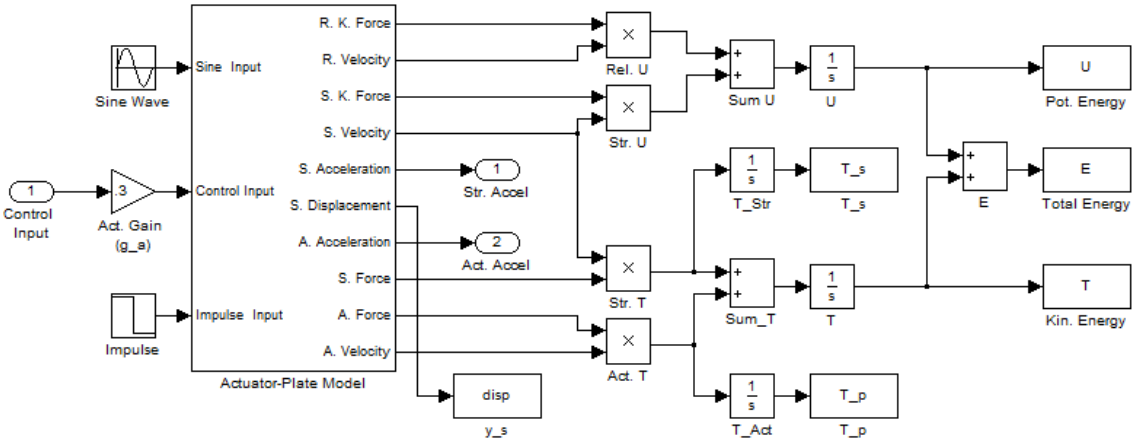

Figure E.7: Schematic of the open-loop actuator-plate model block, including the sine and impulsive inputs for the plate and the control input for the actuator. The potential, kinetic, and total mechanical energy is ascertained using the blocks to the right of the model.

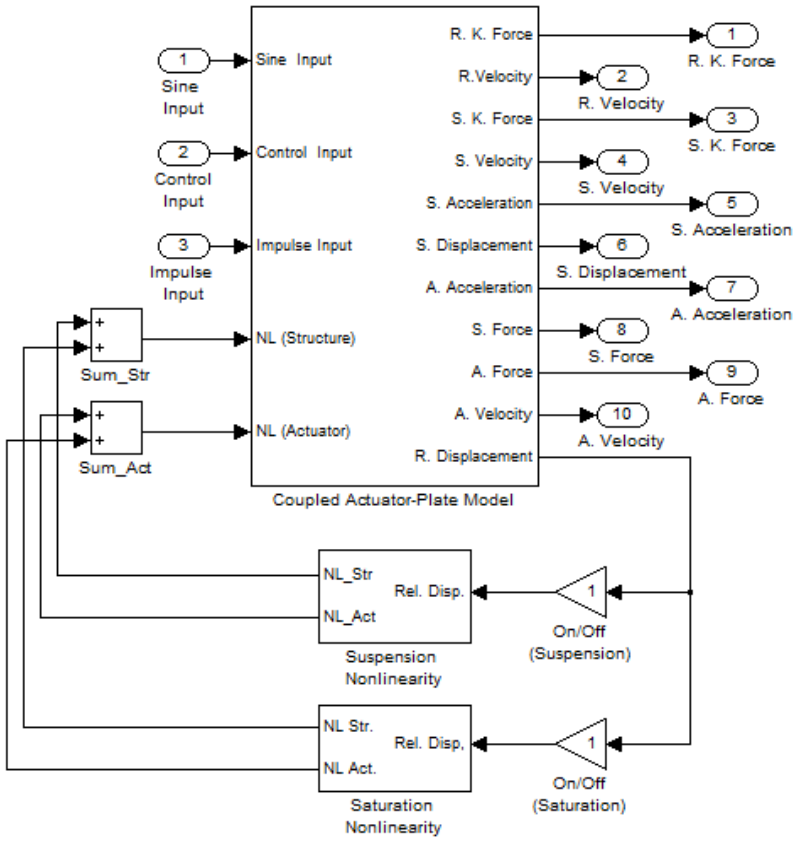

Figure E.8: Schematic of the actuator-plate model block, including the suspension and saturation nonlinearities and the coupled actuator-plate model block.

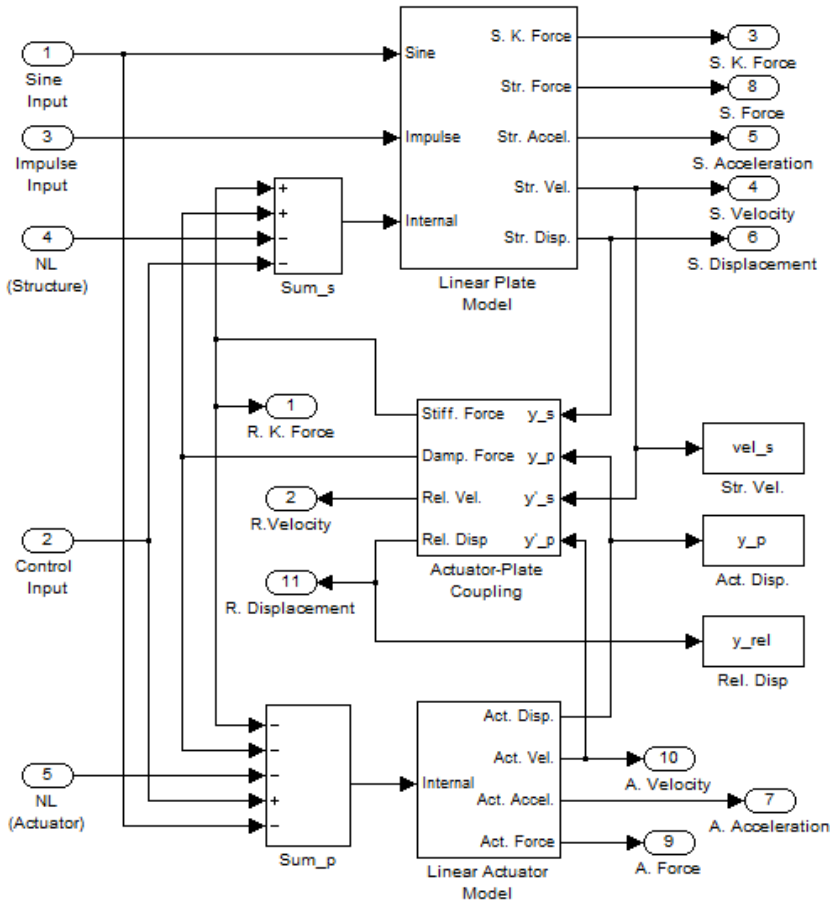

Figure E.9: Schematic of the coupled actuator-plate model block, which includes the linear uncoupled plate and actuator dynamics, the coupled actuator-plate dynamics, and the nonlinear damping.

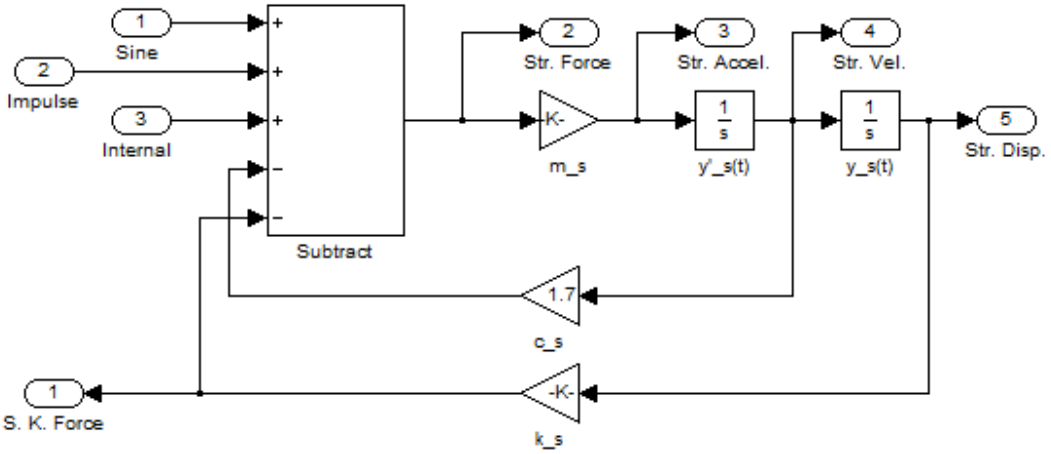

Figure E.10: Schematic of the linear plate model block, which contains the linear uncoupled plate dynamics.

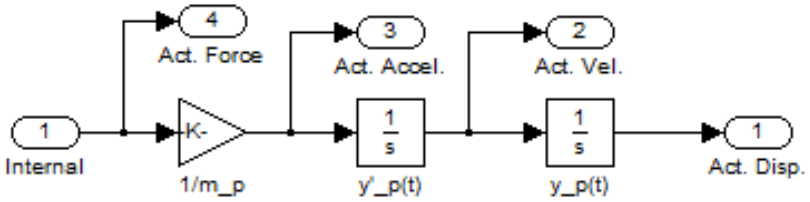

Figure E.11: Schematic of the linear actuator model block, which contains the linear uncoupled actuator dynamics.

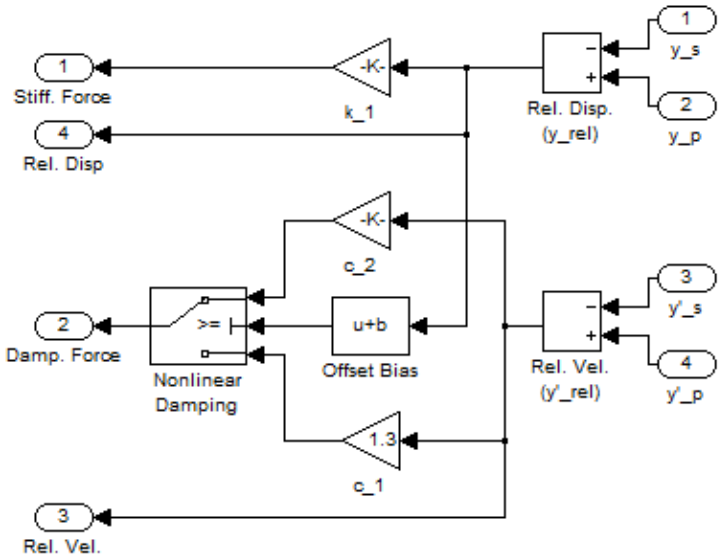

Figure E.12: Schematic of the actuator-plate coupling block, which contains the linear coupled dynamics and the nonlinear damping.

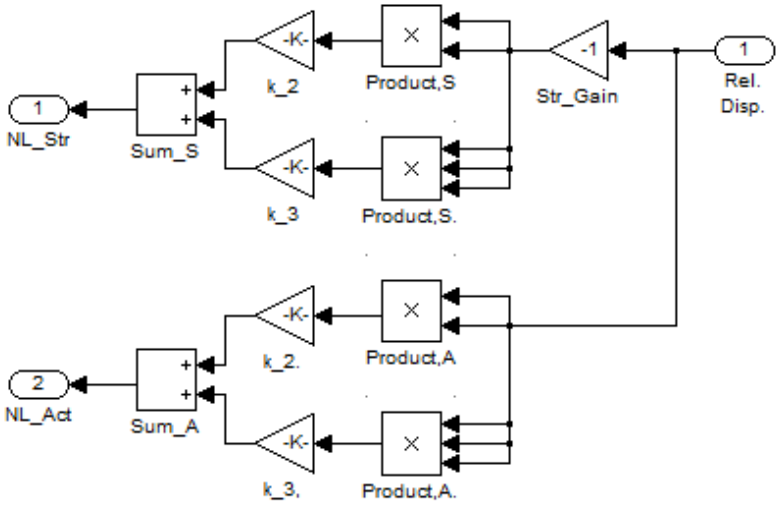

Figure E.13: Schematic of the suspension nonlinearity block used for the actuator-plate configuration. The nonlinearity is subdivided into two paths to account for the plate and actuator separately.

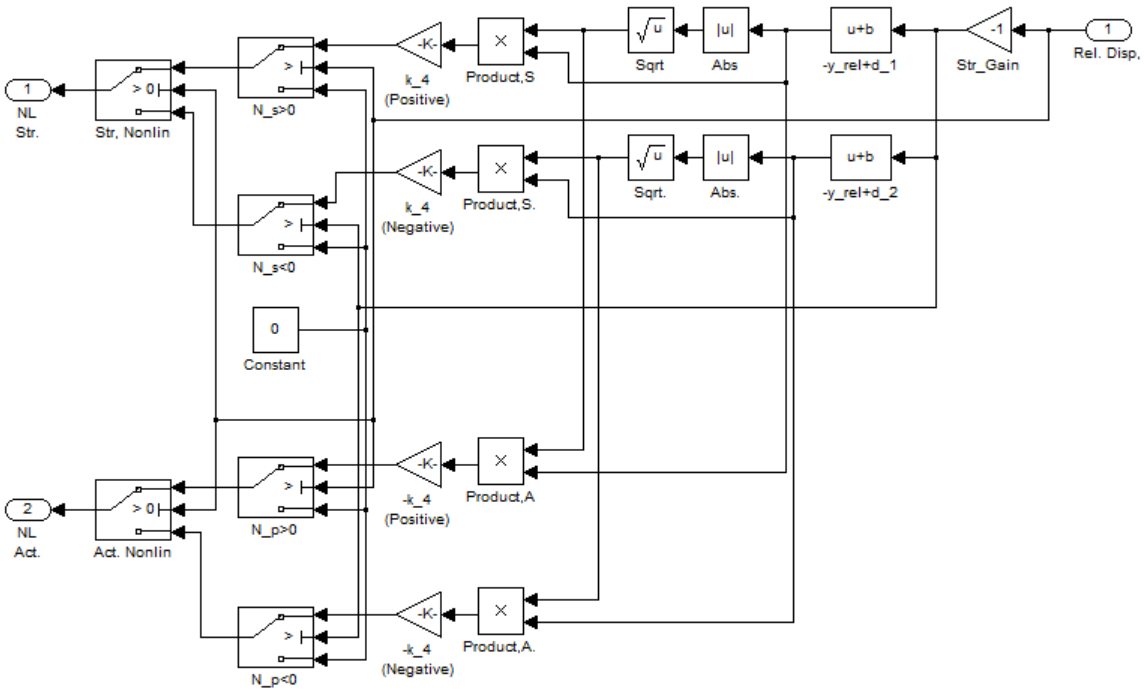

Figure E.14: Schematic of the saturation nonlinearity block used for the actuator-plate configuration. Four independent paths are used to account for the plate and actuator in the positive and negative directions. The bias of the relevant blocks are d_1 and d_2. Note that the gains of the third and fourth path are $-k_4$ to ensure consistency.

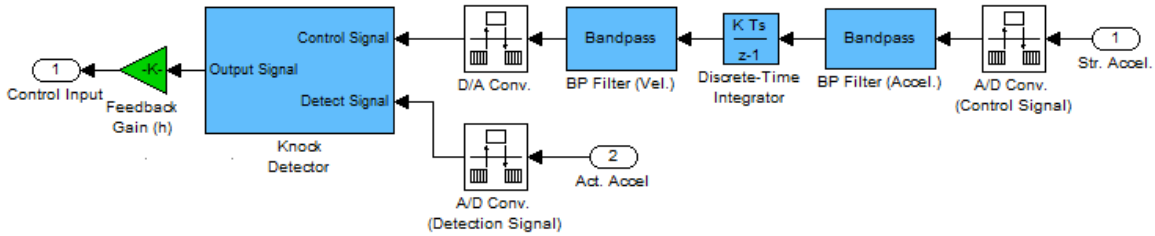

Figure E.15: Schematic of the velocity feedback controller block, including the integrator and bandpass filters for the structural acceleration, the downsampling and upsamping with the Rate Transition blocks, the knock detector, and the feedback gain.

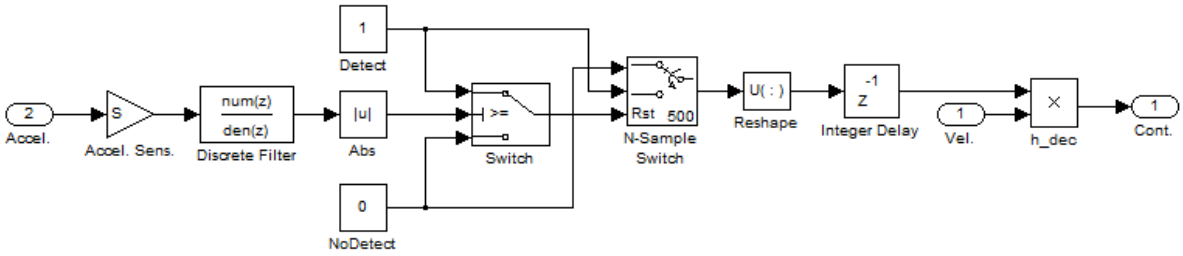

Figure E.16: Schematic of the knock detector block, including the accelerometer sensitivity, the 1-3 kHz bandpass filter, and the detection and N-sample switches.

Appendix F

Gain-Scheduling Control of Stroke Saturation

F.1 Control of stroke saturation with an actuator and a rigid block

In this section, we provide a demonstration of the gain scheduling approach discussed in subsection 6.5.3 using simulations and experiments. Used as a stand-alone control scheme, the controller is effective at reducing the effects of stroke saturation, but is not capable of acting as a stabilising control law. For this reason, the gain scheduling control law should be used in conjunction with another controller, such as on-off VFC, to provide effective stabilisation.

In this case, the emphasis of the control law is to prevent stroke saturation from occurring regularly. This is achieved by means of an additional, secondary loop that feeds back the actuator velocity. The gain of the feedback loop is increased incrementally when stroke saturation is detected, which has the effect of increasing the apparent damping of the actuator, thereby decreasing the actuator response until saturation no longer occurs.

For purposes of simplicity and to prevent issues with actuator-plate coupling, the gain scheduling approach is applied to a single Micromega IA-01 inertial actuator that is attached to a rigid block, using the configuration described in chapter 4 and illustrated in Figure F.1. The actuator is excited using a monoharmonic input voltage, whose amplitude is sufficiently large to saturate the actuator. An accelerometer is then placed on the actuator casing as a means of detecting stroke saturation and generating a detection

signal. In addition, the force sensor that is placed between the actuator and the rigid block is used to provide velocity feedback for the actuator itself, using the relation,

$$\dot{y}_p(t) = \frac{1}{m_p} \int f(t)\, dt \tag{F.1}$$

where $f(t)$ is the measured force-time signal. The control signal is applied directly to the actuator input to increase the effective damping of the actuator. This has the effect of attenuating the monoharmonic voltage signal, which will prevent stroke saturation from occurring if the control effort is sufficiently large. However, the control effort required to prevent stroke saturation is unknown, and an overly large effort may destabilise the closed-loop system. Therefore, the control effort is adaptively increased using the detection-dependent controller until stroke saturation is no longer present in the accelerometer signal.

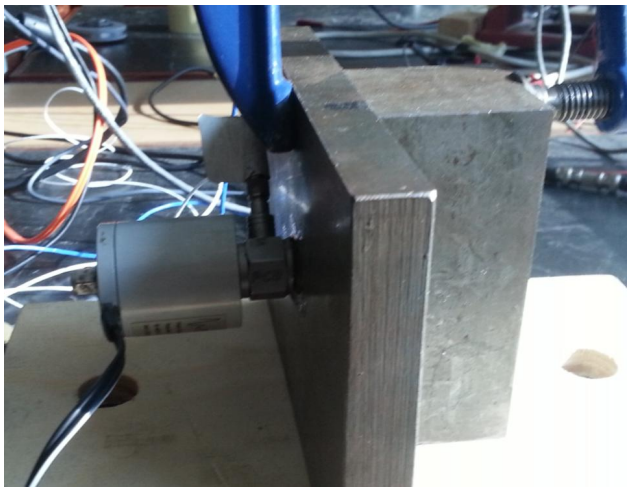

Figure F.1: Illustration of the experimental gain scheduling setup, including the actuator, the force sensor used for velocity feedback, and the accelerometer used for saturation detection.

The overall gain of the control signal is determined by a static gain h and the detection-dependent gain h_{dec}. Initially, the gain h_{dec} is set to zero, and no feedback control is applied to the actuator. As stroke saturation is detected in the accelerometer signal, h_{dec} increases as shown in Figure 6.42, and the controller starts to attenuate the input signal. Eventually, the levels of attenuation are sufficient to ensure that stroke saturation does not occur, and h_{dec} remains constant. This approach is advantageous for establishing the

minimum control gain in the feedback loop that prevents stroke saturation from occurring. Having said this, the static gain h and the detection period N_τ should be carefully chosen to remove stroke saturation in a sufficiently short time period whilst ensuring that the adaptive gain does not overshoot and render the closed-loop system unstable.

F.1.1 Simulations

A simple nonlinear single-degree-of-freedom actuator model with pure-gain velocity feedback control was developed in Simulink for the purpose of illustrating the effects of the detection-dependent controller. In this case, the lumped-parameter actuator model is replaced with the underlying linear displacement-voltage transfer function, followed by the hard-clip saturation block, for purposes of simplicity. An input sine wave block, denoted by $V_{in}(j\omega) = V\sin(\omega t)$, is used to excite and saturate the actuator model, which has a stroke limit of ± 1 mm. This has the effect of clipping the displacement-time signal, which is then differentiated to obtain the velocity-time and acceleration-time signals. These signals are applied to the detection subsystem featuring the detection-dependent elements shown in Figure 6.41, and the control signal is then amplified by the static gain h and summed to the actuator input. This Simulink configuration is shown in Figure F.2.

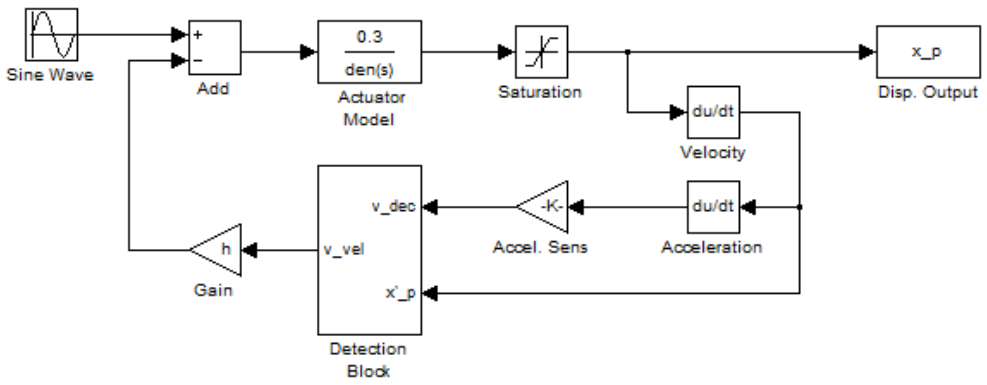

Figure F.2: Simulink model of actuator with hard clipping, velocity feedback control and saturation detection. The Accel. Sens gain block accounts for the accelerometer sensitivity, which is defined as 10.2 mV/ms^{-2}.

It was established in chapter 5 that the underlying linear closed-loop displacement-voltage transfer function of the actuator, denoted by $H_c(j\omega)$, can be written in the form,

$$H_c(j\omega) = \frac{g_a}{k_1 - m_p\omega^2 + j\omega(c_p + h_c)} \tag{F.2}$$

where h_c is the composite gain of the static gain h and the detection-dependent gain h_{dec}. This shows that provided $h_c > -c_p$, the closed-loop system is otherwise unconditionally stable. It is then assumed that the excitation frequency ω is relatively close to the peak resonance frequency ω_p of the actuator; provided that stroke saturation occurs, this is a reasonable assumption, since the resonance frequency shifts upwards with amplitude, as shown in chapter 4, and encompasses ω when stroke saturation is present. In this case, the relationship between the input excitation $V_{in}(j\omega)$ and the actuator velocity $V_{vel}(j\omega)$ is given by,

$$V_{vel}(j\omega) = j\omega H_c(j\omega)V_{in}(j\omega) = \frac{j\omega g_a V_{in}(j\omega)}{k_1 - m_p\omega^2 + j\omega(c_p + h_c)} \approx \frac{g_a V_{in}(j\omega)}{c_p + h_c} \tag{F.3}$$

such that the actuator velocity is approximately in-phase with the input excitation. The modified input excitation level, denoted by $V_{mod}(j\omega)$, can then be expressed as,

$$V_{mod}(j\omega) = V_{in}(j\omega) - h_c V_{vel}(j\omega) \approx \left(1 - \frac{g_a h_c}{c_p + h_c}\right) V_{in}(j\omega) \tag{F.4}$$

Therefore, the modified input excitation to the actuator, $V_{mod}(j\omega)$, is reduced in relation to $V_{in}(j\omega)$ as h_c increases, provided that h_c is comparable to c_p. Since the feedback control loop has the effect of decreasing $V_{mod}(j\omega)$, the gain scheduling scheme is used within the feedback loop to increase h_{dec}, and therefore h_c, whenever stroke saturation is detected. In this manner, the modified input excitation continually decreases until the actuator displacement-time response falls beneath the saturation threshold and h_c converges to a constant value.

For the simulations, a relatively fast sample rate of 51.2 kHz was utilised for the purpose of accurately capturing the impulses associated with stroke saturation. The detection period N_τ in the detection subsystem was set to 500 samples, such that h_{dec} increases over a period of approximately 10 milliseconds when stroke saturation is detected. The detection threshold for saturation was also defined as $T_{dec} = 6 \times 10^{-4}$ Volts for the filtered accelerometer signal. The numerator and denominator filter coefficients, defined as num and den respectively, of the third-order band-pass filter were,

$$\text{num} = \begin{bmatrix} 2.0509 & 0 & -6.1527 & 0 & 6.1527 & 0 & -2.0509 \end{bmatrix} \times 10^{-4}$$

$$\text{den} = \begin{bmatrix} 1 & -5.7222 & 13.6783 & -17.4831 & 12.6026 & -4.8577 & 0.7822 \end{bmatrix}$$

Using the fixed-step ode3 solver over a period of one second, the simulated dispalcement-time and filtered acceleration-time histories of the open-loop actuator model, in response to monoharmonic excitation of amplitude $V = 1$ Volts and $\omega = 75$ rad/s, are shown in Figures F.3a) and F.3b) respectively. In these illustrations, it is apparent that the excitation amplitude is sufficiently large to saturate the actuator model, resulting in hard clipping in Figure F.3a). Furthermore, Figure F.3b) indicates that this simple model is capable of crudely emulating the impulses associated with stroke saturation in the filtered acceleration-time signal, which are well above the detection threshold.

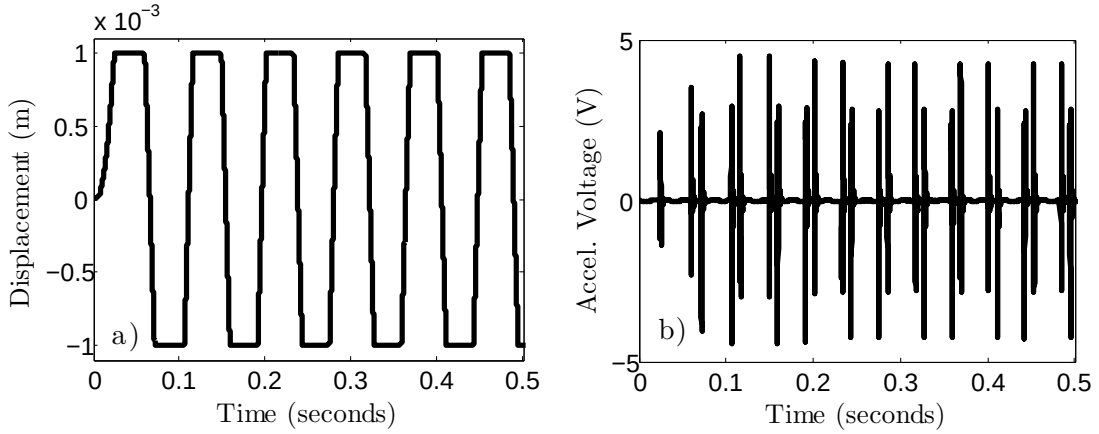

Figure F.3: Open-loop simulation results, with a) the displacement-time signal and b) the filtered acceleration-time signal.

Next, we apply detection-dependent control by closing the loop with an initial static gain $h = 5$. Figure F.4a) shows a comparison of the simulated open-loop and closed-loop displacement-time signals, whereas Figure F.4b) illustrates the composite gain h_c of the feedback loop with regards to the filtered acceleration-time signal. These figures indicate that the composite feedback gain increases incrementally over time as a result of the knock detection, thereby reducing the amplitude of the displacement-time response. After a period of approximately two seconds, the displacement-time response falls beneath the stroke limit and becomes monoharmonic, such that stroke saturation is prevented from occurring. As a result of this, the impulses disappear from the acceleration-time signal and the composite gain converges to the constant $h_c \approx 8.79$. Since the displacement-time

signal is very close to the stroke limit, this constant corresponds to the minimum gain value required for the feedback loop to prevent stroke saturation in this particular case.

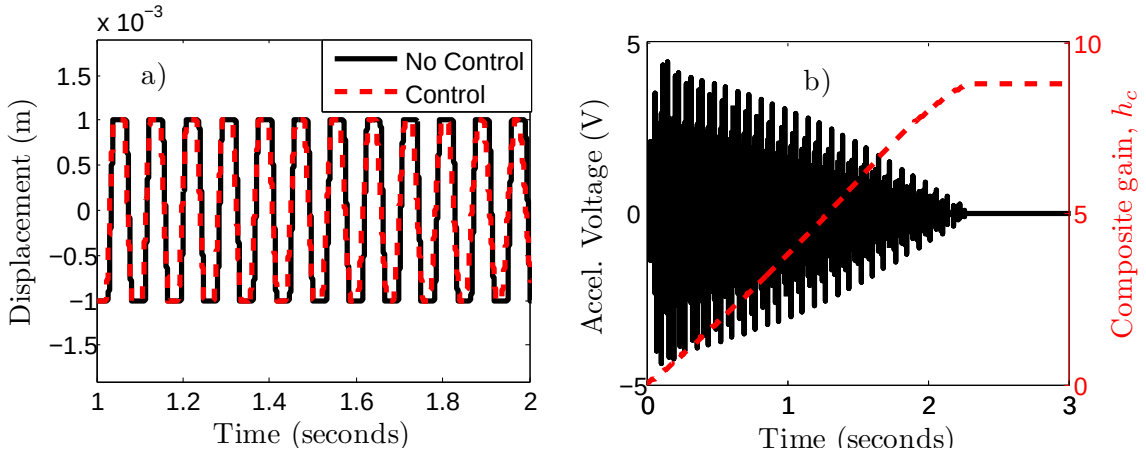

Figure F.4: Closed-loop simulation results for $h = 5$, featuring a) the displacement-time signals and b) the feedback gain h_c (dashed line) with the filtered acceleration-time signal (solid line).

Now, we increase the static gain to $h = 20$, and examine the performance of the controller as a result of this change. The simulation results are shown in Figures F.5a) and F.5b).

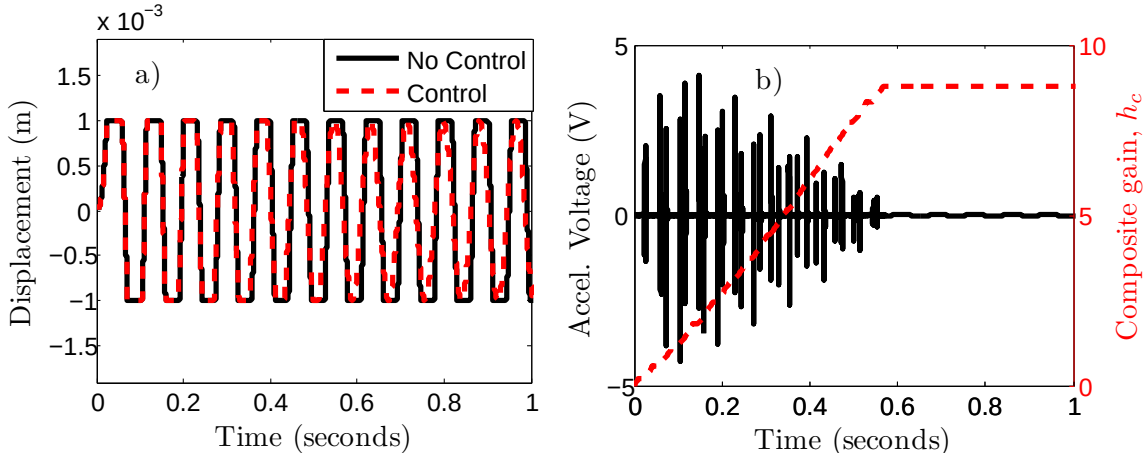

Figure F.5: Closed-loop simulation results for $h = 20$, featuring a) the displacement-time signals and b) the feedback gain h_c (dashed line) with the filtered acceleration-time signal (solid line).

Here, we can observe two primary features of interest. Fistly, the displacement-time signal falls beneath the stroke limit over a much shorter duration of several hundred milliseconds, which demonstrates that increasing the static gain results in faster controller performance.

Secondly, the effective feedback gain converges on the same constant, regardless of the rate of convergence. This confirms that the constant is the minimum feedback gain required for the displacement-time signal to fall beneath the saturation threshold.

F.1.2 Experiments

The gain scheduling procedure is now applied to the experimental configuration shown in Figure F.1, which features a Micromega IA-01 inertial actuator, a PCB 208C01 force transducer that is used to create the velocity feedback loop, and a Dytran 3035BG that is used to detect stroke saturation. In this manner, the control signal is obtained from the blocked velocity of the actuator, which is utilised to improve the signal-to-noise ratio in comparison with the accelerometer signal. The controller is implemented in Simulink using the dSpace DS1103 PPC Controller Board and ControlDesk, using the measured force-time and acceleration-time signals as the inputs and the control signal as the output. The force sensor signal was conditioned using a PCB ICP Sensor Signal Conditioner Model 480B10, and the data was recorded using the NI modules.

Previously, the actuator was modelled as a single-degree-of-freedom system that is unconditionally stable when negative velocity feedback is utilised. In practice, however, the actuator does not behave exactly as a single-degree-of-freedom system, but instead exhibits higher-order torsional and bending modes. This renders the actuator itself prone to instability from high-frequency spillover and/or stroke saturation destabilisation, which limits the composite feedback gain that can be applied experimentally.

In order to apply the gain scheduling scheme to the experimental setup, it is necessary to modify the procedure outlined in the simulations section. The modifications are as follows. Firstly, the continuous-time Simulink model, as shown in Figures 6.41 and F.2, was converted to a discrete-time model, and a discrete solver is utilised.

Secondly, the actuator model is replaced by the physical actuator, such that the simulated velocity-time and acceleration-time signals are replaced by the measured signals from the force transducer and accelerometer.

Thirdly, the voltage signal from the force transducer is converted to the velocity-time signal by applying a gain factor $1/T_s m_p$, where $T_s = 112$ mV/N is the sensitivity of the force transducer, to obtain the acceleration-time signal, which is then integrated using discrete-time integration. This process requires the signals to be high-pass filtered, before and after integration, to remove the DC offset. In order to facilitate this whilst retaining

the intended measurement, the signal is down-sampled to 1.28 kHz, and a digital high-pass filter with a cut-off frequency of 5 Hz is applied on both sides of the discrete-time integrator. After filtering and integration, the signal is then upsampled to the original sample rate of 51.2 kHz.

Fourthly, an external Feedback Variable Phase Generator VPG608 signal generator is used to provide the monoharmonic input excitation signal $V_{in}(j\omega)$ to the actuator instead of using a MATLAB-defined function. The control signal is summed to this excitation signal at the actuator amplification stage. This demonstrates that the controller is effective for independent disturbances.

Fifthly, a saturation block, with a set limit of 10, is applied to the detection-dependent gain h_{dec} for the purpose of preventing a runaway increase in h_c in the event of closed-loop destabilisation, to avoid damage to the actuator.

A schematic of this modified Simulink-based controller is shown in Figure F.6, which includes the elements in the velocity signal processing block and the detection block.

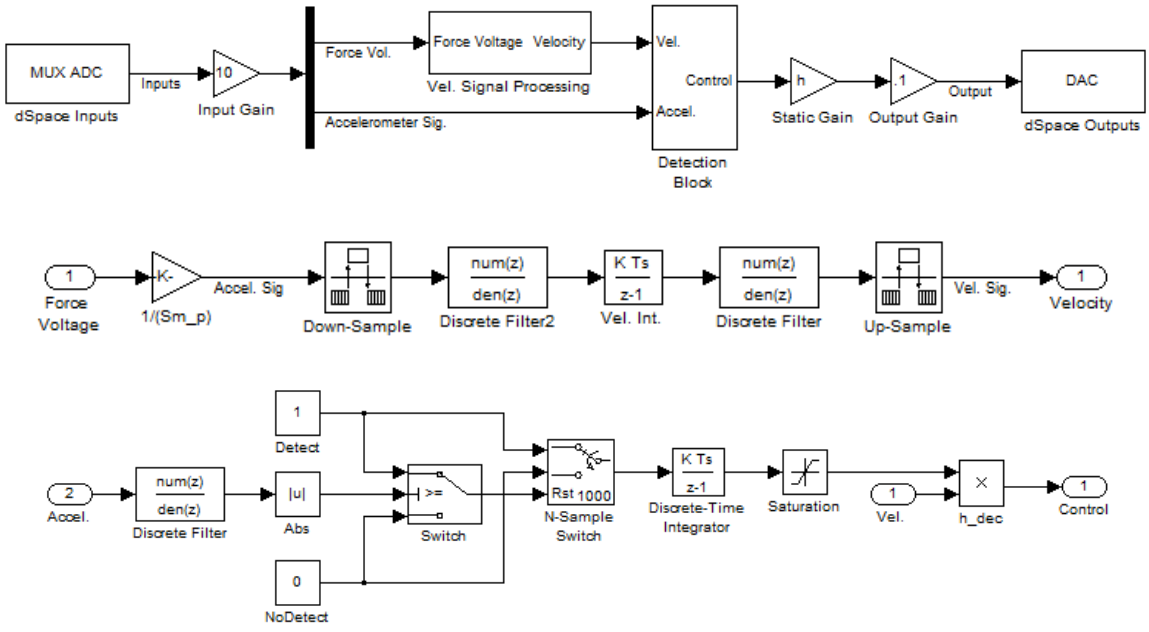

Figure F.6: Schematic of the digital controller in Simulink, including the primary control path, the velocity signal processing block, and the detection block.

Using this controller schematic, the gain scheduling procedure was applied to the inertial actuator to control the stroke saturation phenomenon. The sinusoidal excitation signal was of amplitude $V = 0.4$ Volts and frequency $\omega = 20\pi$ rad/s, where the latter is very close to the linear peak resonance frequency of the actuator ($\omega_p \approx 61.4$ rad/s). In this resonant region, the initial input amplitude is sufficiently large to saturate the actuator, resulting in impulses in the accelerometer signal. Additionally, the detection threshold was set to $T_{dec} = 10^{-3}$ Volts, which is relatively close to the background noise level of the accelerometer signal, and the detection period was specified as 1,000 samples (i.e. approximately 20 milliseconds). Setting a low detection threshold increases the controller's sensitivity to small knocks, where the proof-mass hits the end stops at a low velocity, and the detection signal remains at unity for a longer duration until the signal falls beneath the detection threshold after an impulse. This ensures that h_{dec} increases at a higher rate than if a larger detection threshold was specified; however, h_{dec} also requires a longer convergence time as a result of the increased sensivity.

Figures F.7a) and F.7b) illustrate the effects of the detection-dependent controller on the actuator dynamics when an initial static gain $h = 2$ is used in the control loop. The accelerometer signal is shown with regards to the composite gain h_c in Figure F.7a); here, it is apparent that the impulses associated with stroke saturation reduce in magnitude as h_c, eventually disappearing completely as the composite gain tends to the constant $h_c \approx 14.25$. This indicates that the input voltage is no longer sufficient to saturate the actuator, such that the displacement of the proof-mass remains within the stroke limit. However, since the static gain is relatively small, the controller requires a relatively long time period (of a few seconds) to reduce the input voltage beneath the saturation limit.

By deactivating the detection-dependent elements and setting the static gain to the converged value of h_c (i.e. $h = 14.2$), the closed-loop actuator response to a hammer impulse is measured by the accelerometer and shown in Figure F.7. As the response decays to the equilibrium positon, this demonstrates that the closed-loop system is stable for the specified control gain.

Now, we repeat this procedure using a higher static gain $h = 15$, where the results are illustrate in Figures F.8a) and F.8b). Figure F.8a) shows that a shorter duration (400 milliseconds) is required for the input voltage to fall beneath the saturation threshold, which indicates that the increased static gain results in a faster controller and, therefore, a faster convergence time for h_{dec}. These findings are in agreement with the predictions

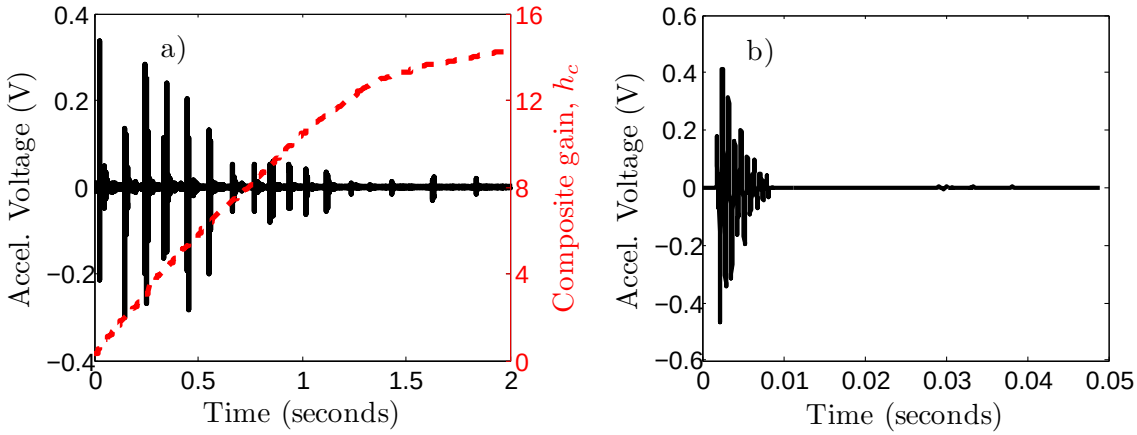

Figure F.7: Experimental gain-scheduling results for $h = 2$, with a) accelerometer signal (solid line) and composite gain (dashed line), and b) closed-loop impulse response.

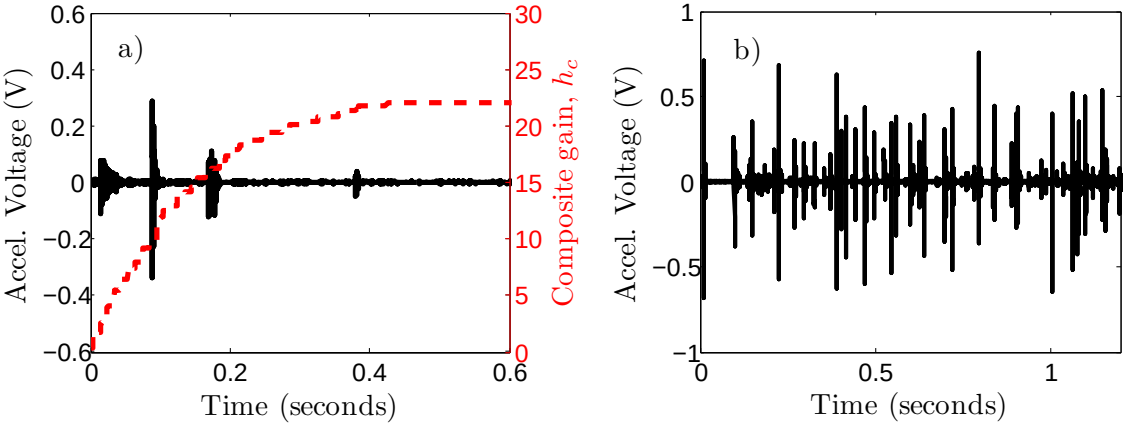

Figure F.8: Experimental gain-scheduling results for $h = 15$, with a) accelerometer signal (solid line) and composite gain (dashed line), and b) closed-loop impulse response.

made using the Simulink model. However, it is also apparent that the composite gain converges to a much larger constant ($h_c \approx 22.1$) than for the previous case. This phenomenon indicates that the controller overshoots the optimal feedback gain value, due to the larger static gain. As a consequence, the closed-loop impulse response, shown in Figure F.8b), tends towards a quasi-random LCO, which infers that that stroke saturation is capable of destabilising the closed-loop system when h_c is sufficiently large. Therefore, the static gain h must be chosen carefully to optimise performance (i.e controller speed) whilst retaining closed-loop stability.

To summarise, both the simulated and experimental results show that the gain scheduling scheme shown in section 6.5 can be applied to an inertial actuator to adaptively reduce the input voltage to the actuator, such that the proof-mass displacement is beneath the saturation threshold. In the experimental case, it is necessary to consider the closed-loop stability, which may be compromised if the static gain is sufficiently large. It should be noted that this gain scheduling scheme is not capable of preventing stroke saturation occurring from impulsive excitation, as it relies on steady-state input excitation for the adaption procedure. Therefore, the gain scheduling scheme cannot be used as a stand-alone control strategy for applications that feature transient or random excitation. Furthermore, the scheme is not suitable for preventing closed-loop destabilisation from occurring as a result of stroke saturation, as observed in Figure F.8b).

Having said this, the advantages of the gain scheduling scheme become more apparent when considering control cases where the control effort is large enough to regularly saturate the actuator, yet the closed-loop system is inherently stable. For example, a control law that is capable of preventing closed-loop destabilisation from actuator saturation, as discussed in the next section, may be introduced to stabilise the control system, but is not sufficient to prevent stroke saturation from occurring, particularly if the control gain is large. In this case, the gain scheduling scheme may be used to tune the feedback loop and adaptively reduce the input gain to the actuator to ensure that stroke saturation occurs less regularly, at the expense of a slightly reduced control effort. These control strategies, operating in conjunction, offer the possibility of optimising the feedback gain of the closed-loop system, such that the performance of the controller is maximised whilst minimising the occurrence of stroke saturation.

Appendix G

Plate Theory

In order to establish the mode shapes and natural frequencies of the plate used in chapters 6 and 7, we assume for purposes of simplicity thaat an isotrophic Kirchhoff model with simply supported boundaries gives a reasonable representation of the physical plate. The governing differential equation of motion for the plate model is given by [137],

$$D\nabla^2(x_1,x_2)\nabla^2(x_1,x_2)w(x_1,x_2,t) = -q(x_1,x_2,t) - \rho h_t \ddot{w}(x_1,x_2,t) \tag{G.1}$$

where $w(x_1,x_2,t)$ is the nodal deflection, x_1,x_2 are the nodal coordinates along the plates main dimensions, ρ is the average plate density, $q(x_1,x_2,t)$ is the force per unit area, h_t is the plate thickness, ∇^2 is the Laplacian operator, and D is the rigidity constant,

$$D = \frac{Eh_t}{12(1-\nu^2)} \tag{G.2}$$

with E being the Young's modulus and ν being the Poisson's ratio of the plate. The simply supported boundary conditions of the plate are,

$$w([\,0\,;\,a\,],[\,0\,;\,b\,],t) = 0, \;\; \nabla^2 w([\,0\,;\,a\,],[\,0\,;\,b\,],t) = 0 \tag{G.3}$$

where a and b represent the length and width of the plate respectively. Using Eq. G.1 and the boundary conditions given by Eq. G.3, we can define the solution of $w(x_1,x_2,t)$,

$$w(x_1,x_2,t) = F(t)W(x_1,x_2) \tag{G.4}$$

where $F(t)$ is time-harmonic of the form,

$$F(t) = Ae^{j\omega t} + Be^{-j\omega t} \tag{G.5}$$

and $W(x_1, x_2)$ is the spatial solution, which is defined as a summation of mode shapes,

$$W(x_1, x_2) = \sum_{m=1}^{\infty} \sum_{n=1}^{\infty} A_{mn} \sin\Big(\frac{m\pi x_1}{a}\Big) \sin\Big(\frac{n\pi x_2}{b}\Big) \tag{G.6}$$

Substituting Eq. G.4 into Eq. G.1 with $q(x_1, x_2, t) = 0$ (free vibration) results in the following expression,

$$\nabla^2(x_1, x_2)\nabla^2(x_1, x_2)W(x_1, x_2) = \frac{\omega^2 \rho h_t}{D} W(x_1, x_2) \tag{G.7}$$

This is a classic eigenvalue problem with an infinite number of solutions, each one corresponding to a particular mode. Substituting $W(x_1, x_2)$ at a single mode into Eq. G.7 yields,

$$\frac{\omega_{mn}^2 \rho h_t}{D} = \left(\Big(\frac{m\pi}{a}\Big)^2 + \Big(\frac{n\pi}{b}\Big)^2 \right)^2 \tag{G.8}$$

where ω_{mn} represents the natural frequencies of the plate. These natural frequencies are obtained by rearranging Eq. G.8, which yields,

$$\omega_{mn} = \pi^2 \sqrt{\frac{D}{\rho h_t}} \left(\frac{m^2}{a^2} + \frac{n^2}{b^2} \right) \tag{G.9}$$

In order to apply this expression, it is necessary to obtain the physical parameters of the plate. The measured plate dimensions are $a = 0.414$ m, $b = 0.314$ m, and $h_t = 0.001$ m respectively. The plate mass (M_s) was measured as $M_s = 0.41$ kg, which is slightly higher than the mass $\hat{M}_s = abh_t\hat{\rho} = 0.36$ kg estimated using $\rho = 2700$ kg/m^3, the standard density for aluminium. Instead, the measured plate mass is used to obtain the average plate density $\rho = 3150$ kg/m^3. It should be noted that the structural mass value $m_s = 0.162$ kg obtained in chapter 6 is the first modal mass of the plate, which is related to M_s through the proportionality constant β. Here, the proportionality constant is found to be $\beta = 0.39$, which appears to be reasonable.

The additional plate parameters are estimated using the physical properties of aluminium, and are shown in Table G.1. By applying these parameter values to Eq. G.9, the first few natural frequencies of the plate can be estimated. These estimations are compared to the first few resonance frequencies observed in $H_f(\omega, V)$, which is shown in Table G.2. In general, the estmated natural frequencies are larger than the observed

Table G.1: Plate properties and dimensions.

Parameter	**Value**
a	0.414 m
b	0.314 m
h_t	0.001 m
ρ	3150 kg/m^3
E	70 GPa
ν	0.33

resonance frequencies, for two reasons. Firstly, the peak resonance frequencies are slightly lower than the natural frequencies as a result of structural damping. Secondly, $H_f(\omega, V)$ illustrates the plate frequencies when coupled to the actuator, whereas the plate model estimates the uncoupled natural frequencies. Accounting for these effects, the estimated natural frequencies are reasonably consistent with the observed modal frequencies, which suggests that the plate behaves in a similar manner to an isotropic Kirchhoff plate in the frequency region of interest.

Table G.2: Comparison of estimated and observed plate frequencies.

Modal Freq.	ω_{11} (rad/s)	ω_{21} (rad/s)	ω_{12} (rad/s)	ω_{31} (rad/s)	ω_{22} (rad/s)
Estimated	227.3	476.4	660.2	891.4	909.3
Observed	200	420	620	780	920
Deviation	13.7 %	13.4 %	6.5 %	14.3 %	-1.2 %

The normalised mode shapes that are associated with these natural frequencies, as shown in Figure G.1, confirm that the dominant mode of the actuator-plate configuration corresponds to the first structural resonance at $\omega \approx \omega_{11}$. The unobservable mode in the acceleration-voltage FRFs relates to ω_{21}, where the nodal line lies in the middle of the plate, perpendicular to a. This suggests that the accelerometer is located close to the centre of the plate; however, the presence of the third plate mode at ω_{12} in the acceleration-voltage FRFs indicates that the accelerometer is not placed exactly at the exact centre of the plate, and so the higher-order modes are observable.

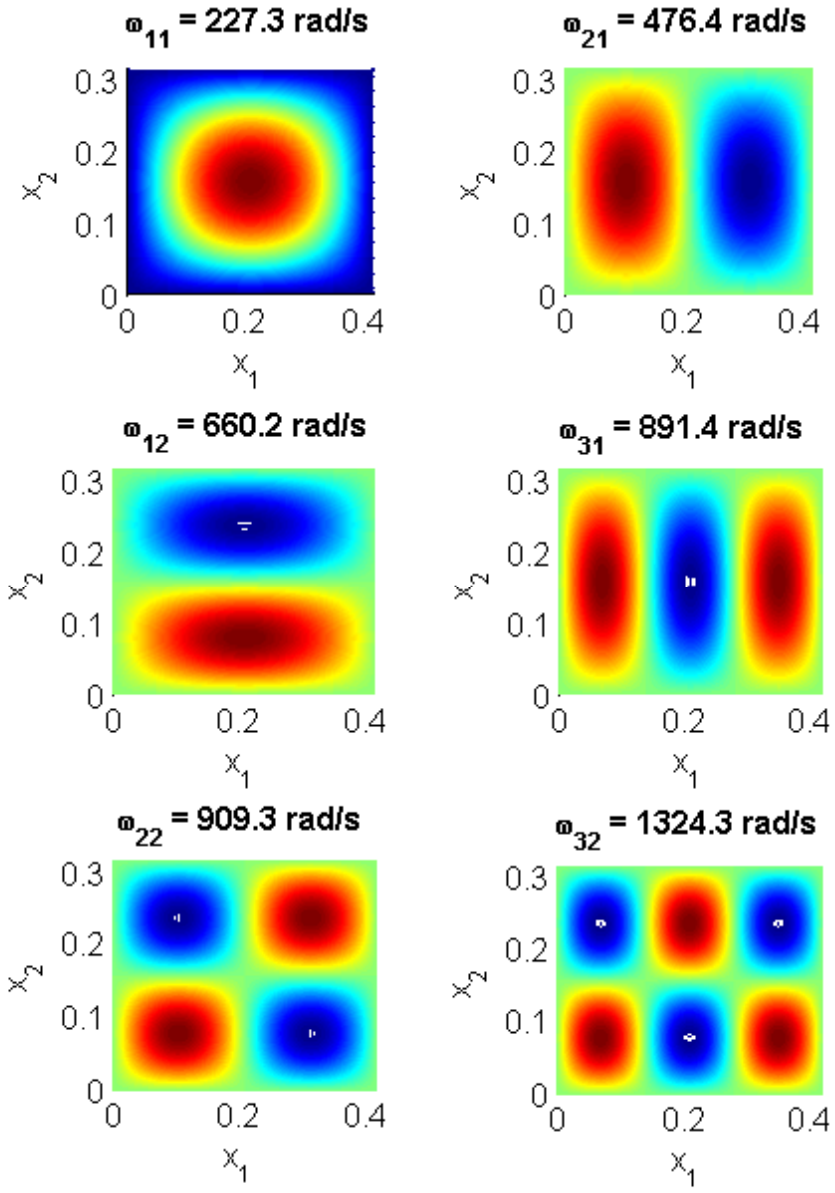

Figure G.1: Illustrations of the first six plate mode shapes. The second plate mode is unobservable in the accelerometer and the sixth plate mode is outside the frequency region of interest.

References

[1] K. J. Aström and R. M. Murray, *Feedback systems: an introduction for scientists and engineers*. Princeton University Press, 2010.

[2] E. M. Ku, *Modelling the human cochlea*. PhD thesis, University of Southampton, 2008.

[3] J. A. Stolwijk and J. D. Hardy, "Control of body temperature," *Comprehensive Physiology*, 1977.

[4] J. Hansen, A. Lacis, D. Rind, G. Russell, P. Stone, I. Fung, R. Ruedy, and J. Lerner, "Climate sensitivity: Analysis of feedback mechanisms," *Climate Processes and Climate Sensitivity*, pp. 130–163, 1984.

[5] "How cruise control systems work." URL : `http://auto.howstuffworks.com/cruise-control2.htm` [Accessed 01 May 2015].

[6] S. J. Elliott, *Signal processing for active control*. Academic Press, 2000.

[7] Y. Achkire and A. Preumont, "Active tendon control of cable-stayed bridges," *Earthquake engineering & structural dynamics*, vol. 25, no. 6, pp. 585–597, 1996.

[8] J. E. Mottershead, M. Ghandchi Tehrani, S. James, and P. Court, "Active vibration control experiments on an Agusta-Westland W30 helicopter airframe," *Proceedings of the Institution of Mechanical Engineers, Part C: Journal of Mechanical Engineering Science*, 2011.

[9] D. A. Swanson, "Active engine mounts for vehicles," tech. rep., SAE Technical Paper, 1993.

[10] K. Popp and P. Stelter, "Nonlinear oscillations of structures induced by dry friction," in *Nonlinear dynamics in engineering systems*, pp. 233–240, Springer, 1990.

[11] L. Ma and T. Wang, "Nonlinear bending and post-buckling of a functionally graded circular plate under mechanical and thermal loadings," *International Journal of Solids and Structures*, vol. 40, no. 13, pp. 3311–3330, 2003.

[12] K. Worden and G. R. Tomlinson, *Nonlinearity in structural dynamics: detection, identification, and modelling*. Taylor & Francis, 2001.

[13] D. Wagg and S. Neild, *Nonlinear vibration with control: for flexible and adaptive structures*. Springer, 2010.

[14] C. C. Fuller, S. J. Elliott, and P. A. Nelson, *Active control of vibration*. Academic Press, 1996.

[15] P. Reynolds and A. Pavic, "Vibration performance of a large cantilever grandstand during an international football match," *Journal of Performance of Constructed Facilities*, vol. 20, no. 3, pp. 202–212, 2006.

[16] S. Daley, F. Johnson, J. Pearson, and R. Dixon, "Active vibration control for marine applications," *Control Engineering Practice*, vol. 12, no. 4, pp. 465–474, 2004.

[17] J. E. Mottershead, M. G. Tehrani, S. James, and Y. M. Ram, "Active vibration suppression by pole-zero placement using measured receptances," *Journal of Sound and Vibration*, vol. 311, no. 35, pp. 1391 – 1408, 2008.

[18] M. Zilletti, S. J. Elliott, and P. Gardonio, "Self-tuning control systems of decentralised velocity feedback," *Journal of Sound and Vibration*, vol. 329, no. 14, pp. 2738 – 2750, 2010.

[19] A. Preumont, *Vibration control of active structures: an introduction*. Springer Science and Business Media, 2011.

[20] M. Gopal, *Control systems: principles and design*. McGraw-Hill, Inc., 2002.

[21] I. M. Díaz and P. Reynolds, "Acceleration feedback control of human-induced floor vibrations," *Engineering Structures*, vol. 32, no. 1, pp. 163–173, 2010.

[22] O. N. Baumann and S. J. Elliott, "Destabilization of velocity feedback controllers with stroke limited inertial actuators," *The Journal of the Acoustical Society of America*, vol. 121, no. 5, pp. EL211–EL217, 2007.

[23] D. K. Lindner, G. A. Zvonar, and D. Borojevic, "Performance and control of proof-mass actuators accounting for stroke saturation," *Journal of Guidance, Control, and Dynamics*, vol. 17, no. 5, pp. 1103–1108, 1994.

[24] J. G. Chase, M. Yim, and A. A. Berlin, "Integrated centering control of inertially actuated systems," *Control Engineering Practice*, vol. 7, no. 9, pp. 1079–1084, 1999.

[25] M. J. Balas, "Direct velocity feedback control of large space structures," *Journal of Guidance, Control, and Dynamics*, vol. 2, no. 3, pp. 252–253, 1979.

[26] S. Sherrit, "Smart material/actuator needs in extreme environments in space," in *Smart Structures and Materials*, pp. 335–346, International Society for Optics and Photonics, 2005.

[27] D. C. Zimmerman and D. J. Inman, "On the nature of the interaction between structures and proof-mass actuators," *Journal of Guidance, Control, and Dynamics*, vol. 13, no. 1, pp. 82–88, 1990.

[28] P. Gardonio and S. J. Elliott, "Smart panels with velocity feedback control systems using triangularly shaped strain actuators," *The Journal of the Acoustical Society of America*, vol. 117, no. 4, pp. 2046–2064, 2005.

[29] S. Cinquemani, F. Resta, and M. Monguzzi, "Limits on use of inertial actuators in active vibration control," in *9th International Conference on Computing, Communications and Control Technologies*, 2014.

[30] O. N. Baumann and S. J. Elliott, "The stability of decentralized multichannel velocity feedback controllers using inertial actuators," *The Journal of the Acoustical Society of America*, vol. 121, p. 188, 2007.

[31] D. K. Lindner, G. A. Zvonar, and D. Borojevic, "Nonlinear control of a proof-mass actuator," *Journal of Guidance, Control, and Dynamics*, vol. 20, no. 3, pp. 464–470, 1997.

[32] I. M. Díaz and P. Reynolds, "On-off nonlinear active control of floor vibrations," *Mechanical Systems and Signal Processing*, vol. 24, no. 6, pp. 1711–1726, 2010.

[33] J. E. Mottershead and Y. M. Ram, "Receptance method in active vibration control," *AIAA Journal*, vol. 45, no. 3, pp. 562–567, 2007.

[34] M. G. Tehrani, L. I. Wilmshurst, and S. J. Elliott, "Receptance method for active vibration control of a nonlinear system," *Journal of Sound and Vibration*, vol. 332, no. 19, pp. 4440 – 4449, 2013.

[35] G. Kerschen, K. Worden, A. F. Vakakis, and J.-C. Golinval, "Past, present and future of nonlinear system identification in structural dynamics," *Mechanical Systems and Signal Processing*, vol. 20, no. 3, pp. 505–592, 2006.

[36] A. H. Nayfeh and B. Balachandran, *Applied nonlinear dynamics*. Wiley lnterscience, New York, 1995.

[37] G. Kerschen, *On the model validation in non-linear structural dynamics*. PhD thesis, These de doctorat université de Liege, 2002.

[38] I. Kovacic and M. J. Brennan, *The Duffing equation: nonlinear oscillators and their behaviour*. John Wiley & Sons, 2011.

[39] M. O. L. Hansen, J. N. Sørensen, S. Voutsinas, N. Sørensen, and H. A. Madsen, "State of the art in wind turbine aerodynamics and aeroelasticity," *Progress in Aerospace Sciences*, vol. 42, no. 4, pp. 285–330, 2006.

[40] S. C. McIntosh Jr, R. E. Reed Jr, and W. P. Rodden, "Experimental and theoretical study of nonlinear flutter," *Journal of Aircraft*, vol. 18, no. 12, pp. 1057–1063, 1981.

[41] D. Tang and E. Dowell, "Flutter and stall response of a helicopter blade with structural nonlinearity," *Journal of Aircraft*, vol. 29, no. 5, pp. 953–960, 1992.

[42] L. Mrton, S. Fodor, and N. Sepehri, "A practical method for friction identification in hydraulic actuators," *Mechatronics*, vol. 21, no. 1, pp. 350 – 356, 2011.

[43] Y. Khulief, F. Al-Sulaiman, and S. Bashmal, "Vibration analysis of drillstrings with self-excited stick–slip oscillations," *Journal of Sound and Vibration*, vol. 299, no. 3, pp. 540–558, 2007.

[44] G. A. Gottwald and I. Melbourne, "A new test for chaos in deterministic systems," *Proceedings of the Royal Society of London. Series A: Mathematical, Physical and Engineering Sciences*, vol. 460, no. 2042, pp. 603–611, 2004.

[45] B. van der Pol, "On "relaxation-oscillations"," *The London, Edinburgh, and Dublin Philosophical Magazine and Journal of Science Ser.7*, vol. 2, pp. 978–992, 1926.

[46] A. Askenfelt, "Measurement of bow motion and bow force in violin playing," *The Journal of the Acoustical Society of America*, vol. 80, no. 4, pp. 1007–1015, 1986.

[47] A. Chaigne, C. Touzé, and O. Thomas, "Nonlinear vibrations and chaos in gongs and cymbals," *Acoustical Science and Technology*, vol. 26, no. 5, pp. 403–409, 2005.

[48] B. Zaghari, M. Ghandchi Tehrani, and E. Rustighi, "Mechanical modelling of a vibration energy harvester with time-varying stiffness," *Eurodyn 2014: IX International Conference on Structural Dynamics*, 2014.

[49] D. M. Storer and G. R. Tomlinson, "Recent developments in the measurement and interpretation of higher order transfer functions from non-linear structures," *Mechanical Systems and Signal Processing*, vol. 7, no. 2, pp. 173–189, 1993.

[50] V. Volterra, *Theory of Functionals and Integral Equations*. Dover, 1959.

[51] D. Graham and D. T. McRuer, *Analysis of nonlinear control systems*. Wiley, 1961.

[52] A. Bacciotti and L. Rosier, *Liapunov functions and stability in control theory*. Springer, 2005.

[53] A. M. Lyapunov, "The general problem of motion stability," *Annals of Mathematics Studies*, vol. 17, 1892.

[54] H. K. Khalil and J. Grizzle, *Nonlinear systems*. Prentice Hall: New Jersey, 3rd ed., 1996.

[55] F. Verhulst, "On averaging methods for partial differential equations," *Symmetry and Perturbation Theory*, 2001.

[56] P. Glendinning, *Stability, instability and chaos: an introduction to the theory of nonlinear differential equations*. Cambridge University Press, 1994.

[57] J. Cole and J. Kevorkian, "Multiple scale and singular perturbation methods," *Appl. Math. Sci*, vol. 114, 1996.

[58] S. A. Neild and D. J. Wagg, "Applying the method of normal forms to second-order nonlinear vibration problems," in *Proceedings of the Royal Society of London A: Mathematical, Physical and Engineering Sciences*, vol. 467, pp. 1141–1163, 2011.

[59] L. Jezequel and C. H. Lamarque, "Analysis of non-linear dynamical systems by the normal form theory," *Journal of Sound and Vibration*, vol. 149, no. 3, pp. 429–459, 1991.

[60] M. King and A. Vakakis, "An energy-based approach to computing resonant nonlinear normal modes," *Journal of Applied Mechanics*, vol. 63, no. 3, pp. 810–819, 1996.

[61] C. Pierre, D. Jiang, and S. Shaw, "Nonlinear normal modes and their application in structural dynamics," *Mathematical Problems in Engineering*, vol. 2006, 2006.

[62] R. Bhattacharya, G. J. Balas, M. A. Kaya, and A. Packard, "Nonlinear receding horizon control of an F-16 aircraft," *Journal of Guidance, Control, and Dynamics*, vol. 25, no. 5, pp. 924–931, 2002.

[63] D. M. Dawson, J. Hu, and T. C. Burg, *Nonlinear control of electric machinery.* Marcel Dekker, Inc., 1998.

[64] L. Gaul and R. Nitsche, "The role of friction in mechanical joints," *Applied Mechanics Reviews*, vol. 54, no. 2, pp. 93–106, 2001.

[65] D. Tang and E. Dowell, "Effects of geometric structural nonlinearity on flutter and limit cycle oscillations of high-aspect-ratio wings," *Journal of Fluids and Structures*, vol. 19, no. 3, pp. 291–306, 2004.

[66] R. H. Rand, "Lecture notes on nonlinear vibrations," 2012.

[67] M. Brennan, I. Kovacic, A. Carrella, and T. Waters, "On the jump-up and jump-down frequencies of the Duffing oscillator," *Journal of Sound and Vibration*, vol. 318, no. 4, pp. 1250–1261, 2008.

[68] W. Klippel, "Tutorial: Loudspeaker nonlinearities - causes, parameters, symptoms," *Journal of the Audio Engineering Society*, vol. 54, no. 10, pp. 907–939, 2006.

[69] F. Moon and P. J. Holmes, "A magnetoelastic strange attractor," *Journal of Sound and Vibration*, vol. 65, no. 2, pp. 275–296, 1979.

[70] S. Novak and R. Frehlich, "Transition to chaos in the Duffing oscillator," *Physical Review A*, vol. 26, no. 6, p. 3660, 1982.

[71] F. Jian-Shu, H. Wen-Hua, and Z. Xi-Li, "An analytical study for controlling chaos in Duffing oscillator with weak periodic perturbation," *Chinese Physics Letters*, vol. 18, no. 3, p. 334, 2001.

[72] C. Lu and R. Evan-Iwanowski, "Period-doubling bifurcation problems in the softening Duffing oscillator with nonstationary excitation," *Nonlinear Dynamics*, vol. 5, no. 4, pp. 401–420, 1994.

[73] H. Hu, E. H. Dowell, and L. N. Virgin, "Resonances of a harmonically forced Duffing oscillator with time delay state feedback," *Nonlinear Dynamics*, vol. 15, no. 4, pp. 311–327, 1998.

[74] G. Chen, J. L. Moiola, and H. O. Wang, "Bifurcation control: theories, methods, and applications," *International Journal of Bifurcation and Chaos*, vol. 10, no. 3, pp. 511–548, 2000.

[75] M. Nagurka and S. Huang, "A mass-spring-damper model of a bouncing ball," in *American Control Conference, 2004. Proceedings of the 2004*, vol. 1, pp. 499–504, 2004.

[76] L. I. Wilmshurst, M. Ghandchi Tehrani, and S. J. Elliott, "Nonlinear vibrations of a stroke-saturated intertial actuator," *11th International Conference on Recent Advances in Structural Dynamics*, 2013.

[77] L. I. Wilmshurst, M. Ghandchi Tehrani, and S. J. Elliott, "Nonlinear identification of proof-mass actuators accounting for stoke saturation," *Proceedings of the 2014 International Conference on Noise and Vibration Engineering, ISMA*, 2014.

[78] A. Luré and V. Postnikov, "On the theory of stability of control systems," *Applied Mathematics and Mechanics*, vol. 8, no. 3, 1944 (in Russian).

[79] W. E. Arthur Gelb, V. Velde, *Multiple-input describing functions and nonlinear system design.* New York: McGraw-Hill, 1968.

[80] M. B. Özer, H. N. Özgüven, and T. J. Royston, "Identification of structural nonlinearities using describing functions and the Sherman–Morrison method," *Mechanical Systems and Signal Processing*, vol. 23, no. 1, pp. 30–44, 2009.

[81] A. Mees, "The describing function matrix," *IMA Journal of Applied Mathematics*, vol. 10, no. 1, pp. 49–67, 1972.

[82] Z. Q. Lang, S. A. Billings, R. Yue, and J. Li, "Output frequency response function of nonlinear Volterra systems," *Automatica*, vol. 43, no. 5, pp. 805–816, 2007.

[83] Z. Peng, Z. Lang, S. Billings, and G. Tomlinson, "Comparisons between harmonic balance and nonlinear output frequency response function in nonlinear system analysis," *Journal of Sound and Vibration*, vol. 311, no. 1, pp. 56–73, 2008.

[84] H. Sato and K. Asada, "Laplace transform transient analysis of a non-linear system," *Journal of Sound and Vibration*, vol. 121, no. 3, pp. 473–479, 1988.

[85] S. J. Gifford, *Volterra series analysis of nonlinear structures.* PhD thesis, Heriot-Watt University, 1989.

[86] D. M. Storer, *Dynamic analysis of non-linear structures using higher order frequency response functions.* PhD thesis, University of Manchester, 1991.

[87] G. Christensen, "On the convergence of Volterra series," *IEEE Transactions on Automatic Control*, vol. 13, no. 6, pp. 736–737, 1968.

[88] Z. Peng and Z. Lang, "On the convergence of the Volterra-series representation of the Duffing oscillators subjected to harmonic excitations," *Journal of Sound and Vibration*, vol. 305, no. 1, pp. 322–332, 2007.

[89] G. Tomlinson, G. Manson, and G. Lee, "A simple criterion for establishing an upper limit to the harmonic excitation level of the Duffing oscillator using the Volterra series," *Journal of Sound and Vibration*, vol. 190, no. 5, pp. 751–762, 1996.

[90] L. Li and S. Billings, "Continuous time non-linear system identification in the frequency domain," *International Journal of Control*, vol. 74, no. 11, pp. 1052–1061, 2001.

[91] J. C. Butcher, *The numerical analysis of ordinary differential equations: Runge-Kutta and general linear methods.* Wiley-Interscience, 1987.

[92] P. Bogacki and L. F. Shampine, "A 3 (2) pair of Runge-Kutta formulas," *Applied Mathematics Letters*, vol. 2, no. 4, pp. 321–325, 1989.

[93] O. M. Boaghe and S. A. Billings, "Subharmonic oscillation modeling and MISO Volterra series," *IEEE Transactions on Automatic Control on Circuits and Systems I: Fundamental Theory and Applications*, vol. 50, no. 7, pp. 877–884, 2003.

[94] S. A. Billings and O. M. Boaghe, "The response spectrum map, a frequency domain equivalent to the bifurcation diagram," *International Journal of Bifurcation and Chaos*, vol. 11, no. 7, pp. 1961–1975, 2001.

[95] M. Friswell and J. Penny, "Stepped sine testing using recursive estimation," *Mechanical Systems and Signal Processing*, vol. 7, no. 6, pp. 477–491, 1993.

[96] H.-D. Chiang, M. W. Hirsch, and F. F. Wu, "Stability regions of nonlinear autonomous dynamical systems," *IEEE Transactions on Automatic Control*, vol. 33, no. 1, pp. 16–27, 1988.

[97] L. Arnold and V. Wihstutz, *Lyapunov exponents: a survey*. Springer, 1986.

[98] N. H. El-Farra, P. Mhaskar, and P. D. Christofides, "Output feedback control of switched nonlinear systems using multiple Lyapunov functions," *Systems & Control Letters*, vol. 54, no. 12, pp. 1163 – 1182, 2005.

[99] Y. Ohta, T. Wada, and D. Siljak, "Stability analysis of discontinuous nonlinear systems via piecewise linear Lyapunov functions," in *American Control Conference, 2001. Proceedings of the 2001*, vol. 6, pp. 4852–4857, 2001.

[100] S. Engelberg, "Limitations of the describing function for limit cycle prediction," *IEEE Transactions on Automatic Control*, vol. 47, no. 11, pp. 1887–1890, 2002.

[101] A. Rantzer, "On the Kalman-Yakubovich-Popov lemma," *Systems & Control Letters*, vol. 28, no. 1, pp. 7–10, 1996.

[102] W. M. Wonham, "On pole assignment in multi-input controllable linear systems," *IEEE Transactions on Automatic Control*, vol. 12, no. 6, pp. 660–665, 1967.

[103] L. Meirovitch, *Dynamics and control of structures*. John Wiley & Sons, 1990.

[104] F. Liu, "Pole placement control for nonlinear systems via neural networks," in *Advances in Neural Networks - ISNN 2004* (F.-L. Yin, J. Wang, and C. Guo, eds.), vol. 3174 of *Lecture Notes in Computer Science*, pp. 123–128, Springer Berlin Heidelberg, 2004.

[105] S.-K. Yang, C.-L. Chen, and H.-T. Yau, "Control of chaos in Lorenz system," *Chaos, Solitons & Fractals*, vol. 13, no. 4, pp. 767 – 780, 2002.

[106] M. Ghandchi-Tehrani, L. I. Wilmshurst, and S. J. Elliott, "Bifurcation control of a Duffing oscillator using pole placement," *Journal of Vibration and Control*, 2014.

[107] N. M. Krylov, N. N. Bogoliubov, and S. Lefschetz, *Introduction to Nonlinear Mechanics*. Annals of mathematics studies, Princeton University Press, 1943.

[108] J. Sherman and W. J. Morrison, "Adjustment of an inverse matrix corresponding to a change in one element of a given matrix," *The Annals of Mathematical Statistics*, vol. 21, no. 1, pp. 124–127, 1950.

[109] S. F. Masri, H. Sassi, and T. K. Caughey, "Nonparametric identification of nearly arbitrary nonlinear systems," *Journal of Applied Mechanics*, vol. 49, p. 619, 1982.

[110] D. H. Formenti and M. L. Richardson, "Parameter estimation from frequency response measurements using rational fraction polynomials (twenty years of progress)," in *SPIE proceedings series*, Society of Photo-Optical Instrumentation Engineers, 2002.

[111] A. C. Luo and J. Huang, "Approximate solutions of periodic motions in nonlinear systems via a generalized harmonic balance," *Journal of Vibration and Control*, vol. 18, no. 11, pp. 1661–1674, 2011.

[112] L. Li and S. Billings, "Analysis of nonlinear oscillators using Volterra series in the frequency domain," *Journal of Sound and Vibration*, vol. 330, no. 2, pp. 337–355, 2011.

[113] E. Ott, C. Grebogi, and J. A. Yorke, "Controlling chaos," *Phys. Rev. Lett.*, vol. 64, pp. 1196–1199, 1990.

[114] A. H. Nayfeh and N. E. Sanchez, "Bifurcations in a forced softening Duffing oscillator," *International Journal of Non-Linear Mechanics*, vol. 24, no. 6, pp. 483–497, 1989.

[115] S.-Y. Kim and Y. Kim, "Dynamic stabilization in the double-well Duffing oscillator," *Phys. Rev. E*, vol. 61, pp. 6517–6520, 2000.

[116] M. Balajewicz, F. Nitzsche, and D. Feszty, "Application of multi-input Volterra theory to nonlinear multi-degree-of-freedom aerodynamic systems," *AIAA Journal*, vol. 48, no. 1, pp. 56–62, 2010.

[117] Z. Peng, Z. Lang, and S. Billings, "Non-linear output frequency response functions of MDOF systems with multiple non-linear components," *International Journal of Non-Linear Mechanics*, vol. 42, no. 7, pp. 941–958, 2007.

[118] S. A. Billings, *Nonlinear System Identification: NARMAX Methods in the Time, Frequency, and Spatio-Temporal Domains*. Wiley, 2013.

[119] C. Paulitsch, P. Gardonio, S. Elliott, P. Sas, and R. Boonen, "Design of a lightweight, electrodynamic, inertial actuator with integrated velocity sensor for active vibration control of a thin lightly-damped panel," in *Proceedings of the 2004 International Conference on Noise and Vibration Engineering, ISMA*, pp. 239–253, 2004.

[120] J. G. Ribeiro, J. L. Freire, and J. T. De Castro, "Some comments on digital integration to measure displacements using accelerometers," in *SPIE Proceedings Series*, pp. 554–559, 1999.

[121] J. G. Ribeiro, J. T. de Castro, and J. L. Freire, "New improvements in the digital double integration filtering method to measure displacements using accelerometers," in *Proceedings of the International Modal Analysis Conference*, vol. 1, pp. 538–542, International Society for Optical Engineering, 2001.

[122] M. Daparti, "Numerical and experimental investigation of double impacts on a beam," Master's thesis, DIPL-99, Institute B of Mechanics, University of Stuttgart, Stuttgart, 2003.

[123] H. Hu, "Solution of a quadratic nonlinear oscillator by the method of harmonic balance," *Journal of Sound and Vibration*, vol. 293, no. 1, pp. 462–468, 2006.

[124] J. Hammond, "Fundamentals of signal processing," *Fundamentals of Noise and Vibration*, pp. 311–370, 1998.

[125] D. Čelič and M. Boltežar, "Identification of the dynamic properties of joints using frequency–response functions," *Journal of Sound and Vibration*, vol. 317, no. 1, pp. 158–174, 2008.

[126] B. Peeters, W. Hendricx, J. Debille, and H. Climent, "Modern solutions for ground vibration testing of large aircraft," *Journal of Sound and Vibration*, vol. 43, no. 1, p. 8, 2009.

[127] H. M. Lankarani and P. E. Nikravesh, "Continuous contact force models for impact analysis in multibody systems," *Nonlinear Dynamics*, vol. 5, no. 2, pp. 193–207, 1994.

[128] "Active damping devices and inertial actuators," 2003. URL : `www.micromega-dynamics.com/doc/ADD_Catalog_Rev2.pdf` [Accessed 28 May 2013].

[129] K. L. Johnson, *Contact mechanics*. Cambridge University Press, 1987.

[130] H. Hertz, "On the contact of elastic solids," *J. Reine Angew. Math*, vol. 92, no. 110, pp. 156–171, 1881.

[131] K. R. Rajagopal, "A note on a reappraisal and generalization of the Kelvin–Voigt model," *Mechanics Research Communications*, vol. 36, no. 2, pp. 232–235, 2009.

[132] C. Rajalingham and S. Rakheja, "Analysis of impact force variation during collision of two bodies using a single-degree-of-freedom system model," *Journal of Sound and Vibration*, vol. 229, no. 4, pp. 823–835, 2000.

[133] D. Roylance, "Engineering viscoelasticity," *Department of Materials Science and Engineering–Massachusetts Institute of Technology, Cambridge MA*, vol. 2139, pp. 1–37, 2001.

[134] E. H. Moussi, S. Bellizzi, B. Cochelin, and I. Nistor, "Nonlinear normal modes of a two degrees-of-freedom piecewise linear system," *Mechanical Systems and Signal Processing*, 2013.

[135] G. Gilardi and I. Sharf, "Literature survey of contact dynamics modelling," *Mechanism and Machine Theory*, vol. 37, no. 10, pp. 1213 – 1239, 2002.

[136] W. Serweta, A. Okolewski, B. Blazejczyk-Okolewska, K. Czolczynski, and T. Kapitaniak, "Lyapunov exponents of impact oscillators with Hertz's and Newton's contact models," *International Journal of Mechanical Sciences*, vol. 89, pp. 194 – 206, 2014.

[137] S. Timoshenko and S. Woinowsky-Krieger, *Theory of plates and shells*. McGraw-Hill, New York, 1959.

[138] J. T. Machado, "Discrete-time fractional-order controllers," *Fractional Calculus and Applied Analysis*, vol. 4, no. 1, pp. 47–66, 2001.

[139] N. F. Macia and G. J. Thaler, *Modeling and control of dynamic systems*. Cengage Learning, 2005.

[140] R. M. Murray, Z. Li, S. S. Sastry, and S. S. Sastry, *A mathematical introduction to robotic manipulation*. CRC Press, 1994.

[141] L. I. Wilmshurst, M. Ghandchi Tehrani, and S. J. Elliott, "Active control and stability analysis of flexible structures using nonlinear proof-mass actuators," *Eurodyn 2014: IX International Conference on Structural Dynamics*, 2014.

[142] G. Brecq, J. Bellettre, and M. Tazerout, "A new indicator for knock detection in gas SI engines," *International Journal of Thermal Sciences*, vol. 42, no. 5, pp. 523–532, 2003.

[143] F. Millo and C. V. Ferraro, "Knock in SI engines: a comparison between different techniques for detection and control," tech. rep., SAE Technical Paper, 1998.

[144] T. Barszcz and R. B. Randall, "Application of spectral kurtosis for detection of a tooth crack in the planetary gear of a wind turbine," *Mechanical Systems and Signal Processing*, vol. 23, no. 4, pp. 1352–1365, 2009.

[145] C. Pachaud, R. Salvetat, and C. Fray, "Crest factor and kurtosis contributions to identify defects including periodical impulsive forces," *Mechanical Systems and Signal Processing*, vol. 11, no. 6, pp. 903 – 916, 1997.

[146] L. I. Wilmshurst, M. Ghandchi Tehrani, and S. J. Elliott, "Prevention of stroke saturation in inertial actuators using a detection scheme," *The 21st International Congress on Sound and Vibration*, 2014.

[147] B. Paijmans, W. Symens, H. Van Brussel, and J. Swevers, "A gain-scheduling-control technique for mechatronic systems with position-dependent dynamics," in *American Control Conference, 2006*, pp. 639–650, 2006.

[148] H. Schulte and H. Hahn, "Fuzzy state feedback gain scheduling control of servo-pneumatic actuators," *Control Engineering Practice*, vol. 12, no. 5, pp. 639–650, 2004.

[149] S. K. Menon and A. G. Parlos, "Gain-scheduled nonlinear control of U-tube steam generator water level," *Nuclear Science and Engineering*, vol. 111, no. 3, pp. 294–308, 1992.

[150] J. Jiang, "Optimal gain scheduling controller for a diesel engine," *Control Systems, IEEE*, vol. 14, no. 4, pp. 42–48, 1994.

[151] A. Nassirharand and H. Karimi, "Nonlinear controller synthesis based on inverse describing function technique in the MATLAB environment," *Advances in Engineering Software*, vol. 37, no. 6, pp. 370–374, 2006.

[152] K. Shin and J. Hammond, *Fundamentals of signal processing for sound and vibration engineers*. Wiley, 2008.